UNIVERSITY OF ILLINOIS
URBANA

AERONOMY REPORT NO. 74

THE URBANA METEOR-RADAR SYSTEM: DESIGN, DEVELOPMENT, AND FIRST OBSERVATIONS

by
G. C. Hess
M. A. Geller

October 1, 1976

Library of Congress ISSN 0568-0581

Supported by
National Aeronautics and Space Administration
Grant NGR 14-005-181 and
National Science Foundation Grant ATM-76-01773

Aeronomy Laboratory
Department of Electrical Engineering
University of Illinois
Urbana, Illinois

UILU-ENG 76 2505

A E R O N O M Y R E P O R T

N O. 74

THE URBANA METEOR-RADAR SYSTEM: DESIGN, DEVELOPMENT, AND FIRST OBSERVATIONS

by

G. C. Hess
M. A. Geller

October 1, 1976

Supported by
National Aeronautics and Space
Administration Grant NGR 14-005-181
National Science Foundation
Grant ATM 76-01773

Aeronomy Laboratory
Department of Electrical Engineering
University of Illinois
Urbana, Illinois

ABSTRACT

The design, development, and first observations of a high-power meteor-radar system located near Urbana, Illinois are described. The roughly five-fold increase in usable echo rate compared to other facilities, along with automated digital data processing and interferometry measurement of echo arrival angles, permits unsurpassed observations of tidal structure and shorter period waves. Such observations are discussed at length. Also, the technique of using echo decay rates to infer density and scale height and the technique of inferring wind shear from radial acceleration are examined. Lastly, an original experiment to test a theory of the *D*-region winter anomaly is presented.

TABLE OF CONTENTS

LIST OF TABLES

LIST OF FIGURES

1. INTRODUCTION

1.1 *Upper Atmosphere Winds*

It is instructive to decompose the neutral winds of the upper atmosphere into three components. In order of increasing temporal and spatial scales these components are the prevailing wind, the tidal wind, and the irregular wind [*Beer*, 1972].

Under an equilibrium situation among gravity, pressure, and Coriolis forces a geostrophic wind system results. We identify this geostrophic wind with the prevailing wind component. A decomposition of the prevailing wind is also possible, into a zonal mean wind (an average around a latitude circle, not to be confused with the mean zonal wind observed at any single location) and planetary wave contributions [*Charney and Drazin*, 1961; *Schoeberl and Geller*, 1976]. The zonal prevailing wind component generally dominates over the meridional component at midlatitudes.

Superimposed on the prevailing wind are tidal wind perturbations. These tides are predominantly solar tides forced by heating of ozone and water vapor rather than by gravitational effects [*Chapman and Lindzen*, 1970]. A 24-hour period component, the solar diurnal tide, results from the superposition of many modes comparably excited, some propagating, some evanescent. A 12-hour mode of substantial vertical wavelength is the principally forced solar semidiurnal tidal mode. However, this mode can be vertically evanescent in regions below the meteor zone and thus higher order propagating modes of somewhat shorter wavelengths can sometimes dominate the 12-hour variation there. This is because for vertically propagating waves free from dissipation mechanisms tidal theory predicts wave amplifications as $\rho^{-1/2}$, where the neutral gas density ρ decreases approximately exponentially with altitude. An additional factor which may enhance higher order modes is mode

coupling. Such coupling allows forcing of one mode to excite another mode indirectly. Tidal modes of 8-hours, 6-hours, etc. are theoretically possible but quite weak relative to the 12 and 24 hour oscillations.

Due to gravitational stratification of the atmosphere, a class of waves called internal gravity waves exists in which air particle motions approximately transverse to the direction of the wave propagation occur. In fact the tidal winds themselves can be considered members of this class, but tides have such long temporal and spatial scales that rotational effects are important and thus they are normally considered separately. *Hines* [1960] has shown that many properties of the supposedly random irregular wind can, in fact, be explained in terms of internal gravity waves. For example, chemical and meteor trail "snapshots" of the irregular wind show it to be predominantly horizontal, increasing in amplitude with height, and with temporal and vertical scales of about 100 minutes and 6 km, resprectively. True turbulence also contributes to the irregular wind, at least below the turbopause height of roughly 110 km. The separation of these two constituents, turbulence and small scale wave motions, is far from straightforward [*Stewart*, 1969].

1.2 *Experimental Techniuqes*

A summary of some experimental techniques used in exploring the atmosphere is given in *McAvaney* [1970]. We will follow this summary, updating it as appropriate with more recent developments. Figure 1.1 illustrates the parameters measured and height ranges encompassed by many of the experimental techniques. Note that the techniques have been divided into the general categories of direct and indirect methods. In general direct methods cannot be used routinely at meteor altitudes because of the high cost per sounding. However, despite their inability to provide temporal resolution,

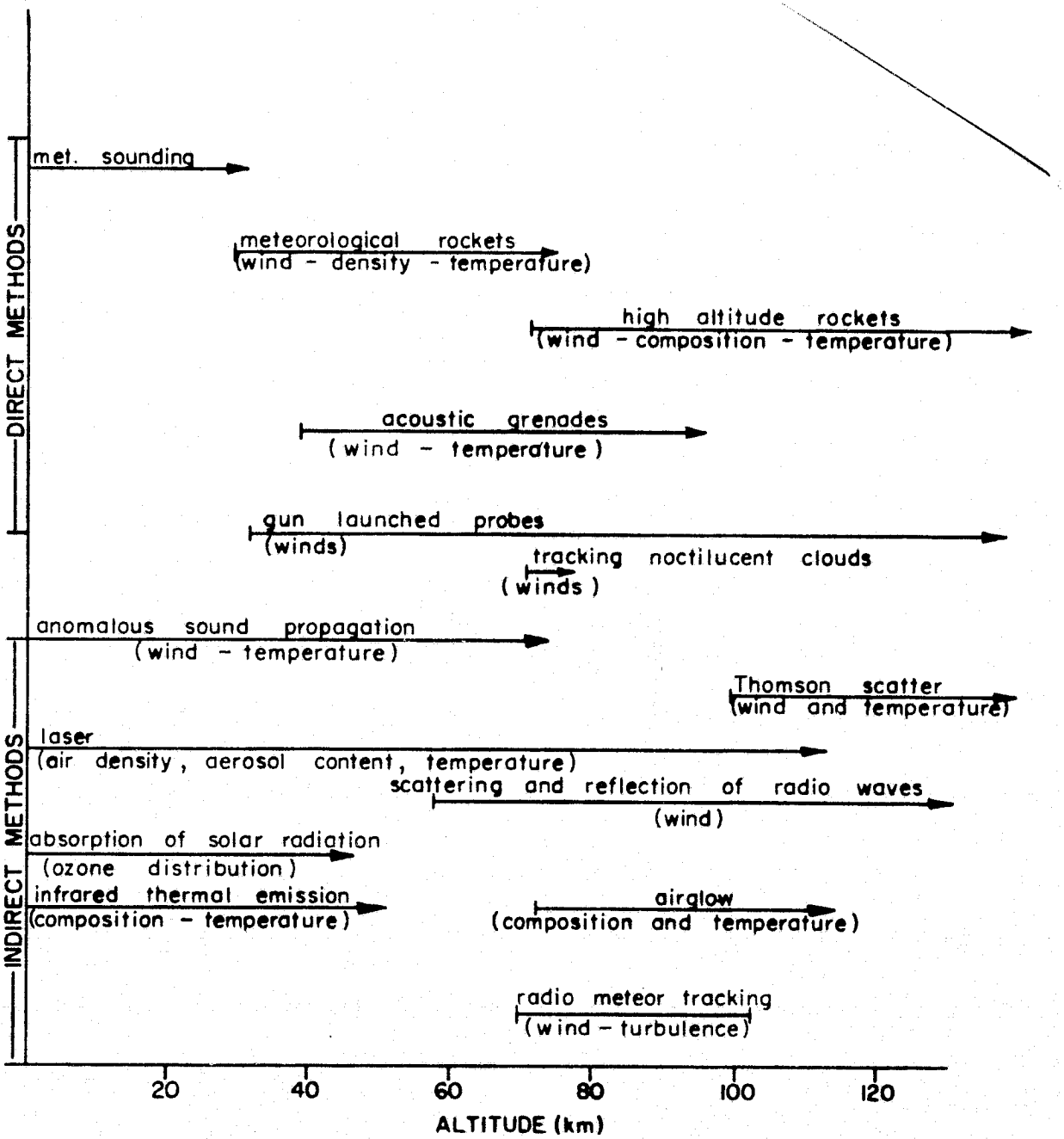

Figure 1.1 Experimental methods in exploring the atmosphere [*Fedele*, 1968].

they do give very accurate "snapshots" of the vertical structure of each parameter measured. Also, because of their high accuracy, direct methods are useful as references in evaluating the accuracy of indirct methods, which generally suffer from limited height resolution.

1.2.1 *Direct methods*

Meteorological Rockets

Rockets capable of reaching altitudes up to 65 km are relatively inexpensive today and permit measurement of the main meteorological parameters: wind, temperature, and density. Radar chaff, inflatable spheres, and reflectorized parachutes have been used in conjunction with precision tracking radars to obtain winds. The falling sphere technique also yields atmospheric density via the drag acceleration [*Bartman et al.*, 1956]. The Meteorological Rocket Network [*Webb et al.*, 1961] utilizes an active package containing a bead thermistor for temperature measurement which is lowered through the region of interest by parachute.

Acoustic Grenades

In this technique a sequence of grenades is fired at intervals of a few kilometers as the rocket ascends through the desired height region. Each explosion is precisely resolved in time and space by photographic and photoelectric monitors and the times and directions of arrival of the acoustic waves at ground level are recorded by a microphone array. The wave fronts are traced back through an assumed model atmosphere to find "virtual" positions for each explosion. Gradual modifications of the assumed wind and temperature structures in the model permit a closer and closer approximation to the true structure to be achieved [*Groves*, 1960].

Contaminant Releases

Ejection of certain chemicals from high altitude rockets is a convenient

means of studying winds and turbulence above about 70 km. Alkali vapors, particularly sodium, resonantly scatter sunlight and if the background sky illumination is low enough they can be tracked by photographic triangulation [*Kochanski*, 1964]. The background requirement restricts use of these chemicals to twilight and sunrise periods. Use of materials like trimethylaluminum which react photochemically with atomic oxygen produces luminous trails at night and thus eases the background requirement [*Rosenberg et al.*, 1963]. In fact by use of appropriate spectral filters, lithium vapor trails can be tracked during any part of the day. [*Bedinger*, 1973].

Gun-Launched Probes

Gun-launched probes have been used to inject radar chaff and chemicals up to altitudes of 150 km [*Murphy et al.*, 1966]. The tremendous accelerations severely limit their use as active payloads but the technique is an attractive economic alternative to rocket programs.

Noctilucent Clouds

The occasional appearance of these high altitude clouds (80 km) at high latitudes in summer permits detailed study of both spatial and temporal wind behavior [*Witt*, 1969]. These clouds, which are composed of small dust and ice or supercooled water particles, show bodily movement and wave motion often in different directions. While noctilucent cloud photography is unique in character, it is severely hampered by its restrictive altitude span and the rarity of appearance of the clouds.

1.2.2 *Indirect methods*

Ionospheric Drifts

The reflection of radio waves from the ionosphere results in a diffraction pattern being formed on the ground. Sampling with spaced antennas allows one to determine parameters which describe the pattern behavior and

enable estimates of ionospheric drift velocity [*Guha*, 1968]. The technique has mainly been applied to *E*-region drifts but the technique has also been applied to the weak *D*-region partial reflections [*Manson et al.*, 1974]. In this latter case drifts can be obtained down to about 60 km around local noon. However, difficulties arise in interpreting the derived drifts as synonymous with neutral winds [*Kent and Wright*, 1968; *Guha and Geller*, 1972].

Incoherent Scatter

An interesting possibility for measuring winds above about 95 km is by the use of incoherent (Thomson) scatter. The Doppler shift due to ions can be determined from the spectrum of received pulses [*Evans*, 1969], and up to an altitude of perhaps 115 km the collision frequency is high enough that ions should travel with the neutral air. *Bernard* [1974] presents results obtained at the Saint-Santin (France) facility.

By evaluating the auto-covariance function of returned pulses, due to coherent motions at scales one-half the probing wavelength, mesospheric and even stratospheric winds can be determined [*Woodman and Guillen*, 1974; *Rastogi and Bowhill*, 1976].

Airglow

The word "airglow" was introduced in 1950 for optical emissions other than the polar aurora originating in the Earth's upper atmosphere. Photometer measurements of such emissions permit inferences on upper atmosphere chemistry, temperature, and winds [*Armstrong and Dalgarno*, 1955; *Hernandez and Roble*, 1976].

Meteor Radar

The first measurements of winds by radar tracking of meteor trails were made by *Manning et al.* [1950], although detection of meteors and investigations of their astronomical properties via radar was accomplished

much earlier. The basic parameters which must be determined for wind analysis are the spatial coordinates of the meteor trail reflection point and the radial velocity of the trail at that point. Two main radar configurations have been developed to accomplish these tasks: phase-coherent pulse radars and continuous wave radars. The former offer simple time discrimination against airplane reflections and monostatic operation. Bistatic operation is necessary in the CW case, but the narrower receiver bandwidths permissible mean that much lower transmitter powers can yield comparable echo rates. This improves reliability while reducing system cost and complexity. The phase-coherent pulse method developed by *Greenhow* [1952] is employed by the University of Illinois meteor radar. CW systems have recently been freed from the need of a companion pulse transmitter for ranging thanks to the phase difference ranging method developed at Garchy [*Spizzichino et al.*, 1965].

1.3 *Unique Aspects of the Urbana Meteor-Radar System*

Table 1.1 lists locations of other meteor-radar facilities which have reported results and their normal mode of operation. Major limitations of systems previous to ours centered around low data rates, typically only on the order of 50 usable echoes per hour maximum, and long delays between data collection and availability of processed results. Lack of sufficient height resolution for measuring vertical wind structures also has been a common shortcoming. The following paragraphs outline our solutions to each of these three common limitations.

At Urbana we have achieved usable echo rates of several hundreds per hour even with a conservative 20 dB signal-to-noise requirement (compared to a maximum of about 50 per hour at other facilities). This has been accomplished through the use of a very high power pulsed transmitter and highly

Table 1.1

Meteor-radar facilities.

Station	Latitude	Longitude
Mawson CW & Pulse	68 S	67 E
Molodeshnaya	67 S	57 E
Christchurch	44 S	173 E
Adelaide CW & Pulse	35 S*	130 E
Mogadishu	2 N	47 E
Kingston Pulse	18 N	77 W
Eglin Coded Pulse	31 N	87 W
Ashkabad	37 N	59 E
Stanford Coded Pulse	37 N	122 W
Dushanbe Pulse	38 N	69 E
Havana Pulse	40 N*	90 W
Lexington Pulse	42 N	71 W
Frunze Pulse	43 N	75 E
Durham Pulse	43 N	71 W
Garchy CW	47 N	3 E
Breisach	48 N	7 E
Kiev Pulse	50 N	31 E
Kharkov Pulse	50 N	36 E
Bracknell Pulse	51 N	1 W
Jodrell Bank Pulse	53 N	2 W
Sheffield Pulse	53 N	1 W
Obninsk Pulse	56 N	38 E
Kazan Pulse	56 N	49 E
Tomsk Pulse	57 N	85 E
College CW	65 N	148 W
Heiss Island	80 N	38 E
Hayes Island Pulse	79 N	58 E
White Sands Pulse	33 N	106 W
Moscow Pulse	59 N	37 E
Atlanta CW	34 N	84 W

* Multi-station

This list compiled from *Teptin* [1972], *Roper* [1971], *Barnes* [1972], and *McAvaney* [1970].

directive antennas for both receive and transmit functions. Our rates apply to peak power levels of 1 MW, and since the transmitter is ostensibly capable of 4 MW levels, a further doubling of echo rate may still be achieved.

The presence of a PDP 15 computer at our field station has made it possible for us to fully exploit our substantial data rate. Data collection is fully automated and the pertinent parameters for each echo are actually generated in real time. This not only gives us immediate feedback on the state of atmospheric winds but verifies proper system operation as well.

A spaced antenna interferometry arrangement allows us to resolve height with accuracy (0.02r in azimuth and elevation, 1.5 km in height) comparable to the best achieved at other stations, i.e., Garchy and Durham. Time has not yet permitted calibration of the long arm vernier for further refinement of height, but it is anticipated that once complete such an interferometer will yield unsurpassed height resolution.

Special target generator hardware permits us to evaluate actual, as opposed to theoretical, performance of receiving hardware and software algorithms. The hardware can form dual targets with independently set range, Doppler shift, and signal-to-noise ratio.

1.4 *Summary of 1975-1976 Urbana Meteor-Radar Campaign*

Table 1.2 summarizes the extended operation periods (24 hours or more) of the University of Illinois meteor radar in 1975-1976. Stacked Yagi interferometer height determinations were first available in September, 1975. Radial acceleration measurements were added in December, 1975 in an attempt to monitor wind shears from a single site. Azimuthal measurements were first included in April 1976. Power levels were approximately 1 MW peak except for December, 1975 to Jan. 1976, when a capacitor failure in one of

Table 1.2

Summary of University of Illinois meteor-radar operation.

Nr	Date	Run Length hr	Collection Software	Height Decay	Height Interferometer	Radial Acceleration	Azimuth	Usable Echoes
1	Jan. 17,18, 1975	24	METP4	X				2597
2	Jan. 31 - Feb. 1	24	METP4					4400
3	Feb. 28 - March 1	24	METP4	X				3713
4	March 7,8	24	METP4	X				2896
5	April 4,5	24	METP5	X				4342
6	May 27,28	24	METP5	X				2801
7	July 14,15	24	METP5	X				3522
8	July 30, 31	24	METP5	X				4062
9	Aug. 21,22	24	METP5	X				3012
10	Sept. 13,14	24	METP6	X	X			2850
11	Oct. 13-18	96	METP6	X	X			11050
12	Dec. 4-6	48	METP6*	X	X	X		2520
13	Dec. 12-13	24	METP6	X	X	X		1927
14	Jan. 14-16, 1976	48	METP6**	X	X	X		3399
15	Jan. 21-23	48	METP6**	X	X	X		3196
16	April 18-19	24	METP6***	X	X	X	X	3550
17	June 30 - July 1	30	METP6***	X	X	X	X	4500

* modified to store all raw data samples

** modified to include least squares fit of velocity vs. time

*** modified to include azimuth angle determination

our output amplifiers forced us to run the driver power directly to the transmitter antenna. This dropped us to a power level of about 375 kW peak.

1.5 *Objectives and Scope of this Study*

The five principal objectives of this study are: (1) to describe in detail the design and development of a high-power meteor-radar system at Urbana, Illinois which achieves significant improvements in usable echo rate, processing speed, and parameter accuracy, (2) to describe meteor wind observations made at Urbana, with emphasis on the character of atmospheric tides and internal gravity waves, (3) to interpret these observations in terms of existing theories of upper atmosphere dynamics, (4) to use our improved radar to test the validity of density and wind shear inferences, and (5) jointly with a partial-reflection experiment, to test a theory of the *D*-region winter anomaly. An outline deliniating the scope of this study follows.

Chapter 2 establishes scientific objectives and specifications for our system. Each hardware subsystem is discussed in detail, as are the various measurement algorithms. Lastly, our collection and post-processing software are described.

Our procedure for generating uniform wind values in time and height is set forth in Chapter 3. This chapter also discusses the effects of various selection criteria on meteor radar winds.

Chapter 4 summarizes meteor characteristics and Chapter 5 investigates the statistics of various parameters we measure.

Chapter 6 contains a brief presentation of classical tidal theory. This is followed by comparisons of our Urbana tidal observations with classical theory and with observations previously made at other sites.

Internal acoustic-gravity wave theory is discussed in Chapter 7.

Urbana gravity wave observations are compared to this theory and studies made earlier at Garchy and Jicamarca.

In Chapter 8 we investigate a possible explanation of the winter anomaly in radio wave absorption, a phenomenon of the *D*-region.

Chapters 9 and 10 are related to validity tests with our improved radar of methods for inferring density and wind shear from single-site meteor radar data.

The principal observations and conclusions of this study, along with suggestions for future research, appear in Chapter 11.

2. UNIVERSITY OF ILLINOIS METEOR-RADAR SYSTEM

2.1 *Scientific Criteria and Specifications*

2.1.1 *Scientific objectives.* Meteor-radar investigations of upper atmosphere winds can be separated into two categories: those which require a coordinated network of observations and those which yield useful scientific information from just a single location. Examples of the first class are investigations of planetary-wave propagation up to the lower thermosphere, winter changes in mesospheric and lower thermospheric circulations and their relation, if any, to stratospheric warmings, latitudinal structure of atmospheric tides and seasonal behavior of that structure, and geographical variability of atmospheric turbulence at meteor heights. Single station meteor-radar observations of importance include vertical structure and seasonal behavior of "daily variations", diurnal and seasonal changes in atmospheric turbulence, small-scale structure of atmospheric gravity waves, and simultaneous observation of ionospheric parameters such as *D*-region electron density and neutral winds at similar heights. The objective of the Illinois meteor-radar program was to construct a system that would be compatible with both classes of investigations, and extend the state of the art in temporal and spatial resolution of the data as well as the processing of that data.

2.1.2 *Echo rate and measurement accuracy requirements.* To establish system requirements for our radar, we begin by considering the character of winds in the meteor region as measured by chemical releases. [*Rosenberg*, 1968] shows instantaneous meridional and zonal wind components based on 60 observations of chemical releases from rockets. *Rosenberg and Zimmerman* [1972] summarize shear-related properties of winds in the upper part of the meteor region. To produce meteor-radar wind profiles of comparable accuracy

to those from chemical releases, we require our system to:

1. Measure horizontal winds up to 100 m s^{-1} with accuracy a small fraction thereof. For individual echoes 10 m s^{-1} should be sufficient to resolve small-scale waves.
2. Resolve vertical wind shears up to 50 m s^{-1} km^{-1}.
3. Measure height correctly to within a small fraction of the vertical wavelength of the atmospheric waves of interest.
4. Achieve an echo rate which allows generation of wind profiles in time periods small relative to the periods of the atmospheric waves of interest.

The accuracy of meteor-radar results will necessarily be somewhat less than that of chemical releases because the former measures winds averaged over a Fresnel length, about 1 km in vertical extent for our radar, whereas resolution of chemical releases is limited only by the optics used in triangulation.

The Brunt-Vaisala frequency represents an upper limit on internal-gravity wave frequency and this limiting period is about five minutes at meteor heights [*Georges*, 1967]. If one is to resolve waves with such a period, at least one usable meteor trail must occur every 2.5 minutes in each height bin. Height segmentation of the data is essential to prevent waves being obscured by vertical phase variations. The height bins, based on Rosenberg and Zimmerman's limiting wavelengths, must involve steps of 2 km or less. Since meteor echoes are concentrated near 92 km with 8 km standard deviation (Section 5.3), we find a minimum required echo rate of about 320 hr^{-1}. Appreciably less stringent echo rate and height accuracy requirements apply to tidal and synoptic feature studies and prevailing wind determinations. See, for example, *Lindzen* [1969] and *Barnes and Pazniokas* [1968]. Of course for these longer period dynamic regimes we

should be capable of resolving quadrature horizontal components and must operate for continuous periods of at least 24 hours so the major tidal components can be resolved.

2.1.3 *Estimate of system echo rate.* To estimate the echo rate we might attain with our radar, we consider the appropriate transmission equation. The predominant type of meteor trail echoes seen by long wavelength sensitive radars such as ours are the underdense variety, for which the received to transmitted power ratio is [*Sugar*, 1964]:

$$\frac{P_R}{P_T} = \frac{G_T G_R \lambda^3 q^2 r_e^2}{32\pi^2 R^3} \exp\left(\frac{-8\pi^2 r_o^2}{\lambda^2}\right) \exp\left(\frac{-32\pi^2 Dt}{\lambda^2}\right) \qquad (2.1)$$

where

P_T, P_R = the transmitted and received power, respectively

G_T, G_R = the power gains of the transmitting and receiving antennas relative to an isotropic radiator in free space

λ = the radar wavelength

R = distance from the radar to the trail

r_e = classical radius of the electron

q = electron density of the trail in electrons per unit length

r_o = initial radius of the meteor trail

D = ambipolar diffusion coefficient

t = time, measured from formation of the trail which is assumed instantaneous.

The equivalent noise input to a low noise figure receiver is given by:

$$P_N = kT_S B \qquad (2.2)$$

where k = Boltzmann's constant, 1.38×10^{-23} W Hz^{-1} K^{-1}

T_s = antenna temperature due to sky noise.

Using the following system parameters

$P_T = 5 \times 10^6$ W (This is perhaps too optimistic for long-term operation; to conserve tube life values of 1 to 2 MW are more reasonable)

$G_T = 50$ (17 dB)

$G_R = 31.6$ (15 dB)

$\lambda = 7.3314$ m (40.92 MHz)

$T_S = 4000$ K [*Hogg and Mumford*, 1960] (Varies with sky coordinates; 10,000 K may be a more realistic average value)

$B = 73$ kHz

we obtain a signal-to-noise ratio of

$$S/N = 10 \log\left[\frac{7.82635 \times 10^{-20}(q^2/R^3) \exp(-0.46759 r_o^2)}{4.03 \times 10^{-15}} \exp(-5.87592 Dt)\right] \tag{2.3}$$

Figure 2.1(a) shows the variation of peak S/N, i.e., when r_o and time are zero, versus q for a median range of 100 $\sqrt{2}$ km. Figure 2.1(b) shows the corresponding receiver input voltage assuming an input impedance of 50 Ω. Trails with electron line densities on the order of 10^{11} m^{-1} provide a comfortable S/N value of 20 dB. However a typical r_o value is actually about 2 m [*Sugar*, 1964], resulting in a signal drop of 8.12 dB. The diffusion time constant is [*Sugar*, 1964]

$$\tau = \lambda^2/16\pi^2 D \tag{2.4}$$

Using a typical value for D of 3 $m^2 s^{-1}$ this leads to an additional 8.7 dB signal loss over the echo lifetime, which through (2.4) is 113 ms for these weakest echoes. If 30 interpulse periods are required to accumulate the needed target data, a drop of 5.7 dB in signal power occurs during data

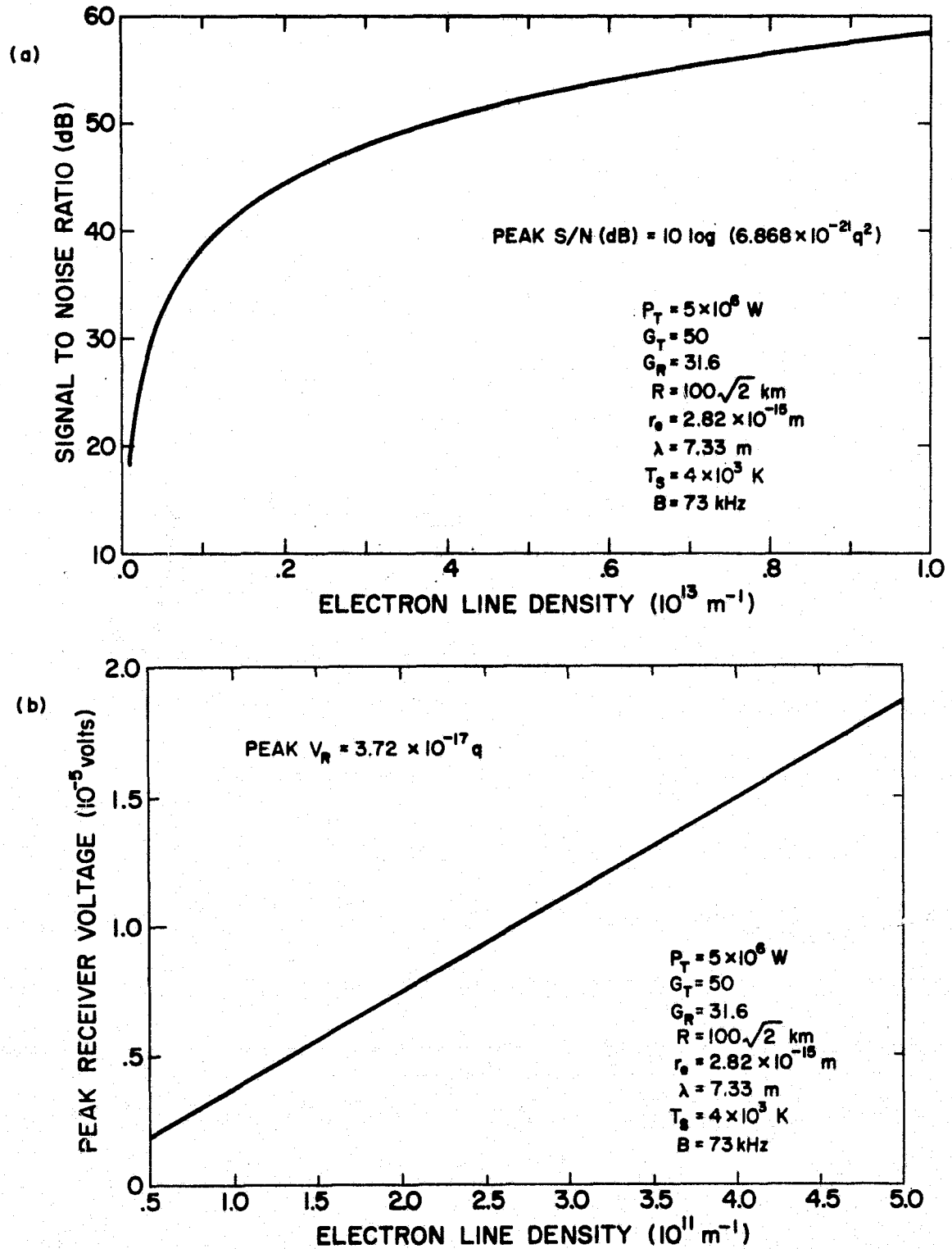

Figure 2.1 (a) Peak signal-to-noise ratio versus q, electron line density, (b) Peak receiver voltage (50 Ω load) versus q, electron line density.

collection. Using our maximum range of 230 km implies yet 6.3 dB more loss. We can guarantee at least 20 dB S/N ratio for all echoes during the data collection process provided q is sufficiently above 10^{11} m^{-1} to compensate for the losses just cited, i.e., $q \simeq 10^{12}$ m^{-1}.

The number of meteor trails with q exceeding some reference line density q_o is described by [*Sugar*, 1964]:

$$N(q>q_o) = Kq_o^{-c}, \quad c \cong 1.0 \tag{2.5}$$

where $K = 1.6 \times 10^2$ m^{-3} s^{-1} for sporadic meteors and $N(q>q_o)$ has the units of trails incident per m^2 s. Using $q_o = 10^{11}$ m^{-1} we find that 99% of the accepted trails will have line densities in the range $10^{11} < q < 10^{13}$. Thus a dynamic range of 60 dB, 40 dB for signal variation and 20 dB for minimum S/N, permits us to accumulate data from nearly all desired trails. If q exceeds about 10^{13}, the trail is likely overdense and possibly must be ignored anyway, since it is likely to have multiple reflection centers which produce misleading Doppler shifts, or if underdense the return will quickly decay to nonsaturation levels. The 60 dB value fits nicely with a 9-bit plus sign A/D converter (54 dB), but stringent linearity requirements must be achieved by the receiver to capitalize on the large dynamic range. The linearity requirements can be eased substantially by design of parameter extraction algorithms which are relatively insensitive to nonlinearities.

With the following antenna beamwidth information

Function	Azimuth centered at 0°	Elevation centered at 45°
Transmitting	48°	11.5°
Receiving	30°	64°
Round Path (Transmitter-Trail-Receiver)	30°	11.5°

we find our average system viewing area is 4500 km^2 at 100 km height. Thus, in an hour we can expect to see 2592 trails exceeding a 20 dB S/N threshold, assuming 10% of all trails have orientations suitable for return reflection [*Whipple and Hawkins*, 1956]. A sky temperature of 10,000 K drops the echo rate to 1639 hr^{-1} and conservative operation at 1 MW drops the rate further to 733 hr^{-1}. The usable echo rate must of course be even somewhat lower because high altitude returns will decay too rapidly to allow reliable Doppler determinations. Also the scanning nature of our data input to computer, many signal lines multiplexed via a single A/D converter, will cause numerous echoes near the threshold to be missed.

2.1.4 *Estimate of system height accuracy.* Under a flat earth assumption, our meteor-radar geometry is as depicted in Figure 2.2, and the height of the specular reflection point of a meteor trail is given by the relation

$$h = R \sin \alpha \tag{2.6}$$

where R is the slant range, and α is the elevation angle. The most likely height for meteor-trail reflection is roughly 92 km but even with our antennas aimed north with their main lobes elevated 45° a representative slant range for our echoes is 140 km, somewhat larger than the most likely range (2.6) predicts because of the asymmetrical range distribution.

A relation between height accuracy and range and elevation angle accuracies, provided the errors in range and elevation angle measurements are reasonably small, is found by differentiating equation (2.6):

$$dh = \frac{\partial h}{\partial R} dR + \frac{\partial h}{\partial \alpha} d\alpha = \sin\alpha \, dR + R \cos\alpha d\alpha \tag{2.7}$$

The error in height Δh is thus related to range and elevation angle errors, ΔR and $\Delta\alpha$, respectively, through

$$\Delta h \simeq \sin\alpha \Delta R + R \cos\alpha \Delta\alpha \tag{2.8}$$

Assuming both types of errors are zero mean Gaussian distributed, the standard deviation in height is [*Backof and Bowhill*, 1974]

$$\sigma_h = [(\sin\alpha\ \sigma_R)^2 + (R\ \cos\alpha\ \sigma_\alpha)^2]^{\frac{1}{2}} \tag{2.9}$$

where σ_h, σ_R, and σ_α are standard deviations for height, range, and elevation angle measurements, respectively. Our desired σ_h for resolving fine wind structure is roughly 0.5 km. This value is less than the Fresnel averaging interval but nevertheless is large enough to be achievable. Of course even with perfect height measurements, the Doppler shifts observed by our radar will still be the result of winds averaged over trail segements of about 1.4 km.

To see what magnitudes the error sources σ_α and σ_R will actually have, we begin by considering range. Next we must consider Doppler and azimuth angle measurements because they help determine elevation angle performance.

2.1.4.1 *Estimate of system range accuracy.* Range is determined by measuring the time between transmission and reception of a pulse waveform. The returned pulse is digitized by an A/D converter with a sampling rate of 100 kHz, thus apparently limiting range accuracy to only ± 750 m (± 5 μs) taking the pulse center as reference. However, by fitting a parabola to the peak video and adjacent two samples, range accuracy can be improved about fivefold (Section 2.2.3.1.3). For a given meteor echo this error is not random, but rather depends on the range offset from the peak video sample and how well a parabola models the video detector pulse response. Presumably, a table lookup procedure could nullify such errors. But, it should be noted that the response of the receivers we use is a function of signal strength. This means that the correction table would have to be two dimensional, accounting both for estimated range offset and signal strength.

Furthermore, it is doubtful that over an extended period of time the receiver bandpass would remain stable enough for a non-updated table to continue doing more good than harm. And keeping in mind our 1.4 km Fresnel length, it is doubtful that range resolutions exceeding ± 150 m have much significance anyway.

Thus far we have tacitly ignored the range error component introduced by noise and the finite risetime of the video detected pulse. The uncertainty in time is [*Barnes and Pazniokas*, 1968]

$$\Delta T_R = T_R/(S/N) \tag{2.10}$$

where T_R is the risetime and S/N is the signal-to-noise ratio. T_R and bandwidth BW in r s^{-1} are related approximately through [*Van Valkenburg*, 1964]

$$T_R \simeq \pi/BW \tag{2.11}$$

Using a receiver bandwidth of 73 kHz and signal-to-noise ratio of 10 (20 dB in voltage) gives a range error component of ± 102 m. Figure 2.3(a) plots the estimated total range error versus number of independent range calculations averaged and signal strength (noise standard deviation normalized to unity).

2.1.4.2 *Estimate of system Doppler accuracy.* Our elevation and azimuth angle determinations will be made via an algorithm which requires knowledge of the echo Doppler frequency ω_d. Section 2.2.3.2 discusses two such algorithms, referred to as the Backof algorithm and the Bowhill algorithm. Thus, errors in Doppler lead to errors in angles of arrival and echo height. It has been shown [*Edwards*, 1973a] that the error in Doppler angle $\Delta\alpha$ for the Backof velocity algorithm is bounded by

$$\frac{\sqrt{2}}{A} \geq \Delta(\alpha \stackrel{\Delta}{=} \omega_d T) \geq \frac{1}{A} \tag{2.12}$$

where A = signal strength (unit noise standard deviation)

T = radar interpulse period.

The corresponding bounds for radial velocity uncertainty are

$$\frac{\sqrt{2}\lambda}{4\pi AT} \geq \Delta v \geq \frac{\lambda}{4\pi AT} \tag{2.13}$$

Using our radar wavelength 7.3314 m, an interpulse period of 3 ms (PRF = 333 Hz), and a voltage signal-to-noise ratio of 20 dB gives 27.5 m $s^{-1} \geq \Delta v \geq$ 19.5 m s^{-1}. To resolve individual echo winds, which are predominantly horizontal, to within 10 m s^{-1} we must typically resolve the radial winds, i.e., those winds which we observe directly, to within 7.07 m s^{-1}. This value pertains to our mean elevation angle of 45° and corresponds to an error of just ±0.04 r in Doppler angle. To achieve this we must average about

$$N \geq \lambda^2/800(\pi AT)^2 \tag{2.14}$$

independent velocity calculations per echo. N is at most 15 if we limit ourselves only to echoes 20 dB or more above the noise floor. Figure 2.3(b) displays the worst case Doppler error versus signal strength and number of calculations averaged using a 500 Hz PRF.

2.1.4.3 *Estimate of system azimuth accuracy.* A horizontal resolution of just 10-100 km is sufficient to discriminate the spatial variation of short period gravity waves [*Lindzen*, 1969], obviously a very weak requirement relative to that for height accuracy. The horizontal displacement of echoes from due north is given by

$$x = R \cos\alpha \sin\gamma \tag{2.15}$$

using the geometry of Figure 2.2. Differentiating equation (2.15) gives the relation between accuracy in horizontal displacement as a function of range, elevation angle, and azimuth angle accuracies. Since the first two

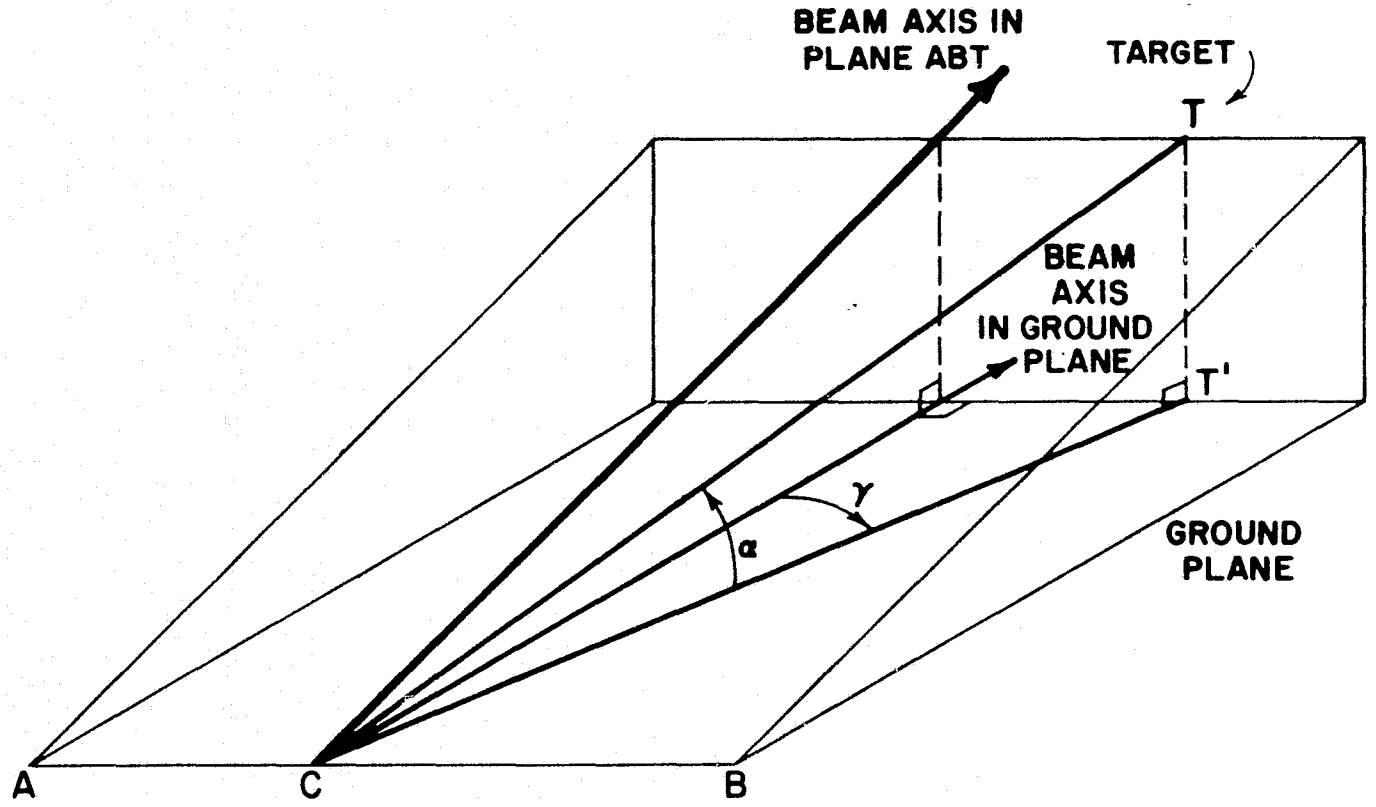

Figure 2.2 Illustration of the various angles of measurement.

parameters must be measured so precisely to achieve our height accuracy goal, an approximate error equation is [*Backof and Bowhill*, 1974]

$$\sigma_x \simeq R \cos\alpha \cos\gamma \, \sigma_\gamma \tag{2.16}$$

where σ_x and σ_γ are the standard deviations in x and γ. Using R and α as in Section 2.1.4 and $\gamma \simeq 0$ gives $\sigma_\gamma \cong \sigma_x/100$. A horizontal displacement accuracy of 10 km thus results if azimuth is measured to within 0.1 r (6°).

Consider now the spaced arrangement of receiving antennas shown in Figure 2.4(a). The phase difference between received fields at antennas A_1 and A_2 for a meteor echo from elevation angle α and azimuth angle γ is

$$\phi_{12} = (2\pi d_{12}/\lambda)\cos\alpha \cos\gamma \tag{2.17}$$

Likewise the phase difference between antennas A_2 and A_3 is

$$\phi_{32} = (2\pi d_{23}/\lambda)\cos\alpha \sin\gamma \tag{2.18}$$

The azimuth angle in terms of these measureable phase differences is found via

$$\phi_{32}/\phi_{12} = (d_{23}/d_{12}) \tan\gamma \tag{2.19}$$

Azimuth accuracy is then related to phase difference accuracy through

$$d\gamma = \frac{\partial\gamma}{\partial\phi_{12}} d\phi_{12} + \frac{\partial\gamma}{\partial\phi_{32}} d\phi_{32} = \frac{d_{12}}{d_{23}} \frac{\cos^2\gamma}{\phi_{12}} [d\phi_{32} - (\phi_{32}/\phi_{12}) d\phi_{12}] \tag{2.20}$$

The azimuth error $\Delta\gamma$ as a function of ϕ_{12}, ϕ_{32} and their measurement errors $\Delta\phi_{12}$, $\Delta\phi_{32}$ is

$$\Delta\gamma \simeq \frac{d_{12}}{d_{23}} \frac{\cos^2\gamma}{\phi_{12}} \sqrt{\left[1 + (\phi_{32}/\phi_{12})^2\right]} \frac{2}{N} \frac{1}{A} \tag{2.21}$$

assuming $\Delta\phi_{12}$ and $\Delta\phi_{32}$ are essentially equal to the worst-case error in Doppler angle given in equation (2.12) and averaging N independent calculations of azimuth angle. Figure 2.3(c) shows a plot of equation (2.21) using

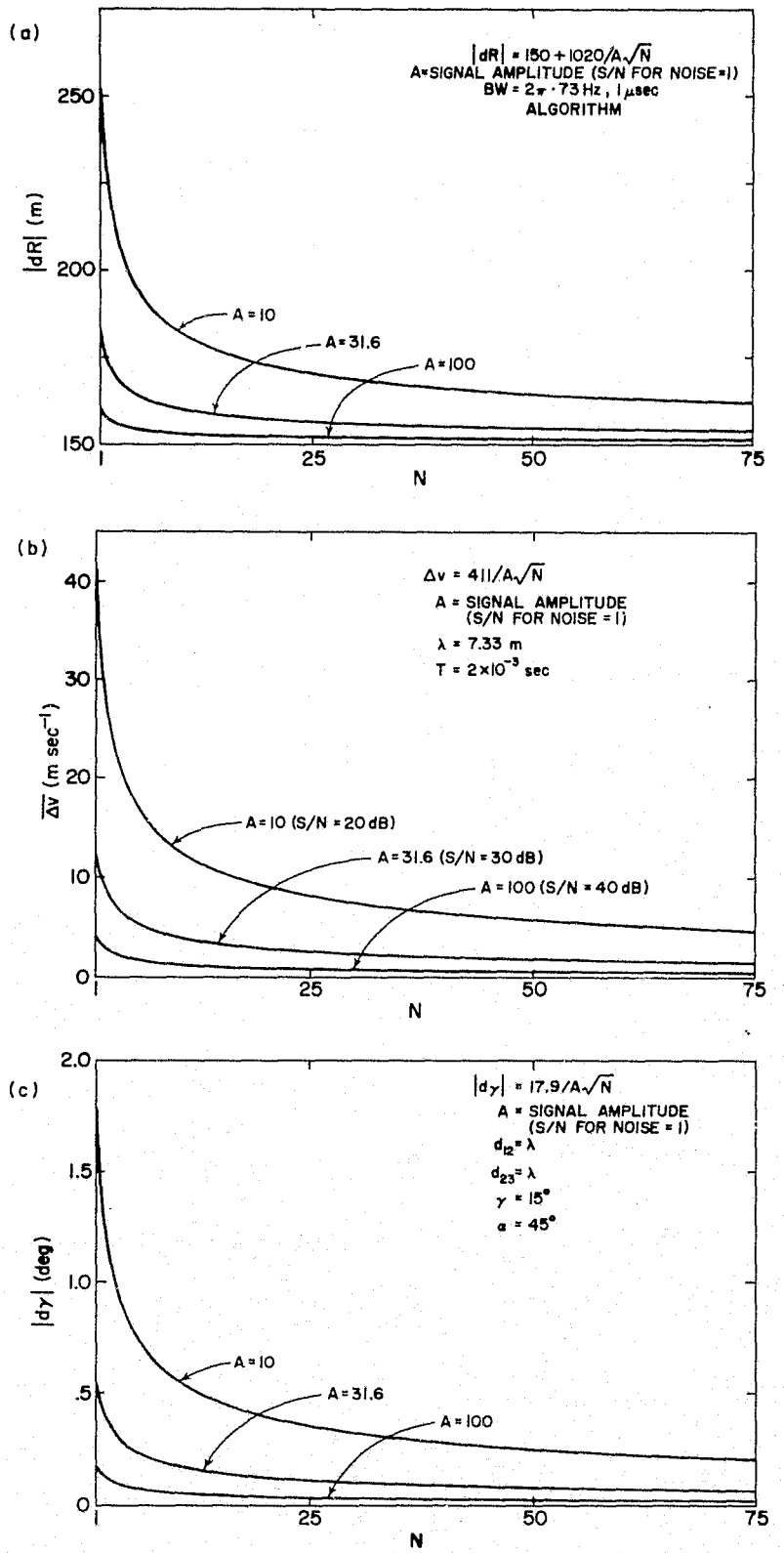

Figure 2.3 (a) Range error, (b) Doppler error, (c) Azimuth error versus number of calculations averaged.

typical parameter values.

2.1.4.4 *Estimate of system elevation accuracy.* The elevation angle α can be deduced from equation (2.17) once the azimuth angle has been determined.

$$\cos\alpha = \frac{\phi_{12}\lambda}{2\pi d_{12}} [\cos\gamma]^{-1} \tag{2.22}$$

With the help of equation (2.21) we can express the elevation angle error $\Delta\alpha$ as

$$\Delta\alpha = \frac{\lambda}{2\pi d_{12} \sin\alpha \cos\gamma} \left[1 + \left(\frac{d_{12}}{d_{23}} \sin\gamma \cos\gamma\right)^2 \left(\left[\frac{\phi_{32}}{\phi_{12}}\right]^2 + 1\right)\right]^{\frac{1}{2}} \sqrt{\frac{2}{N}\frac{1}{A}} \tag{2.23}$$

Finally, inserting values from Figure 2.3(a) and equation (2.23) into equation (2.9), we obtain the standard deviation in height. In Figure 2.4 the phase difference between A_2 and A_4 can act as a vernier to refine $\Delta\alpha$ by the factor (d_{24}/d_{12}). This improvement is necessary to meet the height accuracy figure with the weaker returns. Based on results obtained April 18-19, 1976 without the antenna A_4 vernier, our actual system performance is characterized by the following mean measurement precisions: (1) 0.02 r in azimuth, (2) 0.02 r in elevation, and (3) 1.5 km in height.

2.2 *System Description*

2.2.1 *Block diagram.* A block diagram of the present operating system hardware is shown in Figure 2.5. Changes incorporated into the meteor radar since its original operation in August 1974 include:

1. All four 5682 output tubes in the transmitter have been brought into operation.
2. A second coaxial feedline has been constructed for the second pair of output tubes.
3. The 24-element narrow azimuth version of the transmitting antenna has been completed.

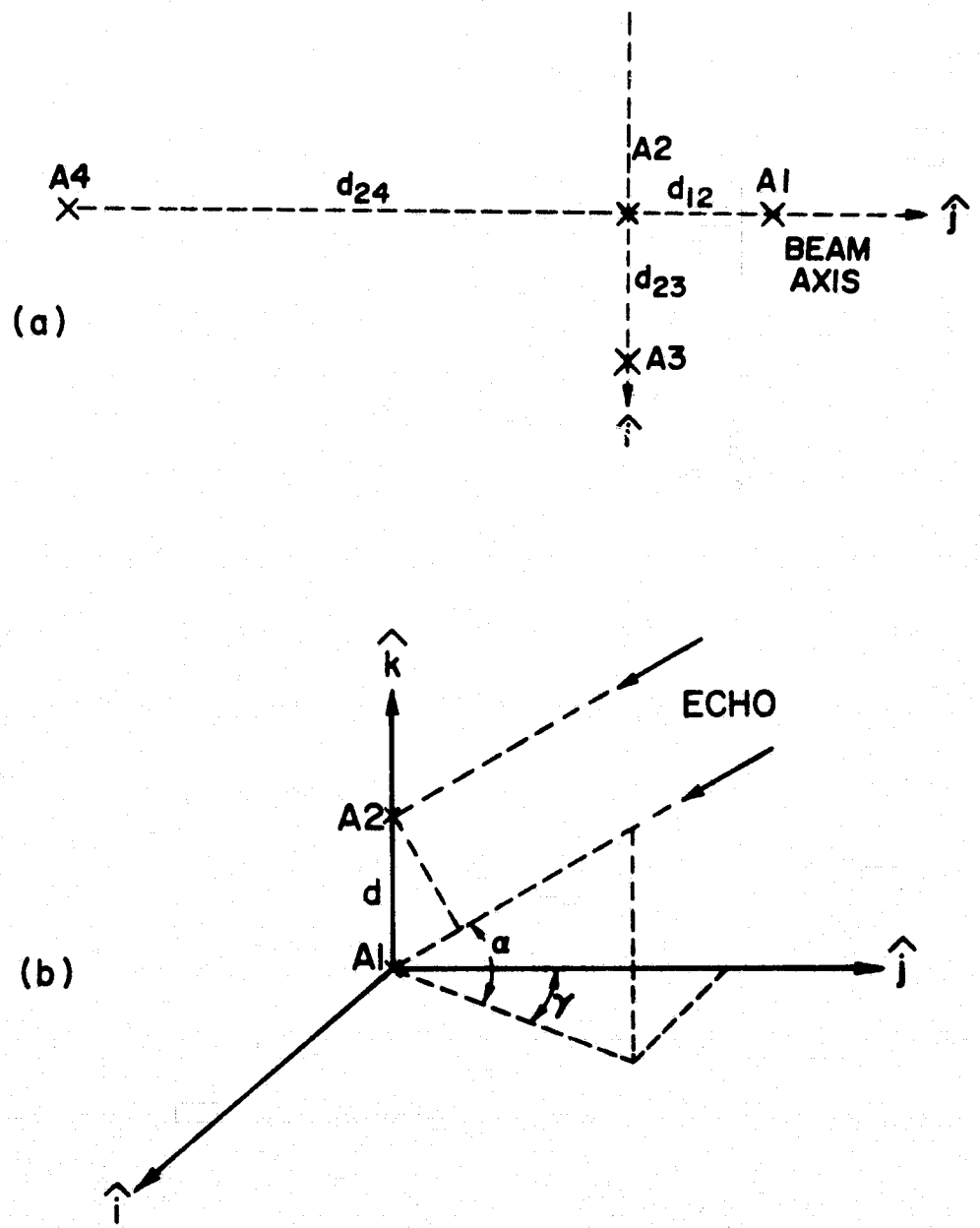

α = ELEVATION ANGLE

γ = AZIMUTH ANGLE, POSITIVE EAST OF NORTH

Figure 2.4 (a) Four antenna interferometer,
(b) Stacked Yagi interferometer.

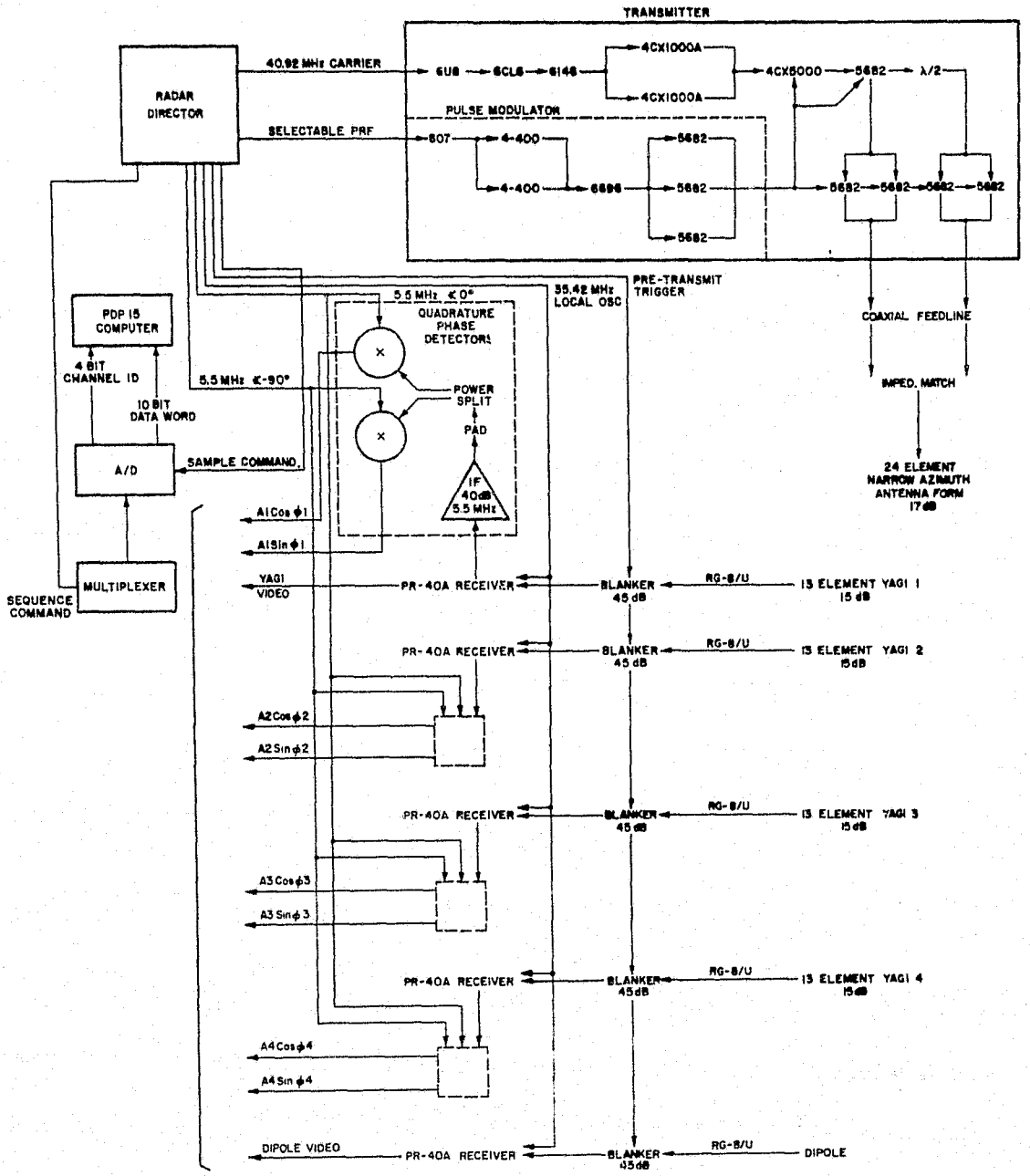

Figure 2.5 Meteor-radar system block diagram.

4. Spaced receiver antennas, with accompanying receivers and phase detectors, for interferometer determination of echo height and azimuth have been completed.
5. Major software revisions in going from a 7-channel to a 15-channel data frame have been made.

In terms of hardware, we can divide the meteor-radar system into 7 subsystems: (1) radar director, (2) transmitter, (3) transmitting antenna, (4) receiving antennas, (5) receivers, (6) phase detectors, and (7) computer and interface. Each of these subsystems will be discussed individually in the sections which follow.

2.2.2 *Hardware subsystems*

2.2.2.1 *Radar director.* This unit is composed of a simple frequency synthesizer for coherent radar operation, timing logic to synchronize the various subsystems in the radar, and a target generator for analysis of system performance. These latter two items are intimately related and thus will be considered the target gererator as a whole. It is then convenient to discuss the radar director subsystem in terms of two parts, the frequency synthesizer and the target generator. In Figure 2.6, a block diagram of the radar director, it is evident that the frequency synthesizer is analog in nature while the target generator has a distinctly digital portion, the timing logic, as well as a hybrid portion, the actual target gaters.

2.2.2.1.1 *Frequency synthesizer.* The purpose of the frequency synthesizer is to generate all the high-stability reference signals required to make the meteor-radar phase coherent. The required frequencies are:

1. 40.92 MHz - transmitter carrier frequency
2. 35.42 MHz - local oscillator for receivers

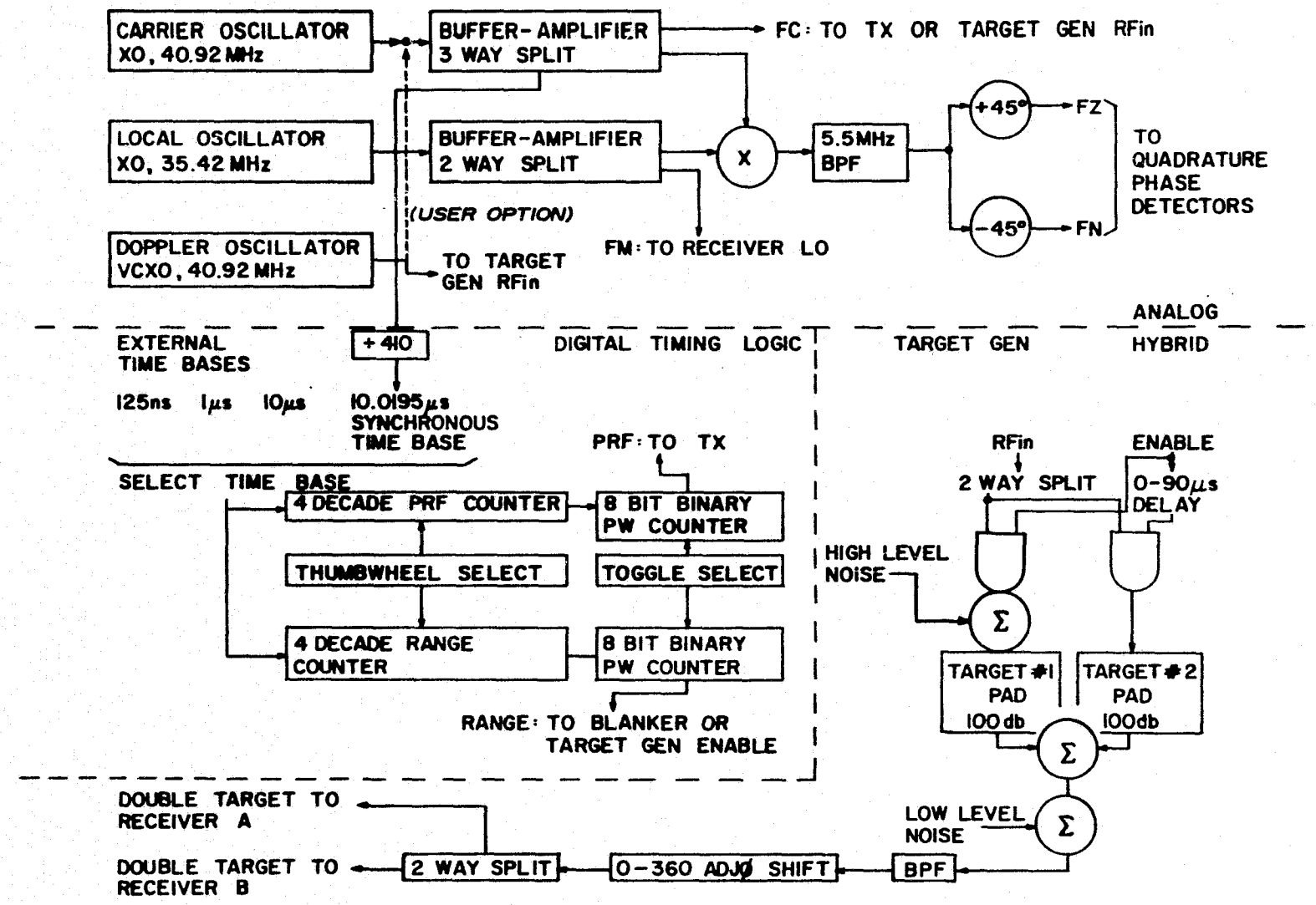

Figure 2.6 Radar director block diagram.

3. 5.5 MHz @ 0 and -90 degrees - reference for quadrature phase detectors
4. 100 kHz - PRF generation and range gating
5. 40.92 MHz plus or minus 100 Hz - simulation of Doppler on returns.

It is important to note that the Doppler algorithms used at the University of Illinois extract Doppler information from the rate of change of absolute phase between echo returns separated in time by a single interpulse period. Thus, frequency drifts of our 35.42 MHz and 5.5 MHz signals relative to the 40.92 MHz transmitted signal result in an apparent Doppler frequency indistinguishable from true Doppler shift. However, long-term frequency drifts pose little problem, only the drift between the time that energy is transmitted and when a return echo appears leads to uncancelled Doppler errors. An analysis of the Doppler errors in a radar with four independent frequency sources is presented in *Edwards* [1974]. With oscillator stabilities of one part in 10^8, the Doppler error is at most 2.1 m s^{-1} (1.4 m s^{-1} rms). The overal system goal is 7.07 m s^{-1} radial velocity accuracy so these results are acceptable, providing other error sources are also small. However, to achieve high echo processing rates relatively low signal-to-noise returns may have to be accepted. Consequently, oscillators with drifts under one part per 10^9 are advisable so larger velocity errors due to noise can be tolerated.

The upper part of Figure 2.6 shows a block diagram of the frequency synthesizer actually built for the University of Illinois meteor radar. Note that only two oscillators rather than the maximum possible four need be used at any one time, one at 40.92 MHz (a 40.92 MHz voltage-controlled oscillator is made available for Doppler simulation) and another at 35.42 MHz. The 5.5 MHz signal references for the quadrature phase detectors are

developed by a mixing and low pass filter operation. Because the upper sideband to lower sideband ratio is 13.88, undesired signal rejection in excess of 60 dB is quite straightforward. The only source of error comes from relative drift of the 40.92 MHz and 35.42 MHz signals between the time energy is transmitted and a return is received. The radar PRF and other necessary timing signals can be formed from the clock signal CPRF. This clock is the result of dividing the 40.92 MHz transmit frequency digitally by a factor of 410. The resulting frequency is slightly under 100 kHz (99,804.87805 Hz) but this is essential because the A/D converter which will be used to interface the receivers to a PDP-15 processing computer has a sampling rate upper limit of 100 kHz. Because CPRF is just under this limit it can control the A/D in a command mode at almost the free-run speed limit. By using high-speed synchronous TTL integrated circuits to form CPRF, it is possible to achieve time references with under 5 ns jitter.

Appendix I shows functional schematics of the various frequency synthesizer units (designated FS-FS1 through FS-FS7). The oscillator designs are based on techniques presented by *Healey* [1966], *Healey and Driscoll* [1967], and *Anderson and Merrill* [1960], while the RF amplifiers were designed utilizing a procedure given by *Meyer et al.* [1968].

2.2.2.1.2 *Target generator.* The target generator portion of the radar director permits evaluation of radar system performance by simulating targets with known range, Doppler, and signal-to-noise ratios (S/N). By plotting S/N versus output error in range and Doppler frequency, or equivalently radial velocity, error bounds based on actual system performance can be established. Furthermore, by varying the pulse repetition frequency (PRF) and pulse width, system performance can be optimized for a given receiver response and set of software algorithms.

In normal system operation, of course, target generation is unnecessary. However, the logic required for the target generation forms all the timing and command signals needed to properly synchronized the various subsystems of the radar: PRF for the transmitter, blanking for the receivers, sampling and channel sequencing for the A/D converter. Hence, the target generator is an integral part of the meteor radar even when it is not needed for simulation purposes.

A detailed list of the target generator capabilities is as follows:

1. Basic time-base selection -
   a. 8 MHz from the A/D converter, followed by an internal divide-by-eight for a 1 μs time base.
   b. 1 MHz (or 100 kHz) from the Sulzer frequency standard for a 1 μs (or 10 μs) time base.
   c. CPRF, internally generated and equal to the 40.92 MHz carrier frequency divided by 410 (99,805 Hz) for a 10.0195 μs time base.
2. Thumbwheel selection of the PRF pulse rate, 2 to 9999 times the basic time base.
3. Thumbwheel selection of the range pulse delay from the PRF pulse, 1 to 9999 times the basic time base but the range work must always be less than or equal to the PRF word.
4. Toggle switch selection of the PRF and range pulse widths, 1 to 255 times the basic time base.
5. Formation of 100 negative edge pulses at 610 μs to 1600 μs delay from the PRF leading edge when a 10 μs time base is used. This is for externally commanding the A/D converter to encode.
6. TTL level control of an analog RF gate for creation of a pulsed RF target.

7. Addition of high level noise to the RF pulse of 6 to establish a given input signal-to-noise ratio. Alternately low level sky noise from an antenna can be added via a hybrid just prior to the receiver input.

When the system is in normal operation, the receiver blank command is given by the rising edge of the range pulse, where the range word is set to a value of one less than the PRF word so that blanking begins 10.0195 μs (or 10 μs if an external time base is used) prior to transmitter turnon. The A/D multiplexer is sequenced to a new channel each PRF by a buffered and inverted PRF signal labeled SEQ. Since a 4-digit code denoting the active channel is always sent by the A/D to the PDP-15 memory, no direct synchronizing link between the computer and the target generator is necessary.

The target generator consists primarily of combinatorial and sequential digital logic elements of straightforward design (for example, see *Kohavi* [1970]). Standard 7400 series TTL integrated circuits have been used to minimize cost and the number of different types of circuits required. Appendix I contains schematic diagrams of the functional schematics which comprise the target generator (TG-FS1 through TG-FS7). Only the hybrid portions which form RF targets will be elaborated on below.

To facilitate finer range positioning than the normal system clock CPRF allows, and to test system software under multiple target conditions, a second target gater was designed. The unit is triggered by the main target generator RANGE pulse and can provide a gated 40.92 MHz RF pulse at 0 to 90 μs delay relative to the main target and with a variable duration, nominally set to 10 μs. Figure 2.7(a) shows the circuit schematic (note the similarity to TG-FS7 in Appendix I). When the logic signal RANGE pulses high, monostable multivibrator MM1 produces a logic low on pin 1. This pin stays

(a)

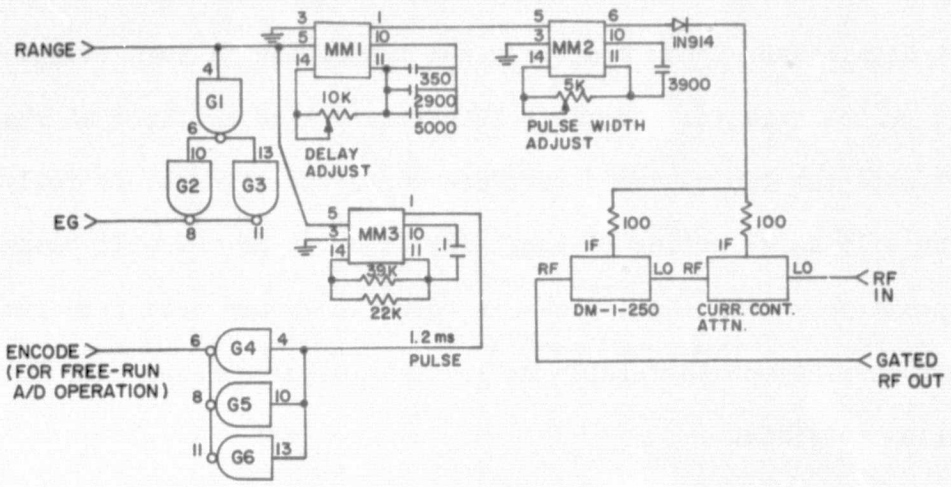

(b)

Dual target

Video response

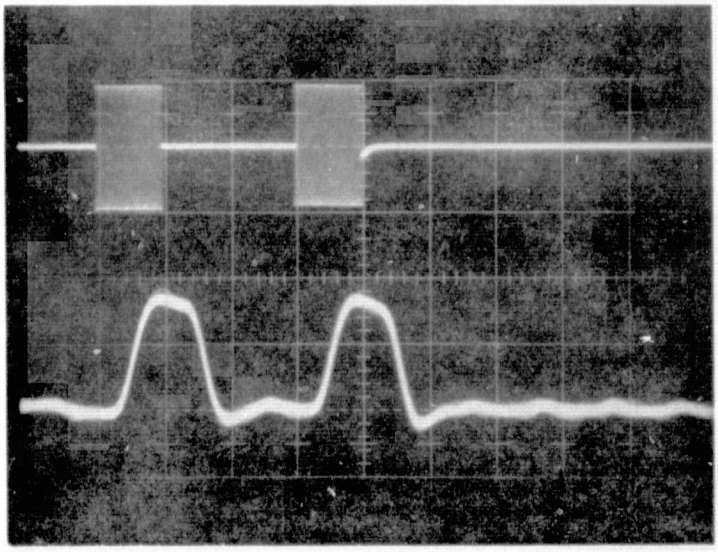

Figure 2.7 (a) Adjustable secondary target.
(b) Dual target and receiver response.

low for a period of time determined mainly by the external capacitor and rheostat values (about 0 to 90 μs control range) after which it returns to the quiescent high state. Such a dynamic one transition in turn triggers MM2 and pin 6 pulses high for nominally 10 μs controlled by the 5 kΩ rheostat. This action biases the two cascaded current-controlled attenuators fully ON thus producing a 10 μs RF pulse. A logic low at pin 6 of MM2 will normally be slightly positive so the 1N914 diode is added to ensure near zero current flow in such cases (attenuators fully OFF). This makes greater than 70 dB ON-OFF isolation possible.

Because the main target generator has but a single buffered RANGE output, gates G1, G2 and G3 were provided to send back the command to the initial target generator, lead EG. The final double target is formed by summing a padded version of the main target generator RF pulse E/N with a padded RF pulse from the second target gater. This summation is most simply accomplished by use of a PD-20-55 Merrimac hybrid. Figure 2.7(b) shows a typical dual target and receiver response. Target amplitudes are 6.3 μV_{pk} and yield receiver peaks of about 35 mV_{pk} (receiver #5 was used with 20 dB internal padding). Target spread is set to 30 μs for this particular photo and obviously no target interference resulted. In fact it was learned that with present receiver bandwidths, multiple target processing would suffer from the coarse A/D sampling before target overlap problems appeared.

Figure 2.7(a) also shows circuitry for a purpose unrelated to target generation. Monostable multivibrator MM3 is also triggered by the rising edge of the RANGE pulse and produces a fixed 1.2 ms pulse. This pulse can be connected to the HP A/D encode/free-run bit so the meteor-radar system is operable in a free-run mode rather than external command mode. To do this the target generator RANGE word should be 61, corresponding to a first

sample at a range delay of about 610 us. The time to take 100 free-run samples is 1 ms but MM3 has a 1.2 ms period to provide an ample safety factor. Also the receiver blankers should be driven by the PRF pulse rather than the RANGE pulse.

2.2.2.2 *Transmitter.* The transmitter was built in 1958 by Continental Electronics Manufacturing Company of Dallas, Texas and operated originally by the Smithsonian Astrophysical Observatory at the ESSA Longbranch Station near Havana, Illinois [*Green et al.*, 1960]. In 1971 the transmitter was given to the University of Illinois and the task of moving tons of transmitter components from Havana, Illinois to the Aeronomy Field Station some 90 miles distant began. This move was directed by Mr. J. D. Gooch and to him also should go full credit for reconditioning a transmitter which was in poor condition.

The unusually large power capability of the transmitter makes it a particularly useful addition for obtaining data in the Aeronomy Laboratory's research programs involving meteor radar and incoherent scatter. The transmitter has a 4 MW peak output power rating, with a nominal average output power of 20 kW (40 kW maximum). Operation is at 40.92 MHz with pulse width and repetition rate ranges from 3 us pulses at 1330 pps to 100 μs pulses at 40 pps. Output and driver tubes are water cooled and also pressurized to inhibit sparking. The water coolant lines, compressed air lines and cable troughs have been installed at an 11-ft elevation to allow room for a hoist. Outside the main field station building are an air-intake duct for the heat exchanger, transmission line junctions for the antenna feedlines, and a transformer bank for three-phase 200 kVA electric service.

The floor plan of the transmitter is given in Figure 2.8. The main transmitter components are as follows:

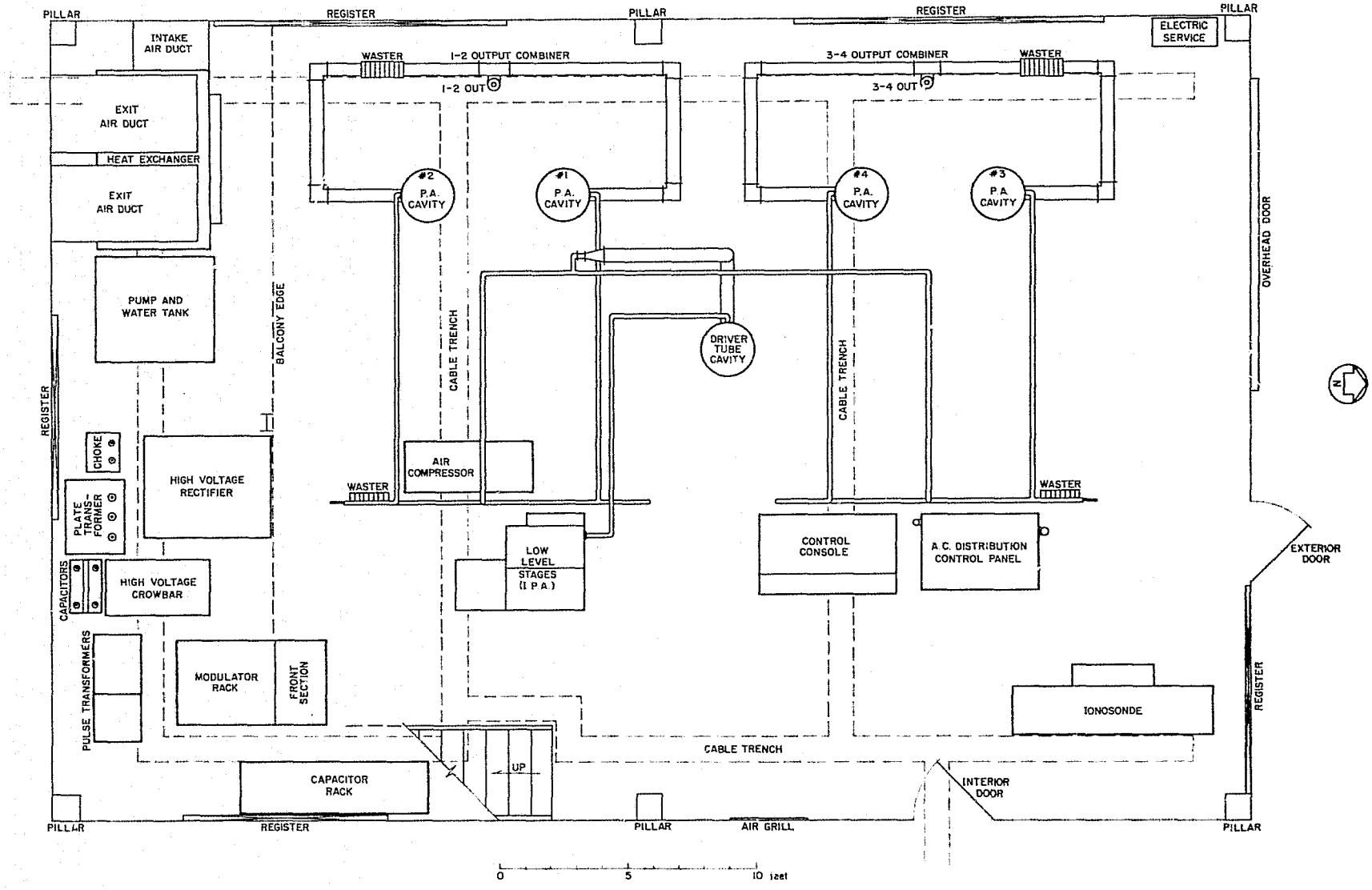

Figure 2.8 Floor plan of the transmitter.

1. Final Amplifier Stage
2. Hybrid Ring Combiners
3. Driver Amplifier Stage
4. Intermediate Power Amplifier
5. CEC 814B 3kW Amplifier
6. Low Level Stages
7. High Voltage Rectifier
8. Pulse Modulator
9. Distribution/Control Panel
10. Control Console
11. Cooling System
12. Pressurized Air System

The final amplifier stage consists of four water-cooled triode tubes (Machlett ML-5682) arranged for grounded grid operation. The tubes are mounted in cylindrical housings, 8 ft tall and 2 ft in diameter, which contain a coaxial input resonator plus a plate output resonator and load control. A π-network output circuit is realized by use of an adjustable-length circular drum center conductor in the output coaxial cavity. The position of the drum face near the tube anode is adjusted to resonate the output capacitance of the tube. The side of the drum provides a loading capacitance to the coaxial housing inner wall. Loading is varied by telescoping the length of the drum. The three motor-driven tuning adjustments for each output tube are made through teflon shafts and load screws. 6-1/8 in diameter rigid coaxial line transfers RF output from the tube anodes while cooling water is carried to and from the tube anode by pipes within the center conductor of the coax. The center conductor also supplies the pulsed plate voltage, up to 50 kV, developed by the pulse modulator.

The tubes are operated in pairs, with the first pair driven 180° out of phase with the second so a balanced 100 ohm output impedance can readily be achieved. The two tubes of each pair have their RF outputs fed to a hybrid ring combiner which adds the powers yet avoids interaction between the tubes [*Brown et al.*, 1949]. The combiner consists of a rectangular ring of 6-1/8 in rigid coaxial line, 1-1/2 wavelengths in circumference.

The driver amplifier uses a single ML-5682 tube, housed like the output tubes. A pulsed-power peak of about 0.6 MW can be developed by the driver. The hybrid ring combiners operated in reverse split this power equally to drive the two pairs of output tubes. An extra half wavelength of coax to the pair #3 and #4 creates the desired 180° phase difference between final amplifier tube pairs.

The intermediate power amplifier uses a 5-kW plate dissipation tube, type 4CX5000. It operates at reduced plate voltage, relative to that of the driver and output tubes, obtained from the pulse modulator transformer through a resistance-capacitance divider. This tube and circuitry are in a pressurized chamber with water cooled walls.

To improve the reliability of the transmitter, the pair of 4-400 tubes used originally to drive the 4CX5000 has been replaced by a Continental Electronics 814B VHF transmitter. This unit operates in a linear mode and produces drive pulses with a peak power of 3 kW using a pair of 4CX1000 A's connected in parallel.

The low level stages take an RF carrier supplied by the radar director and amplify it via a 6U8, 6CL6, 6146 tube lineup. The latter two tubes are held cutoff by a 6DJ8 DC pulse amplifier except when transmitting. A 6U8 crystal oscillator is also available for operating the transmitter independent of the radar director.

The plate transformer is an 87kVA three-phase unit with a ratio tap switch for coarsely varying the output voltage, and thus controlling the transmitter output power. The maximum voltage setting results in a 24 kV output from the rectifier-filter. An eight henry 3 amp filter reactor along with up to twenty 1.5 μf filter capacitators helps to minimize drooping during transmission (up to 100 μs). Less capacitance is used for shorter pulse operation.

The high voltage rectifier cabinet originally contained twelve mercury vapor tubes in a three-phase, full-wave circuit. Each leg used two tubes in series to meet the peak inverse voltage requirement and supply an average power of up to 3 amp at 24 kV. The narrow operating temperature range of the tubes hampered operation, so for improved reliability the tubes were replaced by silicon rectifier stacks early in 1974.

The pulse modulator is discussed in detail by *Martin-Vegue* [1961]. It contains amplifiers for low-level shaped pulses and uses transformer coupling into and out of the final switching stage. That stage uses three parallel ML-5682 tubes to switch up to 24 kV to the primary of the pulse modulation transformer. A step up ratio from unity to two in six discrete steps can be selected for the secondary. Alternate transformers are required depending on whether or not the pulse duration exceeds 10 μs.

The 230 V ac distribution panel contains control switches, relays, and circuit breakers for a sequenced transmitter start-up. By monitoring power levels and temperatures, interlocked shut-down is provided automatically in case of malfunctions in the air or water cooling systems.

A tuning and monitor console serves as the operator's position. Here are located a considerable number of meters which monitor the state of the transmitter and oscilloscopes for observing command signals and

transmitted pulse shape.

The heat exchanger-water cooling system circulates 100 gallons of distilled water to remove heat from large tube anodes. Cooling is provided by two water-to-air radiators. Air flow is the result of two 2 hp motor-driven blower fans.

An air compresor furnishes 60 to 80 psi air to an accumulator where a pressure reducing valve and air dryer feed 15 psi air to the tube housings and coaxial lines. This reduces sparkover and helps blowers inside the tube housings to operate effectively.

To increase the versatility of our radar system and to reduce downtime due to transmitter failures, two modified forms of transmitter operation have been developed. The first form bypasses the four output amplifier cavities and associated hybrid combiners. Instead, power from the driver output phase shifting network is sent via RG-17 coaxial cables directly to the transmitting antenna. Although the driver tube can handle peak powers in excess of 1 MW, we normally operate at no more than 500 kW to prevent arcing in the RG-17 connectors. To establish this mode of operation one need only connect the receiving end of the RG-17 cables in place of the 7-inch coax normally used at the antenna terminals, take out two sections of 3-inch pipe associated with the driver, and in their place attach the sending end RG-17 via connectors. The former operation takes just minutes outdoors and the latter requires only a few hours of indoor work. Thus little time is required to set up this mode of operation and it can be done in all weather conditions.

To permit unattended operation over much longer periods, a low power transmitter mode is available. For this we use only the low level amplifier stages and the 3 kW 814B transmitter. Operation of the high voltage

rectifier, pulse modulator, water cooling, and air pressure units is thus avoided. A single RG-8 cable delivers the 3 kW peak pulses to a balun which transforms the 50 Ω unbalanced line to the 100 Ω balanced line required by the transmitting antenna.

2.2.2.3 *Transmitting antenna.* Design and construction of a practical transmitting antenna subsystem for our radar has been accomplished under the direction of Mr. G. W. Henry [*Edwards*, 1973b] and with the help of preliminary investigations by Mr. W. Lee [*Lee and Geller*, 1973]. The following discussion is based on unpublished notes of Mr. Henry. The desired transmitting antenna characteristics are:

1. It must be able to handle peak power levels of 4 MW.
2. It should have sufficient gain to enable the reception and processing of an adequate number of meteor trails.
3. It should radiate most of its power in a beam that is reasonably narrow in elevation angle and is centered at 45° elevation.
4. Its radiated beam should intersect the meteor wind zone (approximately 80 - 120 km) with angular width sufficient to resolve two horizontal wind components (around 45° in azimuth extent).

Of prime importance in the antenna design is the pattern produced by the array. The requirements of the experiment are to illuminate a fan-shaped sector of the sky whose -3 dB locus is bounded by the altitudes 80 and 120 km and by the direction NNE (022.5°) and NNW (337.5°). The plane of this locus is defined as being a surface 100 km to the north of the transmitter that is perpendicular to the surface of the earth. These requirements translate into antenna parameters of approximately 11.6 degrees elevation -3 dB beamwidth and 45 degrees azimuthal beamwidth, measured across the center of the beam, which is located at 45 degrees elevation and

directed to the north. Because of practical construction considerations, the linear-dipole type of antenna array was chosen for the transmitting antenna. Pattern calculations of uniform linear arrays were conducted using the PDP-15/40 computer at the Field Station and the equations developed below.

I. Dipole Pattern

The electric field intensity of a single dipole of length d_1 can be expressed as (Figure 2.9(a), *Kraus* [1950]):

$$E_D \simeq \frac{\cos(\pi[d_1/\lambda]\ \cos\beta) - \cos(\pi[d_1/\lambda])}{\sin\beta} \tag{2.24}$$

where the angle β is related to the elevation angle α and azimuth angle γ via

$$\cos\beta = \cos\gamma\ \cos\alpha$$

$$\sin\beta = (1-\cos^2\gamma\ \cos^2\alpha)^{\frac{1}{2}}$$

Thus,

$$E_D \simeq \frac{\cos(\pi[d_1/\lambda]\ \cos\gamma\ \cos\alpha) - \cos(\pi[d_1/\lambda])}{(1-\cos^2\gamma\ \cos^2\alpha)^{\frac{1}{2}}} \tag{2.25}$$

It is desirable to normalize the dipole pattern to a maximum gain of unity. If we restrict ourselves to dipoles of length $d_1 \leq \lambda$, then

$$AD \triangleq \left|\frac{E_D}{E_{D\max}}\right| = \left|\frac{\cos(\pi[d_1/\lambda]\ \cos\gamma\ \cos\alpha) - \cos(\pi[d_1/\lambda])}{1-\cos(\pi[d_1/\lambda])\quad(1-\cos^2\gamma\ \cos^2\alpha)^{\frac{1}{2}}}\right| \tag{2.26}$$

II. Line of Point Sources

The line of point sources (Figure 2.9(b)) consists of N elements placed symmetrically about the origin along the y-axis. A progressive phase of δ radians is assumed between successive elements, beginning with the first. The pattern of a far point from a linear array of N point sources,

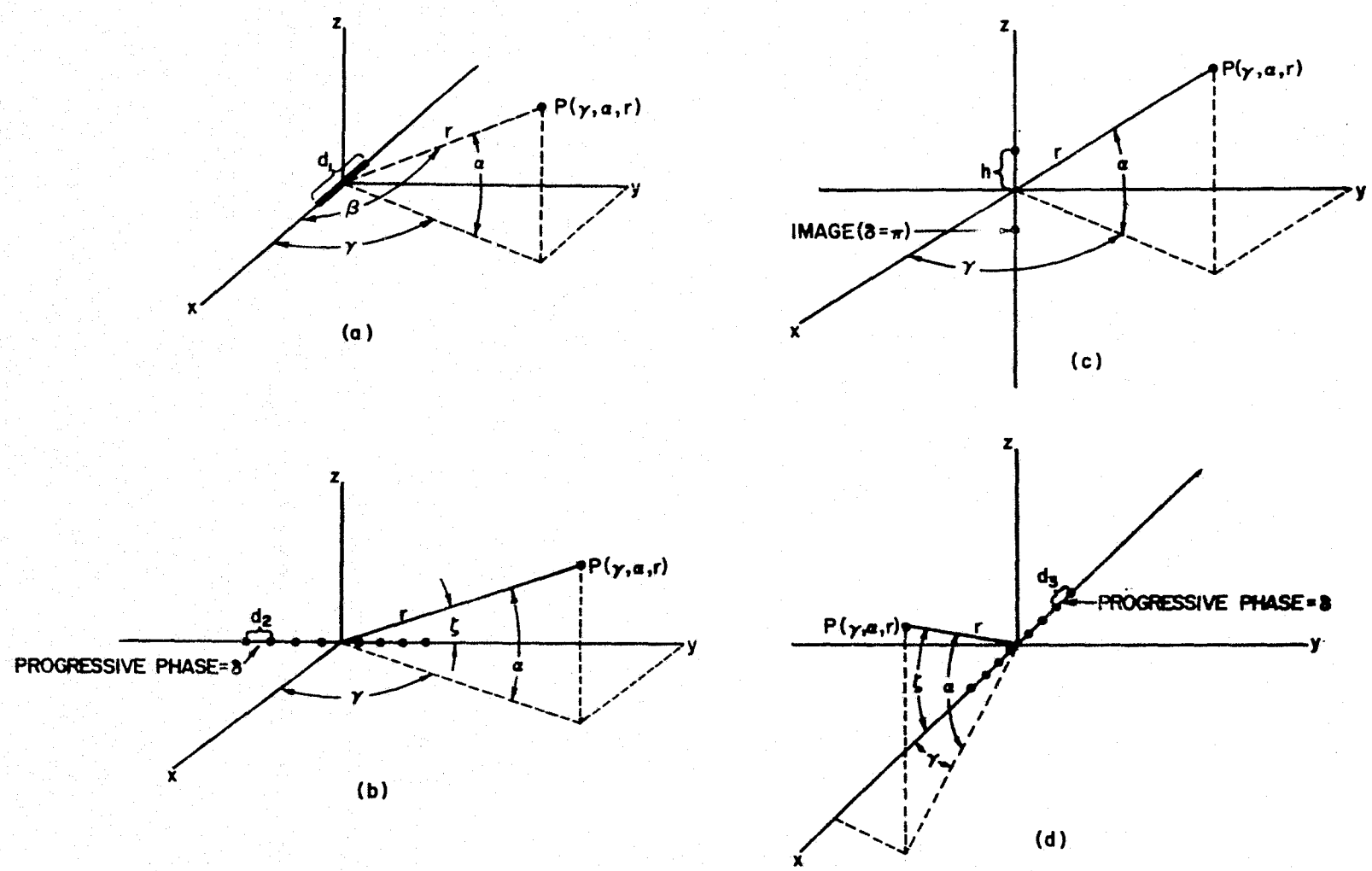

Figure 2.9 (a) Dipole geometry, (b) Line of point sources geometry, (c) Ground plane geometry, (d) Row of elements geometry.

each spaced at a distance d_2, is given by *Kraus* [1950]:

$$E_{LA} = E_o \sin(N\psi/2)/\sin(\psi/2) \tag{2.27}$$

where E_o = field from a single point source

ψ = total phase difference of the field from adjacent line sources, i.e.,

$\psi = 2\pi(d_2/\lambda)\cos\xi + \delta = 2\pi(d_2/\lambda)\cos\alpha \sin\gamma + \delta$

The effect of multiple sources in a line can thus be described by the normalized array factor

$$AL \triangleq \left|\frac{E_{LA}/E_o}{(E_{LA}/E_o)_{max}}\right| = \frac{|E_{LA}/E_o|}{N} = \frac{1}{N}\left|\frac{\sin(N\pi(d_2/\lambda)\cos\alpha \sin\gamma + N\delta/2)}{\sin(\pi(d_2/\lambda)\cos\alpha \sin\gamma + \delta/2)}\right| \tag{2.28}$$

III. Effect of Ground-Plane

A single-element antenna at height h above the ground can be considered an array in the z-direction. The reflection of the signal from the ground can be modeled by an image source ($\delta = \pi$) at a distance h below the ground. The pattern modification due to the image is a function of α only due to symmetry (Figure 2.9(c)):

$$AI \triangleq |\sin(2\pi(h/\lambda) \sin\alpha)| \tag{2.29}$$

No normalization is required provided $h \leq \lambda/4$.

IV. Rows of Linear Elements (Figure 2.9(d))

Similar to equation (2.27) we have

$$E_{RA} = E_o \frac{\sin(M\eta/2)}{\sin(\eta/2)} \tag{2.30}$$

where

$\eta = 2\pi(d_3/\lambda)\cos\zeta + \delta = 2\pi(d_3/\lambda)\cos\alpha\cos\gamma + \delta$

The effect of multiple rows of elements can then be described b the normalized array factor

$$AR \triangleq \frac{1}{M} \left| \frac{\sin(M\pi(d_3/\lambda)\ \cos\alpha\ \cos\gamma + M\delta/2)}{\sin(\pi(d_3/\lambda)\ \cos\alpha\ \cos\gamma + \delta/2)} \right| \tag{2.31}$$

V. Total Patterns

Using results from the first four sections, we can express the total pattern amplitudes for two antenna configurations of particular interest:

A. Single-row uniform linear array

$$TA1 \triangleq AD \cdot AI \cdot AL = \left| \frac{\cos(\pi(d_1/\lambda)\ \cos\gamma\ \cos\alpha) - \cos(\pi(d_1/\lambda))}{\{1 - \cos(\pi[d_1/\lambda])\}\ (1 - \cos^2\gamma\ \cos^2\alpha)^{\frac{1}{2}}} \right| \tag{2.32}$$

$$\cdot \left|\sin(2\pi(h/\lambda)\ \sin\alpha)\right| \cdot \frac{1}{N} \left| \frac{\sin(N\pi(d_2/\lambda)\ \cos\alpha\ \sin\gamma + N\delta/2)}{\sin(\pi(d_2/\lambda)\cos\alpha\ \sin\gamma + \delta/2)} \right|$$

B. Double-row uniform linear array

$$TA2 \triangleq TA1 \cdot AR\Big|_{M=2} = TA1 \cdot \frac{1}{2} \left| \frac{\sin(2\pi(d_3/\lambda)\ \cos\alpha\ \cos\gamma + \delta)}{\sin(\pi(d_3/\lambda)\ \cos\alpha\ \cos\gamma + \delta/2)} \right| \tag{2.33}$$

VI. Tapered Aperture Linear Array

A simple taper of the amplitude distributions of element currents in the dipole arrays discussed in V. can yield significant improvements in sidelobe suppression, while maintaining other pattern specifications. If as in II. we assume that all elements of the array (or each row of the array) are equally spaced, with a uniform progressive phase shift in the feed along the array, then the array factor is given by the series [*Weeks*, 1968]:

$$AL^* = \sum_{n=0}^{N-1} A_n\, e^{jn\psi/FN} \tag{2.34}$$

where $\psi = 2\pi(d_2/\lambda)\cos\alpha \sin\gamma + \delta$

A_n = amplitude of current in element n

N = number of elements in array (or each row of the array)

FN = normalization factor = $\left| \sum_{n=0}^{N=1} A_n \right|$

Using equation (2.34) in place of AL in the expression for $TA1$ allows modified equations (2.32) and (2.33) to express the total patterns for single- and double-row arrays with current tapering.

Examination of equation (2.27) reveals that the function E_{LA} goes to a maximum value of 1.0 when $\psi = 0$. Therefore, at the maximum

$$\xi_{max} = \cos^{-1}(-\delta/2\pi(d_2/\lambda)) \qquad (2.35)$$

For a given value of the direction of maximum radiation, ξ_{max}, (2.35) specifies a relation between the required phase shift and the spacing, but not unique values.

The requirements of the meteor-radar experiment are that the transmitting antenna produce a beam centered at an elevation angle of 45 degrees to the horizon, i.e., ξ_{max} is either 45 degrees or 135 degrees. The progressive phase shift term, δ, is considered to be positive for a phase advance (lead) and negative for a phase retard (lag). Practical considerations of available land at the Aeronomy Field Station for the antenna indicated that the antenna would have to be placed south of the transmitter building. Since it was required to direct the beam to the north and the shortest feedline length between transmitter and antenna was desired, it followed that (1) the elements would be placed in a north-south line with element 1 to the north, (2) the transmitter would be connected to element 1 first, (3) the angle ξ_{max}, would have to be 135.0 degrees. Since the cosine function is negative in the second quadrant, the ratio $\delta/2\pi(d_2/\lambda)$ will be

positive and, therefore, δ is positive (leading).

Examination of equation (2.27) also shows that E_{LA} is periodic with period 2π. These additional major maximums are called "grating" lobes and are not desirable for this antenna design. Therefore, it is apparent that the maximum value of ψ should not exceed 2π. If δ is positive, the sum $\delta + 2\pi(\frac{d_2}{\lambda})(\xi = 0.0)$ should not exceed 2π. Moreover, since a desirable pattern characteristic is that there be no sidelobe at $\xi = 0.0$ or 180 degrees, we set δ and $(\frac{d_2}{\lambda})$ so that their sum is equal to a value that produces a null in the function E_{LA}. The nulls of E_{LA} occur when the numerator $\sin\frac{N\psi}{2}$ goes to zero, or when

$$\psi = \frac{n}{N} 2\pi, \quad n = 1, 2, \ldots, N - 1 \tag{2.36}$$

where n = number of null, counting from the major lobe.

Also, in the interest of minimizing the number of elements required, it is desirable to choose parameters of the array so that the minimum possible beamwidth for a given number of elements is achieved. This is achieved by making the sum $\delta + 2\pi(\frac{d_2}{\lambda})$ as large as possible, within the above-mentioned constraints. The constraints of a null in the $\xi = 0$ direction and maximum "visible range" are met if n in equation (2.36) is set to $N - 1$, the last null in E_{LA} before $\psi = 2\pi$. Under these conditions, we have two equations relating δ and $(\frac{d_2}{\lambda})$ and solving for the optimum conditions:

$$(d_2/\lambda)_{opt} = (\frac{N-1}{N})\ (1-\cos\xi_{max})^{-1} \tag{2.37}$$

$$\delta_{opt} = -2\pi(\frac{N-1}{N})\ (\frac{\cos\xi_{max}}{1-\cos\xi_{max}}) \tag{2.38}$$

Thus for any uniform linear array with a specified number of elements, N, and a desired direction of maximum radiation, ξ_{max}, a unique value of the element spacing, $(\frac{d_2}{\lambda})$ and progressive phase shift, δ, can be found that

will produce the narrowest beamwidth while still giving a null along the line of the antennas. When the effect of the ground plane is considered, equation (2.29), we obtain a third equation for maximizing radiation in the ξ_{max} direction:

$$\frac{h}{\lambda} = 1/4 \sin\xi_{max} \tag{2.39}$$

When the elevation requirement of 45 degrees elevation is considered, calculations indicate -3 dB elevation beamwidths of 12.1 degrees for an 11-element optimum array and 11.1 degrees for a 12-element optimum array. Since neither array exactly meets the 11.6 degree beamwidth requirements and because it is also desirable to improve the -13.7 dB 1st sidelobe rejection, the effect of tapering the current distribution to the elements was also given consideration in the computer calculations. Various linear and functional aperture tapers were computed, but the most promising from both a performance and ease of construction viewpoint was a three-step taper. In this distribution, one-half of the available transmitter power is delivered to the center one-third of the elements. The remaining half of the transmitter power is split evenly between the two outside thirds of the elements. Thus, for a 12-element array and 4 MW of transmitter power, 2 MW would be coupled to the center four elements and the groups of four elements on each end would receive 1 MW. This distribution will produce a -3 dB beamwidth of 11.7 degrees and a first sidelobe rejection of -20.2 dB, a 7 dB improvement over the uniform linear array. The inter-element spacing and phase shift of the tapered array remain at the optimum values chosen previously.

Since the direction of maximum radiation from the linear array is neither vertical (broadside) nor horizontal (end-fire), the expression of azimuthal beamwidth is a function of both the elevation angle and the ground

azimuth angle, greatly complicating pattern calculations. In fact, the general form of the projected pattern is not fan-shaped as desired, but cusped with the -3 dB locus at maximum elevation in the north direction and dipping considerably (to as low as 40-km height) in the NE and NW directions. This effect is particularly pronounced if only a single line of approximately full-wavelength dipoles are used. Use of two rows of dipoles gives much better control over the azimuth pattern and allows a much closer fit to the original specifications. However, use of the double-row array does restrict most of the radiated energy to the center of the desired sector and there is a 10-dB amplitude variation over the full sector. The sector is somewhat more evenly illuminated with the single-row array, but a great deal of sky outside the desired region is also heavily illuminated. Since the two-row array is simply twice the elements and feed system of the single-row array, the larger, two-row system was constructed and the feed system arranged so that either can be selected by changing transmission lines. Likewise, the choice between uniform feed or tapered feed can be made by changing feedlines. Computed patterns for the single-row array and the double-row array are shown in Figures 2.10(a) and (b), respectively.

Azimuthal pattern requirements dictated use of element lengths of the order of one wavelength. Moreover, since a large number of 0.45 wavelength long pieces of aluminum tubing were on hand, an economical choice of a center-fed 0.9 wavelength dipole was made. Computations and field measurements showed the feed-point impedance of this dipole (0.35 wavelength height above ground) to be of the order of 800 to 1000 ohms. This is a rather high impedance for an antenna feed system, particularly when problems of corona are considered at our very high transmitter power level. Designing for the worst-case where the tapered feed would be used and only one of the two rows

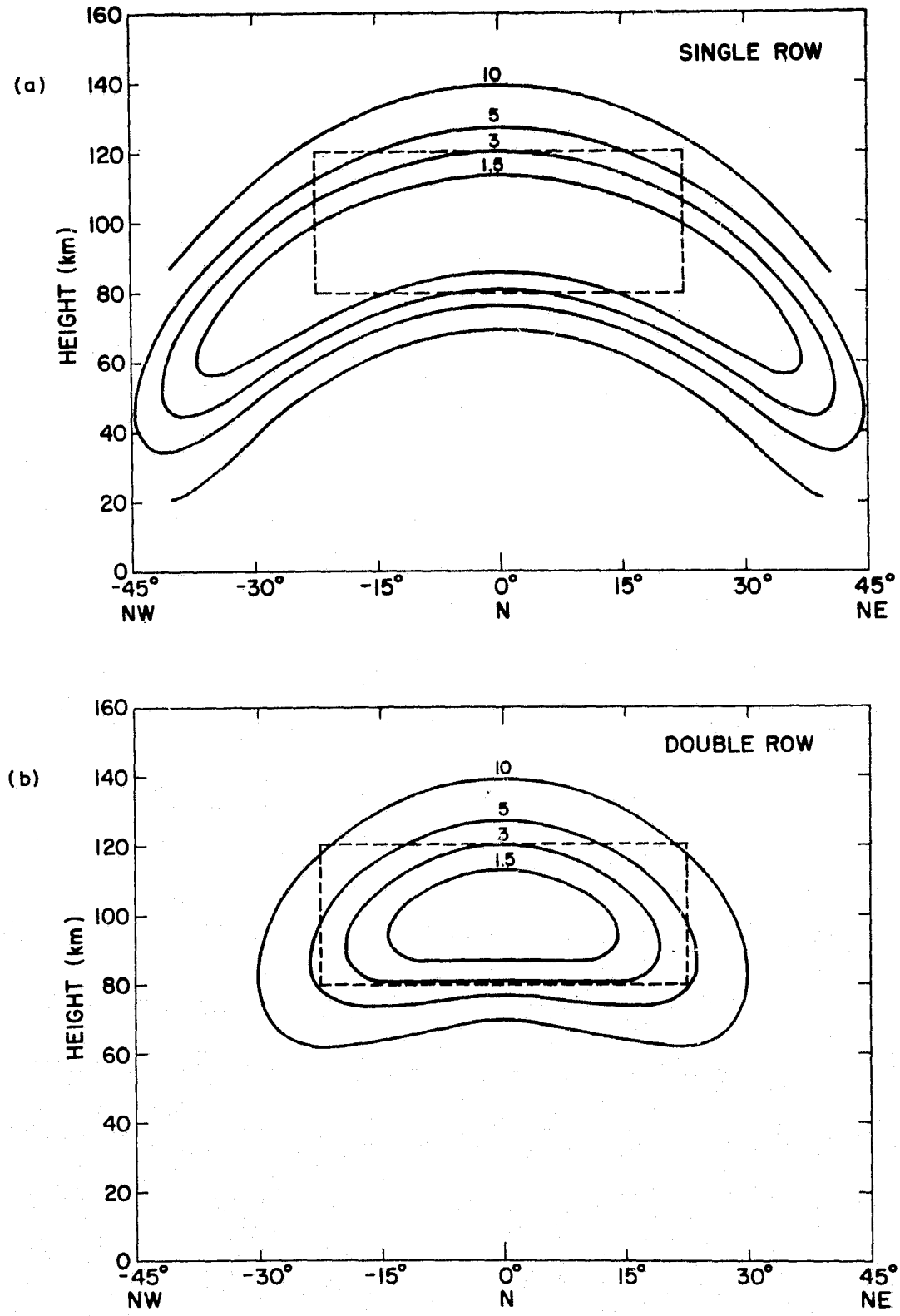

Figure 2.10 (a) Total pattern, single row array;
(b) Total pattern, double row array.

would be connected, the center four elements would each receive 1/4 x 1/2 x 4 MW, or 500 kW each. This corresponds to a terminal voltage of 32 kV for a 1000 ohm dipole. If dry-air corona is assumed to occur at fields of approximately 70 kV/inch, corona will form on any piece of the antenna structure at this potential with a radius less than 0.075 inches. To allow for humid conditions, a safety factor of 2 is considered adequate and therefore, all hardware at the antenna feed point was rounded so that no radius was less than 0.15 inches. Since the elements are essentially one wavelength long, the voltage at the outermost tips is of similar magnitude to that at the middle and the ends must also be rounded. The tubing from which the elements were constructed is 2 inches in diameter, but has sharp ends which were capped by round covers to minimize sharp edges. Feed hardware was restricted to large, well-rounded materials as much as possible and high-voltage coatings applied to assure additional protection.

Open-wire transmission line construction is generally restricted to characteristic impedances between 600 and 300 ohms because of minimum wire size imposed by maximum power handling considerations and maximum spacing imposed by radiation considerations. Therefore, the feed-point impedance of the antenna is first transformed in a quarter wavelength section down to approximately 360 ohms. This impedance transformer is designed so that the impedance and therefore the transformation ratio can be changed in the field by changing the wire spacing. This allows for compensation of interactive mutual-coupling effects between elements.

A consequence of the choice of neither a broadside nor endfire design for the linear array is that the length of the air-insulated transmission line required to give the desired phase shift is not the same as the physical spacing required. In our case, the length of the phasing line is greater

than that of the spacing between elements. Therefore, we "used up" the excess phasing line length by allowing the center of the span to be raised above the ends, creating a "peaked" appearance. Another design consideration for the phasing lines is that the phase shift along the line is only a true linear function of distance if the line is matched (no standing wave), the phase function becoming highly nonlinear and stepped in 180 degree increments for high standing wave ratio conditions. Therefore, all phasing lines are matched exactly and impedance transformations in the system are only carried out with quarter-wavelength (90 degrees phase shift) lines.

To allow for tapering the aperture as discussed previously, the feed system of the array is broken into three sections of four elements per section. Each section is further divided into two subsections of two elements each. The last chain of subdivision is necessary to assure that the feed-line impedance requirements do not fall below 300 ohms for the phase delay lines. Each time in the feed system that the impedance drops to the lower end of the allowable impedance range, the impedance is transformed back up to 600 ohms before further interconnection.

The complete feed system as designed for a two-row 12 element linear array is shown in Figure 2.11. Feedlines numbered 1 transform the dipole impedance down to approximately 360 ohms, lines 2, 3 and 8 are quarter-wavelength impedance transformers, and lines 4, 5, 6 and 7 are phasing lines. Line 9 is actually two parallel coaxial quarter-wavelength sections to match the antenna to the 100 ohm balanced coaxial line from the transmitter. If only a single row of elements is desired, Section 9 is changed as noted and elbows substituted for Tee fittings at the point of connection to the coaxial cables. The choice of the stepped taper is controlled by the impedance chosen for matching section 8. Since changing line 8 will

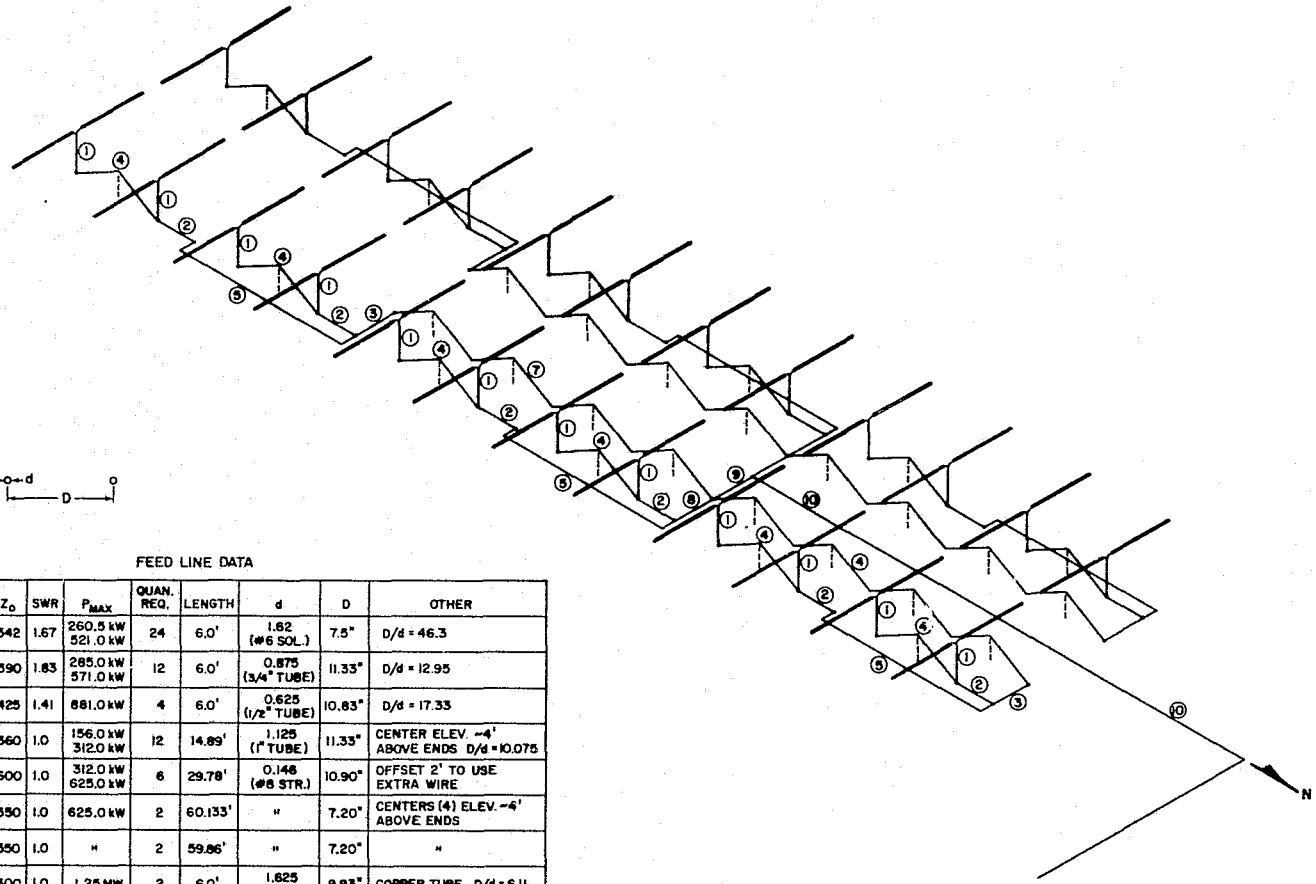

FEED LINE DATA

LINE NO.	USE	Z_o	SWR	P_{MAX}	QUAN. REQ.	LENGTH	d	D	OTHER
1	Q-1000Ω→360	542	1.67	260.5 kW 521.0 kW	24	6.0'	1.62 (#6 SOL.)	7.5"	D/d = 46.3
2	Q-180→600	390	1.83	285.0 kW 571.0 kW	12	6.0'	0.875 (3/4" TUBE)	11.33"	D/d = 12.95
3	Q-300→600	425	1.41	881.0 kW	4	6.0'	0.625 (1/2" TUBE)	10.83"	D/d = 17.33
4	ϕ-224.5°	360	1.0	156.0 kW 312.0 kW	12	14.89'	1.125 (1" TUBE)	11.33"	CENTER ELEV. -4' ABOVE ENDS D/d = 10.075
5	ϕ-449.0°	600	1.0	312.0 kW 625.0 kW	6	29.78'	0.146 (#8 STR.)	10.90"	OFFSET 2' TO USE EXTRA WIRE
6	ϕ-902.0°	550	1.0	625.0 kW	2	60.133'	"	7.20"	CENTERS (4) ELEV. -4' ABOVE ENDS
7	ϕ-898.0°	550	1.0	"	2	59.86'	"	7.20"	"
8	ϕ-90°	300	1.0	1.25 MW	2	6.0'	1.625 (1 1/2" TUBE)	9.93"	COPPER TUBE D/d = 6.11
9	Q-150→200	173	1.15	2.89 MW	2	6.0'	1.625 O.D. INNER	7"O.D. OUTER	COAX LINE (TWIN)
10	F.L.	100	1.0	5.0 MW	1	111.0'	3.00 O.D. INNER	7"O.D. OUTER	COAX LINE (TWIN)

TO USE ONLY 1/2 OF ARRAY, DELETE 1 SECTION OF ANTENNAS AND CHANGE FEEDLINE 9 AS FOLLOWS:

9a	Q-150→100	122	1.22	6.1 MW	1	6.0'	2.5" TUBE		COAX LINE (TWIN)

Figure **2.11** Meteor-radar transmitting antenna feed system.

also change the composite feed-point impedance of the array, it is also necessary to change line 9 impedance at the same time.

2.2.2.4 *Receiving antennas.* Commercial 13-element Yagi antennas, Telerex Model CY13-40-42, are used in an interferometer arrangement to allow measurement of echo elevation angle as discussed in Section 2.2.3.3. These antennas were originally used by the Smithsonian Astrophysical Observatory near Havana, Illinois. Forward gain of 15 dB, front-to-back ratio of 30 dB, and -3 dB beamwidths of 30° in azimuth and 64° in elevation are typical.

To provide a means for rejecting echoes from azimuths far off due north, a single dipole antenna is also used. The pattern for this antenna is directed to the east and west at the suggestion of S. A. Bowhill. Thus, wide azimuth echoes will have approximately equal video levels for the dipole and a Yagi directed northward, while echoes with azimuths near due north will be much stronger in the Yagi.

2.2.2.5 *Receivers.* The receivers used in the meteor radar project are transistorized single conversion superheterodyne units manufactured by Aerospace Research, Inc., model number PR-40A. These receivers were also originally used by the Smithsonian Astrophysical Observatory near Havana, Illinois. Specifications listed in the operation manual are:

Input center frequency	40.92 MHz
Input signal form	pulsed or AM
IF bandwidth	230 kHz at -3 dB pts
(By tuning for minimum bandwidth	100 kHz is achievable)
	67 kHz at -3 dB pts
(When modified IF filter is used)	
Image and spurious rejection	greater than 70 dB
Noise figure	less than 4 dB

Input impedance	50 ohms
Gain control	Manual, 38 dB in 1, 2, 5, 10, and 20 dB steps
Detector response	linear or logarithmic
Video output impedance	less than 100 ohms
Power	115 ± 15 V ac, 50-62 Hz, 3 W

The receiver front end consists of a broadband filter and low noise RF amplifier as shown in the block diagram of Figure 2.12. The filter is braodband to keep insertion loss at a minimum. The amplified signal passes through a doubly-tuned filter on the RF amplifier collector load for spurious and image frequency rejection before being applied to the base of the mixer transistor. Here mixing with a 35.42 MHz local oscillator signal obtained from the radar director results in an upconverted version of the input signal at 76.34 MHz and a downconverted version at 5.5 MHz. The narrowband 5.5 MHz filter following the mixer selects the lower sideband and acts as the primary determinant of the receiver passband. A pseudo-Gaussian frequency response is desired here so that the symmetry of input pulse shapes is preserved. Then the techniques discussed in Section 2.2.3.1 will work well as range estimators.

After passband shaping, the signal is applied to a series of front panel selectable attenuators and then amplified by three broadly tuned IF stages. Receiver response can be selected as either linear or logarithmic relative to the input signal amplitude. In the latter case, diode-resistor networks are utilized within each of the IF stages. Detection is accomplished by a half-wave rectifier-lowpass filter arrangement. This detected signal is buffered by an emitter follower output stage. A variable rheostat, accessible at the receiver front panel, has been added to the bias network

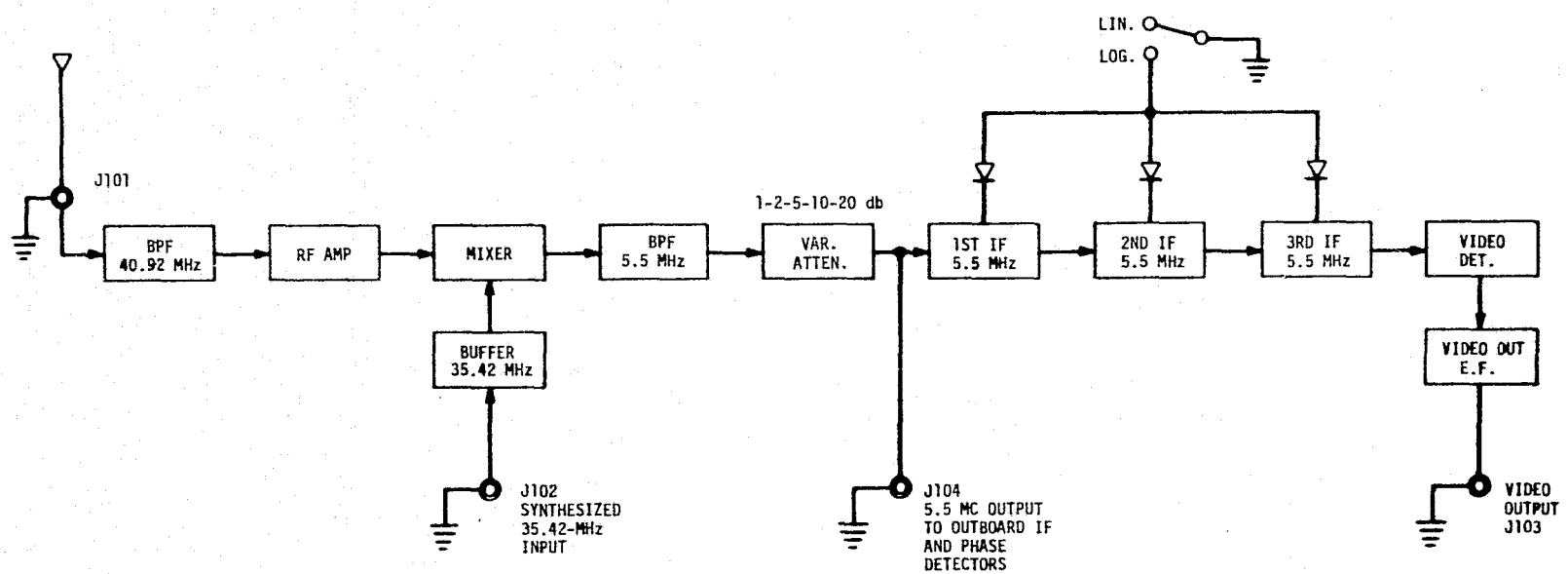

Figure 2.12 Block diagram of receiver, ARI model PR-40A.

of this output stage to provide a convenient means of zeroing the video DC offset. An IF output is also provided for use by the outboard phase detectors described in Section 2.2.2.6.

Passband characteristics of the PR-40A receiver are shown in Figure 2.13(a). As noted in the receiver specifications, one of the receivers was modified for a narrower bandwidth. Details of the IF filter used are contained in *Harrington and Geller* [1975]. The narrower bandwidth offers an improvement in signal-to-noise ratio and a better pulse response fit to the parabola used in ranging. However, wideband receiver performance is quite adequate for ranging (Section 2.2.3.1.3) and the lower Q results naturally in a filter that is easier to tune and less subject to drift after tuning. The large difference in response time between the wideband and narrowband IF filters means that all of the receivers would have to be modified if we go the narrowband route. Such modifications are not easy because of the compact PR-40A construction and after weighing potential advantages versus drawbacks it was decided to stay with the wideband units. Use of narrowband filtering on all phase detector outputs, where, due to the coherent nature of detection, baseband filtering with active integrated circuits is possible, does seem to be a possible means of improving radar performance.

A typical voltage transfer plot for the PR-40A receiver in the linear mode is shown in Figure 2.13(b). The software RXVID used to obtain data for these curves has an automatic mode wherein a computer controlled attenuator sets the radar director target level in steps as small as 1 dB.

To protect the receiver front end from damage during the transmit pulse, a controllable RF attenuator with minimal insertion loss is necessary. The schematic of a compact solid-state blanking unit for up to six receivers is shown in Figure 2.14. Blanking for each receiver is achieved by positively

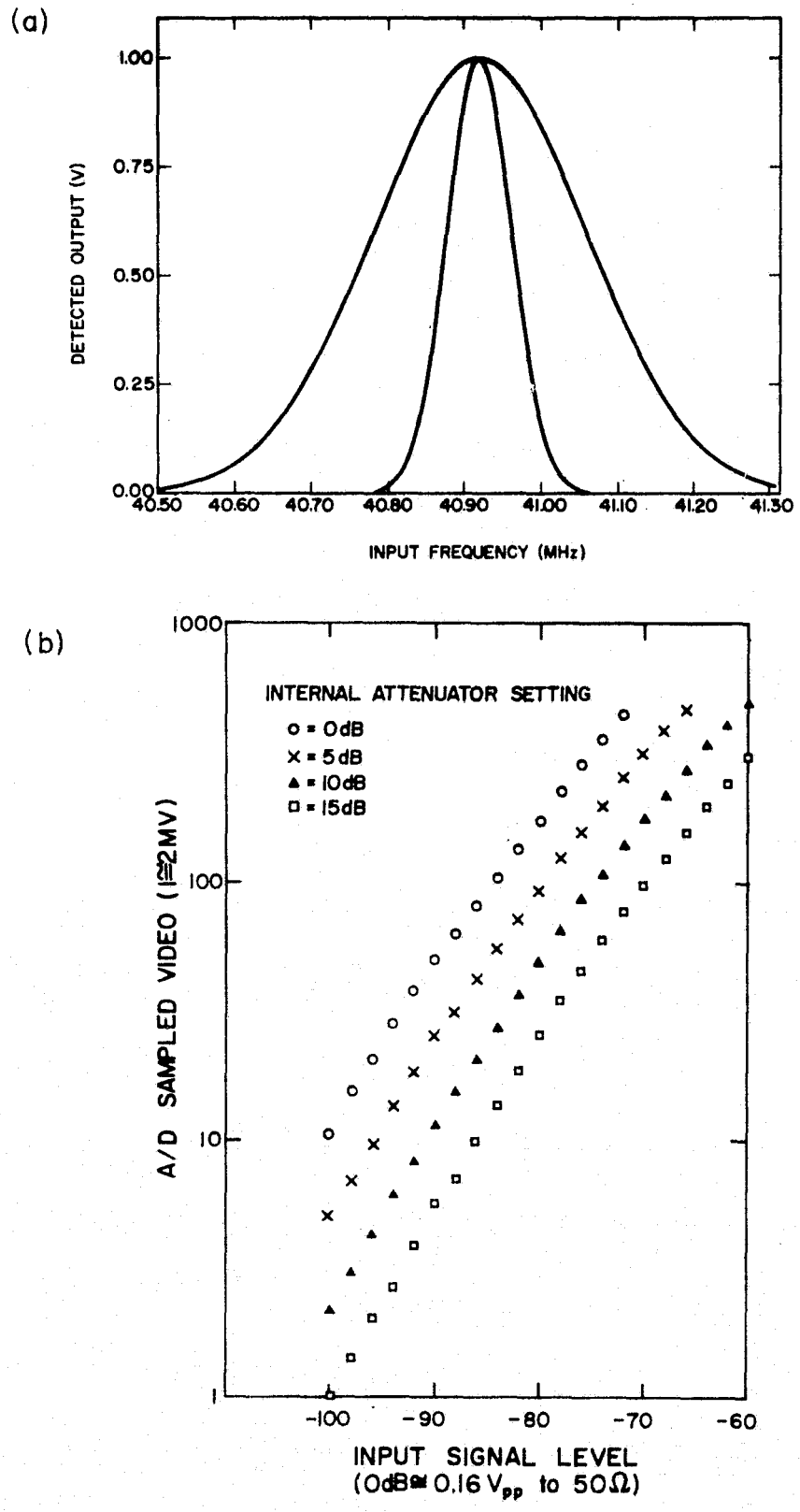

Figure 2.13 (a) Receiver passband characteristics [*Harrington and Geller*, 1975]; (b) Receiver transfer functions.

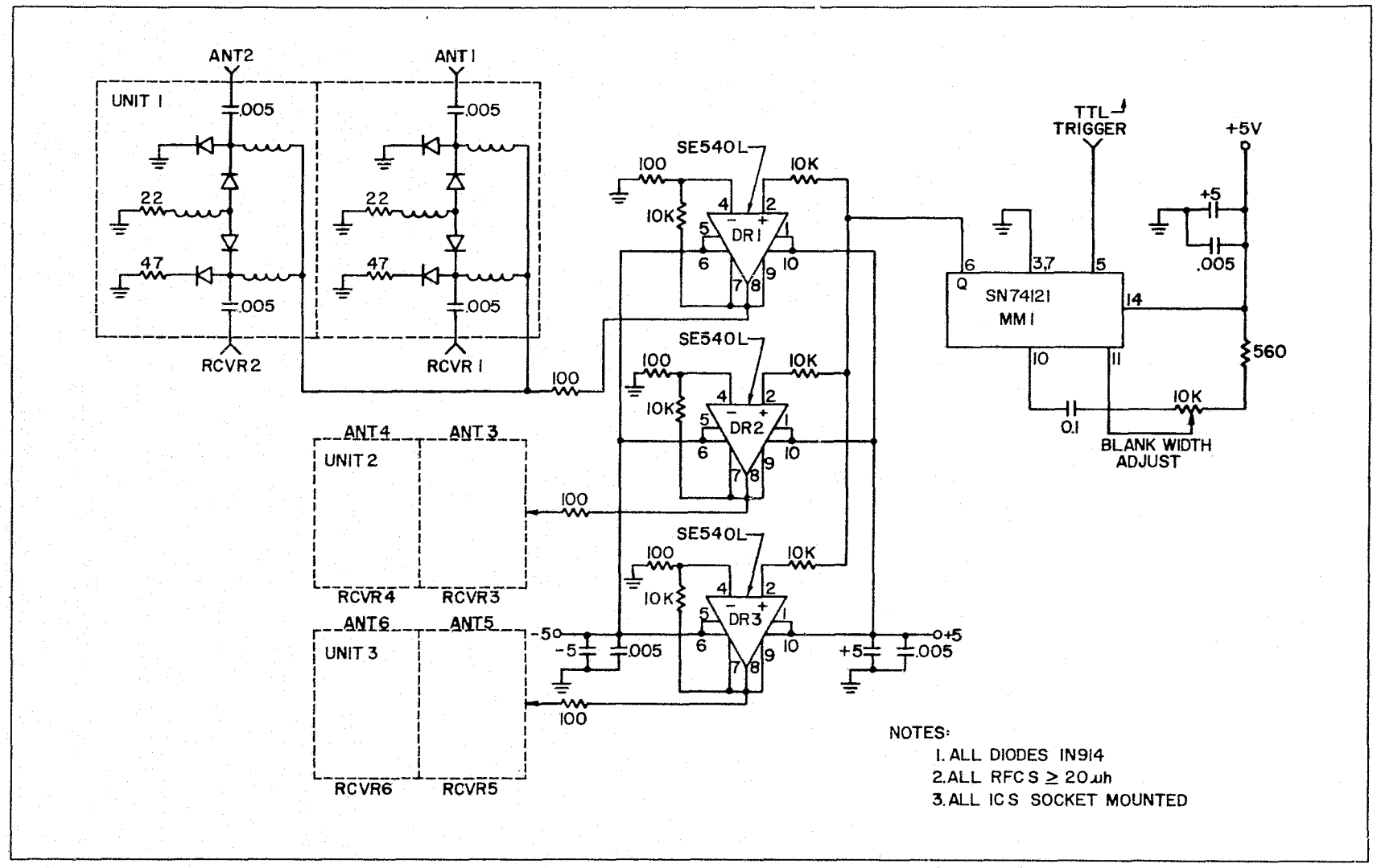

Figure 2.14 Six receiver diode blanker.

biasing a diode quad shunt-series-shunt switch arrangement. The blanking duration is controlled by the rheostat setting of monostable multivibrator MM1. After MM1 times out, the bipolar drivers DR1, DR2, and DR3 negatively bias all diode quads and thus incoming signals from the antennas are passed to the receivers. Shunt diode capacitance of the two series diodes in each quad limits the blanker "ON" isolation but 45 dB is easily achievable and is adequate. The amount of forward current through the same diodes is the main determinant of blanker "OFF" signal loss. With 20 mA an insertion loss of 1 dB is representative.

This blanker arrangement differs substantially from the one originally used and described by *Harrington and Geller* [1975]. The wideband transformers required by the original design were simply too expensive and it was highly desirable to replace the complicated discrete biasing circuits with simpler integrated circuit drivers. Use of two power supplies rather than three as required in the older blanker form is a further improvement.

The long arm interferometry arrangement described in Section 2.2.3.3 entails the use of five receivers, four driven by Yagis, one driven by a dipole. In anticipation of such operation, a five-way power splitter for the 35.42 MHz receiver local oscillator has been designed. As Figure 2.15 shows, each of five identical 250 Ω to 50 Ω impedance transformers are paralleled so that 50 Ω is also seen by the local oscillator source, FM. Any unused receiver outputs are simply terminated by 50 Ω dummy loads.

2.2.2.6 *Phase detectors.* The algorithms for Doppler frequency, and azimuth and elevation angles (Sections 2.2.3.2 and 2.2.3.3) require phase comparisons between each receiver IF signal and quadrature 5.5 MHz signals synchronous with the transmitted frequency. It is imperative for algorithm accuracy that the phase comparator pairs be exactly in quadrature and of

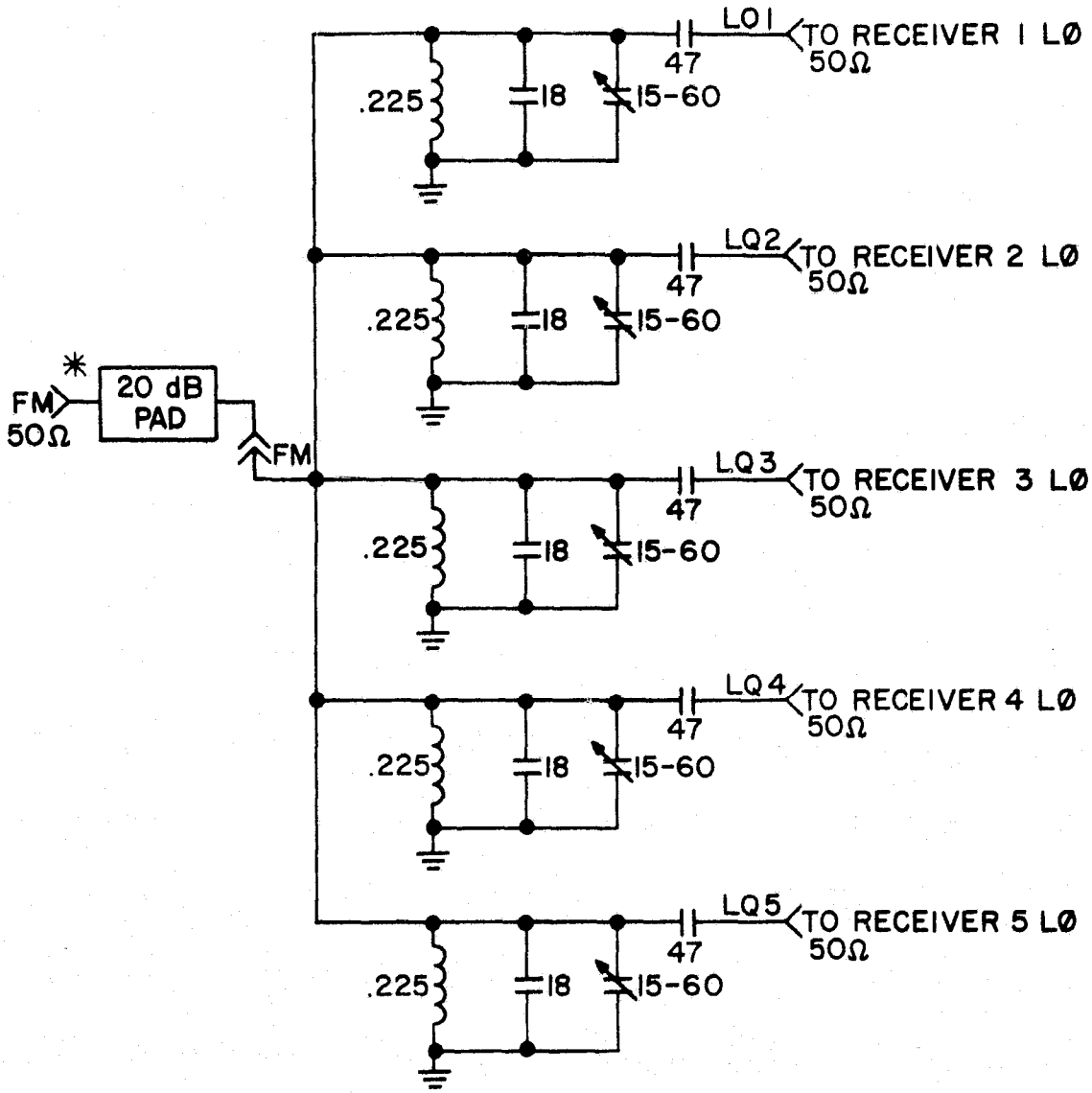

* PAD LOCATED ON RADAR DIRECTOR RACK

Figure 2.15 Five-way splitter for receiver local oscillator.

equal gain and these criteria must be met over the entire input signal dynamic range.

An ideal choice of device for this application is the MC1496 monolithic balanced modulator-demodulator. Operation of the balanced modulator-demodulator is described in Section 7.5 of a book by *Grebene* [1972]. Figure 2.16 shows the MC1496 used as a demodulator in the high-level AC mode, about 200 mV_{rms} 5.5 MHz carrier input, and biased as suggested in Motorola data sheet notes. The 50 kΩ potentiometer provides for nulling the carrier feed-through to the output. Because the MC1496 provides a balanced output about a non-zero DC reference level, one half of a μA747 operational amplifier is included to null out the DC component and produce a single-ended signal. A second half of the μA747 provides adjustable gain and filtering capability. The schematic shows a 100 kHz low pass filter set by the 100 pf and 10 kΩ in the feedback arm.

Quadrature phase comparisons are made by using a signal named FZ (5.5 MHz at 0 degrees) as the carrier in one balanced demodulator and a signal named FN (5.5 MHz at -90 degrees) in the second balanced demodulator. To improve the output signal-to-noise ratio, an IF strip is inserted between the receiver IF output and balanced demodulator inputs. The strip has three tuned stages and gain in excess of 40 dB, far too much, so a 30 dB pad is also used.

Periodic calibration of amplitude and quadrature operation is most easily done by injecting a Doppler shifted 40.92 MHz carrier into the receiver antenna terminal and displaying the phase comparator pair outputs on a dual trace oscilloscope. By examining the zero crossing times of Figure 2.17(a) quadrature operation can be verified.

Because the phase comparator bandwidth is somewhat less than the PR-40A

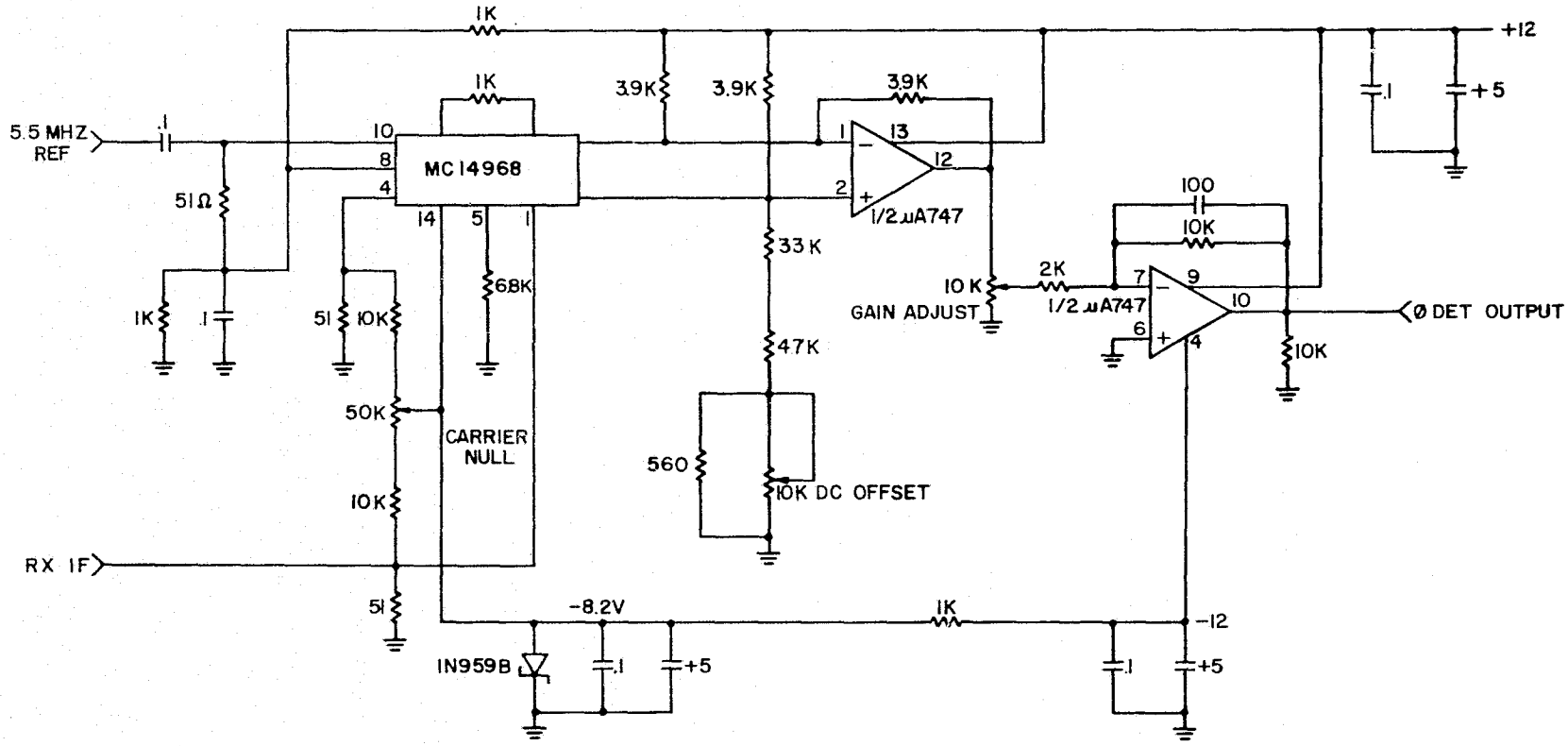

NOTE: 8 BALANCED DEMODULATORS ARE USED IN THE SYSTEM, 4 SINE AND 4 COSINE.

Figure 2.16 Balanced demodulator.

(a)

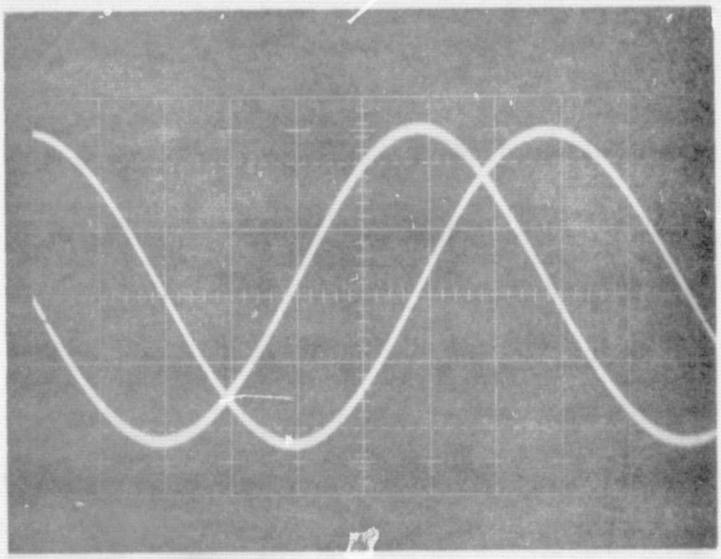

(b)

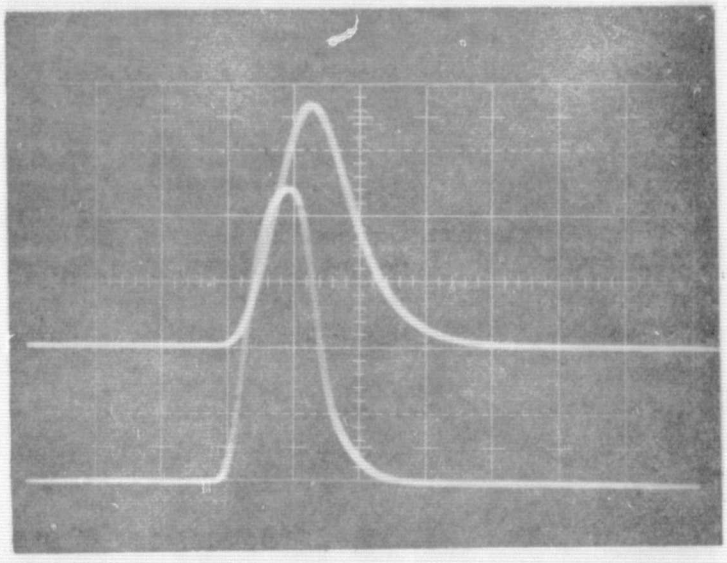

Figure 2.17 (a) Quadrature phase comparator waveforms.
(b) Video-balanced demodulator pulse responses.

receiver video bandwidth, the pulse response of the former is delayed slightly from the latter. Figure 2.17(b) shows this delay by comparing a cosine balanced demodulator output (top) with the receiver #5 envelope detector output (bottom). Software overcomes possible difficulty due to such delays by examining the phase samples at the time video peaks and also one clock period later (Section 2.2.4.1). Algorithm calculations are then centered about whichever sample yields the maximum absolute amplitude.

Since up to four sine and four cosine phase detectors may ultimately be used, four-way power splitters for both the zero (FZ) and 90 (FN) degree carrier signals have been constructed. As Figure 2.18 shows, these splitters consist of four identical 200 Ω to 50 Ω impedance converters driven in parallel. That allows the FZ and FN signals to terminate into 50 Ω loads.

2.2.2.7 *Computer and interface.* The meteor-radar system is supported by a Digital Equipment Corporation Model PDP-15 digital computer with 32k words of 800 nsec core memory. An extended arithmetic element provides hardware multiply and divide. The machine has a real-time clock, and a data channel for high speed input/output.

Several basic peripherals are part of the system. Four DECtapes provide medium-speed bulk storage, and four disks are used for high-speed, online storage. A 50-character-per-second paper tape punch and a 300-character-per-second paper tape reader are used for low-speed storage. Input-output is via teletype, a GE Terminet 1200 which prints 120 characters per second, and an Infoton cathode-ray terminal, which operates at a baud rate of 9600.

A Background/Foreground software monitor manages the system. The monitor supports assembly programming and FORTRAN IV compilation. All system peripherals are supported by the monitor, and all system programs

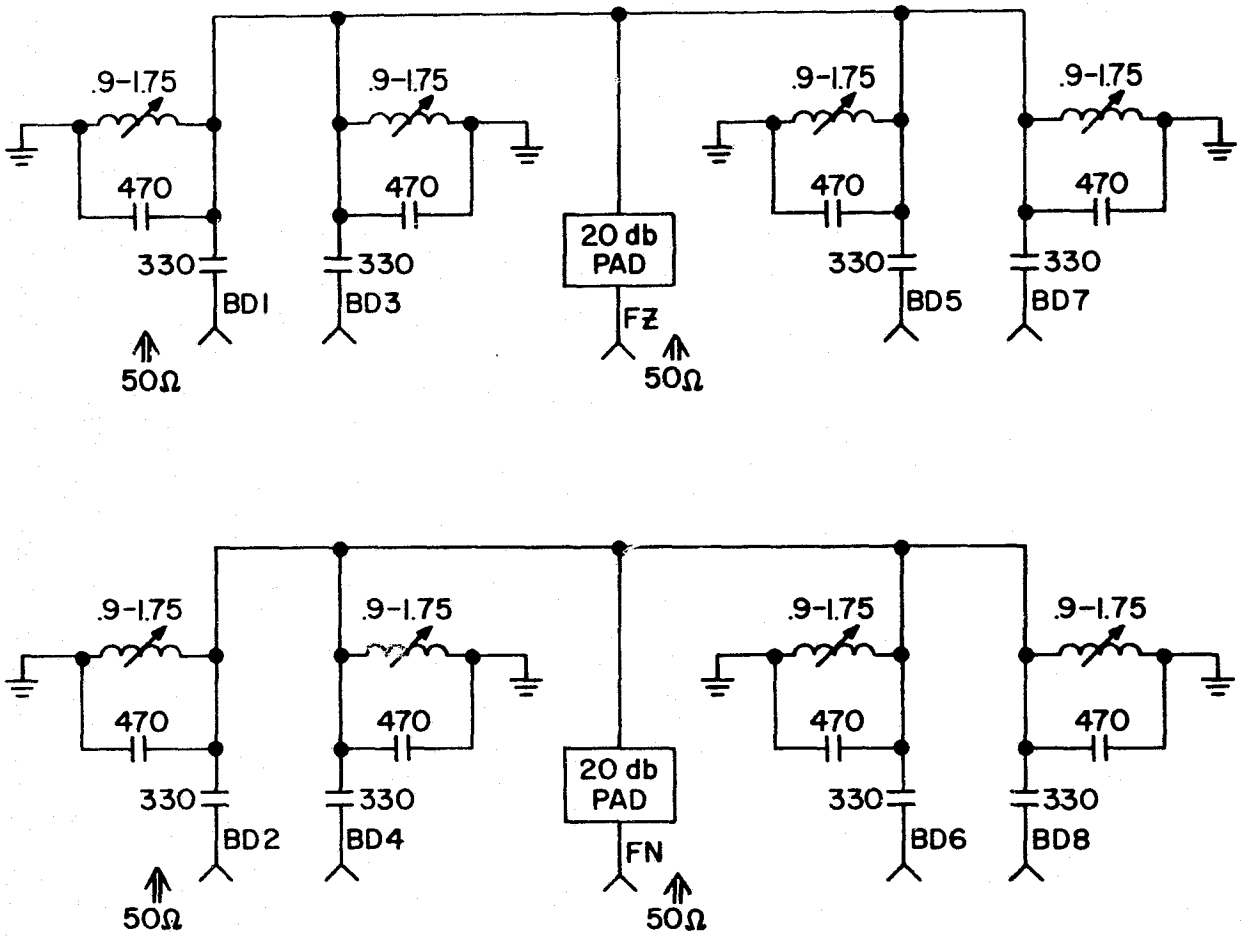

NOTE:

1. PADS LOCATED ON RADAR DIRECTOR RACK
2. SEPARATE ENCLOSURES FOR BD1-7 AND BD2-8

Figure 2.18 Four-way splitters for quadrature phase detector reference signals.

are disk resident for fast access.

Analog-to-digital conversion is provided by a Hewlett-Packard Model 5610 10-bit A/D converter. The device can perform up to 10^5 conversions per second, and is connected to the system by a direct-memory-access interface. The A/D converter has an accuracy of ± 1/2 least significant bit, and uses two's-complement output coding. A multiplexer is also provided at the A/D input so that any one of 16 data lines can be sampled at a time.

To facilitate connection of the numerous coaxial cables to the multiplexer data channels, and to provide random access availability of those data channels, the circuitry shown in Figure 2.19 was built. BNC connectors 0 through 15 go directly to the multiplexer. By appropriately jumpering cables from the receiver video detectors and phase detectors, the desired data sequence as in Table 2.1 can be achieved. Counter C1 is clocked each PRF by the SEQ pulse to update the active data channel by one. If the toggle selected channel was active, C1 reverts to the all zero state. In this way frame sequences with any length from 1 to 16 can be selected without resorting to opening the A/D cover.

To provide the meteor-radar operator with a visual indication of the state of each data line, an array of ten Tektronix Type 360 Indicator CRTs has been assembled. The indicators are triggered each PRF by a buffered pulse which drives a Tektronix Type 162 Waveform Generator. The sawtooth output controls horizontal sweep of all indicators and thus affords an "A-scope" type presentation.

2.2.3 *Measurement algorithms.*

2.2.3.1 *Range determination by curve fitting.*

2.2.3.1.1 *Overview of the ranging problem.* In pulsed radars range is usually deduced from the time difference between the instant of pulse

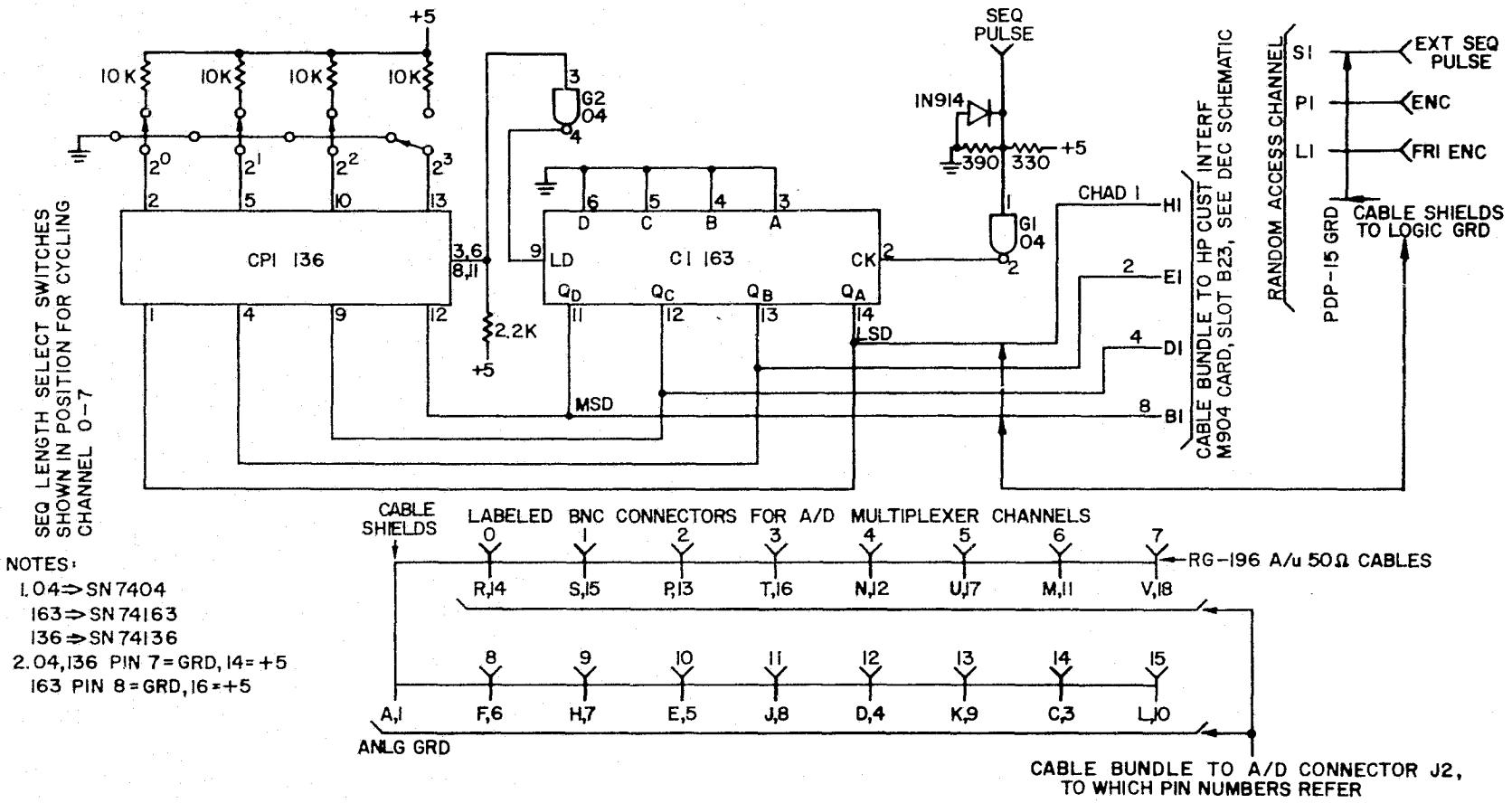

Figure 2.19 A/D multiplexer interface.

Table 2.1

Frame arrangement for stacked Yagi interferometer.

0	1	2	3	4	5	6	7	8	9	10	11	12	13	14
A_{Yv}	S_E	S_D	C_E	C_D	S_E	S_D	C_E	C_D	S_E	S_D	C_E	C_D	A_{Yv}	A_{DIP}

Where each channel (0-14) is sampled 100 times at 10 μs spacing; each radar PRF the next frame channel is activated; nine frames collected per usable meteor echo.

A = envelope detector
S,C = phase detector (sine, cosine)
Yv = Yagi video
E = elevation antenna A1
D = Doppler antenna A2
DIP = dipole video

transmission and the instant of echo reception. We can define the instant of pulse transmission as the instant during transmission when the maximum voltage appears across the transmitting antenna terminals, and the instant of echo reception as that instant during reception when maximum voltage is produced at the envelope detector video output. Of course, delays introduced by receiver filtering and interconnecting cables must first be subtracted from the time difference. Although we utilize separate transmitting and receiving antennas, their separation is so small that the monostatic radar case is applicable. As a further simplification, we will consider the nominal time base to be 10 μs, although when driving the radar director via the internal 40.92 MHz reference oscillator a time base of 10.0195 μs actually results. Carrier leakage into the sensitive receivers proved to be a nuisance on occasion using this arrangement so since September 1974 the radar director has been driven by a 100 kHz signal derived from a double ovenized frequency standard. Phase coherency is still excellent and carrier leakage is avoided since no 40.92 MHz energy can couple into the digital logic portions of the radar director. While the following discussion assumes a nominal time base of 10 μs, the range software (Appendix II) can handle any user specified value.

The time difference for ranging is composed of five parts. First, there is a fixed delay of 610 μs. This allows the system to time-discriminate against airplane echoes and ground clutter. The value is based on an overall antenna -3 dB beamwidth of 30° in elevation, centered at 45°, and extension of the meteor zone from 80 to 120 km (Figure 2.20). Since the A/D converter is not issued convert commands until 610 μs after the transmit command, there is no need to blank the receivers for the full 610 μs. In fact, it is helpful in verifying system performance to make the blank

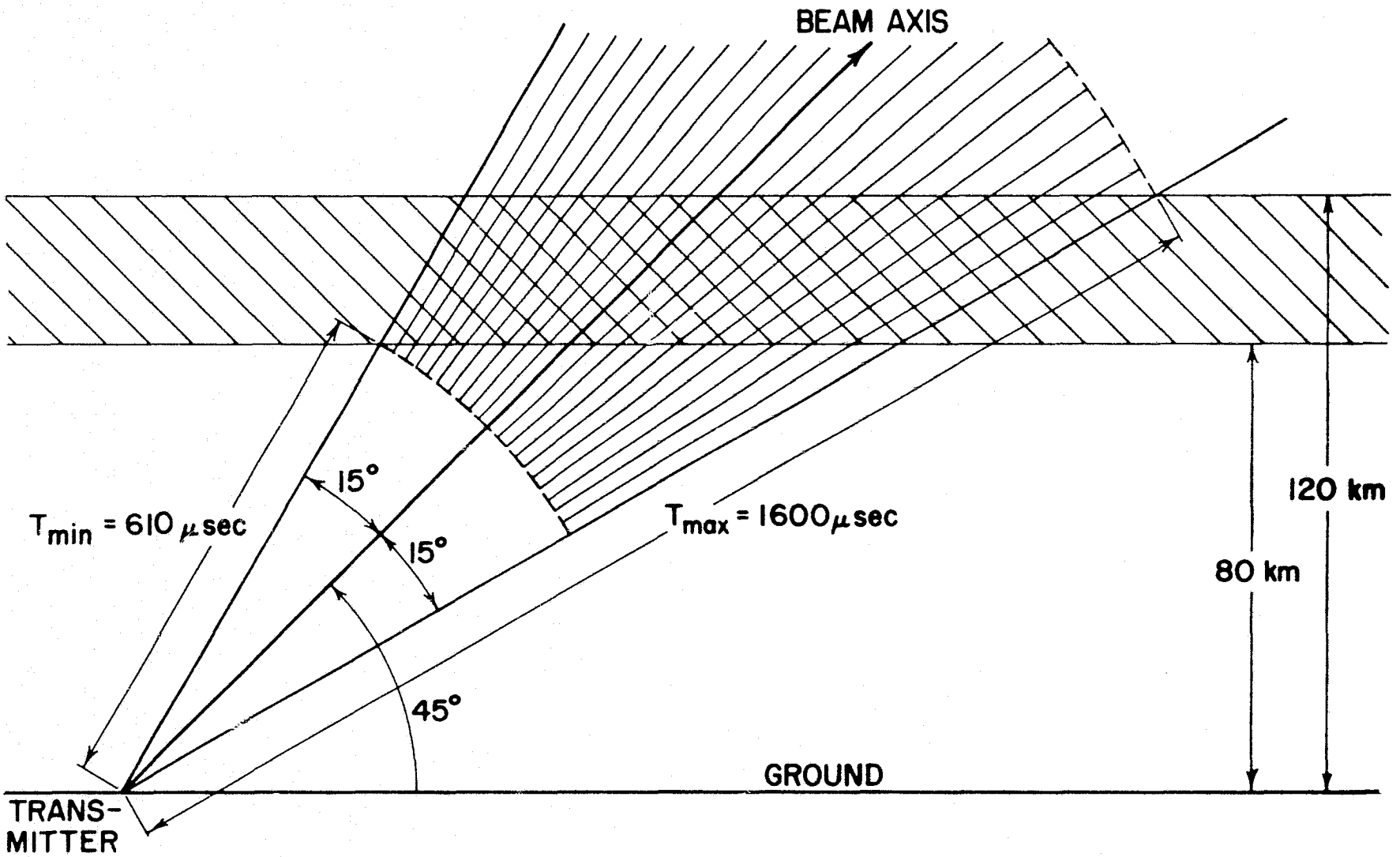

Figure 2.20 Meteor-echo region [*Backof and Bowhill*, 1974].

time small enough that airplane echoes are visible on an A-scope display.

Second, there is the time between collection of the first element in the video line and the instant of sampling of the largest element in the line. The elements are samples taken at equal 10 μs intervals so if the Nth element is the largest, this second time interval equals 10(N-1) μs.

Third, we note that our particular A/D converter has a 2 μs delay between issuance of a sample command and actual execution of the requested sampling.

The instant the largest sample is taken does not necessarily correspond exactly with the instant the largest voltage appears on the video line. Thus a fourth part of the time difference, τ, shown in Figure 2.21, should be considered.

Lastly, we must account for the delay between issuance of the transmitter command and peaking of the actual transmitted pulse. This delay, which we will label as LI, is necessary because the fixed 610 μs delay is referenced to the transmit command, not the transmitted signal.

Range can thus be calculated from the expression

$$R = (610 + 10(N-1) + \tau - LI + 2)0.15 \qquad (2.40)$$

where R is the range in km and τ and LI are in μs. If we do not correct for the sampling offset τ, range may be in error by ± 750 m (± 5 μs). Since our goal is ± 0.5 km accuracy in height and since elevation angle is much harder to measure than range, some method for measuring τ is essential. Any such method constitutes a range algorithm and we will presently discuss two such algorithms, both of which utilize curve-fitting techniques and were studied extensively by C. A. Backof [*Backof and Bowhill*, 1974]. First, however, two aspects of the sampling of the video output must be considered. These aspects are the finite aperture time and sampling rate of the A/D

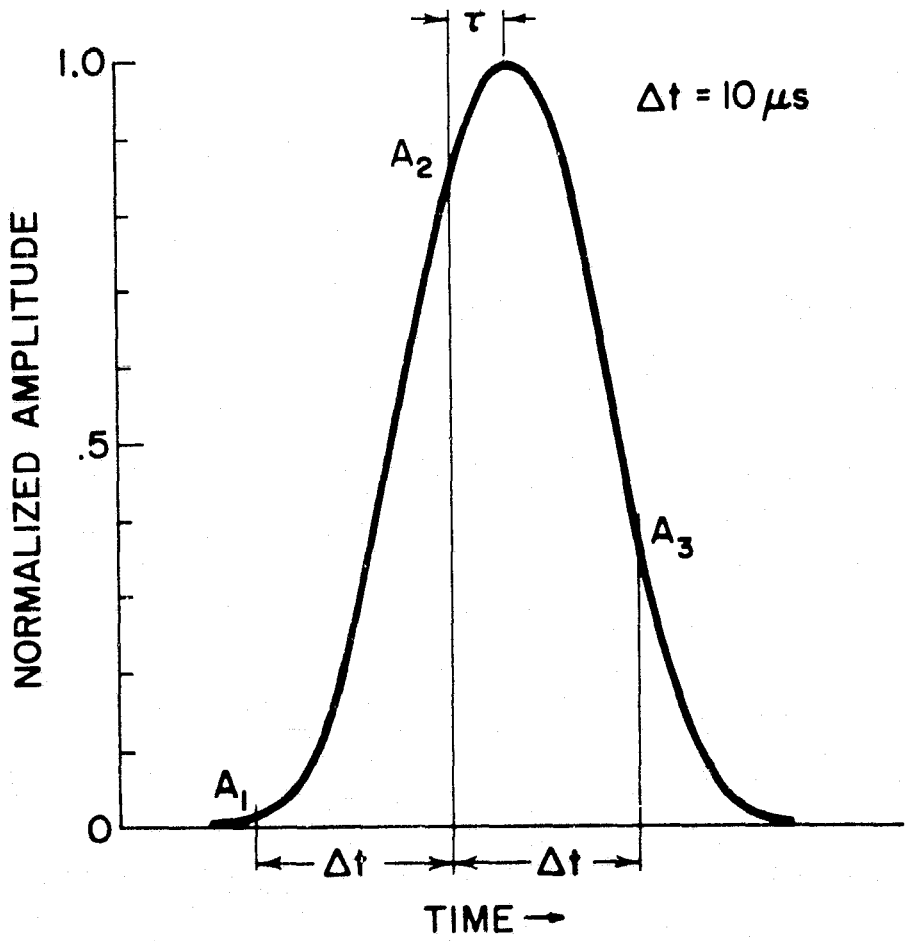

Figure 2.21 Typical receiver output pulse, with sampling superimposed [*Backof and Bowhill*, 1974].

converter.

The finite aperture time of the A/D converter causes an integration of the input signal. But the video output voltage is slowly varying relative to the 0.05 μs aperture time of our A/D converter since the typical receiver bandwidth is under 150 kHz. Thus the output of the A/D converter is a good approximation to the input voltage at the instant of sampling, and the finite aperture time has little effect on sample accuracy.

Each radar system has a characteristic pulse shape, defined as the time record of the voltage at the receiver video output during reception of an echo from a point target, i.e., a target which returns a replica of the transmitted waveform, attenuated and delayed according to target range, to the radar. This characteristic pulse shape is determined only by the transmitted pulse shape and the receiving response function. In our case the receiving antenna and feedline bandwidths are large relative to the receiver bandwidth. Thus we can consider the receiving and receiver response functions synonymous. The characteristic pulse shape can be found by convolving the receiver impulse function with the transmitted pulse shape. The sampling rate of the A/D converter is 10^5 sec^{-1}, so if the characteristic pulse is 10-20 μs at least one sample will always occur during pulse reception; for a width of 20-30 μs, at least two will occur; for a pulse width greater than 30 μsec, three or more samples will occur during pulse reception.

Techniques for finding τ can be developed if three criteria are met [*Backof and Bowhill*, 1974]: (1) The characteristic pulse shape is known. (2) The characteristic pulse width is such that more than one sample is taken in its duration. (3) The received echo is from a hard reflector. Under these conditions, the time record of the video output can be reconstructed from the samples taken during pulse reception. This reconstruction

amounts to fitting the known characteristic pulse shape to the samples. Once the time record of the video output has been reconstructed, the quantity τ is readily determined. Since samples need only be above the noise level to be used in the pulse fitting, the width of the characteristic pulse shape can be defined as the time between 20 dB points. The pulse fitting method used for pulse widths in the range from 20-30 μs takes the ratio of the maximum element to the higher of its two neighbors. The method used for pulse widths greater than 30 μs fits a parabola to the maximum element and its two immediate neighbors.

2.2.3.1.2 *Ratio method.* If the characteristic pulse is 20-30 μs wide, only two useful samples are guaranteed during pulse reception. If the shape of the pulse is known, the ratio of the two samples can be used to imply τ. For any given pulse shape, a table can be formed which relates τ to the ratio of the two samples. For a symmetric pulse, the points of pulse maximum must occur somewhere in the closed interval between the maximum sample, and the midpoint between the two samples; that is, $0 \leq |\tau| \leq 5$ μs. Table 2.2(a) was developed by assuming that a Gaussian pulse is transmitted, and that the receiver has a Gaussian passband. For various receiver bandwidths, the ratio for several values of $|\tau|$ is given.

The accuracy limitations of this technique are twofold. First, the largest practical size for the table is about 6 elements as shown, implying an accuracy of 1 μs in τ. Second, pulse distortion and noise can introduce large errors. For example, compare Table 2.2(a) results with those in Table 2.2(b), where a rectangular transmitted pulse shape has been assumed. For these reasons, the ratio technique is probably limited to an accuracy of about ± 2 μs (± 300 m).

2.2.3.1.3 *Parabola method.* The parabola method assumes that the shape

Table 2.2

Ratio of the highest sample to the higher of its two neighbors for offset $|\tau|$ from 0-5 μs. (a) Receiver bandwidth from 20-150 kHz; transmitted pulse width is 5 μs; transmitted pulse and receiver bandpass are Gaussian [*Backof and Bowhill*, 1974]. (b) Receiver bandwidth from 20-200 kHz; transmitted pulse width is 10 μs and rectangular in shape; receiver bandpass is Gaussian [*Edwards*, 1973a].

(a)

Bandwidth (kHz)	Offset (microseconds) 0	1	2	3	4	5
20	1.43	1.33	1.24	1.16	1.08	1.00
50	4.60	3.39	2.50	1.84	1.36	1.00
75	10.23	6.42	4.04	2.53	1.59	1.00
100	17.22	9.75	5.52	3.12	1.77	1.00
150	29.65	15.05	7.64	3.88	1.97	1.00

(b)

Bandwidth (kHz)	Offset (microseconds) 0	1	2	3	4	5
20	1.30	1.24	1.17	1.11	1.06	1.00
50	3.71	2.83	2.18	1.68	1.29	1.00
75	10.00	6.12	3.81	2.41	1.55	1.00
100	29.00	13.20	6.45	3.34	1.81	1.00
200	5000.00	665.00	74.20	13.40	3.35	1.00

of the characteristic pulse between 20 dB points can be modeled successfully by a parabola. The procedure for finding τ is to first find the coefficients of the function $f(x) = ax^2 + bx + c$, which passes through the maximum element, and each of its immediate neighbors. The first derivative $f'(x)$ is found; τ is equal to the value of x for which $f'(x) = 0$. Elements A_1, A_2, and A_3 are the three points to which the parabola is fitted (Figure 2.21). Relative to the center element, A_1 and A_3 are taken at $x = -10$ and $x = 10$, respectively. Then three equations can be written.

$$\begin{aligned} a(-10)^2 + b(-10) + c &= A_1 \\ a(0)^2 + b(0) + c &= A_2 \\ a(10)^2 + b(10) + c &= A_3 \end{aligned} \tag{2.41}$$

These equations are then simplified and solved giving

$$\frac{1}{100} \begin{bmatrix} 1/2 & 1/2 \\ -5 & 5 \end{bmatrix} \begin{bmatrix} A_1-A_2 \\ A_3-A_2 \end{bmatrix} = \begin{bmatrix} a \\ b \end{bmatrix} \tag{2.42}$$

The first derivative of $f(x)$ is calculated and set to zero giving

$$\tau = \frac{-b}{2a} \tag{2.43}$$

Quantities a and b are substituted from equation (2.42) so the offset τ, in μs, can be found according to

$$\tau = 5 \left[\frac{A_1-A_3}{A_1+A_3-2A_2} \right] \tag{2.44}$$

Note that the parabola method does not require prior knowledge of the

characteristic pulse shape. Even if the pulse shape is distorted by reflector irregularities, the method can give a reasonable approximation to τ. The only limitation is the modeling of the pulse shape between 20-dB points by a parabola. For a Gaussian-shape characteristic pulse, 30 μs wide, the maximum error in τ due to parabola modeling is 1 μs. For no-noise conditions, then, the parabola-fitting technique gives a worst case range accuracy of ± 150 m; this accuracy degrades gracefully with pulse distortion and atmospheric noise.

2.2.3.1.4 *Range algorithm accuracy.* Both the parabola and ratio methods could yield sufficiently accurate range values to meet our goal of ± 0.5 km height accuracy. However, because the parabola method is much less sensitive to variations in the transmitted waveform and receiver response function, it is the preferable technique to use and only it has been incorporated in the range software (Appendix II). The paragraph below explains how the target generator portion of the radar director can be used to evaluate system range accuracy as a function of transmitter pulse width, receiver bandwidth, and signal-to-noise ratio.

Range algorithm accuracy runs can be made using lead ESW to trigger the 1.2 ms free-run monostable multivibrator in the second target generator. Then with a 1 μs time base, A/D sampling begins synchronously 61 μs following the PRF rising edge. Hence, target jitter is absolutely minimal. A starting range word of 500 centers the target in the sample window. Figure 2.22 shows typical low S/N results for a wideband receiver (150 kHz) as pulse width varies 10 to 20 μs. The range errors are somewhat pessimistic since the artificial targets have very rapid rise and fall times. The system transmitter bandwidth is only 200 kHz and this will result in a wider time response with no flat-topping unless the pulse width exceeds about 30 μs. Thus, range errors on the order of 1 μs (150 m) are achievable even with

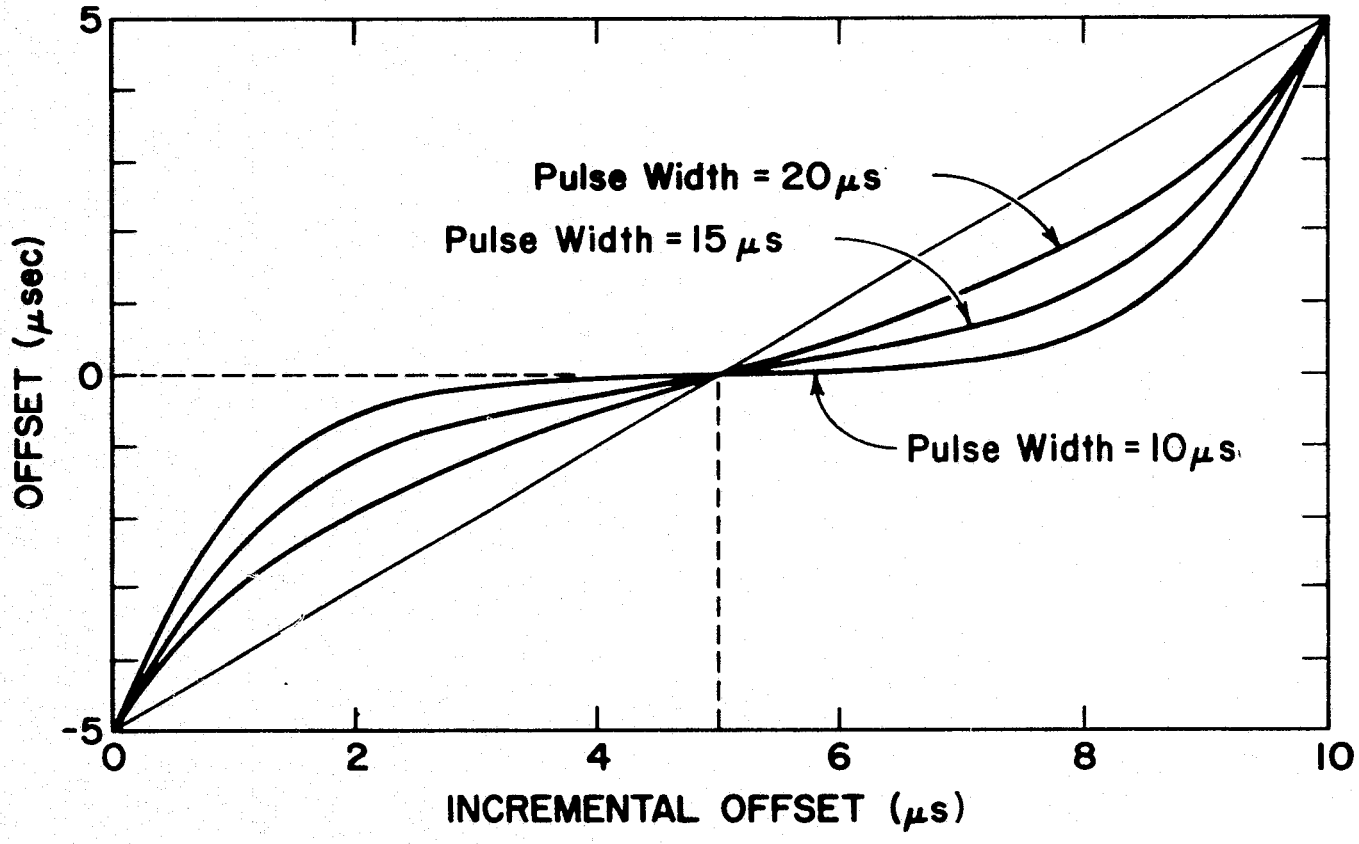

Figure 2.22 Representative wideband receiver range offset error curve [*Harrington and Geller*, 1975].

weak returns and a wide bandwidth receiver.

2.2.3.2 *Doppler measurement.* As meteor trails move with the surrounding atmosphere, a Doppler frequency shift is imposed on reflected radio waves. For a radar pulse with carrier frequency f_T, reflected from a meteor trail moving radially at a velocity v with respect to the pulse source, the received signal frequency f_R will be

$$f_R = \frac{1 + v/c}{1 - v/c} \; f_T \simeq \left(1 + \frac{2v}{c}\right) f_T \tag{2.45}$$

The approximation is valid because wind velocities in the atmosphere are always far less than the speed of light c. The radial wind velocity is related to the Doppler frequency shift through

$$v = \frac{c}{2f_T} \; (f_R - f_T) = \frac{\lambda}{2} f_d \tag{2.46}$$

In a coherent radar system, quadrature phase detectors (Section 2.2.2.6) can heterodyne returned radar pulses with the transmitted frequency to produce pulses of the form

$$\begin{aligned} &A \cos(\phi + \omega_d t) \\ &A \sin(\phi + \omega_d t) \end{aligned} \tag{2.47}$$

where

A = amplitude

ϕ = phase difference between returning signal and transmitter carrier

ω_d = radian Doppler frequency.

If we consider the following measurement sequence of quadrature phase detector outputs,

$$
\begin{aligned}
M_1 &= A \sin(\phi+\omega_d t_1) \\
M_2 &= A \cos(\phi+\omega_d t_2) \\
M_3 &= A \sin(\phi+\omega_d t_3) \\
t_3 - t_2 &= t_2 - t_1 = T
\end{aligned}
\tag{2.48}
$$

then it can be shown [*Backof and Bowhill*, 1974] that

$$
\omega_d = \frac{1}{T} \sin^{-1} \left[(M_3-M_1)/2M_2\right] \tag{2.49}
$$

where T = radar interpulse period.

To avoid excessive error when M_2 is small we take a fourth measurement

$$
M_4 = A \cos(\phi+\omega_d t_4)
$$

and solve for Doppler frequency via

$$
\omega_d = \frac{1}{T} \sin^{-1} \left[(M_2-M_4)/2M_3\right] \tag{2.50}
$$

The theoretical performance of the sampled data velocity algorithm described by equations (2.49) and (2.50) is shown in Figure 2.23(a). The results are somewhat optimistic though, due to the assumption of constant echo amplitude during sampling. A second velocity algorithm, developed by S. A. Bowhill [*Ryan and Bowhill*, 1976], allows for expontntial amplitude decay as theoretically predicted for underdense meteor echoes.

For

$$
\begin{aligned}
M_1 &= A \sin(\phi) \\
M_2 &= A \exp(-kT) \cos(\phi+\omega_d T) \\
M_3 &= A \exp(-2kT) \sin(\phi+2\omega_d T) \\
M_4 &= A \exp(-3kT) \cos(\phi+3\omega_d T)
\end{aligned}
$$

we have

$$
\omega_d = \frac{1}{T} \sin^{-1} \left\{ \frac{M_2M_3 - M_1M_4}{2\left[(M_2^2+M_1M_3)(M_3^2+M_2M_4)\right]^{\frac{1}{2}}} \right\} \tag{2.51}
$$

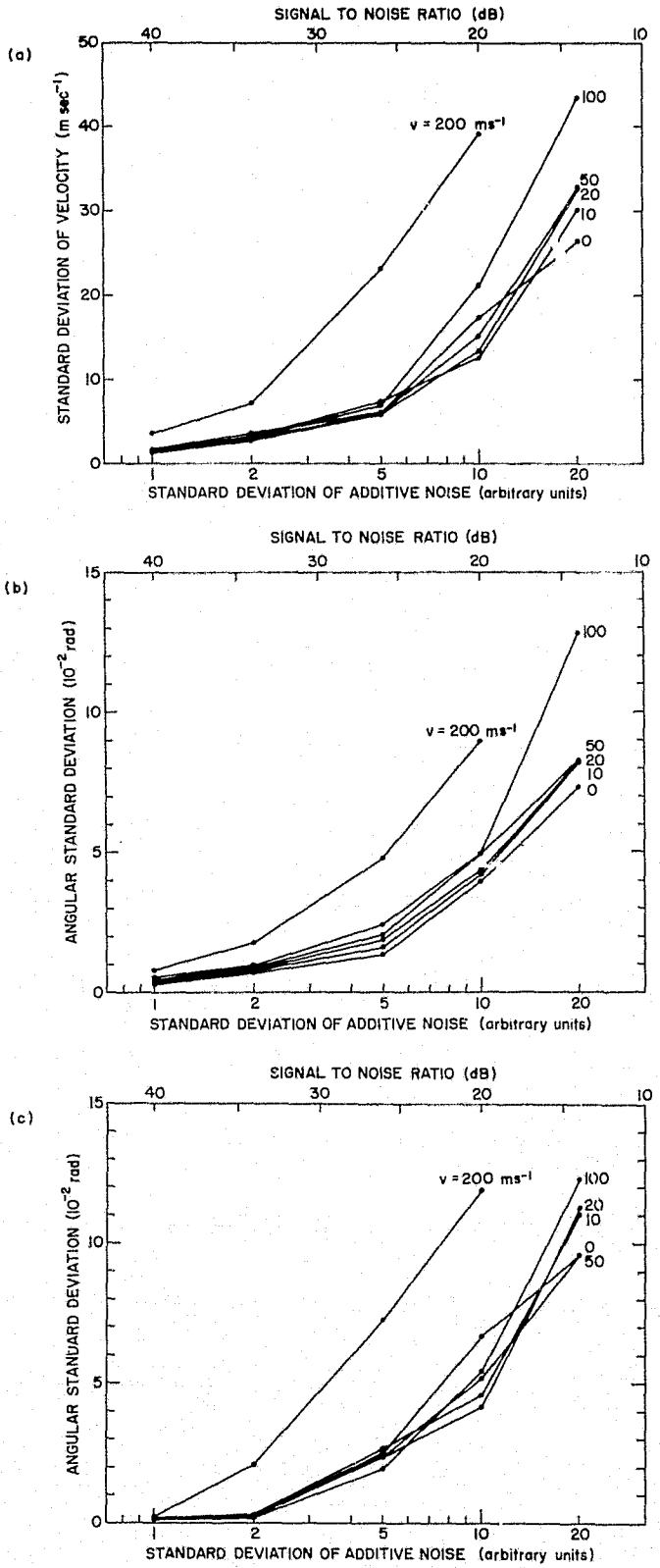

Figure 2.23 (a) Velocity standard deviation (Backof algorithm), (b) Azimuth standard deviation (γ=11°), (c) Elevation standard deviation (α=45°) versus additive noise [*Backof and Bowhill*, 1974].

Figure 2.24(a) and (b) show performance results for the receiving subsystem and Bowhill algorithm obtained using a radar director simulated target. Note that for velocities under 100 m s^{-1}, as we expect to normally find in the meteor region, the standard error is relatively independent of velocity and inversely related to signal-to-noise ratio. Since we will require at least three velocity measurements with signal-to-noise ratio in excess of 20 dB to accept an echo, our maximum measurement uncertainty is on the order of 10 m s^{-1}.

A common method used by other meteor-radar stations for obtaining velocities involves counting zero crossings of the phase channels. However, since meteor echoes typically last only a few tenths of a second, this method strongly discriminates against low velocity returns [*Barnes and Pazniokas*, 1972] (also see Appendix IV, Section 3.4). That the Bowhill algorithm has no such limitations is shown by the continuity through 0 m s^{-1} of the velocity histogram in Figure 2.25.

2.2.3.3. *Spaced antenna phase comparisons for angles of arrival.* The azimuth and elevation angles of a meteor echo can be determined by measuring the phase differences between pairs of spaced receiving antennas [*Lee and Geller*, 1973]. For example, Figure 2.4(a) shows a four antenna interferometer arrangement with a long baseline to act as a vernier for improving the elevation angle accuracy. If we let the symbols ϕ_{ij} and d_{ij} represent the phase difference and ground separation between antennas A_i and A_j, then we have

$$\begin{aligned} \phi_{12} &= \frac{2\pi d_{12}}{\lambda} \cos\alpha \cos\gamma \\ \phi_{23} &= \frac{-2\pi d_{23}}{\lambda} \cos\alpha \sin\gamma \\ \phi_{24} &= \frac{2\pi d_{24}}{\lambda} \cos\alpha \cos\gamma \end{aligned} \qquad (2.52)$$

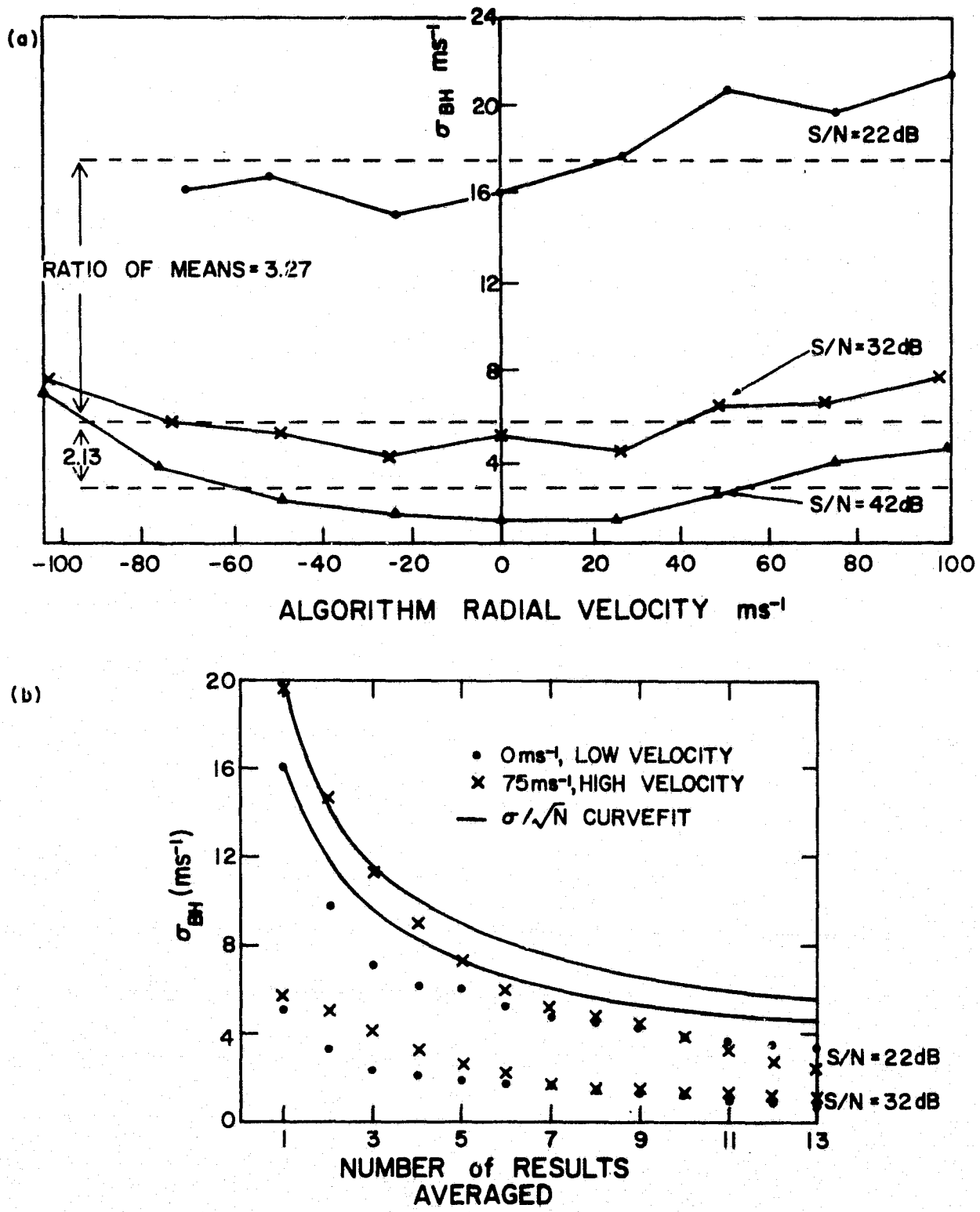

Figure 2.24 Bowhill velocity algorithm standard deviation versus (a) velocity and signal-to-noise ratio, (b) number of velocities averaged, signal-to-noise ratio, and velocity magnitude.

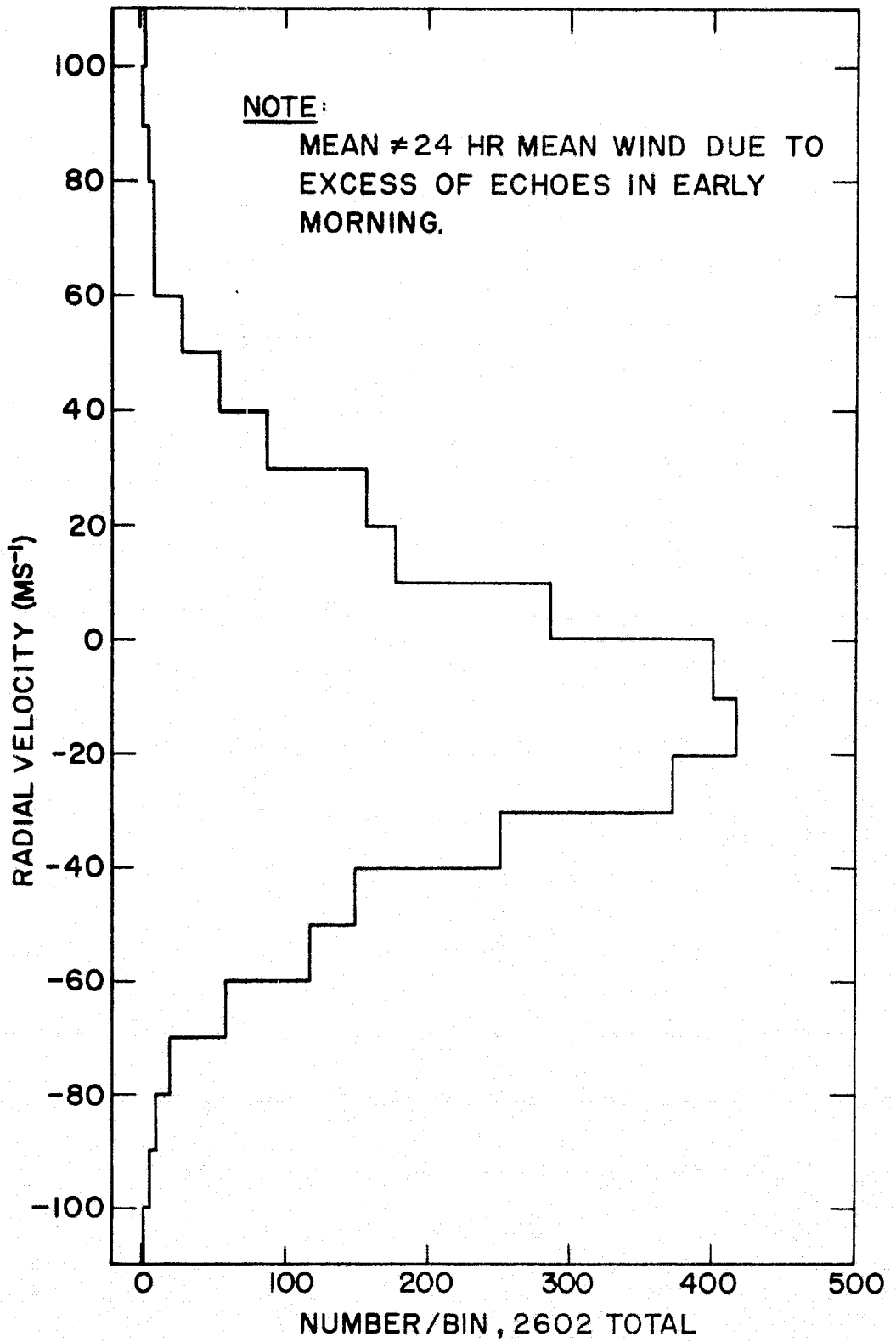

Figure 2.25 Histogram of velocities, January 17-18, 1975.

where α and γ are the elevation and azimuth angles of arrival and λ is the radar wavelength. Thus

$$\gamma = \tan^{-1} [-\phi_{23}/\phi_{12})(d_{12}/d_{23})] \tag{2.53}$$

$$\alpha = \cos^{-1} [\phi_{12}{}'\lambda/2\pi d_{12}\cos\gamma] \tag{2.54}$$

where $\phi_{12}{}'$ represents the ϕ_{12} value refined by the long arm ϕ_{24} phase difference.

The phase differences given by (2.52) cannot be observed directly because all receiving channels are multiplexed to a single A/D converter. However, as shown by *Backof and Bowhill* [1974], if we sequentially sample the sine and cosine channels of receivers connected to antennas i and j then ϕ_{ij} can be determined as follows. Let the four samples be expressed as

$$M_1 = A_i \sin (\phi_i + \omega_d t_1)$$
$$M_2 = A_i \cos (\phi_i + \omega_d t_2)$$
$$M_3 = A_j \sin (\phi_j + \omega_d t_3)$$
$$M_4 = A_j \cos (\phi_j + \omega_d t_4)$$

where

A_k = relative signal strength from antenna k

ϕ_k = absolute phase at antenna k

ω_d = Doppler radian frequency of return.

Defining

$$\omega_d t_1 = \theta_A$$

$$\omega_d t_2 = \theta_B$$

$$\omega_d t_3 = \theta_C$$

$$\omega_d t_4 = \theta_D$$

and using a fixed interpulse period T lets us write

$$\theta_D - \theta_C = \theta_C - \theta_B = \theta_B - \theta_A = \omega_d T \triangleq \alpha$$

Then

$$\sin \phi_{ij} = \sin(\phi_i - \phi_j) = y/(x^2+y^2)^{\frac{1}{2}} \tag{2.55}$$

$$\cos \phi_{ij} = \cos(\phi_i - \phi_j) = x/(x^2+y^2)^{\frac{1}{2}} \tag{2.56}$$

where

$$x \triangleq (M_1M_3+M_2M_4)\cos 2\alpha - M_1M_4 \sin\alpha + M_2M_3 \sin 3\alpha$$

$$y \triangleq (M_1M_3+M_2M_4)\sin 2\alpha + M_1M_4 \cos\alpha - M_2M_3 \cos 3\alpha$$

Equations (2.55) and (2.56) constitute a phase difference algorithm which allows us to solve (2.53) and (2.54) for elevation and azimuth angles provided our sampling sequence is exactly as specified. As pointed out in Section 2.2.4.1 though, it is advantageous to interlace Doppler and angle of arrival samples. In doing so, a sampling order of M_1, M_3, M_2, M_4 results. Under these circumstances we have

$$\theta_B - \theta_C = \alpha$$

$$\theta_A - \theta_D = -3\alpha$$

$$\theta_B - \theta_D = \theta_A - \theta_C = -\alpha$$

and x and y must be modified to

$$x \triangleq (M_1M_3+M_2M_4)\cos\alpha + M_1M_4\sin\alpha + M_2M_3\sin 3\alpha$$

$$y \triangleq (M_1M_3+M_2M_4)\sin\alpha + M_1M_4\cos\alpha - M_2M_3\cos 3\alpha$$

Since typical angle measurement accuracy is on the order of Doppler angle measurement accuracy, one would expect the elevation and azimuth angle accuracy to track that of Doppler accuracy. That such is indeed the case is illustrated by simulation results taken from *Backof and Bowhill* [1974] and reproduced in Figure 2.23.

An interesting application of the phase difference algorithm involves calibration of the two transmitter output cavity pairs for push-pull

operation. As explained in Section 2.2.2.2, when the cavity pairs are operated 180° out of phase, an effective balanced output impedance of 100 Ω is presented to the twin coaxial feedlines and maximum power can be transferred to the transmitting antenna. Figure 2.26 shows the calibration test setup. Line A is used as a reference from the driver cavity, while line B samples first one cavity pair then the other. The inter-pair phase difference is then given by

$$\phi_1 - \phi_2 = 4.73\ (\sin\langle\alpha_2\rangle - \sin\langle\alpha_1\rangle) \tag{2.57}$$

where $\langle\alpha_i\rangle$ = average elevation angle found by METP6 software (Section 2.2.4) with output cavity pair i connected to line B

Use of the driver reference is important because while the directional couplers all have accurate 50 Ω output impedances, the receiver input impedances are generally not 50 Ω and not matched from unit to unit. Hence using line A to cavity pair 1 and line B to pair 2 could give misleading answers, even if the connections were reversed and the average phase difference used. So that the transmitted pulse appears at a target range sampled by the METP6 software, the RANGE pulse (with a RANGE word of 61 to 160 corresponding to a target at delay 610 μs to 1600 μs) should be sent from the radar director to trigger the transmitter rather than the normally used PRF pulse. To simplify angle calculations, the fixed frequency 40.92 MHz crystal oscillator should always be used as the transmitter RF source so the apparent target is zero Doppler.

2.2.3.4 *Echo height determination.* For all but nearly overhead echoes, the flat earth assumption can lead to errors far in excess of that given by (2.6). To avoid such errors we consider the geometry of a spherical earth. By the law of cosines

$$h = a[(1+x^2+2x\sin\alpha)^{\frac{1}{2}}-1] \tag{2.58}$$

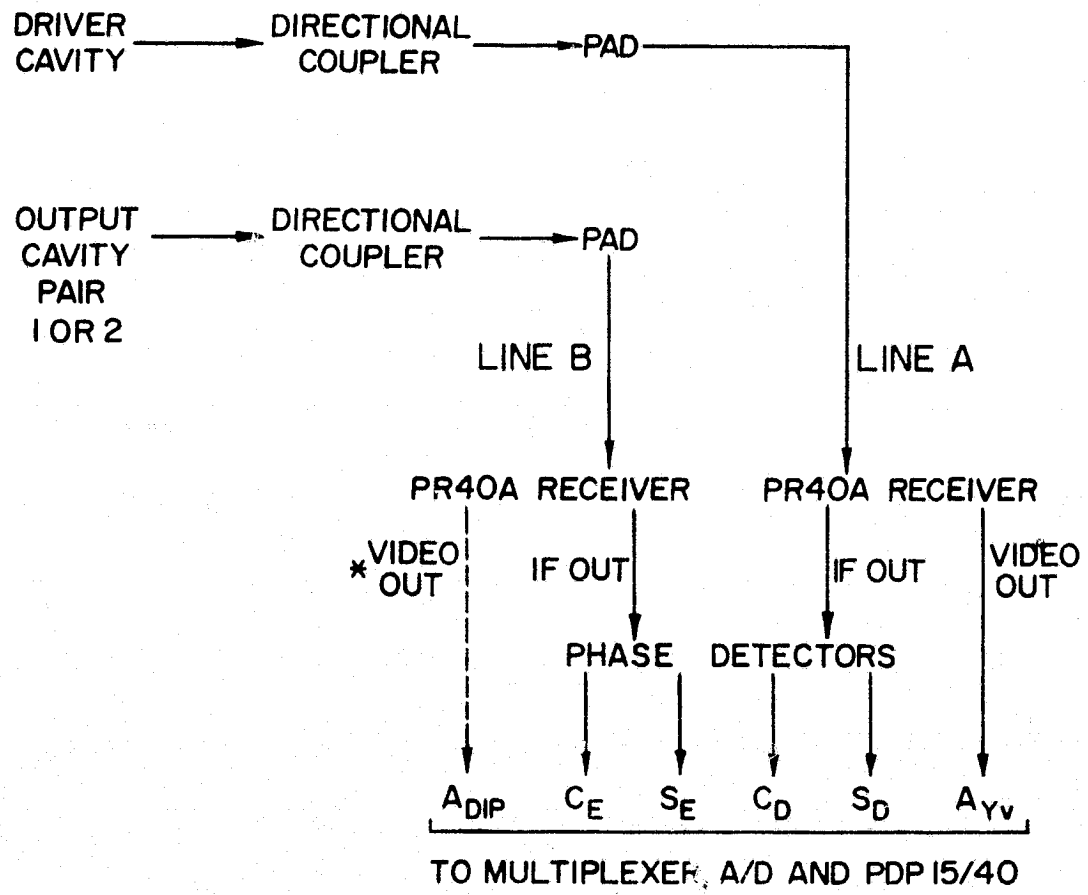

Figure 2.26 Measurement setup for transmitter output cavity pair phase difference.

where a = radius of the earth

$x \triangleq R/a$.

Since $x << 1$ in the meteor radar case, we can expand the radical of (2.58) via the binomial series to obtain

$$h = R\left(\sin\alpha + \frac{x}{2} - \frac{x}{2}\sin^2\alpha\right) + \text{Order}(x^2) \tag{2.59}$$

An alternative to interferometer height measurement is to measure the rate of signal decay of meteor echoes. As discussed in Section 2.2.4.1, it is possible to relate such decay rates to the ambipolar diffusion coefficient for underdense echoes and this in turn can be related via standard atmosphere data to echo height. Such inferred heights are statistical in nature and thus to yield credible results for the upper atmosphere winds, data from large numbers of echoes must be averaged, far larger than when interferometer height data are available.

2.2.4 *System software*

2.2.4.1 *METP6 collection and processing software.* This section describes operation of the METP6 main program and associated subroutines which collect and process meteor echoes with an interferometer meteor radar system. A four antenna interferometer as in Figure 2.4(a) can be handled, although until April, 1976 a special two antenna stacked Yagi configuration was utilized. Figure 2.4(b) shows the stacked Yagi receiving antenna layout, where antennas A1 and A2 permit evaluation of elevation angle independent of echo azimuth angle. The former parameter is of critical importance because, along with range data, it determines the meteor echo height. In vector notation, for a meteor echo from the direction

$$\bar{r} = \cos\alpha\,\sin\gamma\hat{i} + \cos\alpha\,\cos\gamma\hat{j} + \sin\alpha\hat{k} \tag{2.60}$$

where α = elevation angle

γ = azimuth angle,

the relevant phase difference between antennas is

$$\phi_{21} = \phi_2 - \phi_1 = \frac{2\pi d}{\lambda}(\hat{k}\cdot\bar{r}) = \frac{2\pi d}{\lambda}\sin\alpha \qquad (2.61)$$

so $$\alpha = \sin^{-1}(\phi_{21}\lambda/2\pi d) \qquad (2.62)$$

The frame arrangement, a concept of data collection originated by C. A. Backof [*Backof and Bowhill*, 1974], is shown in Table 2.1. The frame arrangement remains the same for three and four antenna interferometers, except that additional phase detectors are involved. In the four antenna case, sine and cosine detectors from antenna A3(A4)(Figure 2.4(a)) are sampled at pulses 5 and 7 (9 and 11). In the three antenna case used in April 1976, the vernier antenna A4 is not included. Since elevation angle accuracy is more important than azimuth angle accuracy, we sample the elevation antenna A1 at pulses 1,3,5, and 7 and the azimuth antenna A3 at pulses 9 and 11, rather than vice-versa. Because the algorithm which extracts antenna phase differences requires knowledge of the Doppler frequency, and because this frequency may vary over the trail lifetime due to Fresnel effects, wind shears rotating the trail, etc., it is important to make Doppler and phase difference calculations as simultaneous as possible. Interlacing these calculations as in Table 2.2 also results in a shortened frame length which is important because the typical usable echo lifetime is so short. No azimuth information is directly available with the stacked Yagi configuration, but by comparing the Yagi video value with that for a dipole aimed east-west one can reject echoes from far off due north.

The METP6 software must perform five main tasks:

	Task	Table 2.3 subroutines
(1)	synchronize	8, 9, 18, 19
(2)	recognize	21

Table 2.3

Meteor-radar software.

1.	ACC1	- determines if meteor echo is acceptable based on RANGE results
2.	ACC2	- determines if meteor echo is acceptable based on VEL results
3.	ACCS	- generates elevation angle when stacked Yagi configuration is used
4.	AFILE	- automatically increments filename by one with each call
5, 6, 7.	ANGLE, XTERM, YTERM	- determines antenna phase angle differences
8.	CHAN	- checks for desired channel active
9.	CHST	- checks for A/D interface failure and restarts collection if necessary
10, 11, 12, 13.	CLOSE, ENTER, FSTAT, SEEK	- system programs for using data files
14, 15.	CTIME2, TICK	- software clock
16.	DECAYH	- calculates echo height based on Yagi video decay
17.	HEIGHT	- calculates echo height from mean range and elevation angle, allows for curvature of the earth
18.	ID2	- checks for data sychronization between the computer and A/D converter
19.	INPAD	- A/D service routine, places specified number of samples into a core buffer
20.	INTER	- reads PDP-15 console data switches, allows bypass of hard printout of echo results
21.	LOOK	- finds largest non-negative Yagi video sample and sets a flag if the threshold is exceeded
22, 23.	MSK, MSN	- remove channel ID's from A/D inputs and convert negative numbers to PDP-15 number format
24.	PPO	- switch controlled halt of echo collection
25.	RANGE	- applies range algorithm to both Yagi video channels in each frame
26.	REC1	- records meteor echo data for a single channel (first frame)
27.	REC2	- records meteor echo data for all channels except the first (completes first frame)
28.	RECF	- records meteor echo data for one complete frame
29.	STORE	- every 50 echoes stores the processed results on data slot 2
30.	TABLE	- fills up height and diffusion vectors based on 1962 standard atmosphere data, also fills elevation and elevation correction vectors used to linearize the stacked Yagi phase response
31.	VEL	- applies the Bowhill velocity algorithm three times per frame

(3)	collect	4, 10, 11, 12, 13, 19, 22, 23, 24, 26, 27, 28
(4)	process	1, 2, 3, 5, 6, 7, 14, 15, 16, 17, 25, 30, 31
(5)	store	4, 10, 11, 12, 13, 20, 29

The numbers to the right refer to the various subroutines involved in performing each task. These subroutines are briefly identified in Table 2.3 and coding appears in Appendix II.

METP6 begins by calling subroutine TABLE. This subroutine fills height and diffusion vectors from file data based on 1962 standard atmosphere values [*Barnes and Pazniokas*, 1972]. The vectors are used later by the subroutine DECAYH to infer meteor echo height based on the rate of video signal decay (which can be related to diffusion). TABLE also fills elevation and elevation correction vectors from file data based on stacked Yagi phase calibration tests. These vectors are then used in the ACC3S subroutine to compensate for nonlinearities in the stacked Yagi phase response.

METP6 next requests the user to input the following information:

(1) date - up to ten alphanumeric characters; for example, 6/10/75, for June 10, 1975

(2) time - four integers; for example, 1354 for 1:54 PM

(3) time base - value in μs of main clock controlling the radar director timing, nominally 10

(4) pulse repetition frequency (PRF) - four digit integer value in Hz, nominally 400

(5) threshold - Yagi video level for target acceptance, set to roughly 20 dB above the noise floor, nominally 40

(6) offset - delay in μs of transmitter turnon after radar director command, used to correct range calculation, nominally 55

(7) (raw data file name - 1) - last file name successfully closed for permanent data storage (data slot 1); for example, if files testa01-39dat exist and the program fails while testa40dat is being filled one would reload METP6 and type testa39dat for (7), AFILE will automatically update the name to testa40dat before opening a file

(8) (processed data file name - 1) - last file name successfully closed for permanent data storage (data slot 2)

(9) number of meteors per raw data file - up to 10 at times of high echo rate, just 1 during afternoon echo rate minima; this value must not be changed until a full group of 50 echoes has been collected and stored on data slot 2.

(10) number of echoes with raw data presently on disk (data slot 1) - value from 0 to 49, necessary when restarting the program so STORE is accessed every 50 echoes

Because of faulty asynchronous design in the interface between the A/D and PDP-15/40 memory, it is possible for the A/D handler to "forget" that the CPU requested samples from it. Because such a request has the highest priority level possible, the CPU is prevented from doing anything else until the samples are delivered. This "forgetfulness" on the part of the A/D handler can completely lock up the computer. To avoid this the subroutine CHST is called before any A/D collection is attempted. CHST monitors for A/D interface failure by noting if a 1.5 second timer ever times out between calls for A/D samples. Such calls normally occur at roughly 40 ms intervals so the timer should never time out. Variable IST is set to one if time out

does occur and the program returns to the synchronization task.

A call to AFILE increments the raw data filename by one and this name, along with the present time updated each echo by CTIME2 and TICK, is printed on the foreground terminal. This allows the operator to monitor the echo rate easily.

The system program ENTER opens the raw data file FNAM on data slot 1 and then a dummy prefix is written at the start of the file.

On occasion very strong echoes can be seen that endure for tens of seconds, but due to wind shear effects echoes are untrustworthy for wind determination after roughly 0.5 seconds. Thus it is desirable to permit the operator to temporarily inhibit echo collection. Via PPO this can be done by setting the leftmost computer console switch to zero. Returning the switch to the one position removes the halt and lets collection proceed as normal.

Synchronization of the computer data requests and A/D active channel must be accomplished since there is no direct link between the computer and radar director, which controls the A/D sampling and active channel. This is done by requesting 100 samples via INPAD and scanning via ID2 the four bit channel code (ID) of the samples. The words loaded into core by INPAD consist of a least significant 10 bit two's complement value for the sampled voltage. In addition bit weights 2^{12} to 2^{15} contain a straight binary code for the sixteen possible multiplexer channels to the A/D converter. If all 100 samples have the same channel ID then we are synchronized and can continue; otherwise the flag IER is set to one and we try again.

Once synchronized, we must wait until channel 0 is active so a full frame can be collected. INPAD is called and the channel ID is scanned by CHAN. When a return flag value of zero for JBK occurs, we know data from

channel 0 was collected and we proceed to collect the remaining fourteen channels in the frame. Otherwise we loop back and repeat the process.

Because of the high PRFs used, we normally have little time to scan the Yagi channel 0 values and compare them with our threshold to check for the presence of a meteor echo. To ease this problem we capitalize on the automatic priority interrupt (API) system of the computer. This allows us to call INPAD to collect the remaining fourteen channels in the frame and simultaneously call LOOK which scans the channel 0 samples for a target. During the dead time between data collection (100 samples delayed 610 to 1600 μs from the transmit command) LOOK is active, selecting the sample location (MRNG) of the largest nonnegative channel 0 sample. If this sample does not exceed the threshold, flag NK remains zero and we return to the synchronization point. If the sample does exceed the threshold, we assume a target is present. However, because the range algorithm requires sample values centered about the target video peak, we must reject the cases of MRNG equal to 1 or 100.

As a safeguard against interpreting noise impulses as meteor echoes, we require that the second Yagi video sample (channel 13, location MRNG) also exceeds the threshold [*Backof and Bowhill*, 1974]. To make this check we must first mask the channel IDs from the LM array samples and then change the 10-bit two's complement numbers to the 18-bit format used in the computer. In the first frame this is done via subroutines REC1 and REC2, which record the echo values at locations MRNG-1, MRNG, and MRNG+1 for each of the 15 channels in frame 1, and MSN, MSK, which put these values into PDP-15/40 format. Because earlier software saved values from locations MRNG-3 to MRNG+3, MSK uses a vector of length seven. Now only the middle three locations, which are truly necessary, are ever assigned values and manipulated.

This allows overall storage requirements to be reduced which is important since METP6 and associated subroutines must fit in a 32k core memory after compilation using individual blocks no larger than 4k in size.

A further savings in storage is made by collecting the remaining eight frames one at a time. This way the 1500 samples per frame can alternately be loaded into one of two 1500 location arrays, IF1 and IF2. While INPAD is filling IF1 (IF2), RECF and MSN, MSK can be reading out IF2 (IF1), and placing the echo samples in array IFR. Thus with just 3000 storage locations we can handle the 13,500 samples collected for each echo (9 frames of 15 channels at 100 samples each). The end result of the collection phase is the IFR (135,3) array which is filled with the echo sample values in a number format compatible with the computer. This array provides the numbers which are manipulated by the range, velocity, and angle of arrival algorithms in the processing section of METP6.

The processing phase begins with a call to CTIME2 to update the time vector ITIM. Then the RANGE subroutine fits a parabola to each set of three Yagi video samples. The offset TAU in μs from the center sample is found by setting the time derivative of the parabola equal to zero (Section 2.2.3.1). The range in km is then given by the sum of TAU and the delay of MRNG clock pulses multiplied by 1.5 km/10 μs. First, however, adjustments are made for the transmitter turnon delay (LI μs) and A/D sampling delay (2 μs or 0.3 km). The center samples of all eighteen Yagi video data sets are scanned to find the frame in which the Yagi video signal peaks, IPKYV denotes the signal value, IPKF the frame number, and IPKC the channel number. This is important since Fresnel effects make Doppler velocity calculations unreliable during echo buildup. If IPKYV is less than the threshold a collection or synchronization error has occurred and we must return to the synchronization phase.

METP6 itself calculates DMAXY, the peak Yagi signal strength in dB, and DYD, the Yagi/dipole video ratio. The former is useful in estimating echo rate versus threshold and transmitter power level while the latter serves to identify echo returns from far off due north.

Subroutine ACC1 finds the largest (RH) and smallest (RL) range values for which the Yagi video level still exceeds the detector threshold. If the difference between these values exceeds 3 km or if the range standard deviation exceeds 1 km, it is likely that the echo is fragmented or rotating via wind shears. Such echoes cannot yield trustworthy winds so IGO is set to zero. IGO is set to zero also if the number of acceptable range results (Yagi video above the detection threshold) is less than three. If that is true then at most one full frame exists with acceptable signal strength and this implies the echo is either too short-lived or weak to give reliable results. Upon return to the main program IGO is examined to see if processing may continue. ACC1 also finds the mean range and sample standard deviation for acceptable range results. These values are used later in evaluating echo height and height accuracy.

The VEL subroutine calculates the radial wind via the Bowhill algorithm (Section 2.2.3.2) three times per frame for frames following that in which the Yagi video value peaks. Note that the effective PRF for the algorithm is one-half the actual PRF due to the interlacing of Doppler and angle of arrival channels. Because the phase channels have somewhat narrower bandwidths than the video channels, it is possible for the phase channel signal strength to peak one sample time after the video signal peak occurs. This means the maximum signal-to-noise for the phase channels occurs in column 3 rather than column 2 of the IFR array. Since algorithm accuracy varies inversely with signal strength, it is important to identify the correct column

value, ICOL. In applying the Bowhill algorithm we reject phase channel sets wherein the peak signal strength is not between 40 and 511. The first value establishes a minimum signal-to-noise level of about 20 dB while the second value represents the A/D saturation level. When a cosine, sine, cosine, sine sequence is used, the algorithm results must be changed in sign. Inconsistencies in applying the algorithm are covered by assigning default value of 999 m s^{-1}.

ACC2 is accessed next to determine whether or not the meteor echo is acceptable on the basis of wind velocity results. We require at least four non-default velocity calculations following the frame in which the Yagi video level peaked. With each acceptable calculation we assign an estimate of instrumental accuracy based on artificial target responses by the receiving subsystem and algorithms (Figure 2.24(a)). The weighted mean velocity and standard deviation of that mean are then formed as are the unweighted mean and sample standard deviation. For echo acceptance we require the weighted and unweighted winds to agree within 15 m s^{-1} and the sample standard deviation to be under 30 m s^{-1}. These checks help to eliminate ill-behaved returns due to trail fragmentation, non-specular reflection, wind shears, and long-enduring echoes. The weighted mean velocity is taken as the best estimate of the true radial wind.

If ACC2 is successfully passed, routine DECAYH is called to infer an echo height based on the rate of decay of the Yagi video signal. Ideally this decay rate is related to the ambipolar diffusion coefficient as

$$D = \frac{-3404 \ \ln(\Delta \text{Video Amplitude})}{\Delta t} \text{cm}^2 \text{s}^{-1} \qquad (2.63)$$

using λ = 7.3314 m. Since from laboratory experiments D is related to temperature and density through

$$D = 5.249 \times 10^{-7} \frac{T}{\rho} \text{ cm}^2\text{s}^{-1}$$

taking $T(z)$ and $\rho(z)$ from standard atmosphere data allows one to relate D, and hence indirectly decay rate, to atmospheric height z. DECAYH makes a least squares fit of all Yagi video samples at or following the peak yet still above the detection threshold to the equation

$$\ln V(t) = a_0 + a_1 t \tag{2.64}$$

Inserting the value a_1 into (2.63) yields D and linear interpolation with data from TABLE then yields decay height (999 is used in cases where interpolation fails).

The subroutine ANGLE applies the angle of arrival algorithm (Section 2.2.3.3) three times per frame to calculate the desired antenna phase differences. Because the feedlines to the Yagi antennas are not necessarily matched in electrical length, provision is made for adjusting all phase calculations by user inserted constants CEADJ, FEADJ, and AZADJ. All phase calculations are put in a unipolar format. To incorporate the most accurate Doppler measurement possible, the pairwise average of the Doppler results is used if possible, i.e. if two Doppler results overlap the angle of arrival samples.

With stacked Yagi operation, subroutine ACC3S solves equation (2.62) for the echo elevation angle. The phase offsets in ANGLE and the unipolar format make it possible to have Yagi phase differences in excess of 2π. Such cases are "unwrapped" at the start of ACC3S. Also tests are made to see if the phase difference exceeds REF, the maximum difference possible for the given antenna spacing. If such is the case the echo is assumed nearly overhead and a value of REF exactly is assigned for the phase difference. At least four usable (999. is the default value) phase differences are required

to proceed with the elevation angle solution. Because the PDP-15/40 version of Fortran has only the arctangent function, it is used indirectly to solve (2.62). To remove premature or highly deviative results, the mean and standard deviation of elevation angle are refined in a two step process. Results differing by more than $\pm \sigma$ from the first pass mean are not included in the second pass analysis. Lastly, the second pass mean elevation angle is adjusted for antenna phase nonlinearities by use of calibration data inputted earlier via TABLE.

When a three-antenna interferometer is used, as in April 1976, subroutine ACC3S1 is called in place of ACC3S. The former allows solution of equations (2.53) and (2.54) for the echo elevation and azimuth angles. If ACC3S (ACC3S1) is successfully passed, HEIGHT is called to determine the echo height and accuracy in km. Curvature of the earth is accounted for with a first order binomial series expansion of the exact solution (Section 2.2.3.4).

Processed results are now temporarily stored on data slot 1 and displayed on the operator's terminal if console switch 01 is activated. The echo count LMN is incremented as is the echoes per file count KL. If the file is filled, system program CLOSE closes it and AFILE updates the file name by one. If 50 echoes have finally been collected subroutine STORE is accessed. All the results on data slot 1 are read, then permanently written in a single file on data slot 2. This allows essentially infinite storage capability if DEC tapes are used and storage of 2800 echoes if a disk is used. The limitation is not the amount of data per se but the maximum of 56 filenames in the storage medium directory. Mean time, radial wind, range, azimuth, elevation, and height are fed back to the operator's terminal to allow real-time monitoring of radar system performance.

2.2.4.2 *Standard post-processing analysis package for meteor radar.*

1. VFILE6: Takes the real-time data files created by the METP6 collection program and compresses all data into a single file.
2. VFILE7: Prints echo data for an entire radar run in chronological order using a VFILE6 output file.
3. DIST1: Forms histograms of range, Yagi video strength in dB, and Yagi/dipole ratio in dB for an entire radar run using a VFILE6 output file.
4. DIST2: Gives statistics and histogram for any single measured parameter utilizing user specified time period and time steps.
5. CORR1(DAR8): Determines linear correlation coefficient between any pair of measured parameters based on DIST2 results.
6. WIND1(GROVES, DAR30): Interpolates N-S winds from VFILE6 output files using the combined Groves-Garchy concepts described in Section 3.1.
7. WIND1G: Produces a graph of wind as a function of both time and height based on WIND1 results.
8. CURFIT, CURFT5 (DAR13, DAR99, FCTN, PHASE): The former fits WIND1 results to prevailing $+S_1(v) + S_2(v) + S_3(v)$ and prevailing $+S_1(v) + S_2(v)$ wind structures at a user specified height. The latter models the wind by a prevailing component with five harmonic components and sequences automatically through all heights.
9. WSPEC, WSPECA (DBPF, NLOGN, GRAF1, DAR26): Calculates radial N-S wind spectra for frequencies of 3 to 24 cycles day^{-1} via a fast Fourier transform. Prevailing, diurnal, and semidiurnal tidal components are subtracted from the time series before

application of the FFT algorithm and a digital bandpass pre-filter is also included to reduce spectral leakage. WSPECA is an automatic version of WSPEC which sequences through all heights and then produces averaged wind energy values at each frequency for user specified height intervals. Such smoothing aids in distinguishing real waves from noise effects.

10. CF1, CFA (NLOGN, DBPF, DAR13, DAR26, DAR99, FCTN, PHASE): Calculates amplitude and relative phase for each of the WSPEC spectral lines. Phase must be corrected for DBPF phase response if phases of two different frequencies are to be compared. Ideally, internal gravity waves would exhibit relatively linear phase slope versus height. CFA is a version of CF1 which automatically steps through all heights.
11. NLIN (DAR22, FUNCTN, DAR17, FDERIV, DAR30): Performs a non-linear least squares curvefit of wave amplitude versus height from CF1 to the theoretical form for a partically reflected internal gravity wave, see Section 7.2.
12. MEMT2, MEMT3 (MEMPR, DAR26): Evaluates the wind spectrum and correlation function via the maximum entropy method.

3. POST COLLECTION ANALYSIS OF ECHO DATA

3.1 *Obtaining Wind Values Uniformly Spaced in Time and Height*

Two basic methods for reconstituting wind variations in time and space from meteor echo data are presently in use by other meteor radar facilities. The least-squares theory of *Groves* [1959] is a generalization of the analysis of *Manning et al.* [1950] and allows the parameters of any assumed wind structure to be determined. Thus, vertical air motion as well as time and height variations in the wind structure can be examined, whereas Manning et al. assumed a constant horizontal wind.

An interpolation method is used at Garchy [*Spizzichino*, 1970b] to obtain wind profiles. Here the two-dimensional autocorrelation function in height and time, $r(t,h)$, is first evaluated from the experimental wind measurements. The interpolation region about some desired time and height, (t_o, h_o), is chosen by solving

$$1 - r(\Gamma,\xi) < \varepsilon'$$

for Γ and ξ. ε' is a small constant usually taken as 0.2. If at least three data points lie within the interpolation region, a regression plane can be fitted to those points. The fitting is done with data weighted inversely with repect to the "distance" from (t_o, h_o), i.e., the weight is unity at (t_o, h_o) and falls to zero at the edge of the interpolation region. Once the regression plane coefficients are known, substituting $t = t_o$ and $h = h_o$ into the plane equation gives the interpolated wind value.

Given azimuth information for the echoes, the Groves theory allows one to simultaneously solve for E-W and N-S wind components. This is not possible with the Garchy method, unless data are collected via two orthogonal antenna systems or the autocorrelation function is expanded to four variables, $r(t,h,x,y)$, where x and y are horizontal coordinates. On the other hand,

while the Groves theory handles tidal variations well, it is not practical for extracting suspected internal gravity waves because their periods are unknown (*a priori*). The Garchy scheme, however, can yield winds uniformly spaced in time and height so that fast Fourier transform (FFT) analysis can be applied. Spectral peaks may then be harmonically analyzed to see if they exhibit wave-like behavior.

The University of Illinois wind analysis software uses concepts from both the Groves and Garchy methods in an attempt to capitalize on the advantages of each. Because the normal methods for calculation of the autocorrelation function $r(t,h)$ assume we already know the wind values uniformly spaced in height and time, we instead assume *a priori* a conservatively sized interpolation region, typically ± 0.5 hr and ± 2.5 km. By being conservative we will somewhat filter the high frequency end of the wind spectrum and thus camouflage internal gravity waves that may be present there. However, by weighting the data inversely with "distance" from the desired point (t_o,h_o) the filtering effect will be important only at times of low echo rate. The height interpolation size represents the expected standard deviation of echo heights deduced from decay rates. With interferometer deduced heights a smaller height interpolation size can safely be specified if desired.

When no azimuth information is available, except for a Yagi/dipole video ratio check which rejects echoes from greater than 30° off due north, we solve for the N-S wind regression plane only. This is done via the method of Groves and the fitting function

$$u(t',h') = At' + Bh' + C \tag{3.1}$$

where

$t' \triangleq (t_i - t_o)/0.5$ $\quad$ N = number of echoes residing in the

$h' \triangleq (h_i - h_o)/2.5$ $\quad$ interpolation region (Γ,ε)

$i = 1,\ldots, N$ $\quad$ $C = u(t_o,h_o)$

Because the coefficients A and B are sometimes statistically insignificant, the wind measurements are also fitted to a constant:

$$u(t',h') = u(t_o,h_o) = D \tag{3.2}$$

A full interferometry arrangement, yielding elevation and azimuth data, became operational in April, 1976. Because of our high echo rate, it has since been possible to solve simultaneously for both N-S and E-W wind components using echoes from the same small region in space. This is in contrast to what has been necessary in the past, i.e. either orthogonal separate regions of the sky were alternately probed or all-sky nondirective antennas were used (or two separate radar facilities illuminating a common portion of the sky were needed).

The vertical structure of prevailing winds and diurnal and semidiurnal tides is found by least-squares curve fits to all successfully interpolated wind values at heights $h_o = h_L, h_L + \Delta h,\ldots, h_H$. Generally we have used h_L = 82.5 km, h_H = 94.5 km, Δh = 1 km for decay height data and h_L = 82 km, h_H = 102 km, Δh = 1 km for interferometer height data. The background wind components are then subtracted from the interpolated values as preconditioning for spectral analysis of short period waves. *Spizzichino* [1970b] shows how important this subtraction is for minimizing power spectra errors. Also, at (t_o,h_o) values for which interpolation was not permissible ($N < 3$), we estimate the wind by a linear fit with the adjacent acceptable wind values at height h_o. Again this tends to diminish the strength of any high frequency waves that are present. In our software, we have actually required $N \geq 4$ for interpolation to be considered permissible, since when $N = 3$

statistical uncertainties are masked.

We can apply the FFT to wind values (nomially 128 points per day) at each of the heights. The results are averaged in height groups to help distinguish true waves from random noise spectral peaks. A least-squares curve fit to the time series obtained via the inverse FFT of each spectral line (one at a time) shows how the phase and amplitude versus height of a suspected gravity wave behave.

To analyze the performance of our processing software (Section 2.2.4.2), the program ARTW was written. This program generates artificial meteor wind measurements at a user specified rate. A mean and two harmonics of user specified amplitude and phase comprise the assumed wind field. A mean plus diurnal echo rate establishes the measurement spacings. In this way the large echo rate variation versus time of day is modeled. This is particularly important for radar systems like that at the University of Illinois since highly directive antennas amplify the diurnal rate variation. Nominal hourly rate ratios of mean:24 hr cosine:24 hr sine = 41.68:0:31.76 are used based on January 1975 rate observations scaled to 1000 echoes/day.

Using a prevailing wind plus diurnal and semidiurnal tidal components for the assumed wind field, one finds (Table 3.1) that amplitudes and phases are recovered accurately with CURFIT even for echo rates as low as 125/day. Even though such a low rate will give a late afternoon-early evening time span where interpolation is not permissible, remember that CURFIT uses only successfully interpolated winds. Since ARTW generates "noiseless" wind measurements, one would thus expect accurate answers even with large time gaps.

A more practical evaluation of WIND1 and CURFIT performances can be made by taking data from an actual radar run and comparing the prevailing

Table 3.1

CURFIT performance in extracting prevailing wind and tidal parameters versus echo rate, based on fit to mean + 24 + 12 + 8 hr components.

Actual Wind Parameters	A m s^{-1}	ϕ hrs
Prevailing	5.0	-
$S_1(v)$	5.0	0
$S_2(v)$	10.0	0

Rate	Prevailing	$S_1(v)$		$S_2(v)$		χ^2
		A	ϕ	A	ϕ	
echoes/day	m s^{-1}	m s^{-1}	hrs	m s^{-1}	hrs	
4000	5.01	4.99	.05	9.91	0.01	4.48
1000	5.01	4.99	.05	9.91	0.02	1.15
500	5.01	5.00	.05	9.91	0.02	0.65
250	5.02	4.99	.06	9.91	0.02	0.44
125	4.98	5.04	.04	9.89	0.02	0.10

wind and tide parameters deduced with various echo rates. The variable rate is effectively achieved by considering only every other echo collected, every third echo collected, etc. Such a procedure was applied to data from September 13, 14, 1975. Graphs of prevailing wind, diurnal and semidiurnal tide amplitude and phase for three heights are presented in Figures 3.1 and 3.2. The results of the first figure pertain to curve fits using 3 harmonics, while the second figure is based on 5 harmonic fits. In these latter cases, reference values from maximum data rate and 3 harmonic fits are also shown. It is apparent that in such cases the 3 and 5 harmonic fit results do not differ appreciably. At lower data rates, however, use of a higher order fit improves the agreement in amplitude with that of the full rate value, which is taken as our best estimate of the true value. This is not apparent for phase because agreement was already excellent to begin with. In fact, as Table 3.2 demonstrates, if the echo rates are sufficiently high, roughly 400/day/height bin, even 2 harmonic fits can define the background wind reasonably well. But because the terdiurnal tide is often significant and because inclusion of additional components allows frequencies higher than 2 cycles/day to be isolated from the main tides, we in general use 5 harmonic fits to estimate the background wind, i.e., prevailing, diurnal tide, and semidiurnal tide components. Use of 3 harmonic fits will not necessarily yield satisfactory estimates of the actual terdiurnal component. For example, for the October 1975 radar runs an average standard deviation of only 1.1 m s^{-1} (8.1% variation relative to mean amplitude) and 7.9° (0.18 hrs) in phase occurred when comparing five harmonic curve fits with FFT analysis. But an average standard deviation of 4.1 m s^{-1} (54.1% variation) in amplitude was noted when comparing three harmonic curve fits with FFT analysis on September 13, 14, 1975 data.

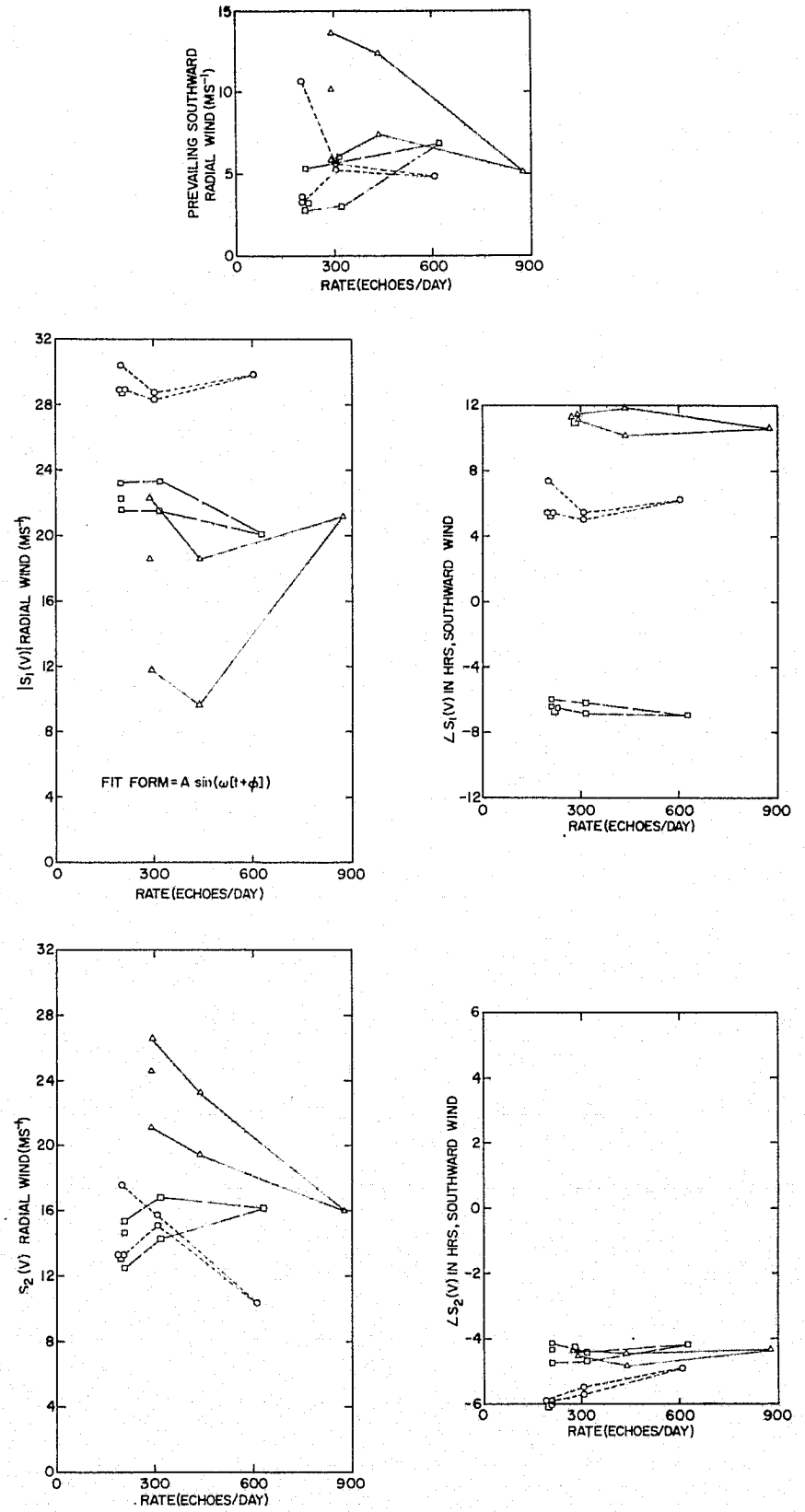

Figure 3.1 Prevailing and tidal winds versus echo rate, mean plus three harmonics fit.

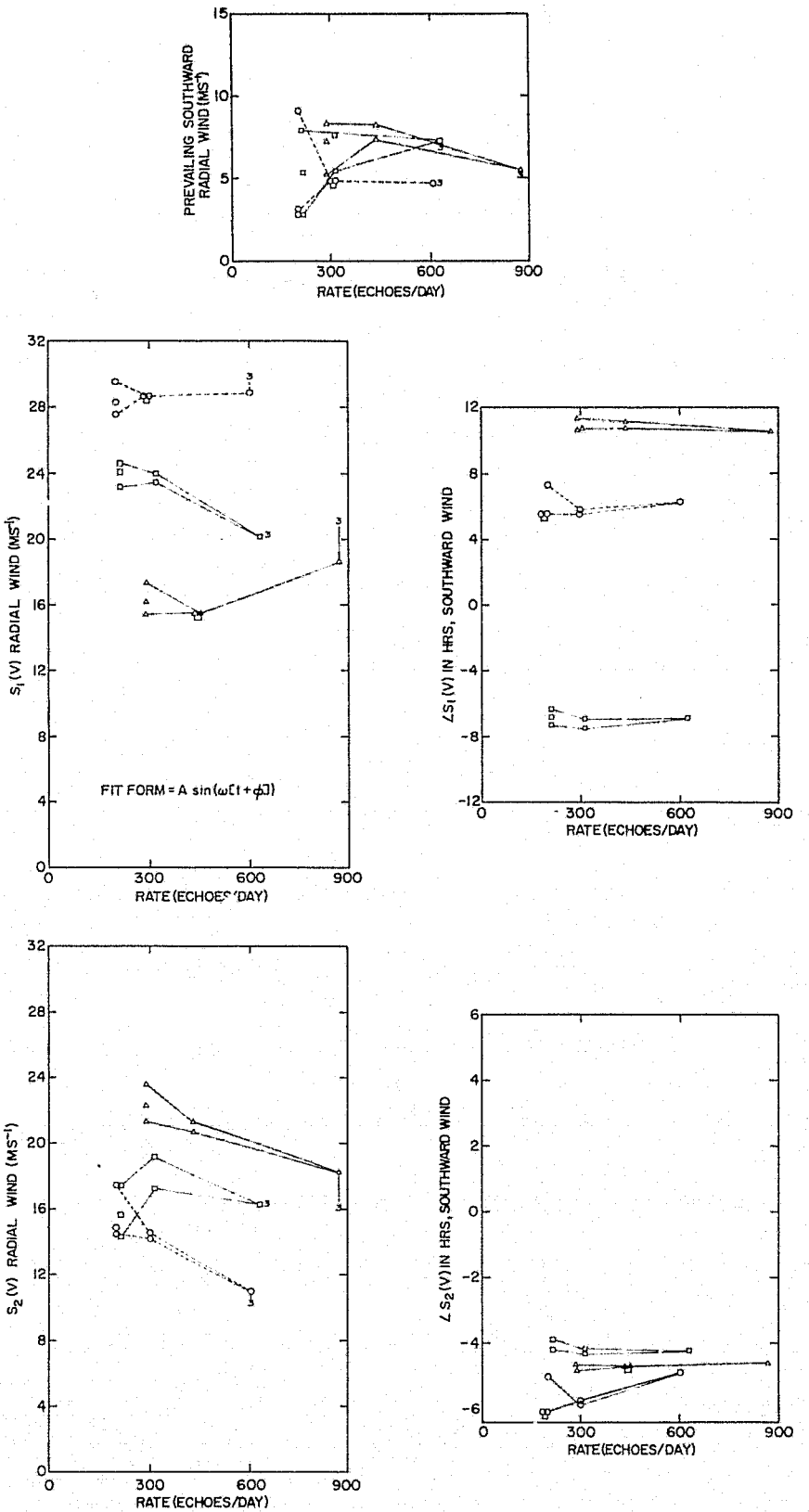

Figure 3.2 Prevailing and tidal winds versus echo rate, mean plus five harmonics fit.

Table 3.2

Comparison of 2, 3, and 5 harmonic curve fit results, September 13-14, 1975.

Prevailing $|S_1(\nu)|$ $|S_2(\nu)|$

All values southward radial ms^{-1}

Ht km	2	3	5	2	3	5	2	3	5
85	6.84	7.33	8.13	27.67	26.66	26.30	9.61	9.88	11.37
86	4.88	4.90	5.33	30.39	30.29	29.66	8.89	9.25	11.34
87	4.30	4.84	4.62	29.84	29.84	28.94	9.35	10.32	10.96
88	1.73	3.01	2.54	30.92	30.12	29.43	11.38	12.24	12.25
89	0.32	1.93	2.89	30.56	30.15	27.53	11.56	13.07	15.19
90	0.75	2.37	3.60	28.43	27.14	24.61	13.15	14.61	17.44
91	1.13	3.40	4.23	25.59	24.15	21.25	11.88	14.61	17.09
92	3.72	5.15	5.51	22.35	21.21	18.70	12.92	16.05	18.19
93	6.39	6.26	6.37	17.62	16.72	16.28	17.68	19.14	20.11
94	8.68	6.14	7.47	15.77	13.74	15.90	21.91	19.79	20.79
95	6.54	4.56	6.47	16.58	15.07	16.79	19.75	16.95	17.94
96	6.80	4.29	6.52	17.67	17.70	18.89	20.66	14.79	16.85
97	7.60	6.99	7.21	19.20	20.01	20.05	19.11	16.16	16.24
98	6.74	5.28	7.27	20.41	20.75	20.29	15.19	12.17	16.08
99	6.10	3.40	5.67	18.47	19.41	19.03	16.68	12.53	16.45
100	6.56	6.40	6.16	14.91	16.26	15.30	24.66	23.55	24.01

Summary:

N=16	2-5	3-5	2-5	3-5	2-5	3-5
mean	-.68	-.86	1.07	0.64	-1.12	-1.70
σ	1.29	0.90	1.77	1.50	2.75	1.21
range	4.31	2.74	5.56	5.06	9.08	3.91

The ability to correctly extract gravity wave parameters from wind data was tested with ARTW by specifying a mean, a semidiurnal tide, and a gravity wave, 20 dB down in energy from the semidiurnal tide and with a frequency of 3 to 11 cycles/day. The spectral analyses of WSPEC show that the gravity wave energy is generally 15 dB above adjacent sideband noise. CF1 results show that as wave frequency increases the recovered amplitude decreases. This is due to the sampling interpulse period (day/128) and interpolation time span(± .5 hr) which make the analysis act like a low pass filter (see Table 3.3, also Figure 19 of *Spizzichino* [1970b]). Based on the one-pole curve fit of Table 3.3 we can compensate for the filtering effect of WIND1 interpolation by multiplying all CF1 amplitudes by $(a + bf)$ and by multiplying all WSPEC energy spectra by $(a + bf)^2$. Although the ARTW inserted wave phase was 0°, significantly positive values were found with CF1. This is because of the phase variation of the prefilter DBPF. This resonator was included to improve the resolution of closely spaced waves and is not essential. Phase recovery is approximately linear versus amplitude and phase and thus CF1 phase values can be adjusted if desired so the relative phase relation between any two waves is correct.

3.2 *Effects of Echo Selection Criteria on Meteor-Radar Wind Results*

The high echo rate of the University of Illinois meteor-radar station makes it an ideal instrument for comparing various wind analysis methods and estimating their precision versus the number of echoes averaged.

Table 3.4 shows a comparison of three analysis methods using two different velocity algorithms and progressively more stringent acceptance criteria. Method 1 is simplest to apply and since it utilizes the largest number of algorithm results one might expect the standard deviation of the mean to be smallest, see Table 3.5. However, some of these results are

Table 3.3

Low pass nature of the amplitude bias of interpolated winds.

128 pts/day, ±.5 hr interpolation time span, inserted wind amplitude = 1.0 m s^{-1}

Frequency, f cycles-day^{-1}	Detected Wind Amplitude, v m s^{-1}
3	0.94
4	0.82
5	0.81
6	0.78
7	0.77
8	0.74
9	0.71
10	0.66
11	0.64

One-pole curve fit:

$$v \simeq \frac{1}{a + bf}, \quad a = 0.937, \quad b = 0.0555$$

Table 3.4

Comparison of three analysis methods on meteor-radar data.

Perseid Shower Run, Aug. 12--13 1974, at Urbana, Ill.

Algorithm	BK	BK	BH	BH	
Method	1	2	1	2	3
Data Group					
2	-12.2	-16.7	-13.2	-17.1	-14.7
3	24.5	28.5	26.5	29.6	37.8
4	32.2	33.8	32.5	34.1	42.0
5	20.2	27.8	20.6	28.2	32.4
6	24.1	26.0	24.9	26.4	32.1

All values refer to mean southward radial wind in ms^{-1}

BK = Backcf Velocity Algorithm

BH = Bowhill Velocity Algorithm

56 echoes/group, 13 algorithm results/echo

Method 1: All algorithm results with signal 6 dB or more above noise floor averaged

Method 2: As in 1, but results associated with repeat echoes, wide azimuth echoes, echoes with sizeable range deviations, and echoes for which A/D synchronization errors occurred are dropped

Method 3: See acceptance criteria, Table 3.7.

Table 3.5

Standard deviation and standard deviation of mean for methods in Table 3.4.

Algorithm	BK	BK	BH	BH	
Method	1	2	1	2	3
Data Group					
2	23.9(3.2)	23.0(3.1)	23.4(3.1)	23.5(3.1)	30.5(4.1)
3	29.2(3.9)	24.4(3.2)	27.7(3.7)	23.3(3.1)	23.8(3.2)
4	25.1(3.4)	22.6(3.0)	25.3(3.4)	23.0(3.1)	17.0(2.3)
5	27.2(3.6)	21.0(2.8)	27.3(3.6)	20.9(2.8)	20.1(2.7)
6	22.3(3.0)	19.3(2.6)	21.7(2.9)	19.4(2.6)	18.9(2.5)

56 echoes/group, radial m s^{-1} units

known to be erroneous due to wide azimuth echoes (returns from far off due north), echoes with sizable range deviations (returns with multiple reflection centers or trail rotation in wind shears), and A/D converter synchronization problems. Thus method 2, though using fewer algorithm results, should be superior to method 1, both in nearness to the true wind (accuracy) and standard deviation of the mean (precision). But neither method 1 or 2 requires sufficient signal strength to make the measurement noise of each accepted algorithm result much less than the geophysical noise. This geophysical noise is the result of turbulence and short period-short wavelength winds which occur throughout the volume of space monitored by the meteor radar. With method 3 ($\geq$20 dB S/N) the measurement noise is at most 10 m s^{-1}, whereas with methods 1 and 2 it may reach 50 m s^{-1}, double the representative geophysical noise of 25 m s^{-1} (Table 3.5). In the former case we are justified in averaging results without weighting while in the latter cases results should be weighted inversely with signal strength. This weighting was not done and may help explain the differences between the results in Table 3.4.

To analyze the significance of differences between the mean winds in Table 3.4, we have used method 3 values as a reference and tabulated key paired differences in Table 3.6. From this table we note the following:

1. The differences in cases involving the Bowhill algorithm are nearly always (9 out of 10 cases) somewhat less than those involving the Backof algorithm.

This is a reflection of the fact that typically the Bowhill algorithm yields a smaller sample standard deviation for usable echo algorithm values than the Backof algorithm. Thus, according to the wind determination criteria of Table 3.7, the Bowhill algorithm is dominant in setting all

Table 3.6

Paired differences for three analysis methods of meteor-radar data.

Perseid Shower Run, Aug. 12 - 13, 1974

$m\ s^{-1}$ units

Data Group	1,BK-3	2,BK-3	1,BH-3	2,BH-3
2	2.5	-2.0	1.5	-2.4
3	-13.3	-9.3	-11.3	-8.2
4	-9.8	-8.2	-9.5	-7.9
5	-12.2	-4.6	-11.8	-4.2
6	-8.0	-6.1	-7.2	-5.7

Check for significant difference in means via Student's t test

	mean	
1. 1,BK-1,BH	-0.5	not significant at 10%
2. 2,BK-2,BH	-0.45	not significant at 10%
3. 1,BH-3	-7.66	significant at 5%
4. 2,BH-3	-5.68	significant at 1%
5. 1,BH-2,BH	-1.98	not significant at 10%

Table 3.7
Method 3: Meteor echo acceptance criteria for the Perseid run data.

Algorithm Results	a. Magnitude of the maximum phase channel sample value for the frame in question must be greater than or equal to 40 but may not exceed the A/D saturation value of 511.
	b. Only values following the frame in which the Yagi video peaks are accepted to remove Fresnel effects.
	c. Velocity sense must be consistent, sign changes are permissible only if the mean echo velocity is near zero.
	d. Each echo must have at least 3 acceptable algorithm results.
Zero Crossing Results	a. As in 1. a. but since this velocity determination method is less sensitive to noise a minimum amplitude of at least 20 is acceptable.
	b. As in 1. b. and c.
General Criteria	a. Wide azimuth returns are defined as those for which the Yagi video value is not at least 6 dB above the dipole video value. Such echoes cannot be used in N-S wind calculations.
	b. Repeat echoes are identified by range similarities for small time increments. Only one wind result per unique echo is permissible to avoid biasing the data.
Determining Mean Winds From Accepted Perseid Data	a. Whichever algorithm result (two different ones are used with each echo) yields the smallest sample standard deviation is used.
	b. Where both algorithm and zero-crossing results are usable the average value is accepted as the wind. Zero-crossing results must exist for at least three half-periods to be considered usable.
	c. All winds are multiplied by the square root of 2 to obtain horizontal values. This assumes an average elevation angle of 45 degrees.

method 3 values. Student's t-test shows that results from both algorithms do not differ significantly for either method 1 or 2 but the Bowhill results of both methods are significantly different from the method 3 results. The latter situation is likewise true for the Backof algorithm.

2. The method 2-3 differences are nearly always (9 out of 10 cases) less in magnitude than the method 1-3 differences.

This is to be expected since method 2 does not utilize certain obviously erroneous algorithm results. The t-test does not show methods 1 and 2 to differ significantly but this must be due to the limited number of data groups. The fact that both methods 1 and 2 differ significantly from method 3 shows that something other than the additional rejection criteria of method 2 is of importance in deducing accurate winds.

3. Behavior of method 1-3 and 2-3 differences suggests that methods 1 and 2 underestimate the magnitude of the wind.

One possible explanation for underestimation of wind amplitude involves Fresnel effects during trail formation. The first few frames of specular echoes have time rate of change of phase set by Fresnel effects as well as neutral winds. One might expect noise effects on algorithm results to average to zero about the correct mean wind, but in frames dominated by Fresnel effects might not the algorithm results average to zero independent of the wind? If so this could explain why methods 1 and 2, which do not reject Fresnel frames, yield consistently smaller amplitudes than method 3, which does reject Fresnel frames. To test such a hypothesis, all Bowhill algorithm values occurring prior to the peak in Yagi video amplitude were averaged for each data group, see Table 3.8. Extreme values ($>3\sigma$) were dropped as unreliable, but since they only comprised 3% of the total, their rejection did not alter results appreciably. It should be noted that such

Table 3.8

Winds deduced from Fresnel frames only of meteor-radar data.
Perseid Shower Run, Aug. 12 - 13 1974, at Urbana, Ill.
Bowhill Algorithm, Extreme Values (>3σ) Deleted

Data Group	Radial Southward Velocity	Std. dev. mean
2	-8.2 m s^{-1}	4.6 m s^{-1}
3	28.8	5.1
4	36.3	6.8
5	35.5	7.0
6	28.4	8.0

Check for significant difference in means via Student's t test

	mean	
1. Fresnel-1, BH	5.9	significant at 10%
2. Fresnel-2, BH	3.92	significant at 10%
3. Fresnel-3	-1.76	not significant at 10%

extreme velocities would never be interpreted as wind Doppler results in zero-crossing schemes. The University of Illinois algorithm scheme though has the potential of outputting Doppler frequencies up to one-half the radar PRF. The t-test results show that our hypothesis is false since Fresnel results do not differ significantly from method 3 values. The weak differences between Fresnel results and methods 1 and 2 actually suggest that for our particular limited set of data groups the Fresnel method is superior to methods 1 and 2 rather than the cause of the underestimation of wind amplitude.

A more likely explanation for the amplitude underestimation is as follows. When the true mean wind deviates from zero, weak echo algorithm results, which of course are the most numerous type, are distributed between $-v_{max}$ and $+v_{max}$, where v_{max} is set by the radar sampling rate. If the probability density of these weak algorithm results has a sufficiently large standard deviation, then the average will be biased toward the smaller side in magnitude of the true mean because of clipping at $\pm v_{max}$. For example, if the true mean is positive, then more algorithm results are likely to exceed $+v_{max}$ than to be less than $-v_{max}$. Since all these extremes are clipped (they represent error situations when attempting to apply the velocity algorithm, sin $\alpha > 1.0$, etc.), the estimate of true mean is biased to the low side. This is demonstrated mathematically in Appendix III.

It is important to note at this time that while clipping imposed by the radar sampling rate can lead to serious underestimation of wind amplitude, a <u>user imposed</u> clipping can actually serve as a robust estimator, provided the standard deviation of algorithm results is not so large that the former type of clipping is significant. A small increase in minimum signal-to-noise ratio can assure this. Then provided the histogram of accepted results is

approximately symmetrical, one can minimize the influence of noisy results by ignoring the smallest and largest X%. And thanks to the near symmetry, such a procedure will yield an unbiased estimate of mean wind. The estimator, called a clipped or trimmed mean, is discussed by *David* [1970].

Analysis of meteor-radar data using thresholds from 10 to 40 (roughly 12 to 24 dB S/N) and X values from 5 to 25 indicated that the standard deviation of the estimated mean decreased slightly as X increased and the threshold dropped (Table 3.9). The conclusion that X = 25 and threshold = 10 are optimal is not, however, always justified. No problems have been encountered related to using X = 25, in fact other empirical studies suggest that for a large class of densities trimming with X = 25 is quite satisfactory for estimating location. But underestimation of wind amplitude can again appear with thresholds as low as 10. For example, using Jan. 17-18, 1975 data in groups of 70 echoes each, 44 mean wind values via analysis methods 4, 5, and 6 were obtained (Table 3.10). It was found that methods 4 and 5, clipped means with thresholds of 10 and 40, respectively, differed significantly at 0.1%, where the manner of disagreement was that 4 underestimated the amplitude relative to 5. Methods 5 and 6, acceptance criteria as in Table 3.7, were not significantly different even at 10%. The cause of underestimation when using a low threshold lies most likely in asymmetry of the density of accepted algorithm values. This asymmetry is likely to occur when large wind shears in height or time are present. This was the case Jan. 17, 18 when the semidiurnal tide actually exhibited characteristics of a standing wave.

Despite potential pitfalls in clipped data analysis, its ability to extract reasonably accurate prevailing winds and tides is demonstrated in Table 3.10. Here the only substantial disagreement involves the amplitude

Table 3.9

Summary of "clipped" data analysis for various thresholds and rejection percentages.

Data	% Rejected	5			15			25		
Group	Threshold	N_1	N_2	N_3						
1	10	282	-1.6	1.6	225	-3.2	1.2	163	-2.5	0.95
	20	236	0.8	1.6	182	-0.5	1.2	134	-0.0	0.90
	40	143	4.4	1.8	115	3.2	1.3	81	5.0	0.90
2	10	271	3.2	1.95	218	5.3	1.4	157	3.7	1.0
	20	193	11.8	1.9	154	10.3	1.4	108	8.8	1.0
	40	113	11.1	2.1	92	12.8	1.7	67	8.3	1.2
3	10	308	-5.7	1.7				181	-9.5	0.9
	20	253	-3.1	1.7				150	-8.5	0.9
	40	185	-4.55	1.9				106	-10.5	0.9

40 echoes/group 13 algorithm results/echo

N_1 = number of results after clipping

N_2 = mean wind in southward radial ms^{-1}

N_3 = standard deviation of clipped data set (smaller than true standard deviation, degree of underestimation depends on % rejected)

Table 3.10

Comparison of four analysis methods used to evaluate prevailing wind, diurnal and semidiurnal tides from meteor-radar data, January 17-18, 1975.

Method	a_0	a_1	b_1	a_2	b_2	
4	-2.2	-9.2	-8.9	7.0	2.3	
5	-4.9	-9.6	-11.9	8.9	1.9	
6	-6.0	-8.2	-11.3	8.5	0.9	
7	-7.2	-9.9	-10.8	14.5	3.8	
7	-7.1	-10.1	-11.0	14.6	4.2	
	$\lvert S_1(v)\rvert$	$\phi_1(v)$	$\lvert S_2(v)\rvert$	$\phi_2(v)$	N	Fit
4	12.8	-8.9	7.4	2.4	62	2
5	15.3	-9.4	9.1	2.6	62	2
6	14.0	-9.6	8.6	2.8	17	2
7	14.6	-9.2	15.0	2.5	128	2
7	14.9	-9.2	15.2	2.5	128	3

Results from least squares fit of southward radial wind values in m s^{-1}, N in number, to $a_0 + a_1 \cos kt + b_1 \sin kt + a_2 \cos 2kt + b_2 \sin 2kt$, where $k = \pi/12$. The alternate form is $a_0 + |S_1(v)| \sin k[t + \phi_1(v)] + |S_2(v)| \sin 2k\,[t + \phi_2(v)]$. When fit = 3 an 8 hr harmonic is also included. Bowhill algorithm used by all methods.

Method 4: Clipped Mean, Threshold = 10, Reject ±25%.

Method 5: Clipped Mean, Threshold = 40, Reject ±25%.

Method 6: like Method 3 of Table 3.6 but no zero-crossing values utilized.

Method 7: WIND1 analysis (Section 3.1) at 90.5 km.

of the semidiurnal tide. Because methods 4, 5, and 6 average all heights together and because of the standing-wave phenomena in $S_2(v)$ (Table 6.2), it is not surprising to find disagreement with WIND1 results. An examination of the relation between height averaging and height quantizing wind analysis methods is given in Section 3.3.

To gauge the seriousness of low velocity discrimination, when zero-crossing methods are used, a simple model is analyzed in Appendix IV. Here for simplicity we have assumed no velocities of magnitude V_D or less ever result. This will yield somewhat pessimistic estimates of bias if arbitrary 0 m s^{-1} assignments are made as at ARCRL [*Barnes and Pazniokas*, 1972]. It is interesting to note that the zero-crossing scheme causes an overestimation of wind amplitude. Thus results from meteor radar stations using zero-crossing schemes for individual echo results then averaging them via a clipped data method should agree well with University of Illinois results using the Bowhill algorithm and the highly selective method 6. This is so because the overestimation of zero-crossing will help compensate for the underestimation of clipped data methods.

The earliest meteor-radar observations made at the University of Illinois inferred echo height from the rate of decay of the Yagi video signal (Section 2.2.4.1). To determine whether or not such a statistical means of generating height data would still allow accurate resolution of vertical wind structures, comparisons between tides based on decay height and interferometer height were made. METP6 software determines both heights for each collected echo, so the problem of nonsimultaneous data sets is avoided. Figure 3.3 shows a representative comparison. It is apparent that the prevailing wind, diurnal tide, and semidiurnal tide agree well in magnitude and phase for both height determinations, except in the case of $|S_1(v)|$.

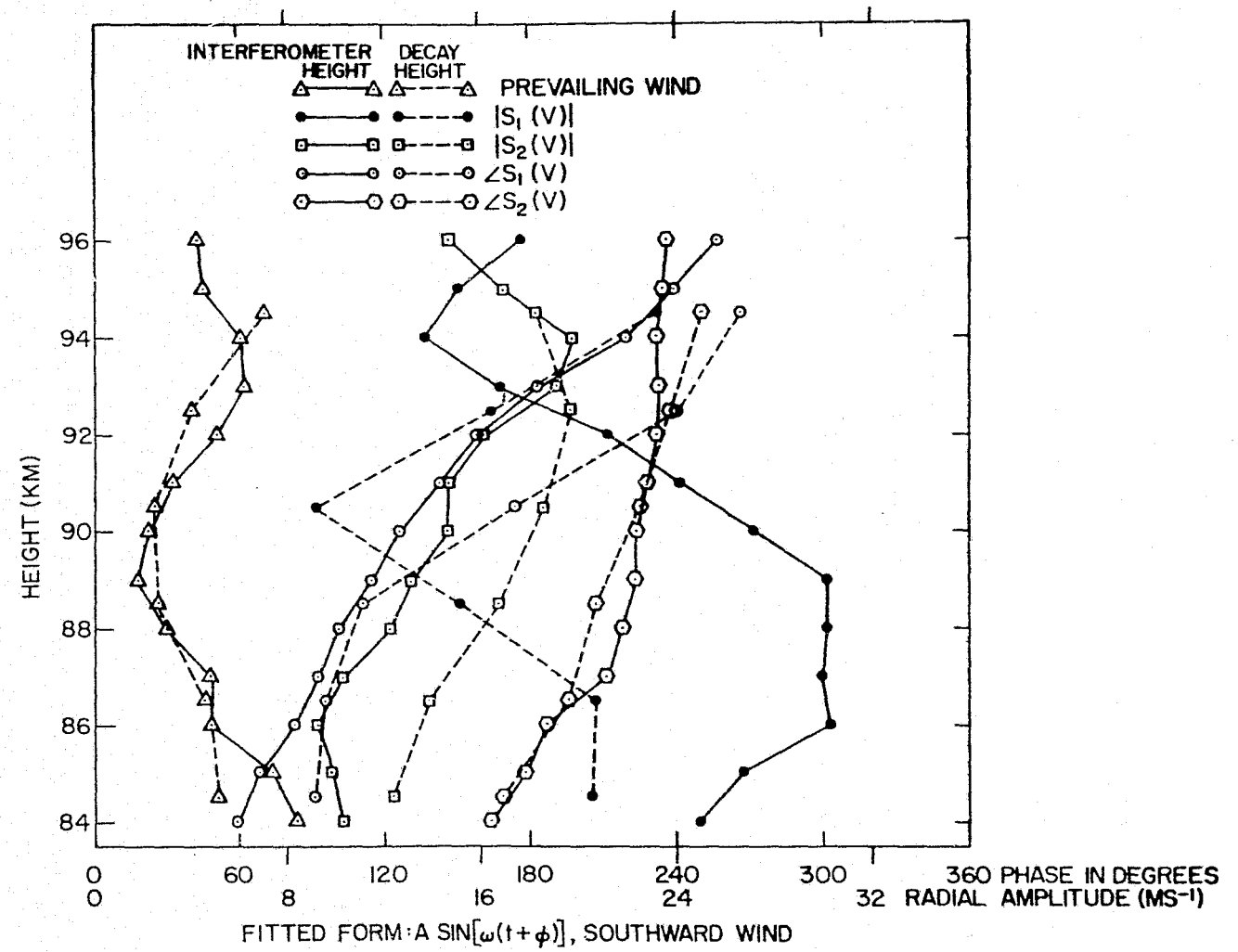

Figure 3.3 Comparison of winds deduced using interferometer and decay height values, September 13-14, 1975.

Even here the structures are similar but the decay height analysis tends to underestimate the amplitude. This error may be related to the fact that the vertical wavelength of $S_1(v)$ is quite short for the particular data set graphed.

3.3 *Averaging Effect of a Meteor-Radar System Without Height Resolution*

The observed motions of an atmospheric wave propagating vertically in an isothermal region and experiencing no energy loss can be described in complex form as

$$u(z,t) = u_o \exp\left[2\pi j\left(\frac{t}{T} - \frac{z}{\lambda}\right)+\alpha z\right] \tag{3.3}$$

where

u_o = wave amplitude at reference height $z = 0$

T = wave period

λ = vertical wavelength, real for propagating waves, imaginary in evanescent cases

α = $1/2H$, where H is the local scale height.

As a result of averaging $u(z,t)$ in height over the meteor region, the apparent wave observed is given by

$$v(t) = \int_{-\infty}^{\infty} u(z,t)p(z)dz \tag{3.4}$$

where

$p(z)$ = the probability of observing a meteor echo in the height range $(z, z + \Delta z)$.

$p(z)$ generally follows a Gaussian law, but rapid diffusion of meteor trails at higher altitudes makes the associated Doppler wind measurements unreliable. Such unreliable measurements can easily be rejected via echo collection software which sets a minimum time of existence for acceptable echoes. This in effect leads to a height ceiling on accepted echoes,

particularly if height is inferred from echo decay rate, and thus $p(z)$ may be more accurately described by a Gaussian law clipped at some maximum height z_m:

$$p(z) = \frac{K}{\sqrt{2\pi\sigma^2}} \exp[-(z-z_o)^2/2\sigma^2], \quad z \leq z_m \tag{3.5}$$

where

K = constant required to adjust $\int_{-\infty}^{z_m} p(z)dz = 1$

σ = standard deviation of echo height

z_o = most probable echo height.

Note that due to the asymmetry of $p(z)$, the mean echo height is not z_o, but rather is

$$\begin{aligned} z_a &= \int_{-\infty}^{z_m} \frac{Kz}{\sqrt{2\pi\sigma^2}} \exp[-(z-z_o)^2/2\sigma^2]dz \\ &= K\left\{\frac{z_o}{2}[1+erf(x)] - \frac{\sigma}{\sqrt{2\pi}} \exp(-x^2)\right\} \end{aligned} \tag{3.6}$$

where

$$x \triangleq (z_m-z_o)/\sqrt{2\sigma}$$

$$erf(x) \triangleq \frac{2}{\sqrt{\pi}} \int_o^x e^{-t^2} dt$$

Substituting (3.5) into (3.4) shows that we observe the wave as

$$v(t) = \frac{Ku_o \exp(2\pi jt/T)}{\sqrt{2\pi\sigma^2}} \int_{-\infty}^{z_m} \exp[(\alpha \frac{2\pi j}{\lambda})z] \exp\left[-\left(\frac{z-z_o}{\sqrt{2\sigma}}\right)^2\right] dz \tag{3.7}$$

Upon evaluation of the integral we find

$$\begin{aligned} v(t) = Ku_o \exp\left[\frac{2\pi jt}{T} + (\alpha - \frac{2\pi j}{\lambda})z_o\right] F \exp(\frac{-2\pi\sigma^2\alpha j}{\lambda}) \\ \cdot (1/2)(1+erf[x-(\alpha-2\pi j/\lambda)(\sigma/\sqrt{2})]) \end{aligned} \tag{3.8}$$

where

$$F \triangleq \exp[(\sigma^2/2)(\alpha^2 - 4\pi^2/\lambda^2)].$$

Substituting (3.6) into (3.3) gives us the actual wave expression for height z_a:

$$u(z_a,t) = u_o \exp\left[\frac{2\pi jt}{T} + (\alpha - \frac{2\pi j}{\lambda})K \left\{\frac{z_o}{2}(1+erf(x)) - \frac{\sigma}{\sqrt{2\pi}}\exp(-x^2)\right\}\right] \tag{3.9}$$

Using the expressions (3.8) and (3.9) gives

$$\frac{v(t)}{u(z_a,t)} = F \exp(\frac{-2\pi\sigma^2\alpha j}{\lambda}) \left[\frac{1+erf(x-(\alpha-2\pi j/\lambda)\sigma/\sqrt{2})}{1 + erf(x)}\right] \cdot \exp\left[(\alpha-\frac{2\pi j)}{\lambda}\sqrt{\frac{2}{\pi}}\frac{\sigma\exp(-x^2)}{1+erf(x)}\right] \tag{3.10}$$

Hence, the amplitude and phase errors are

$$Ae = F \left\{\frac{\exp\left[\sqrt{\frac{2}{\pi}}\frac{\sigma\alpha\exp(-x^2)}{1+erf(x)}\right]}{1+erf(x)}\right\} Mag\left[1 + erf(x-(\alpha - \frac{2\pi j}{\lambda})\sigma/\sqrt{2})\right] \tag{3.11}$$

and

$$Pe = \frac{-2\pi\sigma^2\alpha}{\lambda} - \frac{2\pi}{\lambda}\sqrt{\frac{2}{\pi}}\frac{\sigma\exp(-x^2)}{1+erf(x)} + \angle\left[1 + erf(x-(\alpha - \frac{2\pi j}{\lambda})\sigma/\sqrt{2})\right] \tag{3.12}$$

Letting $z_m \to \infty$ shows that these results agree with those of *Glass et al.* [1975], who treated the situation of no ceiling height. From the NBS Handbook of Mathematical Functions, [*Abramowitz and Stegun*, 1964]:

$$erf(a+jb) = erf(a) + \frac{e^{-a^2}}{2\pi a}[(1-\cos 2ab) + j\sin 2ab] + \frac{2e^{-a^2}}{\pi}\sum_{n=1}^{\infty}\frac{e^{-n^2/4}}{n^2+4a^2}[f_n(a,b)+jg_n(a,b)]+E(a,b) \tag{3.13}$$

where

$$f_n(a,b) = 2a - 2a \cosh nb \cos 2ab + n \sinh nb \sin 2ab$$

$$g_n(a,b) = 2a \cosh nb \sin 2ab + n \sinh nb \sin 2ab$$

$$|E(a,b)| \cong 10^{-16} \; |erf(a+jb)|$$

In our case of interest, $a = x - \frac{\alpha\sigma}{\sqrt{2}}$, $b = \frac{2\pi\sigma}{\lambda\sqrt{2}}$. With $x = \sqrt{2}$, $\sigma = 5$, and $\alpha = 1/14$, computer solutions show:

Tidal Mode	λ	*Ae*	*Pe*	*Ae**	*Pe**
Θ_1^1	26km	.576	-.445r	.514	-.498r
Θ_2^2	200	1.046	-.048	1.053	-.065
Θ_2^4	50	0.900	-.201	.875	-.259
Θ_2^6	31	0.693	-.353	.638	-.418

(* No height ceiling)

Of course if the wave in question is evanescent rather than propagating λ is imaginary and we do not have a complex error function to evaluate.

A second effect which we have thus far ignored further aggravates the differences between height averaged wave results and true values, namely, diurnal variation of mean echo height. Such variation has been observed by numerous meteor-radar experimenters, see for example, *Weiss* [1959]. As *McKinley* [1961] notes, this diurnal variation is most likely due to a combination of zenith angle and velocity effects caused by the daily motion of the earth's apex. Typical variation amplitudes are 3 or 4 km (Figure 5.4), too large to be the result of tidal density perturbations. The latter is also ruled out as the cause because the variation is always diurnal, even when semidiurnal tides dominate, and the phase is relatively constant and thus independent of the diurnal tidal wind phase.

Since we have already shown that the height ceiling effect is generally not substantial, we can examine the effect of diurnal variation of mean echo height by considering

$$p(z) = \frac{1}{\sqrt{2\pi\sigma^2}} \exp[-(z-z_o(t))^2/2\sigma^2] \tag{3.14}$$

with

$$z_o(t) = z_o + z_1 \cos\left(\frac{2\pi t}{T_1} + \phi_1\right)$$

$$T_1 = 24 \text{ hr.}$$

Equation (3.4) becomes

$$v(t) = \int_{-\infty}^{\infty} u_o \exp[2\pi j(\frac{t}{T} - \frac{z}{\lambda}) + \alpha z] \frac{\exp\left[\frac{-(z-z_o(t))^2}{2\sigma^2}\right]}{\sqrt{2\pi\sigma^2}} dz$$

$$= u_o \exp[2\pi j\frac{t}{T} + (\alpha - \frac{2\pi j}{\lambda})z_o(t)] \exp[\frac{-2\pi\sigma^2\alpha j}{\lambda}]F \tag{3.15}$$

and

$$\frac{v(t)}{u(z_o,t)} = \exp\left[(\alpha - \frac{2\pi j}{\lambda})z_1 \cos(\frac{2\pi t}{T} + \phi_1)\right] \exp\left(\frac{-2\pi\sigma^2\alpha j}{\lambda}\right) F \tag{3.16}$$

Thus both the phase error

$$Pe = \frac{-2\pi\sigma^2\alpha}{\lambda} - \frac{2\pi z_1}{\lambda} \cos\left(\frac{2\pi t}{T_1} + \phi_1\right) \tag{3.17}$$

and the amplitude error

$$Ae = \exp\left[\alpha z_1 \cos(\frac{2\pi t}{T_1} + \phi_1)\right] F \tag{3.18}$$

depend on the time of observation. Averaging equations (3.17) and (3.18) over an integral number of days shows

$$\langle Pe \rangle = -2\pi\sigma^2\alpha/\lambda \tag{3.19}$$

and

$$\langle Ae \rangle = FI_o(\alpha z_1) \tag{3.20}$$

where $I_o(\alpha z_1)$ is the modified Bessel function of order zero. Thus if the wave actually behaves as in equation (3.3), diurnal variation of the mean height will cause an overestimation of wave amplitude by the factor $I_o(\alpha z_1)$ (The error factor F is the result of averaging echoes over all heights). This overestimation is independent of wavelength and for $\alpha = 1/14$ km^{-1} and $z_1 = 4$ km, equals about 1.06. But since errors on the order of 50% can be caused by the F factor (Θ_1^1 tidal mode), it dominates over errors due to mean height variations.

4. METEOR CHARACTERISTICS

4.1 *Introduction*

The earth is under continuous bombardment by myriads of meteoric particles. These meteors enter the earth's atmosphere and quickly vaporize, forming long columns of ionized particles. The columns diffuse rapidly but during their brief existence can reflect radio signals, hence the phenomena called meteor scatter. Via such scatter it is possible to study the physics of meteors and the upper atmosphere as well.

The physical processes involved in the interaction of meteors with the upper atmosphere have undergone extensive study since 1946. Much of the work is summarized in a book by *McKinley* [1961]. The purpose of this section is to present those characteristics of meteors pertinent to understanding radar returns from meteor trails. A detailed radar equation will be derived to permit signal-to-noise calculations.

4.2 *Meteoric Particles*

The meteors of interest are those particles which completely burn up due to frictional heating after entering the earth's atmosphere. Smaller particles, the so-called micrometeorites, settle so slowly through the atmosphere that no significant ionization results. The larger meteors, which manifest themselves as fireballs, or meteorites if they reach the earth's surface, are of little concern because they so rarely occur.

Meteors can be divided into two classes, shower meteors and sporadic meteors. The shower meteors are a collection of particles all moving at the same velocity in rather well-defined orbits or streams around the sun. Their orbits intersect the earth's orbit at a specific time each year and at these times meteor showers occur. Sporadic meteors, which are always present, do not move in well-defined streams but rather seem to move in

random orbits. Thus, while shower meteors appear to emanate from a specific point in the sky, the radiant point of the shower, sporadic meteors have radiants which appear random.

Table 4.1 summarizes some basic properties of sporadic meteors; the particles with masses in the range 10^{-7} to 10^{3} grams are the major sources of meteor scatter. Note how the number of meteors of a given mass or greater swept up by the earth each day is inversely proportional to that particular mass. Also note that mass and electron line density are directly proportional.

A recent paper by *Verniani* [1973] presents the most detailed analysis to date of the physical parameters of faint radio meteors. The results are based on an analysis of nearly 6000 meteors detected in 1962 from at least three stations located around Havana, Illinois, under the Harvard Radio Meteor Project. Each station yielded instantaneous values for meteor velocity v and trail electron line density q, thus allowing determination of mean deceleration and a sketch of the ionization curve versus altitude. The latter allows computation of the original meteor mass m_{∞}. With the aid of assumptions, density and ablation coefficient values can also be inferred.

The mean original mass m_{∞} is found to be on the order of 10^{-4} while the mean maximum electron line density q_{max} is near $10^{12.5}$ m^{-1}. These values compare favorably with the results given in Table 4.1. The mean apparent velocity v of about 34 km s^{-1} is rather low and confirms the existence of a systematic shift in the velocity distribution, depending upon the mass of the particles (lower velocities with lower mass). The dependence of q_{max} on the basic meteor parameters (velocity, mass, and zenith angle Z_R) agrees well with the single-body theory [*Verniani*, 1961]. However, meteors are on

Table 4.1

Order of magnitude estimates of the properties of sporadic meteors [*Sugar*, 1964].

	Mass (grams)	Visual Magnitude	Radius	Number of this mass or greater swept up by the earth each day	Electron line density (electrons per meter of trail length)
Particles pass through the atmosphere and fall to the ground	10^{4}	-12.5	8 cm	10	-
	10^{3}	-10.0	4 cm	10^{2}	-
	10^{2}	-7.5	2 cm	10^{3}	-
	10	-5.0	0.8 cm	10^{4}	10^{18}
	1	-2.5	0.4 cm	10^{5}	10^{17}
	10^{-1}	0	0.2 cm	10^{6}	10^{16}
	10^{-2}	2.5	0.08 cm	10^{7}	10^{15}
	10^{-3}	5.0	0.04 cm	10^{8}	10^{14}
	10^{-4}	7.5	0.02 cm	10^{9}	10^{13}
	10^{-5}	10.0	80 microns	10^{10}	10^{12}
	10^{-6}	12.5	40 microns	10^{11}	10^{11}
	10^{-7}	15.0	20 microns	10^{12}	10^{10}
	10^{-8}	17.5	8 microns		
Micro-meteorites (Particles float down unchanged by atmospheric collisions)	10^{-9}	20.0	4 microns	Total for this group estimated as high as 10^{20}	Practically none
	10^{-10}	22.5	2 microns		
	10^{-11}	25.0	0.8 microns		
	10^{-12}	27.5	0.4 microns		
Particles removed from the solar system by radiation pressure	10^{-13}	30	0.2 microns		

the average one magnitude brighter than single-body theory predicts and one-half the predicted duration and length. These results are ascribed to the common occurrence of fragmentation. The median value of computed densities is 0.8 g cm^{-3}, pointing out that radio meteors are as fragile in structure as both ordinary photographic meteors and extremely large ones. Mean values of basic parameters for shower meteors do not differ significantly from the corresponding ones of sporadic meteors. This lack of differentiation is considered proof of the cometary origin of most meteors. Shower meteors are known to be of cometary origin because common orbits have in many cases been found.

Although sporadic meteor radiant points are random they are not uniformly distributed in the sky. Instead they are concentrated toward the ecliptic plane, the plane of the earth's orbit, and move in the same direction around the sun as the earth does [*Hawkins*, 1956]. Furthermore, the orbits are not uniformly distributed around the earth's orbit but are concentrated so as to produce a maximum influx in July and a minimum in February. Figure 4.1(a) shows the yearly variation in the space density of meteors along the earth's orbit.

The influx of sporadic meteors on the earth is modified further by two additional factors. The first of these, shown in Figure 4.1(b), causes a regular diurnal variation in the meteor rate. On the morning side of the earth, meteors are overtaken by the forward motion of the earth as it revolves around the sun. On the evening side the only meteors reaching the earth are those which can overtake it. The result is a maximum influx rate around 6 AM with a minimum rate near 6 PM local time. Figure 4.2 shows a typical graph of diurnal variation in echo rates for the University of Illinois meteor radar while Table 4.2 summarizes least square mean plus

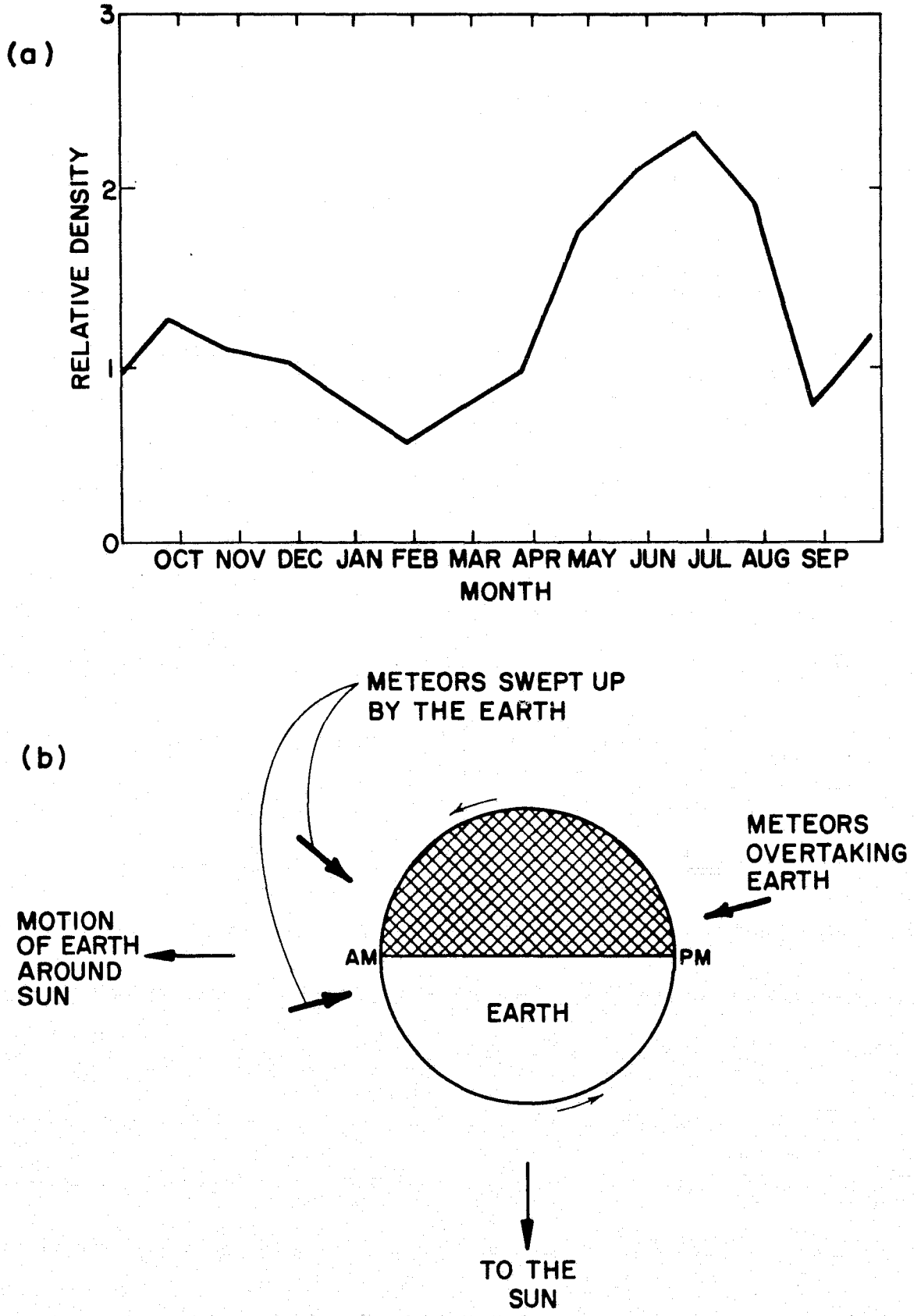

Figure 4.1 (a) Variation in the space density of meteors along the earth's orbit [*Sugar*, 1964], (b) Diurnal variation of meteor rates.

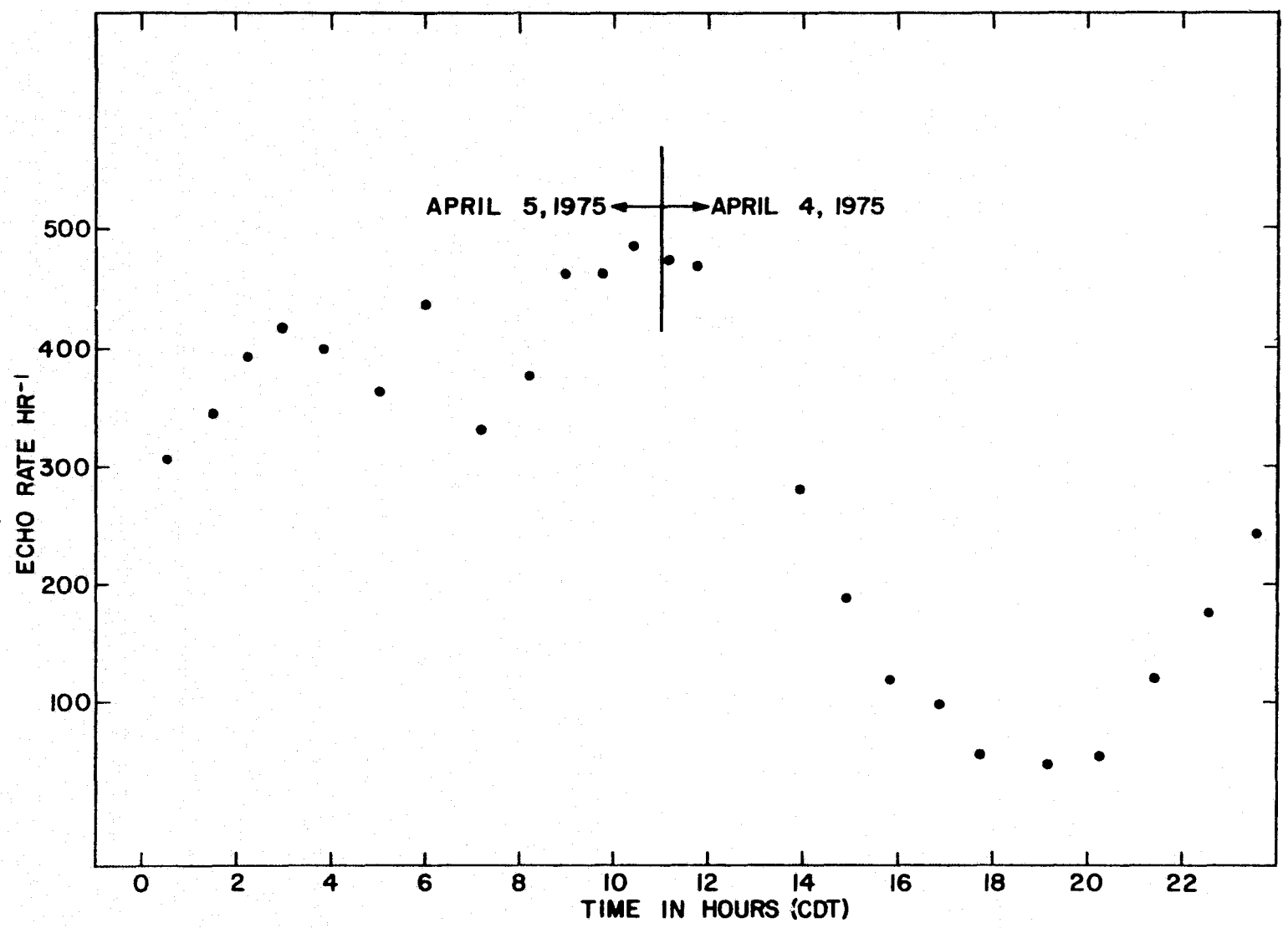

Figure 4.2 Typical echo rate for University of Illinois meteor radar (1 MW peak power).

Table 4.2

Meteor echo collection rate at Urbana, Illinois.

1 MW peak power, 20 dB min S/N

Date	Local time	a_o	a_1	b_1	$\sqrt{a_1^2+b_1^2}$	Collection Software
Jan.17,18, 1975	CST	228	-25	175	177	METP4
Jan.31, Feb. 1	CST	231	16	171	172	METP4
Feb.28, March 1	CDT	295	-67	203	214	METP4
March 7,8	CDT	297	-68	188	200	METP4
April 4,5	CDT	284	-61	185	195	METP5
May 27,28	CDT	227	-38	161	165	METP5
July 14,15	CDT	224	44	164	170	METP5
July 30,31	CDT	249	161	218	271	METP5
Aug. 21,22	CDT	180	29	126	129	METP5
Sept. 13,14	CDT	(200)133	6	65	(98)65	METP6
Oct. 13,14	CDT	(238)158	-29	90	(141)94	METP6
Oct. 14,15	CDT	(226)150	-25	87	(137)91	METP6

Units are echoes per hour

( ) = estimate of equivalent METP5 rate

Fit form to rate is $R(t) = a_o + a_1\cos(\pi/12t) + b_1\sin(\pi/12t)$

diurnal fits to echo rate for various runs made during 1975. The effect of the Delta Aquarid shower in late July is readily seen both in terms of higher echo rate and a substantial shift in diurnal phase (all others are sporadic runs). The back-to-back October runs demonstrate lack of significant day-to-day variability in the echo rate. However, a plot, as in Figure 4.3, of hourly echo rate versus threshold shows that real short term rate variations do occur, and they do so across our full range of acceptable echo strengths. Our observed max/min rate ratio is typically on the order of ten due to the narrow transmitting and receiving antenna beamwidths used. All-sky systems somewhat smooth the diurnal variation; thus, for example, a typical max/min variation of just six is observed at Adelaide [*McAvaney*, 1970].

The second factor affecting the rate of incidence of sporadic meteors is the tilt of the earth's axis relative to the ecliptic plane. This causes a seasonal variation dependent on observation latitude and may change hourly rates by a factor of 1.4.

The velocities of meteors approaching the earth are in the range of 11.3 to 72 km s^{-1}. The lower limit is set by the escape velocity of a particle leaving the earth's gravitational field and is therefore the minimum velocity that a particle falling toward the earth can have. The upper limit is the sum of the velocity of the earth orbiting the sun (30 km s^{-1}) and the escape velocity for a particle leaving the solar system (42 km s^{-1}). The fact that observed meteor velocities hardly ever exceed the upper bound is proof that most, if not all, meteors are indeed members of the solar system.

4.3 *Meteor Trails*

As a meteor enters the earth's atmosphere its heating and ablation begins. Depending on particle mass and velocity these processes start at

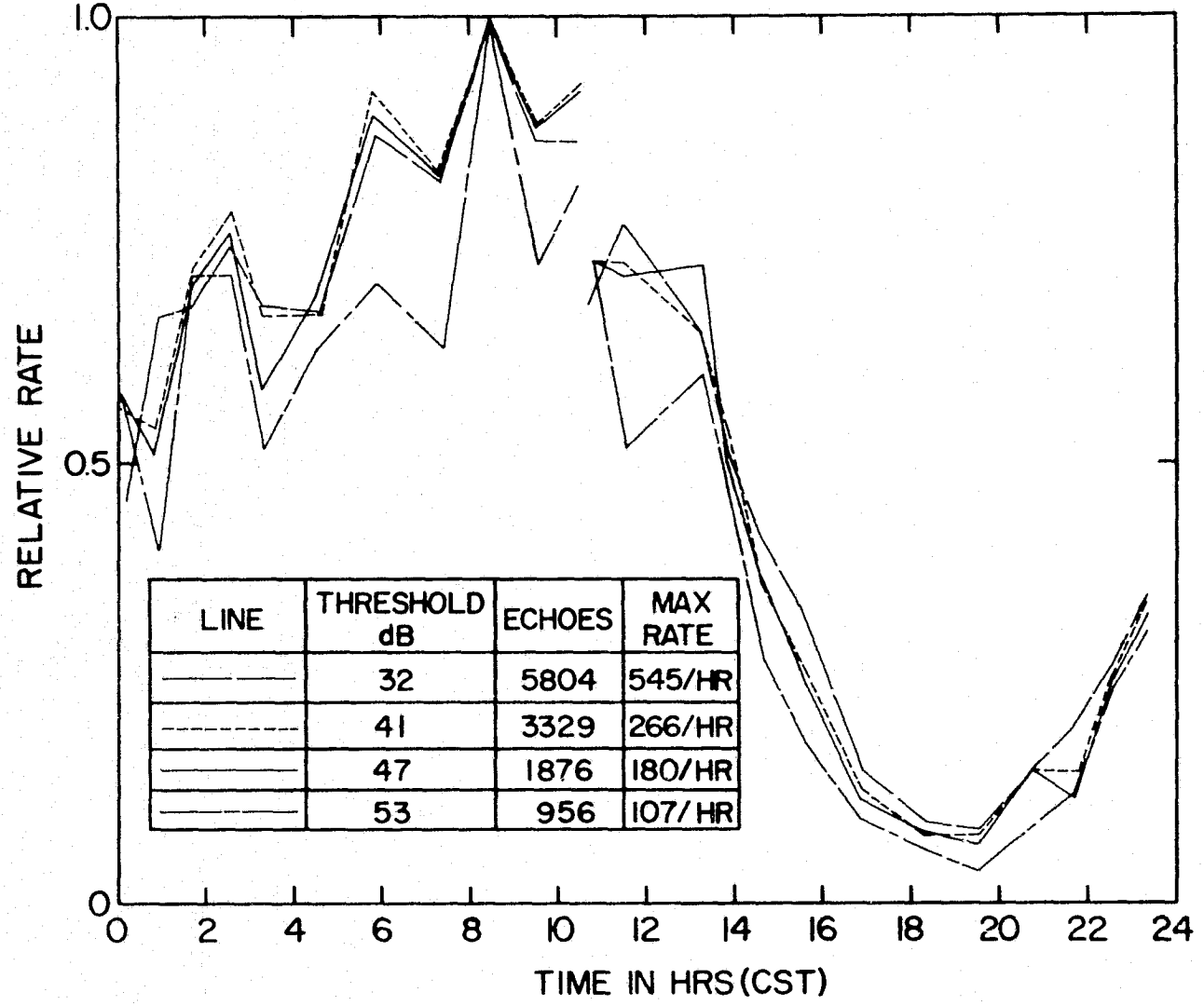

Figure 4.3 Echo rate versus threshold, February 28 - March 1, 1975.

heights of 100 to 120 km where the air density is large enough to generate appreciable friction. As the meteor penetrates further, the exponentially increasing air density leads to an increase in ablation and ionization until the latter reaches a maximum, on the average near 90 km. At lower altitudes ionization rapidly falls off as the meteor diminishes in size and finally disappears altogether. The relatively small thickness of the meteor region, 80 to 120 km, is the result of the rapid change in air density. At 120 km the mean free path is 5.4 m while at 80 km it is only 3.8 mm based on the 1959 ARDC Model Atmosphere. A theoretical distribution of ionization with height [*Eshleman*, 1957] supported experimentally is

$$q/q_{max} = \frac{9}{4} \exp\left(\frac{h_{max}-h}{H}\right)\left[1 - \frac{1}{3}\exp\left(\frac{h_{max}-h}{H}\right)\right]^2 \qquad (4.1)$$

where q is the ionization electron line density at height h (maximum value of q_{max} occurs at height h_{max}), and H is the atmospheric scale height. Eshleman also derived an expression for meteor trail lengths between points of half maximum ionization:

$$L_h = 2H \sec Z_R \qquad (4.2)$$

where Z_R is the zenith angle of the meteor radiant.

The height distribution of meteor trails varies with velocity, mass, and radiant of the meteor. The higher velocity particles produce trails at higher heights. Higher mass particles (same as higher q values) yield lower maximum ionization heights. Trails with large zenith angles reach their ionization maximum at greater heights. A typical frequency-height distribution for the University of Illinois meteor-radar system is shown in Figure 4.4.

The ionization produced by meteors is initially distributed in the form of a long, thin paraboloid of revolution. The initial trail radius r_o

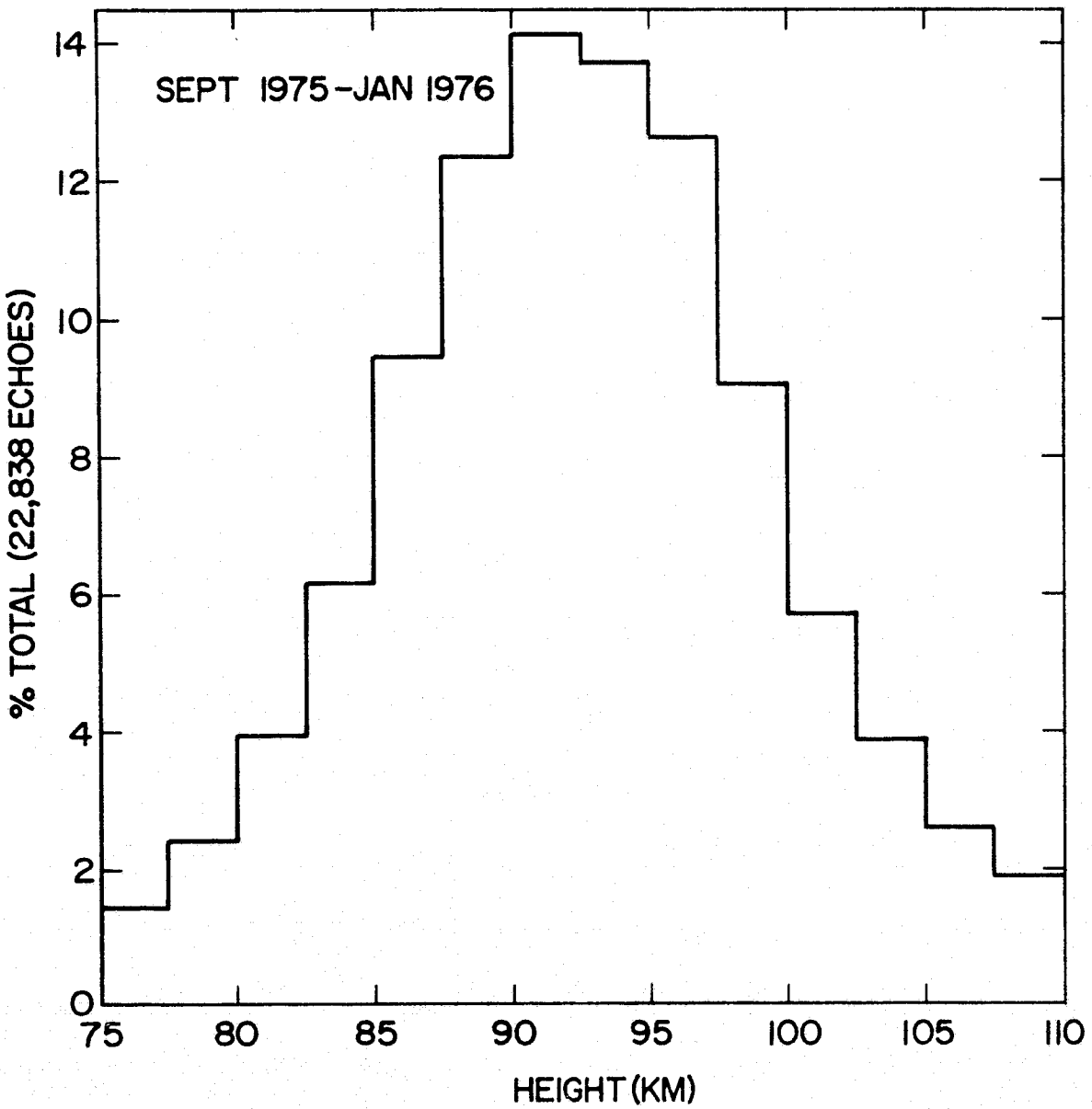

Figure 4.4 Stacked Yagi interferometer height histogram.

derived theoretically by *Manning* [1958] is 14 ionic mean free paths, reached typically in less than 1 ms. However, later photographic and radio measurements [*Hawkins and Whipple*, 1958 and *Greenhow and Hall*, 1960b] have suggested that r_o is significantly larger, probably due to fragmentation. The trail radii measured are in the range 0 to 1.2 m (0.65 m mean) for the photographic work (high mass and electron line density trails) and 0.55 m to 4.35 m for the radio work (smaller mass and electron line density trails). The 0.55 m value was at 81 km where the mean free path is only about 5 mm.

After the trail is formed it expands by diffusion in a relatively slow manner producing a radial distribution that is approximately Gaussian. Several models for the radial distribution of electrons have been investigated by *Herlofson* [1951] and others but the Gaussian model seems physically the most realistic for decay of the trail. Here the trail is formed at time $t = 0$ with initial radius $r_o = 0$ and electron line density q. At time t the electron volume density at radius r from the original line is described by

$$N(r,t) = \frac{q}{4\pi Dt} \exp\left(\frac{-r^2}{4Dt}\right) \tag{4.3}$$

where D is the ambipolar diffusion coefficient for the ion-electron plasma. The diffusion process is mainly controlled by the ions; however, since the plasma has to stay neutral (because otherwise, strong electric fields would be set up through charge separation), electrons and ions diffuse together. The diffusion coefficient D is very height-dependent and given by *Huxley* [1952] as

$$D = 5.249 \times 10^{-7}\, T/\rho \quad \text{cm}^2\text{s}^{-1} \tag{4.4}$$

which is graphed in Figure 4.5. The numbers there in parentheses refer to scale height (slope of line) in km. Some sodium trail results are also plotted as is the regression line found by *Greenhow and Neufeld* [1955] for

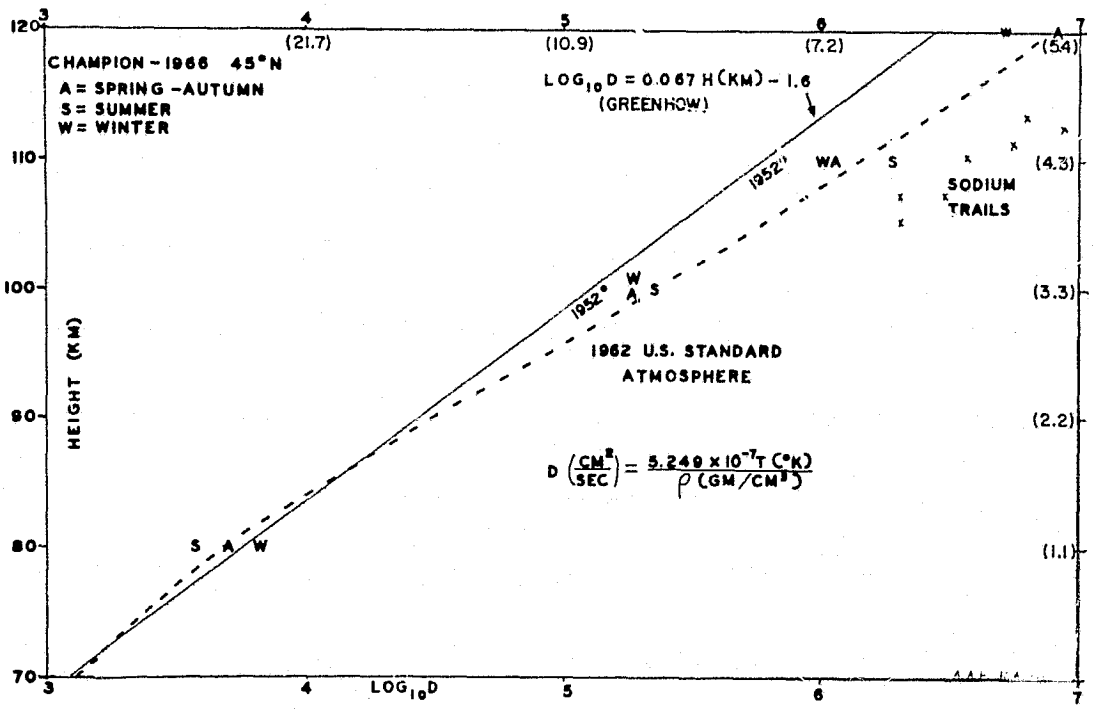

Figure 4.5 Ambipolar diffusion as a function of height [*Barnes and Pazniokas*, 1968].

statistically relating D to echo height. This latter matter is discussed in more detail in Chapter 9. Since temperature is presumed to be approximately isothermal at meteor heights, (4.4) is dominated by the inverse relationship between D and ρ.

4.4 *Reflection Properties of Individual Trails*

The distribution of energy reflected by a meteor trail is a function of many variables. The ionization density distribution across and along the trail, the orientation of the trail, the radio wavelength, the polarization of the incident wave relative to the trail, motion of the trail either as part of the process of formation or due to ionospheric winds, and the straightness of the trail are all significant [*Sugar*, 1964]. In discussing the reflection properties it is convenient to divide the trails into two classes, underdense trails and overdense trails. Underdense trails are those wherein the electron density is low enough so that the incident wave passes through the trail and the trail can be considered as an array of independent scatterers. Overdense trails are those wherein the electron density is high enough to prevent complete penetration of the incident wave and to cause reflection of waves in the same sense that the ordinary ionospheric reflections occur. Due to its high sensitivity, predominantly underdense trails will be processed by the University of Illinois meteor-radar system so the following discussion is limited to such trails.

Assume that the trail is an infinitely long right-circular cylinder of electrons whose diameter is very small compared to the wavelength and that the trail electron density is low enough that the incident wave passes through the trail without major modification. Consider the case of radar-like reflections with the transmitter and receiver at the same location. The signal received can be computed by summing the energy backscattered by

each electron in the trail while taking proper account of the phase relations of these contributions. The transmission equation can be written in terms of the scattering cross section σ_e in the following way:

$$\frac{P_R}{P_T} = \frac{G_T G_R \lambda^2}{16\pi^2 R_o^4} \sigma_e \tag{4.5}$$

where

P_T and P_R are the transmitted and received power, respectively

G_T and G_R are the power gains of the transmitting and receiving antennas relative to an isotropic radiator in free space, respectively

λ is the wavelength

R_o is the distance from transmitter to the trail (i.e., to the specular reflection point)

σ_e is the scattering cross section of the trail (the scattering cross section is defined as the ratio of the power scattered per unit solid angle to the power incident per unit area).

In the simplest case, for a single electron, P_T/P_R can be obtained from field calculations. Applying equation (4.5) to this case and solving for the electron cross section yields [*McKinley*, 1961]

$$\sigma_e = \frac{\mu_o^2 e^4}{16\pi^2 m^2} \tag{4.6}$$

where μ_o is the permeability of free space and e is the charge of the electron of mass m. A similar expression is obtained for the cross section σ_i of an ion. However, since the ion mass is so much larger than the electron mass, $\sigma_e >> \sigma_i$. Thus only the electrons in the ion-electron plasma that forms the trail will contribute noticeably to the radar echo, and the trail can be considered as an electron ensemble. If we assume that our ensemble is a very thin cylindrical column (zero initial trail radius, instantaneously

formed) that expands through Gaussian diffusion, the scattering cross section may be written as [*Eshleman*, 1955]

$$\sigma_e = \left(\sqrt{R_o \lambda/2}\; r_e q\right)^2 \exp\left(-\frac{32\pi^2 D}{\lambda^2}\, t\right) \tag{4.7}$$

where

$r_e = \mu_o e^2/4\pi m = 2.8178 \times 10^{-15}$ m, the classical radius of the electron, and t is time measured from the formation of the trail in seconds. The first of the two factors in equation (4.7) represents the scattering cross section of the initial line distribution of electrons, and the second factor represents the attenuation with time as the trail expands and destructive interference begins.

If the initial radius of the trail is not zero, the extra attenuation associated with a finite radius may be estimated by assuming that the initial distribution of electrons is Gaussian. The effect of the finite initial radius on received power is then equivalent to a shift in the time scale. Using the relation $r = \sqrt{4Dt}$ and equation (4.7), it can be seen that the initial attenuation factor can be written as $\exp(-8\pi^2 r_o^2/\lambda^2)$ where r_o is the initial radius of the trail. Thus we have

$$\frac{P_R}{P_T} = \frac{G_T G_R\; q^2 r_e^2}{32\pi^2 R_o^3} \exp\left(\frac{-8\pi^2 r_o^2}{\lambda^2}\right) \exp\left(\frac{-32\pi^2 Dt}{\lambda^2}\right) \tag{4.8}$$

In the above relation, since it was assumed that trails were of infinite length, every trail had a first Fresnel zone and therefore gave a reflection. In practice, however, this zone may not lie on the trail but rather on an extension of it. In such a case the signal returned from the trail would be a relatively weak one. Thus a radar can "see" only a fraction of all the trails incident on the ionsophere within its range because most trails do not have the proper orientation for the line of sight to be perpendicular

to the trail (specular reflection). The requirement for proper orientation can be restated as requiring that the trail be tangent to a sphere centered at the radar.

The equations developed thus far apply only to instantaneously formed meteor trails. To account for realistic trail formation we proceed as follows. Assuming a receiver input resistance r_i, the peak signal amplitude dA_R from a line element ds of a very thin meteor trail (zero initial trail radius) in which all electrons scatter independently (underdense case) is

$$dA_R = \sqrt{2P_R r_i}\, qds \sin(2\pi ft - \frac{4\pi R}{\lambda} - \beta) \tag{4.9}$$

where

P_R = power scattered to receiver by a single electron at range R via equations (4.5) and (4.6)

$\sin(2\pi ft)$ = assumed transmitted signal form

$4\pi R/\lambda$ = two-way phase delay due to trail range R

β = phase retardation on reflection

Using the geometry shown in Figure 4.6(a) and summing the reflected contributions of all line elements leads to the resultant peak signal amplitude

$$A_R = \int_{s_2}^{s_1} \sqrt{2P_R r_i}\; q \sin(2\pi ft - \frac{4\pi R}{\lambda} - \beta)\, ds \tag{4.10}$$

where s_2 represents the position along the meteor path where the trail begins and s_1 represents the present position of the meteor. Since the contributions from the lower limit is negligible, we can approximate equation (4.10) by integration from $-\infty$ to s_1. For q relatively constant near point P and using

$$R \cong R_o + s^2/2R_o \tag{4.11}$$

one obtains

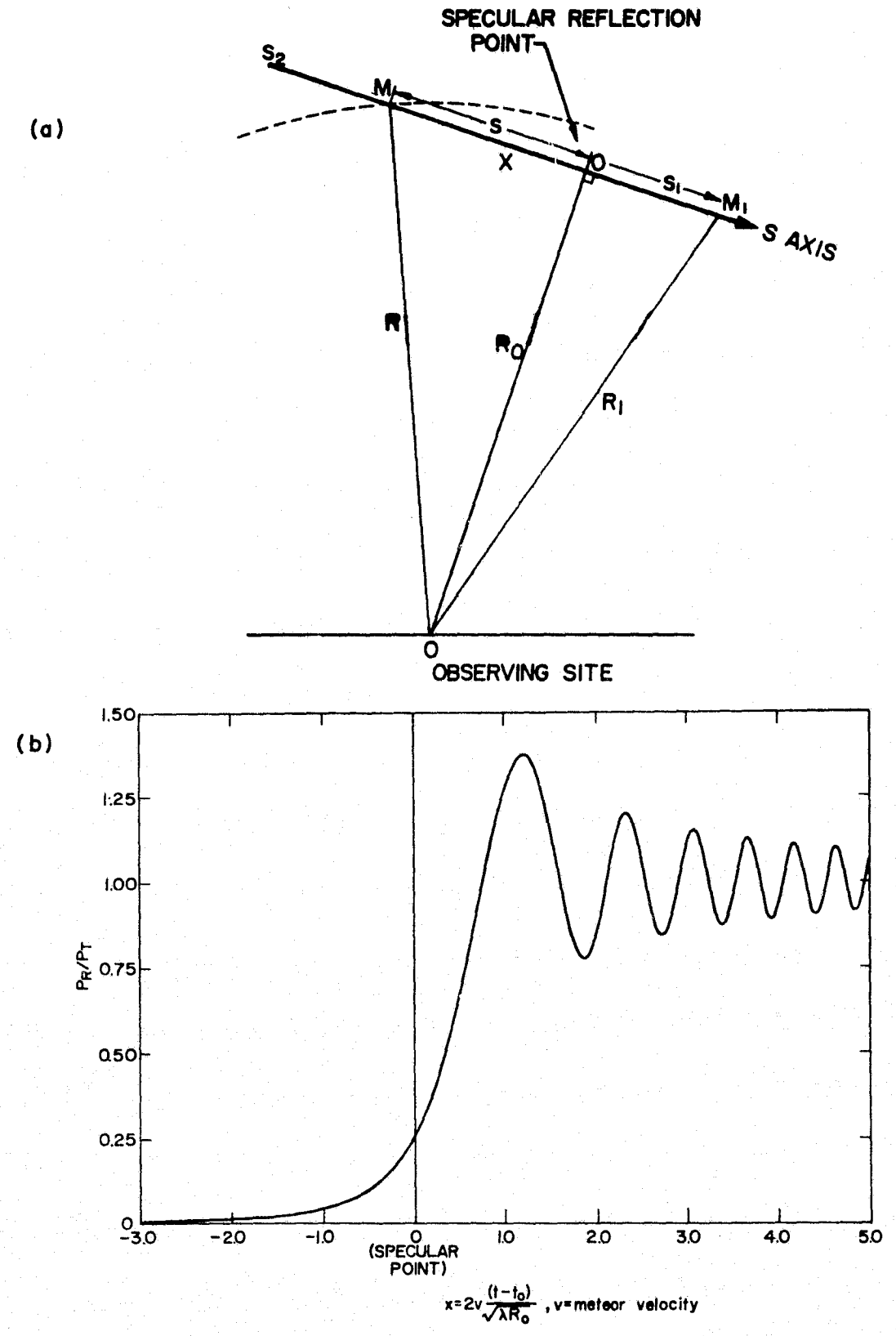

Figure 4.6 (a) The geometry of a meteor path relative to an observing site, (b) Returned power from an underdense meteor trail versus meteor position (zero diffusion).

$$A_R = \sqrt{2P_R r_i}\ q \int_{-\infty}^{s_1} \sin\left(2\pi f t - \frac{4\pi R_o}{\lambda} - \frac{2\pi s^2}{\lambda R_o} - \beta\right) ds \tag{4.12}$$

Defining

$$\Phi \triangleq 2\pi f t - \frac{4\pi R_o}{\lambda} - \beta$$

$$x^2 \triangleq 4s^2/\lambda R_o$$

$$k \triangleq \sqrt{2P_R r_i \lambda R_o}\ q/2$$

gives

$$A_R = k(\sin\Phi\ C - \cos\Phi\ S) \tag{4.13}$$

where

$$C \triangleq \int_{-\infty}^{s_1} \cos(\pi x^2/2)\ dx$$

$$S \triangleq \int_{-\infty}^{s_1} \sin(\pi x^2/2)\ dx$$

are the Fresnel integrals. The received power relation is found by averaging over one RF cycle:

$$\frac{P_R}{P_T} = \frac{G_T G_R \lambda^3 q^2 r_e^2}{32\pi^2 R_o^3} \left(\frac{C^2+S^2}{2}\right) \tag{4.14}$$

If initial trail radius and diffusion effects are included we obtain

$$\frac{P_R}{P_T} = \frac{G_T G_R \lambda^3 q^2 r_e^2}{32\pi^2 R_o^3} \left(\frac{C^2+S^2}{2}\right) \exp\left(\frac{-8\pi R_o^2}{\lambda^2}\right) \exp\left(\frac{-32\pi^2 D t}{\lambda^2}\right) \tag{4.15}$$

Since C and S both approach unity as $s_1 \to \infty$, equation (4.15) reduces to (4.8) for a fully developed trail. Figure 4.6(b) plots the relative returned power versus meteor position when diffusion is negligible.

5. GENERAL COLLECTION STATISTICS

5.1 *Echo Strength Distribution*

Accurate knowledge of the parameters K and c in equation (2.5) is essential for prediction of system echo rates when power levels are varied, thresholds adjusted, antenna gains changed, etc. The value of the exponent c has been previously estimated by many workers. For example, based on analysis of photographic meteors, *Hawkins and Upton* [1958] find $c = -1.34$ for meteors brighter than magnitude +4 (electron line densities in excess of $1.4 \times 10^{14} m^{-1}$). The most direct means of estimating c for radio meteors is to compare the echo rates observed with two different levels of transmitter power or minimum detectable signal level. High power-low power observations published by McKinley were analyzed by *Kaiser* [1953] to obtain $c = -1.0 \pm .02$ for a radio magnitude range of +9.5 to +10.5. A more recent estimate, *Kaiser* [1961], using Sheffield data suggests a small diurnal variation in c with a mean value of -1.17 for sporadic meteors of magnitude +8 to +11. Utilizing observations with different minimum detectable signal levels, *Weiss* [1961] found $c = -1.0$ for $10^{13} < q_{max} < 10^{14} m^{-1}$ and $c = -1.5$ for $q_{max} > 10^{15} m^{-1}$. The meteor-radar results from the high-power transmitter at Havana, Illinois gave $c = -1.01 \pm .05$ over the magnitude range +10 to + 13.

It seems clear that a change on the order of 0.5 occurs in going from the very strong visual meteors to the weak radio echoes. Since our radar system operates in the magnitude vicinity of +11, the correct value of c should be quite near -1.0. However, such a value represents the "true" echo strength distribution. Bias or discrimination on the part of collection software can cause an "apparent" exponent difference, and it is this "apparent" exponent which must be used for estimating echo rates for different transmitter powers and detection thresholds. To evaluate the "apparent"

exponent c, echoes collected with METP4, METP5, and METP6 software were grouped in 6 dB steps of peak Yagi video strength. Table 5.1 shows the groupings and the values of c and log K obtained by least squares fitting. A unique aspect of this analysis is that the substantial echo rate afforded by our high transmitter power allows us to utilize a single floor threshold for echo acceptance, and then effectively vary the minimum "detectable" signal level by considering only echoes with strengths above other user specified levels. Hence we achieve simultaneous looks at echo rate versus various thresholds and avoid problems which non-stationarity of the echo rate might cause. Six dB steps are used for convenience because if c = -1.0, then the cumulative number of echoes should double as the threshold (voltage) is lowered 6 dB (factor of 2). Our results indicate that as the collection software becomes more selective about accepting an echo, the "apparent" exponent c approaches the "true" exponent c. The reason we find c significantly different from -1.0 with METP4 and METP5 is because of the lowest strength bin. Our floor threshold in all cases is 32 dB, and the noise rejection technique of requiring echo strength to exceed that threshold for two widely spaced transmit pulses obviously discriminates against echoes in the 32-41 dB range because of diffusion decay. METP6 has the same noise rejection statements but many additional acceptance criteria which discriminate against the stronger returns as well (most such returns saturate the A/D converter at 54 dB during some part of their existence). The net result of the high end discrimination is to compensate for the low end discrimination and thus we find c near -1.0.

5.2 *Geophysical Noise*

Radial wind measurements from individual meteor echoes exhibit substantial differences, even when only echoes from approximately the same

Table 5.1

University of Illinois meteor radar flux law parameters.

Peak Yagi video in dB	Cumulative echoes	
METP4 Software		
53-up	3,098	c = -0.84 ± .009
47-53	6,309	log K = 5.75
41-47	11,194	
35-41	17,798	
METP5 Software		
53-up	2,068	c = -0.91 ± .014
47-53	4,661	log K = 5.77
41-47	8,674	
35-41	13,594	
METP6 Software		
53-up	1,318	c = -1.01 ± .022
47-53	3,640	log K = 5.86
41-47	7,204	
35-41	10,659	

time and height are compared. Table 5.2 illustrates the relative independence of velocity standard deviation from time and height. Also, the velocity histogram (as in Figure 2.25) is not appreciably changed in shape when the background wind, consisting of prevailing and harmonic components of 24, 12, and 8 hour period, is subtracted. Rather than narrowing the histogram width, background wind subtraction merely translates the histogram to approximately Gaussian zero mean form. This normality of wind velocity probability density agrees with the findings of *Pokrovskiy et al.* [1969]. The most meaningful measure of the significance of mean winds over short time intervals is thus the standard deviation of that mean which, for normal populations, is given by [*Baggaley and Wilkinson*, 1974]:

$$\sigma_{mean} = \sigma/\sqrt{N} \tag{5.1}$$

where

$$\sigma^2 = \left(\frac{N}{N-1}\right)S^2$$

S^2 = sample variance

N = number of samples

The velocity deviations responsible for the large observed S^2 values are the result of positional differences between the grouped echoes, short period-short wavelength internal gravity wave activity, turbulence, and wind shears. The first item is a controllable effect, but the latter three are geophysical in nature and their contributions to S^2 will be termed "geophysical noise". The contribution of instrumental wind measurement variance, mainly the result of sky noise contamination of the radar pulses reflected by meteor trails, is small compared to the observed variance S^2.

Table 5.2

Vertical wind structure at Urbana, January 18, 1975.

Height span	09:21 hours CST				10:05 hours CST			
	Number of echoes	Southward radial wind	Standard deviation	Standard deviation of mean	Number of echoes	Southward radial wind	Standard deviation	Standard deviation of mean
80-85 km	16	-10.16 ms^{-1}	24.52 ms^{-1}	6.13 ms^{-1}	20	0.21 ms^{-1}	15.72 ms^{-1}	3.51 ms^{-1}
81-86	24	-6.69	21.46	4.38	24	-3.75	18.17	3.71
82-87	28	-5.55	21.25	4.02	34	-2.48	19.02	3.26
83-88	39	-1.20	27.16	4.35	42	-3.88	18.97	2.93
84-89	44	1.37	23.53	3.55	49	-0.81	21.99	3.14
85-90	54	-0.54	21.95	2.99	56	-2.52	23.18	3.10
86-91	70	-5.90	21.92	2.62	70	-4.85	22.86	2.73
87-92	77	-8.84	22.38	2.55	84	-7.91	23.31	2.54
88-93	85	-14.49	19.90	2.16	88	-9.46	23.12	2.46
89-94	83	-16.65	19.00	2.09	80	-12.42	22.80	2.55
90-95	76	-18.86	19.23	2.21	69	-14.68	21.38	2.57
91-96	56	-20.37	20.33	2.72	52	-15.48	22.43	3.11
92-97	44	-19.22	21.12	3.18	34	-21.69	22.31	3.83

Based on groups of 50 echoes each we observe a mean horizontal wind standard deviation or geophysical noise level of about 30.7 ± 0.2 m s^{-1} (Figure 5.1). This compares well with similar determinations by *Baggaley and Wilkinson* [1974], *Barnes and Pazniokas* [1972], *Hook* [1970], and *Roper* [1966] but is somewhat higher than the mean 25 m s^{-1} found by *Greenhow and Neufeld* [1959]. The importance of the high data rate achieved with the University of Illinois meteor radar is driven home by an example taken from *Baggaley and Wilkinson* [1974]: if the mean population standard deviation of 31 m s^{-1} is taken and the mean magnitude of the wind velocity observed is 30 m s^{-1}, then to obtain the mean wind to within 6 percent at the 95 percent confidence limits would require 280 meteors.

To see if any temporal variations in geophysical noise occur, the data of Figure 5.1 have been segmented into hourly bins and plotted in Figure 5.2. When the accuracy of individual standard deviations is considered, typically ± 1 m s^{-1}, no significant variations are apparent. Utilizing the maximum and minimum variances gives an F ratio of 1.36 which is not significant at the 5% level and thus we accept homogeneity of the variances. The large increase around 13 hours is the result of very large wind shears present at that time only on August 21, 22, and is not really normal. The σ column for VM data in Table 5.3 is similar to Figure 5.2, except here results from all echoes in each 24 hour run have been analyzed on an hourly basis; the F ratio here is 1.45, also insignificant.

5.3 *Diurnal Parameter Variations*

The high echo rate of our meteor radar allows us to study not only the seasonal variation of collection parameters, but the daily changes of such parameters. We can do so without worry of non-stationarity of the data because we do not need to utilize superimposed epoch analysis. Table 5.3

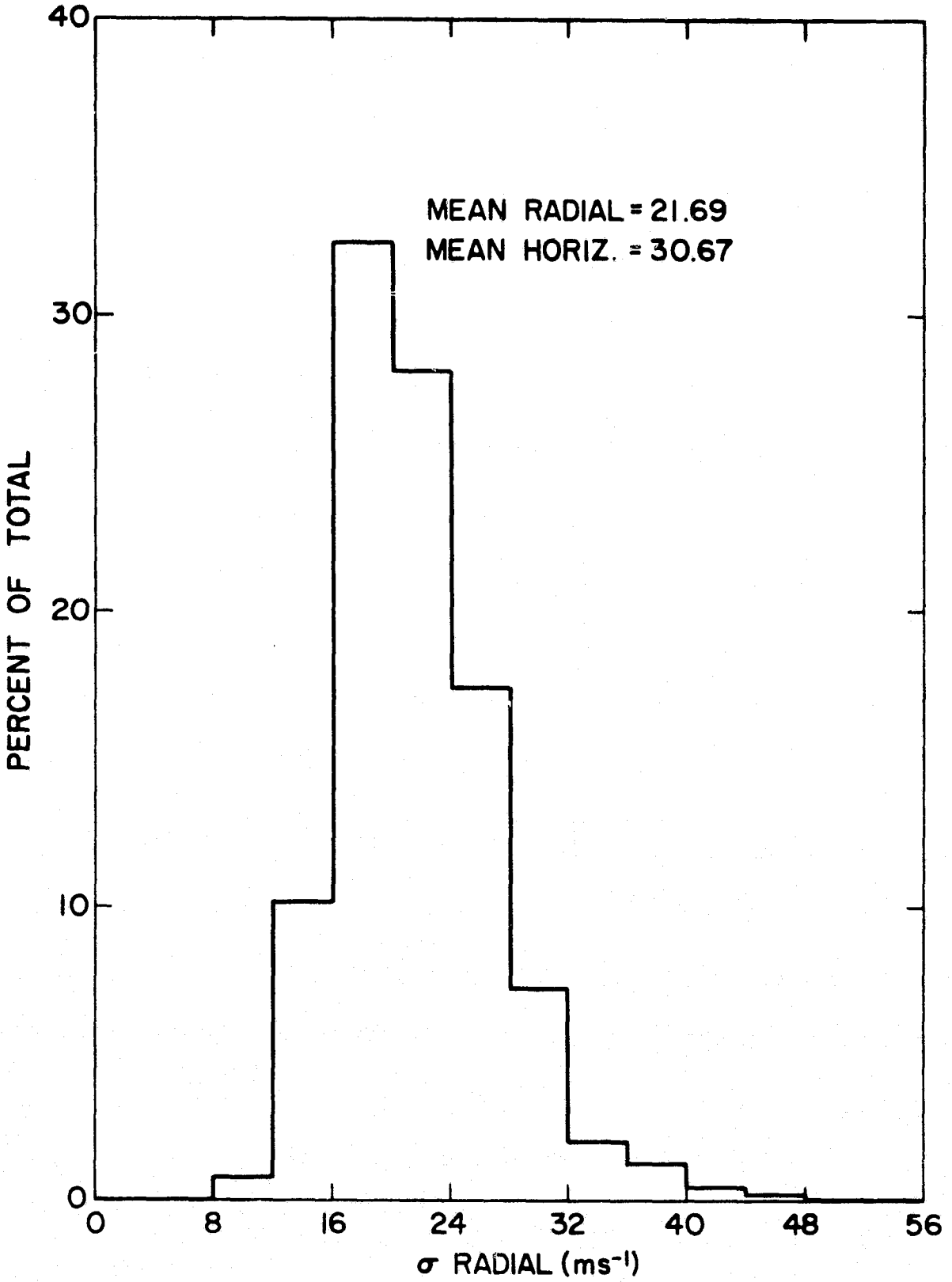

Figure 5.1 Histogram of wind standard deviation for groups of 50 threshold collected echoes.

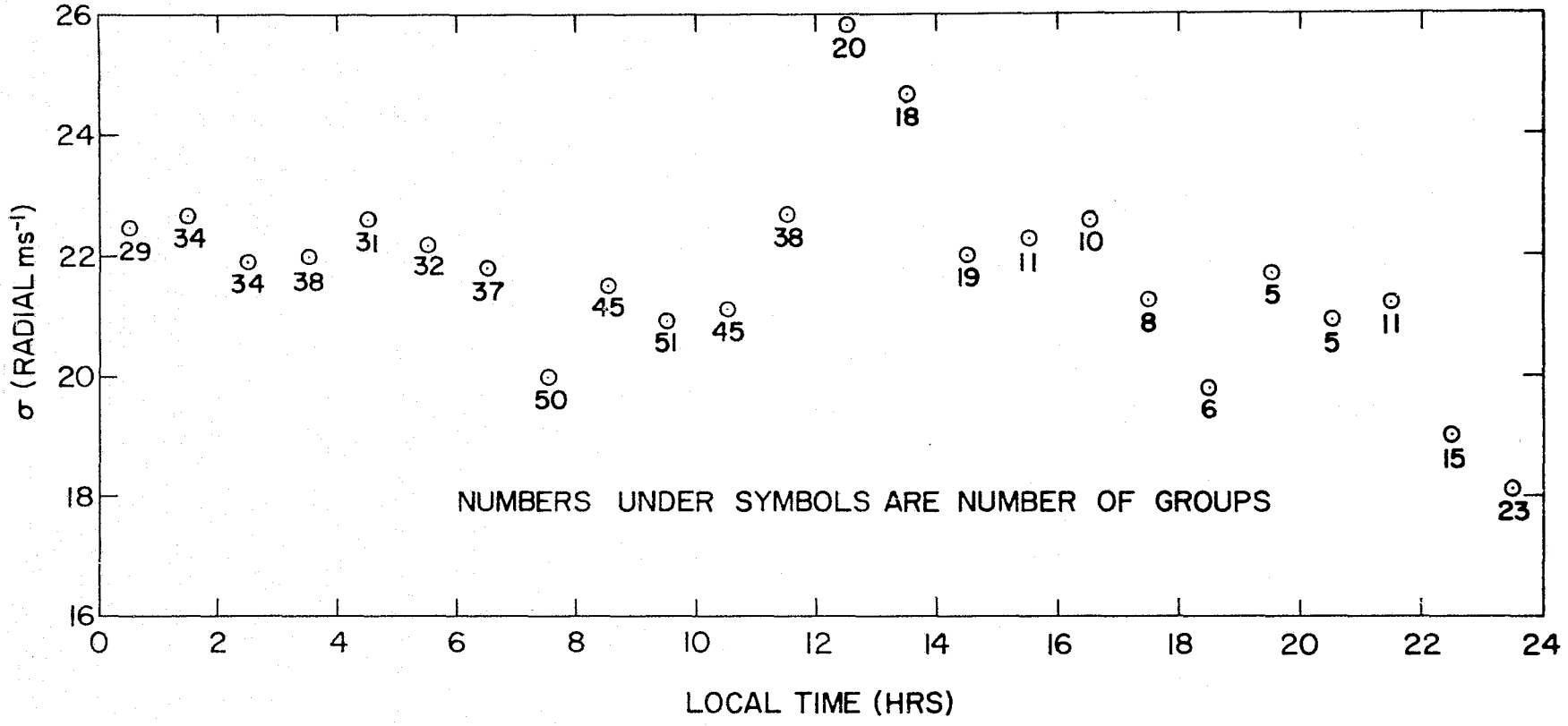

Figure 5.2 Wind standard deviation for groups of 50 echoes.

Table 5.3

Average meteor-radar collection statistics versus time of day, based on eight decay height runs, January-August, 1975.

Time Span (in local hrs)		Nr of echoes	DHT km	σ	σ_{mean}	VM ms^{-1}	σ	σ_{mean}	DMAXY dB	σ	σ_{mean}	VSD_1 ms^{-1}	σ	σ_{mean}	RB km	σ	σ_{mean}	RD km	σ	σ_{mean}
0	1	137	89.19	3.87	0.35	12.43	22.63	2.03	45.47	5.83	0.53	2.60	1.59	0.14	137.01	25.50	2.35	0.32	0.18	0.01
1	2	168	89.58	3.99	0.32	6.08	22.49	1.78	45.15	5.74	0.46	2.75	1.57	0.13	137.52	25.87	2.09	0.31	0.17	0.01
2	3	177	89.79	4.10	0.32	-0.33	21.46	1.64	45.59	5.87	0.46	2.68	1.60	0.13	138.93	26.47	2.07	0.32	0.18	0.01
3	4	190	90.02	4.18	0.31	-6.36	22.84	1.70	45.46	5.98	0.45	2.76	1.60	0.12	138.95	26.50	1.99	0.31	0.19	0.01
4	5	166	90.52	3.82	0.30	-11.75	23.81	1.93	46.00	5.78	0.46	2.64	1.53	0.12	140.92	26.73	2.14	0.30	0.18	0.01
5	6	168	90.77	4.33	0.34	-10.75	24.52	1.93	46.39	5.68	0.45	2.60	1.51	0.12	141.57	27.57	2.17	0.30	0.17	0.01
6	7	169	91.35	3.97	0.31	-6.31	24.85	1.94	46.75	5.54	0.43	2.58	1.47	0.12	144.13	27.55	2.15	0.29	0.19	0.01
7	8	164	91.44	3.86	0.31	-2.59	23.57	1.86	46.72	5.66	0.45	2.58	1.47	0.12	144.60	28.14	2.23	0.30	0.18	0.01
8	9	158	90.74	4.08	0.33	5.29	25.49	2.06	46.23	5.77	0.47	2.61	1.46	0.12	144.29	27.47	2.26	0.31	0.18	0.01
9	10	190	89.99	4.15	0.31	6.86	25.13	1.85	45.74	5.87	0.43	2.63	1.53	0.11	141.53	27.45	2.02	0.31	0.18	0.01
10	11	161	89.78	4.18	0.34	10.57	25.73	2.08	45.53	5.79	0.47	2.64	1.55	0.13	141.80	28.31	2.32	0.31	0.18	0.01
11	12	149	89.39	4.25	0.38	12.66	26.74	2.41	44.96	5.95	0.53	2.77	1.62	0.14	143.15	28.07	2.59	0.28	0.17	0.01
12	13	77	88.74	4.41	0.52	10.49	28.10	3.23	43.93	5.59	0.65	2.92	1.55	0.18	144.81	29.13	3.35	0.24	0.15	0.02
13	14	88	88.89	4.00	0.47	4.35	25.70	2.89	44.60	5.94	0.68	2.85	1.69	0.19	140.99	28.60	3.37	0.23	0.15	0.02
14	15	75	88.95	3.82	0.50	2.56	23.35	3.12	44.58	5.83	0.76	2.79	1.60	0.21	137.54	25.11	3.24	0.27	0.15	0.02
15	16	56	88.30	4.49	0.63	1.45	24.02	3.33	43.94	5.62	0.79	2.83	1.55	0.22	135.61	25.40	3.59	0.29	0.16	0.02
16	17	35	88.47	3.89	0.70	-2.38	22.90	4.04	43.66	5.84	1.06	2.97	1.68	0.31	133.49	24.63	4.41	0.29	0.16	0.03
17	18	24	88.39	3.84	0.81	-7.07	21.96	4.69	43.35	5.60	1.17	3.06	1.68	0.35	134.96	24.52	5.06	0.30	0.16	0.03
18	19	22	87.99	4.86	0.93	-4.49	20.93	4.44	43.85	5.71	1.21	2.80	1.58	0.33	130.31	23.36	4.82	0.29	0.16	0.03
19	20	21	88.14	4.25	0.94	0.05	20.83	4.48	43.38	5.10	1.12	2.84	1.35	0.30	133.80	20.96	4.52	0.32	0.16	0.04
20	21	30	88.20	4.05	0.77	5.50	19.41	3.60	44.79	5.71	1.06	2.68	1.61	0.30	131.49	23.38	4.37	0.31	0.16	0.03
21	22	53	88.49	3.86	0.57	5.97	19.69	2.87	44.22	5.83	0.86	2.81	1.60	0.23	133.38	24.75	3.57	0.33	0.16	0.03
22	23	77	88.74	3.94	0.52	11.45	19.64	2.50	44.32	5.64	0.75	2.78	1.51	0.20	134.38	24.56	3.16	0.33	0.17	0.02
23	24	113	89.19	3.74	0.38	10.98	19.55	2.08	44.70	5.77	0.59	2.78	1.59	0.16	136.03	25.32	2.67	0.34	0.17	0.02

DHT = height inferred from echo signal strength decay rate
VM = weighted southward radial wind
DMAXY = peak Yagi video level in dB (20 $\log_{10}$(A/D value))
VSD = instrumental error (standard deviation of mean)
RB = range at peak Yagi video occurrence
RD = range maximum minus range minimum while the Yagi video level exceeds the detection threshold

shows the hourly behavior of six parameters in terms of mean value, standard deviation, and standard deviation of the mean. Results are based on averages from eight METP5 type radar runs and the average number of echoes considered per hour is likewise listed (multiply by eight for total). Table 5.4 lists the results of harmonic analyses of the hourly variation of each of the six parameters. In all cases except VM, the diurnal period dominates. Semidiurnal domination of the winds is to be expected at midlatitudes (Chapter 6). The diurnal variations of DHT and DMAXY are in phase and in opposition to that of VSD. RB lags DHT and DMAXY somewhat.

To judge the significance of the harmonic fits we have tabulated the ratios of strongest harmonic amplitude to mean, second strongest harmonic amplitude to strongest harmonic amplitude, and weakest harmonic amplitude to second strongest harmonic amplitude. Also, we have constructed a mean correlation coefficient matrix (Table 5.5 (a)) and summary of correlation statistics (Table 5.5 (b)) based on the equation

$$r_{XY} \triangleq \frac{\sum_{i=1}^{N} 1/\sigma_i^2 \sum_{i=1}^{N} X_i Y_i/\sigma_i^2 - \sum_{i=1}^{N} X_i/\sigma_i^2 \sum_{i=1}^{N} Y_i/\sigma_i^2}{\left[\sum_{i=1}^{N} 1/\sigma_i^2 \sum_{i=1}^{N} X_i^2/\sigma_i^2 - \left(\sum_{i=1}^{N} X_i/\sigma_i^2\right)^2\right]^{1/2} \left[\sum_{i=1}^{N} 1/\sigma_i^2 \sum_{i=1}^{N} Y_i^2/\sigma_i^2 - \left(\sum_{i=1}^{N} Y_i/\sigma_i^2\right)^2\right]^{1/2}} \tag{5.2}$$

The strong positive correlations between DHT, DMAXY, and RB are consistent with their agreement in diurnal phase. A strong negative correlation between DMAXY and VSD agrees with the diurnal opposition in phase of VSD relative to DHT, DMAXY, and RB. It is with these four variables that the significance of

Table 5.4

Harmonic fits to hourly mean parameter data, eight radar runs, January-August, 1975.

Parameter	Mean	Dominant Harmonic			Next Strongest Harmonic			Magnitude Ratio of Strongest Harmonics	Magnitude Ratio of Weakest and next to Strongest Harmonic	Magnitude Ratio of Strongest Harmonic and Mean
		Period (hr)	Mag	Phase (hr)	Period (hr)	Mag	Phase (hr)			
DHT	89.39 km (.13)	24	1.36 km (.03)	- .43 (.04)	8	.27 km (.01)	2.80 (.02)	.07/1.36 = .20	.07/.27 = .26	1.36/89.39 = .015
VM	2.25 ms^{-1} (.67)	12	9.70 ms^{-1} (.45)	3.71 (.06)	24	2.10 ms^{-1} (.94)	-10.81 (1.37)	2.10/9.70 = .22	.36/2.10 = .17	9.70/2.25 = 4.31
DMAXY	44.97 dB (.17)	24	1.34 dB (.05)	- .04 (.10)	8	.22 dB (.0)	3.04 (.01)	.22/1.34 = .16	.14/.22 = .64	1.34/44.97 = .030
VSD	2.75 ms^{-1} (.05)	24	.14 ms^{-1} (.0)	11.42 (.09)	4.8	.06 ms^{-1} (.0)	-1.89 (.05)	.06/.14 = .43	.02/.06 = .33	.14/2.75 = .051
RB	138.37 km (.74)	24	5.70 km (.44)	- 2.25 (.02)	6	1.05 km (1.14)	.82 (1.04)	1.05/5.70 = .18	.62/1.05 = .59	5.70/138.37 = .041
RD	.30 km (.01)	24	.02 km (.0)	5.43 (.01)	12,8,6	.01 km (.0)	5.66, 1.20 -2.30 (.01)	.01/.02 = .50	indeterminate	.02/.30 = .067

Values in parentheses are error coefficients (one sigma)

Harmonic phase from the form A Sin ($\omega[t+\phi]$)

Table 5.5

(a) Mean correlation coefficient matrix for decay height runs.
(b) Correlation coefficient statistics for decay height runs.

(a)

x/y	DHT	VM	DMAXY	VSD	RB	RD
DHT	---	-.25	.79	-.30	.57	-.15
VM	-.33	---	-.25	.07	-.14	.05
DMAXY	.78	-.20	---	-.73	.42	.01
VSD	-.28	.03	-.64	---	-.11	-.31
RB	.58	-.09	.40	-.14	---	-.25
RD	-.04	-.06	.15	-.20	-.10	---

(b)

RELATION	MEAN	MAX	MIN	NR OF TIMES SIGNIFICANT
DHT-VM	-.28	.64	-.75	11/16
DHT-DMAXY*	.78	.88	.59	16/16
DHT-VSD	-.24	.27	-.60	8/16
DHT-RB*	.57	.76	.39	15/16
DHT-RD	-.10	.50	-.84	4/16
VM-DMAXY	-.22	.73	-.68	11/16
VM-VSD	.06	.46	-.61	3/16
VM-RB	-.12	.42	-.83	5/16
VM-RD	-.01	.33	-.68	2/16
DMAXY-VSD*	-.69	-.15	-.88	14/16
DMAXY-RB*	.41	.78	17	9/16
DMAXY-RD	.08	.64	-.67	5/16
VSD-RB	-.12	.32	-.56	3/16
VSD-RD	-.26	.04	-.80	6/16
RB-RD	-.15	.45	-.72	7/16

*Implies mean significant at the 5% level
20,745 echoes were considered. Based on 16 data values (x-y and y-x correlations of each run) to test for significance at 5% requires $|r| \geq 0.4$

the diurnal harmonic is most certain. Figure 5.3 shows that the variation is relatively unaffected by season and certainly not related to winds since, for example, Feb. 28-March 1 and July 14-15 were days dominated by $S_2(v)$ tides. Instead, the diurnal modulations must be the result of temporal variations of the meteors themselves. Note that possible variations in DHT are based on echoes from all heights. Since Table 5.6 shows that true echo height itself has a substantial diurnal variation, the pattern of DHT in Figure 5.3 is to be expected.

Weiss [1959] reported a diurnal variation of about 3 km in the heights of nonshower radio meteors with maximum height near midnight. Since the 3 km value was based on 6 hour averages, it is not surprising that the peak-to-peak variation of Table 5.6 is appreciably larger. Our time of maximum, near 6 AM local time, is intimately related to the cause of the height variation, namely, the diurnal variation in average meteor velocity (not wind velocity) caused by the earth's rotation (see Section 4.2). *McKinley* [1961], shows normalized distributions of observed radio velocity based on data from Ottawa and Jodrell Bank. The coincidence of detail may be somewhat fortuitous but the double hump is not. For stations at middle latitudes even a theoretically uniform radiant distribution will yield a double-humped velocity histogram as a result of apex-antapex effects and the radar response function. Higher mean meteor velocity implies higher mean echo height and thus Table 5.6 is explained. This is turn accounts for the DHT variation. The strong correlations between DMAXY, VSD, and DHT are to be expected because VSD is explicitly related inversely to echo strength in the collection software and software acceptance criteria create a bias against weak echoes at high altitudes where echo decay is most rapid. The diurnal variation of DMAXY is probably the result of software

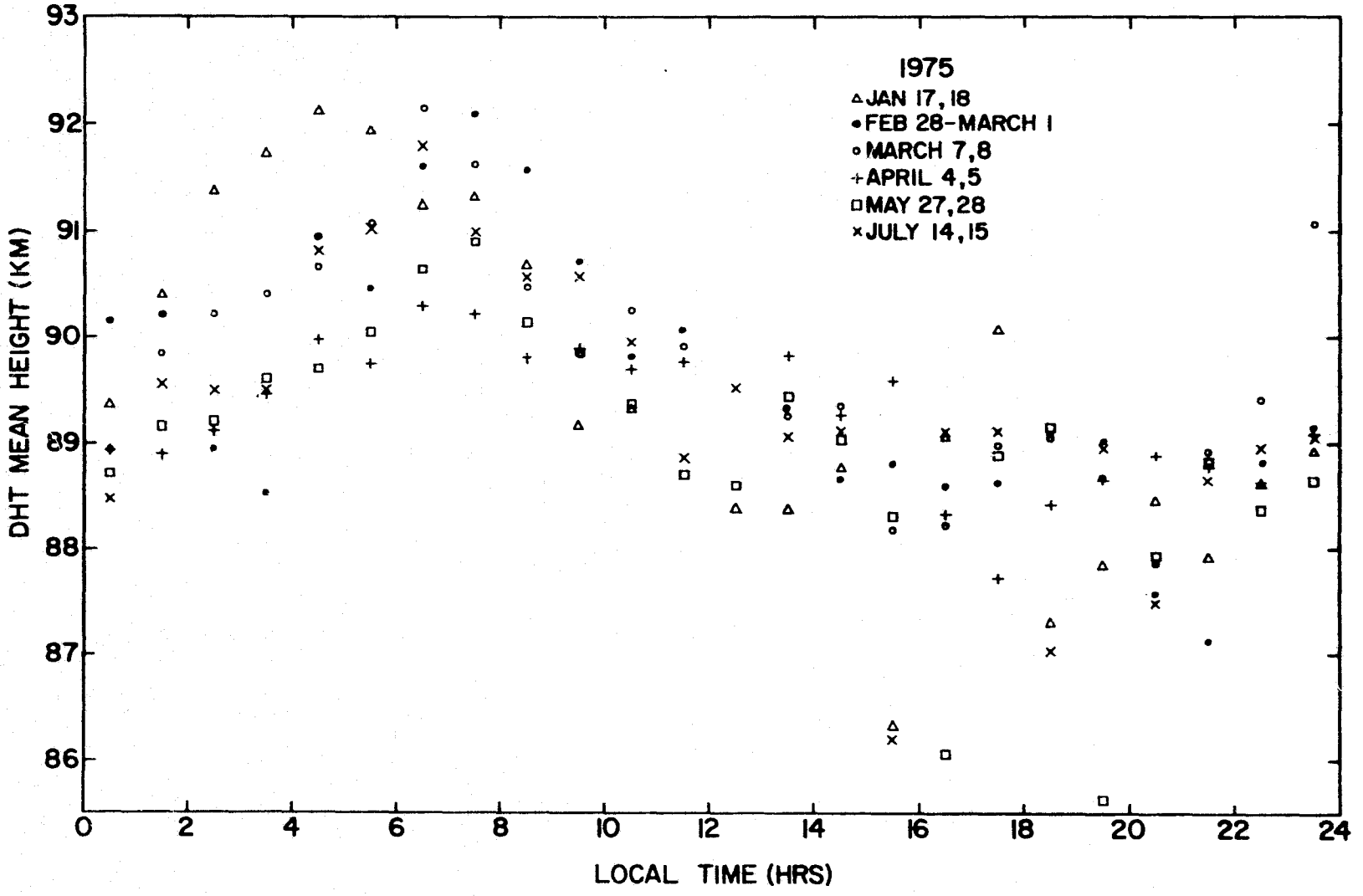

Figure 5.3 Mean decay height versus time of day for selected 24 hr runs.

Table 5.6

Hourly interferometer echo height.

Oct. 13-18, 1975 superimposed data 11,050 echoes

Time Span (local hrs)	Nr of Echoes	HTI (km)	σ	σ_{mean}
0 -1	577	91.81	14.78	0.62
1 -2	679	91.26	13.91	0.53
2 -3	721	91.91	13.51	0.50
3 -4	753	93.22	10.32	0.38
4 -5	610	95.00	13.09	0.53
5 -6	596	94.98	10.41	0.43
6 -7	647	96.26	11.35	0.45
7 -8	645	94.82	10.77	0.42
8 -9	726	94.71	11.31	0.42
9 -10	920	93.90	11.47	0.38
10 -11	753	92.57	13.12	0.48
11 -12	747	91.00	11.26	0.41
12 -13	379	88.52	12.25	0.63
13 -14	393	89.56	9.91	0.50
14 -15	321	89.32	10.19	0.57
15 -16	252	90.94	9.38	0.59
16 -17	177	89.13	11.74	0.88
17 -18	136	89.51	13.56	1.16
18 -19	97	88.23	8.65	0.88
19 -20	106	91.46	15.32	1.49
20 -21	156	90.90	9.80	0.78
21 -22	181	90.84	12.33	0.92
22 -23	246	91.45	12.21	0.78
23 -24	403	90.34	14.53	0.72

biases being made more evident by increases in data rate, a situation that, also being related to the earth's rotation, will occur in phase with the height variation. The variation though real is quite small, about 1.4 dB diurnal amplitude.

If the mean height changes by 8 km through the day and the average sporadic radiant does not, then a variation of 12.5 km in range will result, assuming an average elevation angle of 40°. Since the observed variation in RB is on the order of 20 km and lags height changes by about 2 hours it seems reasonable to conclude that both mean height variation and variation in radiant are important in controlling RB changes.

Data from eight stacked Yagi radar runs has been subjected to an analysis similar to that used on the METP5 radar data. Table 5.7 shows the hourly behavior of seven parameters. Because October and December 1975 and January 1976 runs have been superimposed, the total number of echoes is five times the listed hourly average. Also to permit partial reflection collection near noon, some hourly rates are depressed from the potential rate. Table 5.8 summarizes the harmonic analysis and shows again diurnal dominance of parameter variation, except for radial wind. HTI and log D which are closely related to DHT, have near zero phase, as does DMAXY. Also VSD is essentially out of phase with those parameters. All this is in agreement with METP5 findings. Now, however, RNG (essentially identical to RB) leads mean echo height rather than lagging it. This is to be expected because of annual changes in mean radiant position. The METP5 and METP6 data do not overlap in time and cover approximately one half year each. The yearly mean diurnal range perturbation thus is in phase with HTI, log D, DHT, and DMAXY.

The mean correlation coefficient matrix (Table 5.9(a)) and summary of correlation statistics (Table 5.9(b)) for METP6 runs, show log D, DMAXY, and

Table 5.7

Average meteor-radar collection statistics versus time of day, based on eight stacked Yagi runs, September 1975-January 1976

Time Span (in local hrs)	Nr of echoes	HTI km	σ	σ_{mean}	log D	σ	σ_{mean}	VM ms^{-1}	σ	σ_{mean}	DMAXY dB	σ	σ_{mean}	VSD ms^{-1}	σ	σ_{mean}	RNG km	σ	σ_{mean}	EL rad	σ	σ_{mean}
0 - 1	259	91.67	9.46	.61	4.41	.37	.03	4.40	26.69	1.81	44.38	5.89	.40	1.96	1.57	.12	146.02	31.36	2.12	.74	.24	.02
1 - 2	279	92.32	9.13	.58	4.45	.37	.02	0.51	25.55	1.71	44.26	6.02	.41	2.12	1.77	.13	147.54	31.66	2.11	.74	.23	.02
2 - 3	297	93.23	9.28	.57	4.46	.38	.02	-7.63	27.76	1.87	44.63	5.90	.39	2.01	1.63	.12	146.57	30.53	1.97	.75	.24	.02
3 - 4	321	94.28	8.65	.55	4.52	.38	.02	-10.71	26.82	1.61	45.09	6.06	.38	1.94	1.52	.10	146.63	29.65	1.85	.75	.24	.01
4 - 5	302	94.58	8.68	.52	4.55	.36	.02	-16.31	27.25	1.76	45.34	5.95	.38	1.92	1.50	.11	144.73	27.43	1.71	.76	.23	.01
5 - 6	300	95.74	8.21	.50	4.60	.37	.02	-13.23	29.05	1.88	45.86	5.81	.37	1.87	1.44	.10	146.07	29.13	1.81	.78	.25	.02
6 - 7	312	96.49	7.93	.47	4.61	.36	.02	-9.06	29.05	1.90	45.50	5.93	.37	2.03	1.60	.12	146.82	30.01	1.87	.78	.26	.02
7 - 8	319	96.16	8.14	.50	4.57	.37	.02	2.43	28.13	1.92	45.59	5.84	.38	1.92	1.66	.12	143.51	28.45	1.84	.80	.25	.0[illegible]
8 - 9	340	94.94	8.52	.49	4.52	.37	.02	2.44	26.08	1.63	44.96	6.11	.38	2.07	1.72	.12	138.91	27.63	1.70	.83	.27	.02
9 - 10	389	93.73	8.70	.49	4.45	.37	.02	-.53	26.62	1.59	44.29	5.94	.33	1.04	1.50	.10	136.38	27.41	1.58	.84	.27	.02
10 - 11	269	92.07	9.32	.88	4.41	.41	.05	-.88	25.49	2.49	43.90	5.81	.58	1.99	1.47	.18	136.22	27.95	3.21	.82	.25	.03
11 - 12	238	91.62	9.03	.76	4.37	.37	.03	.21	29.06	2.63	43.66	5.79	.50	2.10	1.75	.17	134.49	25.30	2.10	.82	.24	.02
12 - 13	159	90.71	9.23	.81	4.34	.39	.04	1.13	26.49	2.60	43.54	6.03	.55	2.10	1.74	.18	132.21	24.25	2.25	.84	.27	.03
13 - 14	169	91.26	8.19	.71	4.36	.36	.03	2.64	26.81	2.52	43.21	5.87	.53	2.20	1.81	.17	131.69	24.62	2.16	.85	.26	.02
14 - 15	137	90.25	8.99	.86	4.32	.38	.03	.80	29.66	2.24	43.06	5.85	.57	2.15	1.62	.17	133.42	26.51	2.55	.82	.27	.03
15 - 16	100	90.34	8.23	.93	4.31	.38	.04	-5.26	21.19	2.51	42.92	5.81	.66	2.34	1.86	.24	131.02	23.70	2.69	.83	.26	.04
16 - 17	69	89.59	8.94	1.22	4.26	.37	.05	-4.31	20.98	3.05	42.85	5.75	.82	2.14	1.52	.25	131.68	21.41	3.04	.80	.24	.04
17 - 18	53	89.98	8.84	1.30	4.25	.38	.06	-5.80	23.67	3.80	42.60	6.06	.97	2.15	1.59	.28	126.97	19.95	3.08	.85	.25	.04
18 - 19	47	90.55	8.73	1.36	4.26	.40	.06	1.17	24.50	3.86	42.52	5.69	.89	2.26	1.69	.28	131.37	25.68	4.11	.83	.28	.05
19 - 20	59	91.41	10.07	1.34	4.30	.40	.06	4.49	25.70	2.60	42.96	5.99	.82	2.35	1.86	.28	134.75	28.62	3.67	.82	.27	.04
20 - 21	86	91.32	8.66	.99	4.29	.40	.05	5.04	22.39	2.61	43.19	5.82	.69	2.21	1.91	.25	136.12	25.13	2.65	.80	.26	.03
21 - 22	111	90.84	9.22	.88	4.32	.40	.04	5.82	23.00	2.27	43.34	5.61	.55	2.16	1.64	.17	140.45	30.80	3.02	.77	.26	.02
22 - 23	146	91.16	8.53	.71	4.35	.37	.03	5.85	23.18	1.99	43.39	5.79	.49	2.11	1.62	.15	142.38	30.65	2.60	.76	.24	.02
23 - 24	192	91.19	8.97	.66	4.37	.35	.03	8.23	26.48	2.06	43.83	5.95	.46	2.08	1.89	.16	144.47	31.30	2.42	.75	.25	.02

HTI = interferometer echo height
log D = base ten logarithm of the ambipolar diffusion coefficient in $cm^2\ s^{-1}$
VM = weighted southward radial wind
DMAXY = peak Yagi video level in dB ($20 \log_{10}$(A/D value))
VSD = instrumental error (standard deviation of mean) in estimate of VM
RNG = mean range value of all determinations made after the Yagi video level peaks but before it has dropped below the detection threshold
EL = mean elevation angle

Table 5.8

Harmonic fits to hourly mean parameter data, eight stacked Yagi runs, September 1975-January 1976.

Parameter	Mean	Dominant Harmonic			Next Strongest Harmonic			Magnitude Ratio of Strongest Harmonics	Magnitude Ratio of Weakest and next to Strongest Harmonics	Magnitude Ratio of Strongest Harmonic and Mean
		Period (hr)	Mag	Phase (hr)	Period (hr)	Mag	Phase (hr)			
HTI	92.32 km (.20)	24	2.59 km (.07)	.09 (.07)	12	1.04	-3.81 (.13)	1.04/2.59 = .40	.03/1.04 = .029	2.59/92.32 = .028
log	4.40 (.01)	24	.15 (.0)	.27 (.0)	12	.03 (.0)	-2.82 (.01)	.03/.15 = .20	indeterminate	.15/4.40 = .034
VM	-1.24 ms^{-1} (.52)	12	6.67 ms^{-1} (.07)	4.57 (.03)	24	4.30 (.42)	11.21 (.26)	4.30/6.67 = .64	1.16/4.30 = .27	6.67/-1.24 =-5.38
DMAXY	43.95 dB (.13)	24	1.36 dB (.03)	.54 (.07)	12	.23 (.03)	-2.98 (.19)	.23/1.36 = .169	.03/.23 = .13	1.36/43.95 = .030
VSD	2.09 ms^{-1} (.04)	24	.15 ms^{-1} (.0)	-11.28 (.07)	6	.04 (.0)	-.64 (.01)	.04/.15 = .267	.02/.04 = .50	.15/2.09 = .072
RNG	138.66 km (.55)	24	8.74 km (.73)	2.69 (.31)	8	1.48 (.25)	3.42 (.19)	1.48/8.74 = .169	.37/1.48 = .25	8.74/138.66 = .063
EL	0.80r (.01)	24	.05r (.0)	-7.64 (.01)	12	.01 (.0)	-4.75 (.01)	.01/.05 = .20	.01/.01 = 1.0	.05/.80 = .062

Table 5.9

(a) Correlation coefficient matrix for stacked Yagi runs.
(b) Correlation coefficient statistics for stacked Yagi runs.

(a)

x/y	HTI	Log D	VM	DMAXY	VSD	RNG	EL
HTI	---	.78	-.27	.77	-.45	.41	.10
Log D	.78	---	-.33	.87	-.50	.54	-.26
VM	-.32	-.44	---	-.38	.21	-.26	.26
DMAXY	.79	.90	-.33	---	-.68	.62	-.22
VSD	-.40	-.43	.26	-.67	---	-.33	.14
RNG	.39	.60	-.21	.57	-.32	---	-.82
EL	.18	-.34	.21	-.14	.08	-.63	---

(b)

RELATION	MEAN	MAX	MIN
HTI-Log D*	.78	.90	.52
HTI-VM	-.27	.49	-.78
HTI-DMAXY*	.78	.92	.61
HTI-VSD	-.42	-.09	-.66
HTI-RNG	.40	.69	-.08
HTI-EL	.14	.52	-.46
Log D-VM	-.38	.18	-.88
Log D-DMAXY*	.88	.94	.78
Log D-VSD	-.46	-.02	-.79
Log D-RNG*	.57	.85	.27
Log D-EL	-.30	-.10	-.59
VM-DMAXY	-.35	.15	-.74
VM-VSD	.23	.48	-.08
VM-RNG	-.23	.13	-.63
VM-EL	.23	.43	.06
DMAXY-VSD*	-.67	-.44	-.88
DMAXY-RNG*	.59	.83	.31
DMAXY-EL	-.18	-.03	-.62
VSD-RNG	-.32	.22	-.79
VSD-EL	.11	.41	-.27
RNG-EL*	-.72	-.04	-.93

*implies mean significant at the 5% level.
Require $|r| \geq .49$ for significance at 5%: x-y and y-x combined (10 pts. each).

RNG with strong positive correlations. This is analogous to the correlation of DHT, DMAXY, and RB in the METP5 case; also VSD is again negatively correlated to DMAXY. We find HTI correlated with DMAXY and log D as expected, but the correlation to RNG is not so strong. The negative range-elevation angle correlation is expected due to the thinness of the meteor zone.

5.4 *Annual Parameter Variations*

Table 5.10 summarizes average parameter values for 13 periods spanning one year, from January 1975 to January 1976. Because of the small number of periods, only a single year's coverage, and changes in collection software, results of harmonic analysis would not be very credible. However, we can note that with the exception of VM, any real annual parameter variation is no more significant than the diurnal variation always present. We point out that the drop in VSD when using METP6 software is the result of more velocity calculations being available on the average per echo. The fact that mean echo radiant does indeed control the mean range is clear on the July 30-31, 1975 run, which was influenced by the Delta Aquarid shower. The differences between columns 1 and 2 serve as indications of the strength of each diurnal parameter perturbation. The general trend of southward summer winds and northward winter winds has been observed at numerous meteor-radar installations (see, for example, *Clark* [1975]).

Table 5.10

Summary of average parameter values versus time of year.

METP 4

Software Parameter	Jan. 17 Jan. 18		Feb. 28 March 1		March 7 March 8	
	1	2	1	2	1	2
DHT(km)	90.16	89.51	90.21	89.66	90.18	89.79
VM(ms^{-1})	-10.96	-6.56	1.10	-.67	0.74	2.26
DMAXY(dB)	45.64	44.90	46.07	45.69	46.22	45.92
VSD(ms^{-1})	2.83	2.92	2.64	2.60	2.54	2.55
RB (km)	139.59	136.84	137.03	135.36	135.94	135.81
RD (km)	0.23	0.23	0.36	0.38	0.48	0.50

METP 5

Software Parameter	April 4 April 5		May 27 May 28		July 14 July 15		July 30 July 31		Aug. 21 Aug. 22	
	1	2	1	2	1	2	1	2	1	2
DHT(km)	89.48	89.26	89.47	88.97	89.77	89.33	89.57	89.04	90.10	89.64
VM(ms^{-1})	1.00	2.57	3.00	0.86	5.06	5.36	0.97	12.80	7.30	-.08
DMAXY(dB)	44.90	44.62	44.88	44.53	45.29	44.68	45.58	44.92	45.32	44.79
VSD(ms^{-1})	2.65	2.67	2.98	3.02	2.69	2.80	2.64	2.72	2.60	2.65
RB (km)	137.87	136.57	144.21	140.43	142.16	141.88	137.86	137.82	142.73	141.21
RD (km)	0.31	0.31	0.26	0.24	0.29	0.28	0.30	0.27	0.25	0.24

METP 6

Software Parameter	Sept. 13 Sept. 14		Oct. 13 Oct. 17		Dec. 4-6 12-13	Jan. 14-16 1976	Jan. 21 Jan. 23
	1	2	1	2	1	1	1
HTI (km)	92.49	92.53	92.52	91.74	93.68	94.76	92.64
DHT (km)	89.61	89.38					
log D	4.46	4.44	4.35	4.28	4.46	4.52	4.50
VM(ms^{-1})	2.34	4.82	-2.82	-1.00	-14.31	-6.12	5.61
DMAXY(dB)	43.78	43.61	44.24	43.88	44.11	45.05	45.07
VSD (ms^{-1})	2.14	2.16	2.32	2.40	2.21	1.89	1.94
RNG (km)	141.09	139.45	142.60	140.75	141.70	140.77	141.35
EL (rad)	0.76	0.76			0.79	0.82	0.76

1 = all data (biased toward times of maximum data rate)

2 = average of 24 hourly means

6. TIDES IN THE UPPER ATMOSPHERE

6.1 *Review of Atmospheric Tidal Theory*

An atmospheric tide is defined as a global scale oscillation of the atmosphere with a period that is an integral fraction of a lunar or solar day. The global scale required of a tide rules out sea breeze phenomena, etc. In classical tidal theory the following approximations are generally used [*Chapman and Lindzen*, 1970](valid to heights of about 100 km):

(1) The motion of the atmosphere can be described by the equations for a compressible gas. These equations are most conveniently expressed in spherical coordinates with a frame of reference rotating with the earth.

(2) The atmosphere is always in local thermodynamic equilibrium.

(3) The atmosphere can be treated as a perfect gas of constant composition,

$$p = \rho RT$$

where p is pressure and R is the gas constant.

(4) The atmosphere can be regarded as a geometrically thin fluid layer of small thickness with respect to the earth's radius a.

(5) The atmosphere is taken to be in hydrostatic equilibrium,

$$\frac{1}{\rho}\frac{dp}{dz} = -g$$

where gravitational acceleration g is assumed constant.

(6) The earth's ellipticity is ignored.

(7) The earth's surface topography is ignored.

(8) Dissipative processes such as molecular and turbulent viscosity and conductivity, ion drag, and infrared radiative transfer are ignored.

(9) Tidal fields are considered as linearizable perturbations about some basic state.

(10) Since even linear equations are intractible if the coefficients are too complicated (in the sense of leading to nonseparable partial differential equations), it is assumed that the basic tidal fields are steady (T_0, p_0, and ρ_0 are independent of latitude and longitude) and the basic flow is zero.

Utilizing the preceding assumptions and following normal meteorological convention, the following five equations result (*Dickinson and Geller* [1968]):

$$\frac{\partial u}{\partial t} - (2\Omega\sin\phi)v + \frac{1}{a\cos\phi}\frac{\partial \Phi'}{\partial \lambda} = 0 \tag{6.1}$$

$$\frac{\partial v}{\partial t} + (2\Omega\sin\phi)u + \frac{1}{a}\frac{\partial \Phi'}{\partial \phi} = 0 \tag{6.2}$$

$$\frac{1}{a\cos\phi}\frac{\partial u}{\partial \lambda} + \frac{1}{a\cos\phi}\frac{\partial}{\partial \phi}(v\cos\phi) + \frac{\partial w}{\partial z} - w = 0 \tag{6.3}$$

$$\frac{\partial T'}{\partial t} + w\left(\frac{d\overline{T}}{dz} + \kappa\overline{T}\right) = J/c_p \tag{6.4}$$

$$\frac{\partial \Phi'}{\partial z} - RT' = \frac{\partial \Phi^{(\tau)}}{\partial z} \simeq 0 \tag{6.5}$$

where u = eastward velocity

v = northward velocity

λ = longitude

ϕ = latitude

t = Greenwich mean time

$\kappa = R/c_p$

R = gas constant

c_p = specific heat at constant pressure

a = earth's radius

Ω = earth's rotation frequency

J = rate of solar heating per unit mass

$z = ln\ (p_o/p)$

p, p_o = pressure and surface pressure in the undisturbed state

$w = dz/dt$

$\Phi' = gh' + \Phi(\tau)$ = sum of the tidal potential and perturbation geopotential

$\overline{T}$, T' = mean reference and perturbation temperatures.

Assuming that all perturbations are proportional to exp $[im\lambda + i\nu t]$ (m = zonal wavenumber, ν = tidal frequency) and defining $\mu \triangleq \sin\phi$ leads to

$$i\nu u - 2\Omega\mu v + \frac{im\Phi'}{a(1-\mu^2)^{1/2}} = 0 \tag{6.6}$$

$$i\nu v - 2\Omega\mu u + \frac{(1-\mu^2)^{1/2}}{a}\ \frac{\partial\Phi'}{\partial\mu} = 0 \tag{6.7}$$

$$\frac{imu}{a(1-\mu^2)^{1/2}} + \frac{1}{a}\frac{\partial}{\partial\mu}\left[v(1-\mu^2)^{1/2}\right] + \frac{\partial w}{\partial z} - w = 0 \tag{6.8}$$

$$i\nu T' + w\left(\frac{d\overline{T}}{dz} + \kappa\overline{T}\right) = J/c_p \tag{6.9}$$

$$\frac{\partial\Phi'}{\partial z} = RT' \tag{6.10}$$

Solving the equation pair (6.6) and (6.7) for u and v gives

$$u = \frac{1}{\nu^2 - (2\Omega\mu)^2}\left[\frac{\nu m\Phi'}{a(1-\mu^2)^{1/2}} - \frac{2\Omega\mu(1-\mu^2)^{1/2}}{a}\ \frac{\partial\Phi'}{\partial\mu}\right] \tag{6.11}$$

$$v = \frac{1}{\nu^2 - (2\Omega\mu)^2}\left[-\frac{(2\Omega\mu)im\Phi'}{a(1-\mu^2)^{1/2}} + \frac{i\nu(1-\mu^2)^{1/2}}{a}\ \frac{\partial\Phi'}{\partial\mu}\right] \tag{6.12}$$

Substituting (6.11) and (6.12) into (6.8) yields

C.3

$$i\nu F(\Phi') + (2\Omega a)^2\left(\frac{\partial w}{\partial z} - w\right) = 0 \tag{6.13}$$

where the operator is defined by

$$F \triangleq \frac{\partial}{\partial \mu}\,\frac{(1-\mu^2)}{(\tilde{\nu}^2-\mu^2)}\,\frac{\partial}{\partial \mu} - \frac{1}{(\tilde{\nu}^2-\mu^2)}\left[\frac{m}{\tilde{\nu}}\left(\frac{\tilde{\nu}^2+\mu^2}{\tilde{\nu}^2-\mu^2} + \frac{m^2}{1-\mu^2}\right)\right]$$

with $\tilde{\nu} \triangleq \nu/2\Omega$.

Combining (6.9) and (6.10) leads to

$$i\nu\,\frac{\partial \Phi'}{\partial z} + (2\Omega a)^2\, Sw = \kappa J \tag{6.14}$$

where the spherically averaged nondimensional static stability parameter is

$$S \triangleq \frac{g}{(2\Omega a)^2}\left(\kappa \overline{H} + \frac{d\overline{H}}{dz}\right)$$

with

$$\overline{H} = R\overline{T}/g$$

If we expand all dependent variables and J in (6.13) and (6.14) in terms of *Hough* [1898] functions, which are solutions to the eigenvalue problem

$$F[X_n^{\nu,m}] + \gamma_n^{\nu,m} X_n^{\nu,m} = 0$$

we obtain

$$i\nu\,\frac{d\Phi'^{\nu,m}_n}{dz} + (2\Omega a)^2\, Sw_n^{\nu,m} = \kappa J_n^{\nu,m} \tag{6.15}$$

and

$$-i\nu\gamma_n^{\nu,m}\,\Phi'^{\nu,m}_n + (2\Omega a)^2\left(\frac{dw_n^{\nu,m}}{dz} - w_n^{\nu,m}\right) = 0 \tag{6.16}$$

These equations can be combined into a differential equation in $w_u^{\nu,m}$:

$$\frac{d^2 w_n^{\nu,m}}{dz^2} - \frac{dw_n^{\nu,m}}{dz} + \gamma_n^{\nu,m} w_n^{\nu,m} S = \frac{\gamma_n^{\nu,m}\kappa J_n^{\nu,m}}{(2\Omega a)^2} \tag{6.17}$$

To put (6.17) into the canonical form of a Helmholtz equation we substitute

$w_u^{\nu,m} = e^{(z/2)}\ Y_n^{\nu,m}$, giving

$$\frac{d^2 Y_n^{\nu,m}}{dz^2} + \left[-\frac{1}{4} + \gamma_n^{\nu,m} S\right] Y_n^{\nu,m} = \frac{\gamma_n^{\nu,m} \kappa J_n^{\nu,m} e^{-z/2}}{(2\Omega a)^2} \tag{6.18}$$

Equation (6.18) is known as the "vertical structure equation". It is homogeneous for the gravitationally forced lunar tides but not the thermally forced solar tides. As a lower boundary condition, we assume zero vertical motion at $z = 0$ (generally taken to be $p_o = 1000$ mb). This leads to the first order differential equation

$$\frac{dY_n^{\nu,m}}{dz} + \left[\frac{\overline{H}}{D_n^{\nu,m}} - \frac{1}{2}\right] Y_n^{\nu,m} = \frac{i\nu\Omega_n^{\nu,m}}{gD_n^{\nu,m}} \qquad \text{at } z = 0 \tag{6.19}$$

where "equivalent depth" is defined as

$$D_n^{\nu,m} \triangleq (2\Omega a)^2/g\ \gamma_n^{\nu,m}$$

and $\Omega_n^{\nu,m}$ represents the Hough expansion coefficients of $\Phi^{(\tau)}$. For an upper boundary condition we require decreasing exponential solutions or waves which propagate energy outward for $z \to \infty$. The latter excludes solutions of the form $\exp[+(\ )z]$ while the former dictates a downward phase velocity, i.e. a solution of the form $\exp[+i(\ )z]$.

Solar heating for (6.18) can be modeled by using

$$J = c_p \frac{\partial \tau}{\partial t} = i\nu c_p \tau \tag{6.20}$$

where $\tau = \sum_{a=1}^{G} \sum_{n=1}^{\infty} \tau_a(z,\phi)\ e^{int'}$

and G = number of atmospheric constituents considered as solar radiation absorbers

t' = local time.

To make (6.20) tractable we consider each τ_a separable in z and ϕ, i.e.,

$$\tau_a^{\nu,m}(z,\phi) = f_a^{\nu,m}(z)\, g_a^{\nu,m}(\phi) \tag{6.21}$$

From tables of the Hough function Θ developed by *Flattery* [1967] and vertical grid latitudinal distributions of thermal excitation due to water vapor (H_2O) and ozone (O_3) [*Lindzen*, 1968] we have the semidiurnal expansion

$$g_{O_3}^{2\Omega,2} = 0.249\ \Theta_2^{2\Omega,2} + 0.0645\ \Theta_4^{2\Omega,2} + 0.0365\ \Theta_6^{2\Omega,2} + \ldots$$

$$g_{H_2O}^{2\Omega,2} = 0.0307\ \Theta_2^{2\Omega,2} + 0.00796\ \Theta_4^{2\Omega,2} + 0.00447\ \Theta_6^{2\Omega,2} + \ldots$$

and the diurnal expansion

$$g_{O_3}^{\Omega,1} = 1.6308\ \Theta_{-2}^{\Omega,1} - 0.5128\ \Theta_{-4}^{\Omega,1} + \ldots$$

$$+ 0.5447\ \Theta_1^{\Omega,1} - 0.1411\ \Theta_3^{\Omega,1} + 0.0723\ \Theta_5^{\Omega,1} + \ldots$$

$$g_{H_2O}^{\Omega,1} = 0.157\ \Theta_{-2}^{\Omega,1} - 0.055\ \Theta_{-4}^{\Omega,1} + \ldots$$

$$+ 0.062\ \Theta_1^{\Omega,1} - 0.016\ \Theta_3^{\Omega,1} + 0.008\ \Theta_5^{\Omega,1} + \ldots$$

where all g values are in units of K and only symmetric Hough modes have been considered. The (2,2) mode clearly receives the bulk of the semidiurnal solar forcing, but in the diurnal case no single mode is dominant. In the isothermal case, $S \cong 0.025$, we find the following eigenvalues and vertical wavelengths (e-folding heights for evanescent modes):

Diurnal		Semidiurnal	
$\gamma_1^{\Omega,1} = 127.526$	$\lambda_z \cong 26$ km	$\gamma_2^{2\Omega,2} = 11.2209$	$\lambda_z \cong 200$ km

$\lambda_3^{\Omega,1} = 732.333$ 11 km $\quad \lambda_4^{2\Omega,2} = 41.7604$ 50 km

$\lambda_5^{\Omega,1} = 1820.79$ 7 km $\quad \lambda_6^{2\Omega,2} = 92.1089$ 31 km

$\lambda_{-2}^{\Omega,1} = -7.1804\ L_z \cong 11$ km

$\lambda_{-4}^{\Omega,1} = -48.558$ 6 km

A recent paper by *Lindzen and Hong* [1974] has extended tidal theory to allow for the effects of mean zonal winds and meridional temperature gradients. They find the main result of these effects on the solar semidiurnal tide is generation of substantial mode coupling between the main semidiurnal mode ($\Theta_2^{2\Omega,2}$) and higher order modes, thus enhancing the latter so that they might dominate the semidiurnal wind oscillations at meteor heights.

6.2 *Tides - Comparisons with Theory and Previous Meteor-Radar Observations*

6.2.1 *Early observations.* It is in the observation of tidal oscillations that the meteor radar technique has proven most successful. Actually it is more precise to say that single-station wind observations yield a set of harmonics which should be termed "daily variations" rather than "tides", since the latter are global phenomenon. The first observations of daily variations via meteor radar were made by *Greenhow and Neufeld* [1961] at Jodrell Bank, England (lat. 53° N) and by *Elford* [1959] at Adelaide, Australia (lat. 35° S). These observations generally dealt with average winds over the meteor region, i.e., roughly 80-100 km in altitude, centered near 90 km. A dominant semidiurnal tide of 13 m s^{-1}, compared with just 5 m s^{-1} for the diurnal tide, was found over Jodrell Bank. At Adelaide, however, the dominant tide was diurnal at about 20 m s^{-1} and the semidiurnal amplitude averaged 10 m s^{-1}. These apparently conflicting results were shown by *Lindzen* [1968] to be explained by the latitudinal structure of the relevant Hough functions and thus the results remained consistent with

classical tidal theory. Many of these early observations have been summarized and compared with classical theory in *Chapman and Lindzen* [1970].

6.2.2 *Seasonal tidal behavior at Adelaide.* Some very long series of records are now available which permit study of the seasonal variations of the tides. Such long term averages are necessary for meaningful comparisons between observations and theory because the latter inevitably use seasonally averaged values for basic states and forcing functions. Probably the most consistent and continuous data has been collected by *Elford* [1974] at Adelaide. This data demonstrates the year to year repeatability of seasonal amplitude and phase of the semidiurnal tide based on 8 years of measurements. The phase plots appear to be combinations of nearly constant phase versus height together with sharp phase reversals. Summer behavior suggests the presence of a single propagating mode whose wavelength is in excess of 100 km ($\Theta_2^{2\Omega,2}$ dominance) while winter behavior shows a deep node near 82 km with associated phase jumps. The winter behavior can thus be interpreted in terms of a standing wave, arising perhaps from substantial reflection of a dominant upward propagating mode or superposition of either upward propagating modes forced in different regions or an upward propagating mode and a downward propagating mode forced above the meteor region. Month-to-month study of the semidiurnal tide shows rapid changes from one phase pattern to another occur in March and October.

The tidal structure of the 24-hour wind component as a function of height and season is also discussed by *Elford* [1974]. Yearly repeatability of both amplitude and phase patterns is again evident. Strongest diurnal winds appear in autumn and phase versus height values suggest a progressive wave with vertical wavelength near 120 km. The phase generally does advance with height with maximum rates of change occurring at the lower

heights. In summer the tide appears evanescent above approximately 87 km, prompting the suggestion that summer behavior is the result of progressive and evanescent mode superposition. The latter is suspected of being driven by local heating above the meteor region, thus explaining its dominance at higher altitudes. The results for winter and spring are explained in terms of a combination of standing and progressive waves throughout the meteor region. Zonal components undergo phase shifts of 8-12 hours centered near 92 km in winter and 90 km in spring. Associated with these phase shifts are deep nulls in tidal amplitude. However, the meridional winds do not show such standing wave evidences, and are instead dominated by progressive waves.

6.2.3 *Seasonal tidal behavior at Garchy.* All-sky observations at Adelaide were made on a monthly basis with 4 to 20 days of continuous operation, averaging 250 usable echoes per day. The tidal parameters were extracted using the least squares method of *Groves* [1959] with a cubic polynomial for height structure. A substantial improvement in resolving height structure has been achoived by the meteor radar at Garchy, France [*Spizzichino et al.* 1965]. Here only the zonal wind is probed, though *McAvaney* [1970] states that as of April 1970 the meridional component is also determined. However, in all the Garchy materials which we discuss, only the zonal component is involved. Individual echoes can be defined in height to within ± 1 km. The higher useful echo rate (500-1000 echoes-day^{-1}) allows one to interpolate zonal wind values uniformly in time and height. Such a matrix can then be Fourier analyzed to extract the tides and possibly even distinguish various tidal modes which may be present. Applications of both the Groves analysis and the Garchy analysis to the same set of data has shown that both yield tidal amplitude and phase results which agree,

within the stated error intervals.

In their first series of experimental results [*Spizzichino*, 1969], based on 10 short duration campaigns of 2-3 days each, the phase of the semidiurnal tide increased linearly with height at less than 4 deg km^{-1} in general. Such behavior would be explained by dominance of the $\Theta_2^{2\Omega,2}$ fundamental mode. However, exceptions were noted: in Feb. 1966, the vertical wavelength was only 40 km, corresponding perhaps to $\Theta_2^{2\Omega,4}$ dominance, and in March and April of that year the phase did not increase regularly with height, suggesting the presence of several superimposed modes.

These early Garchy experiments of 1965-1966 also confirmed observations regarding the diurnal tide made even earlier by workers at Jodrell Bank [*Greenhow and Neufeld*, 1961] and Adelaide [*Elford*, 1959], namely that the amplitude and phase of the diurnal tide vary irregularly from day to day. In general the oscillation propagated with downward directed phase velocity and was of short vertical wavelength (20-30 km), agreeing with the hypothesis of $\Theta_1^{\Omega,1}$ mode dominance. In summer, however, an evanescent character was observed with good phase stability.

A second series of experiments, based on six campaigns of 5-10 days each, was described by *Fellous et al.* [1974]. Cases of disagreement with the hypothesis of $\Theta_2^{2\Omega,2}$ dominance were seen. In Jan. - Feb. 1970 the phase slope exceeded 15 deg-km^{-1} (vertical wavelength of 20 km) while in March and early April 1970 the wavelength varied between 20 and 40 km. Such wavelengths correspond to higher order modes and suggest a different physical origin for the semidiurnal tide from January to April. In a few cases significantly non-linear phase variations with altitude were seen. For example, in Jan. 27-29, 1970 a phase rotation of 180° was noted near 88 km, suggesting a standing wave pattern of brief lifetime. June 9-11, 1970

exhibited periodicity in amplitude and phase versus height suggesting a weaker standing wave system. Lastly, April 21-23, 1970 exhibited an extremum in phase versus height suggesting superposition of two different modes.

The 1970-1971 long duration experiments confirmed the presence of short vertical wavelength diurnal tides in March-April and possibly September, though less clearly then. In addition, June-July data confirmed the presence of evanescent modes in summer. Contrary to earlier results though, the tidal phase was not stable on a day to day basis in summer. In addition, evanescent modes were seen on occasion in winter and in 10-20 percent of the cases non-linear phase variation, indicative of mode interactions or reflections, were noted.

In summarizing their long term observations *Fellous et al.* [1974] stress two aspects as most important:

(1) the finding of tidal behavior unexpected in terms of the hypothesis of prevailing $\Theta_1^{\Omega,1}$ and $\Theta_2^{2\Omega,2}$ modes and (2) identification of the presence of superposed waves. The anomalous modes item (1) refers to are short wavelength semidiurnal modes ($\Theta_2^{2\Omega,n}$, $n \geq 4$) and evanescent diurnal modes ($\Theta_1^{\Omega,-n}$), both of which are known to be excited in high latitude zones. With that in mind, it is interesting to note that both winter periods in which diurnal and semidiurnal anomalies were present coincided with stratospheric warmings. Item (2) refers to two situations. The first is interpreted in terms of a reflected wave superimposed on the direct wave, both waves of near equal amplitude (approximately total reflection). The second is interpreted in terms of superposition of two distinct tidal modes since phase extrema cannot occur as the result of interference between two vertical waves of identical wavelength.

The most elaborate study to date on seasonal behavior of tides in the

meteor zone was recently published by *Fellous et al.* [1975]. Their results are based on averaging 130 days of measurements taken from all seasons over a 3 year period. They find the semidiurnal tide generally dominated by the fundamental $\Theta_2^{2\Omega,2}$ mode, but higher-order modes are prevalent in winter, and spring and autumn averages are sufficiently different that a single "equinoctial" model cannot describe them. Figure 6.1(a) shows the mean tidal behavior in comparison with theoretical results of *Nunn* [1967], who developed tidal equations including molecular viscosity and thermal conductivity, and Lindzen [*Chapman and Lindzen*, 1970], who used classical tidal theory. Good agreement for both phase and phase gradient occurs with Lindzen's values, but the observed tidal amplitude is substantially less than predicted by theory.

Figure 6.1(b) shows the average winter semidiurnal tidal averages in comparison with theoretical $\Theta_2^{2\Omega,6}$ mode behavior after *Lindzen and Hong* [1974], who included in their equations realistic models of seasonal distributions of mean wind temperature with respect to latitude and height, and classical $\Theta_2^{2\Omega,6}$ behavior. In the latter case the tide is given by

$$v(z) = A\, e^{\alpha z}\, e^{j(kz + \Phi)} \tag{6.22}$$

A and Φ are taken to coincide with experimental results at 90 km and using a temperature of 180 K, $\alpha = 0.095$ km^{-1}, $k = 12.5$ deg-km^{-1}. Excellent agreement in amplitude and phase up to 95 km occurs with the classical mode. Because their winter data is based on 35 days of measurements, the Garchy group points out that the short vertical wavelength character of the semidiurnal tide in that season is not likely ascribable to occasional events like stratospheric warmings. Rather it seems to be a regular phenomenon of the meteor region zonal wind.

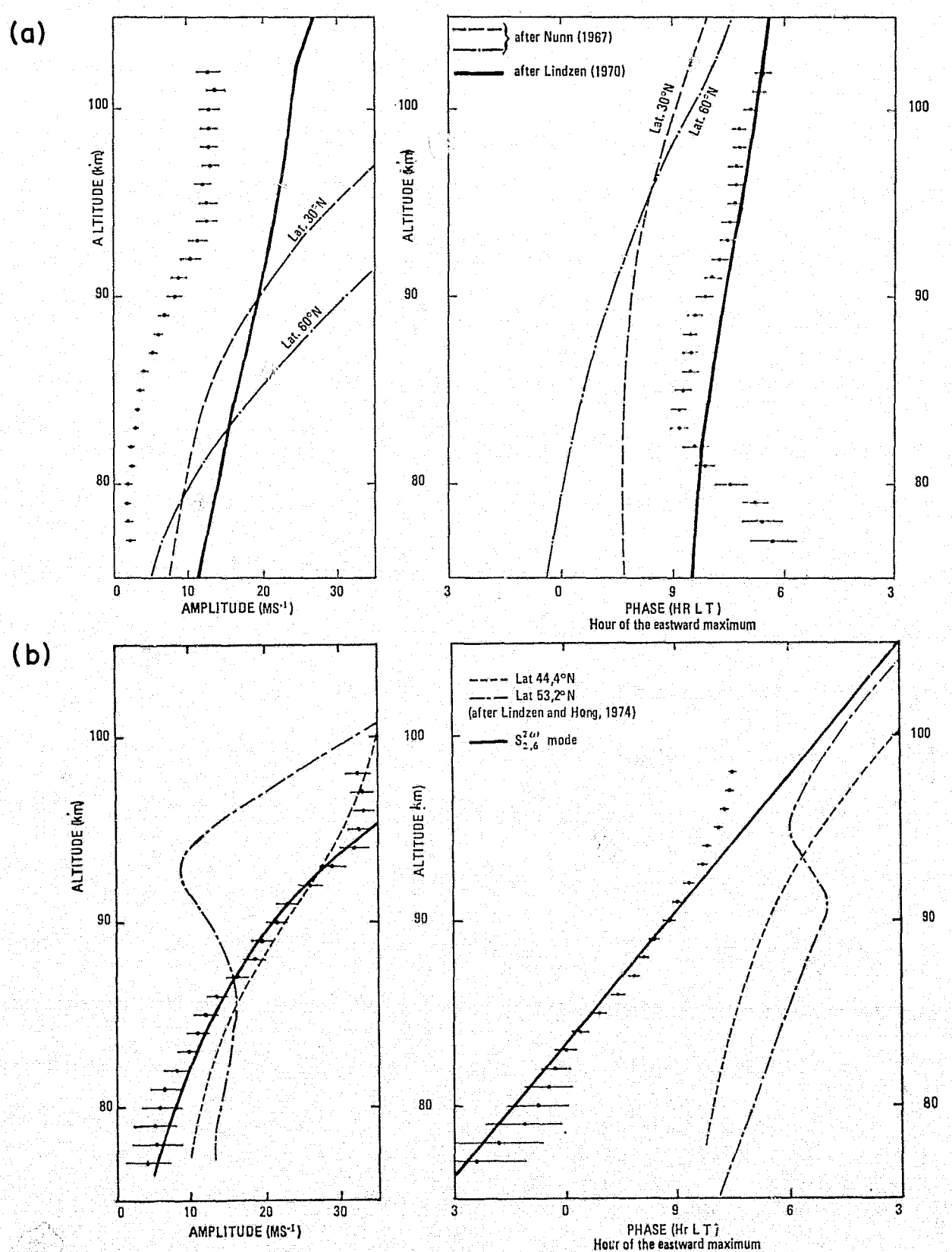

Figure 6.1 Semidiurnal tide: (a) General mean at Garchy (dots) and theoretical curves after *Nunn* [1967], *Chapman and Lindzen* [1970], [*Fellous et al.*, 1975], (b) winter average at Garchy (dots) and theoretical curves for the $\Theta^{2\Omega,2}_{6}$ mode and after *Lindzen and Hong* [1974], [*Fellous et al.*, 1975].

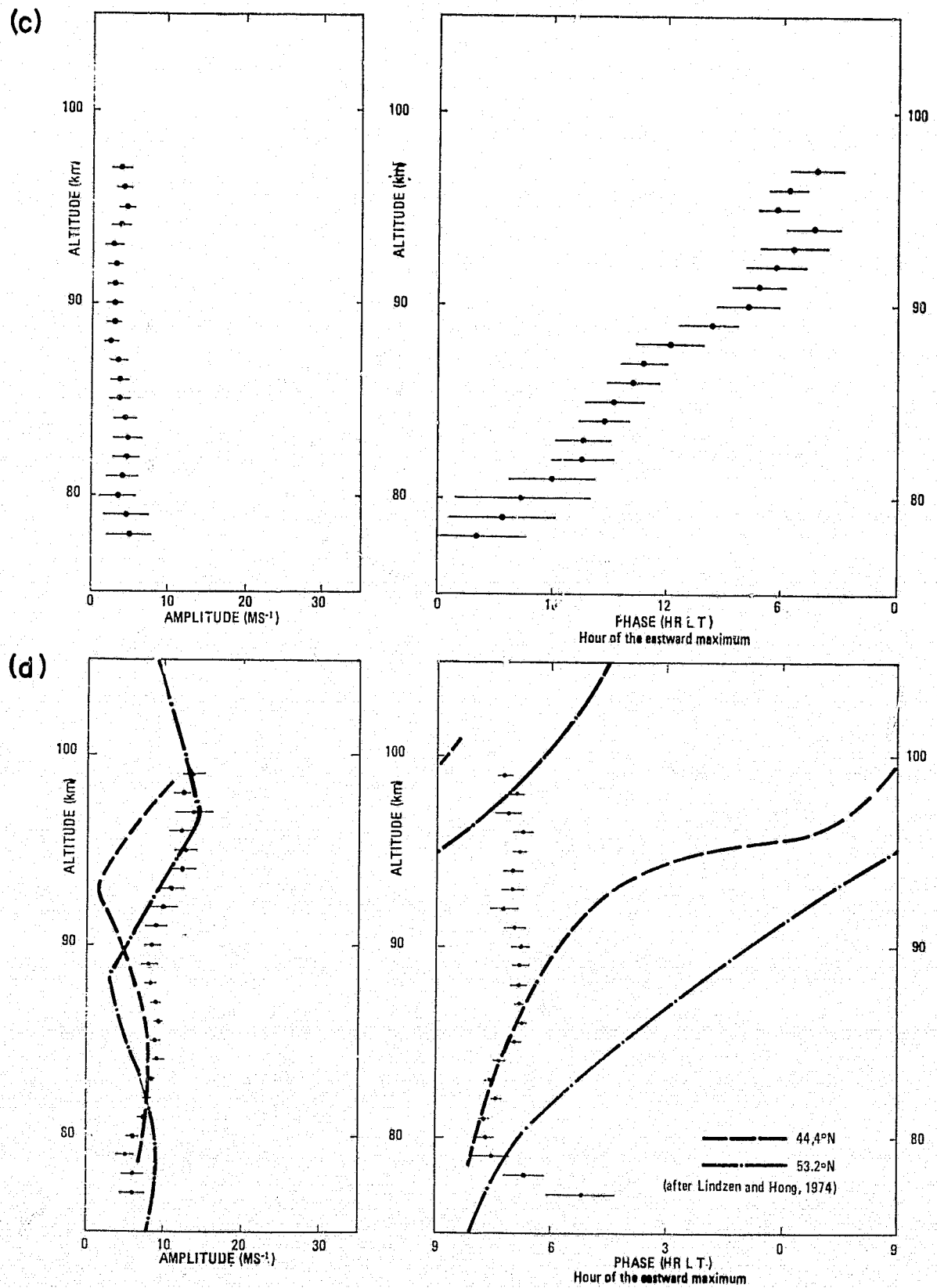

Figure 6.1 (c) Diurnal tide: winter average at Garchy [*Fellous et al.*, 1975], (d) Semidiurnal tide: summer average at Garchy (dots) and theoretical curves after *Lindzen and Hong* [1974], [*Fellous et al.*, 1975].

Figure 6.1(c) plots the winter diurnal tide structure at Garchy. The amplitude is quite weak and essentially independent of altitude, but phase growth implies an apparent vertical wavelength of 27 km, in good accord with the $\Theta_1^{\Omega,1}$ mode. The absence of amplitude growth with height suggests energy loss mechanisms are at work.

Figure 6.1(d) shows summer semidiurnal tide averages in comparison with *Lindzen and Hong's* [1974] theoretical values. Agreement in amplitude is reasonable but strong differences occur in phase, as was the case in winter. The general character of the observations is that of the $\Theta_2^{2\Omega,2}$ mode, which has a very long vertical wavelength and can even be evanescent in the meteor region for temperatures under 235 K.

Summer $S_1(v)$ results again exhibit little amplitude variation with height but now the phase also remains fixed. Both behaviors are correct for evanescent mode dominance. A least squares fit of amplitude to the exponential law $\exp(az)$ gives $\alpha \cong 0.03\ \text{km}^{-1}$, close to that for the theoretical $\Theta_1^{\Omega,-1}$ mode. It is interesting that computations by *Glass* [1973] indicate that the main diurnal evanescent modes $\Theta_1^{\Omega,-1}$ and $\Theta_1^{\Omega,-2}$ are in phase in summer but out of phase in winter.

In spring $S_2(v)$ was actually weaker than $S_1(v)$ with significant nonlinearities in phase. This suggests the presence of different modes during the spring transitional period. The same observation applies to $S_1(v)$ behavior as well. In autumn $S_2(v)$ had no regular behavior and thus its amplitude was depressed by averaging and phase varied irregularly with height.

Table 6.1 lists typical tidal parameters for all four seasons. The averaged $S_1(v)$ is reasonably behaved and quite similar to winter results (constant amplitude, 23 km vertical wavelength). In particular, this table points out the substantial contrast between winter and summer tide structure

Table 6.1

Seasonal tidal behavior at Garchy [*Fellous et al.*, 1975].

	Amplitude at 90 km (ms^{-1})	Amplitude gradient (ms^{-1} km^{-1})	Coefficient α (km^{-1})*	Phase at 90 km (hr LT)	Phase gradient (deg km^{-1})	Vertical wavelength (km)
Diurnal tide						
Winter	4	0	- 0.01	0945	13.5	27
Spring	7	0.4	0.07	1200	7	50
Summer	6	0.4	0.03	1130	2	> 100
Autumn	5	0	0.01	0830	15.5	23
Year	5	0	0.03	1100	7.5	50
Semidiurnal tide						
Winter	20	2	0.08	0930	10	35
Spring	5	0	- 0.02	0830	--	--
Summer	10	0.5	0.03	0700	1	> 100
Autumn	8	0	0.01	0530	0	> 100
Year	6.5	0.5	0.09	0800	2.5	100

*The coefficient α is computed assuming an exponential law for the amplitude variation with height.

for both $S_1(v)$ and $S_2(v)$. *Fellous et al.* [1975] note that such changes are the result of more than just differences in atmospheric structure, but differences in tidal energy sources too since the various modes seen require different physical excitations. Inaccurate models of mean zonal wind and thermal excitation are suggested as the cause of theoretical discrepancies from the observations.

6.2.4 *Day-to-day variations.* Meteor-radar tidal observations have generally shown the semidiurnal tide to be more stable in both phase and amplitude than the diurnal tide [*Clark*, 1975]. However, day-to-day differences in both tides, far in excess of system variance, are nonetheless common. *Karimov et al.* [1971] discuss the differences between true monthly mean tidal parameters and the parameters estimated from time series of one or several superimposed days. Both tidal components have been noted as particularly variable during equinox. Shifts in semidiurnal tidal phase of 180° in just a single day's time can occur at fixed height [*Fellous et al.* 1975].

Comparison of tides simultaneously observed at separate locations has revealed the importance of local effects [*Lysenko et al.* 1972; *Glass et al.* 1975]. Nonmigrating tidal modes are a possible cause of such local effects but wave superpositions seem more likely candidates. In light of the latter, *Fellous et al.* [1975] have performed two-dimensional Fourier analyses on the winds they observed to obtain power spectra in terms of frequency and vertical wavenumber. If superposed waves are present, and the difference between their vertical wavenumbers exceeds the spectrum resolving power [*Glass et al.* 1972], then the waves can be identified. In 20 to 40% of their spectra, more than a single wave appears to contribute to one or both the 12 and 24 hour tides.

Such successes prompted *Fellous et al.* [1975] to try three tentative models of superposed waves, each based on the equation

$$V(z) = e^{\alpha z} \sum_{i=1}^{N} a_i \, e^{(k_i z + \phi_i)} \tag{6.23}$$

where

$V(z)$ = east-west tidal wind

z = height, with origin arbitrarily set to 90 km

$\alpha = 1/2H$

H = scale height corresponding to assumed isothermal temperature T_o

N = number of superposed waves.

The three particular cases treated were:

(1) k_i assumed known for $N = 2$ or 3, and thus the a_i, ϕ_i could be obtained through linear regression

(2) All parameters unknown so nonlinear regression was necessary

(a) α fixed, usually 0.07 km^{-1} (T_o = 240 K), data from short periods

(b) α variable, data from entire recording period

(3) One direct and reflected wave present, so equation (6.23) could be written as

$$V(z) = a \, e^{\alpha z} \left[e^{j(kz+\beta)} + \rho e^{j(-kz+\gamma)} \right] \tag{6.24}$$

where α, β, k are the amplitude and phase at the z origin and the wave number of the direct wave (taken as upward), γ the phase of the reflected wave and ρ the reflection coefficient.

These models are successful in describing semidiurnal tidal behavior but not diurnal tidal behavior, perhaps because of evanescent modes or nonlinear reactions with other components [*Spizzichino*, 1969,1970a]. This last phenomenon, if present, could also account for the general lack of diurnal

tide growth with height in the meteor region, despite phase variation indicative of a propagating tide and no known substantial dissipative processes.

6.2.5 *University of Illinois meteor-radar tidal observations.* This section contains tables which summarize the diurnal and semidiurnal tidal behavior at Urbana for 1975-1976 meteor-radar observations. The tables are referenced by section 6.2.6, but because of their extensive size it was deemed advisable to organize them into a section of their own. In order of appearance are:

Table 6.2 Diurnal tide amplitude and phase versus height

Table 6.3 Semidiurnal tide amplitude and phase versus height

Table 6.4 Amplitude shear and vertical wavelength for $S_1(v)$ and $S_2(v)$

Table 6.5 Mean tidal parameters versus height based on 16 collection periods, Jan. 1975 - Jan. 1976

Table 6.6 90 km seasonal tidal statistics for Jan. 1975 - Jan. 1976

Table 6.7 All height seasonal tidal gradient statistics for Jan. 1975 - Jan. 1976.

6.2.6 *Discussion of University of Illinois observations.* As with the earliest observations, at Urbana we find meteor winds dominated by daily variations, even when data are not segregated by height. Figure 6.2 shows a typical plot of average meteor winds versus local time. Here each data point is based on fifty echoes and horizontal values are obtained from radial values multiplied by $\sqrt{2}$. The dashed line represents the least-squares fit to an assumed wind consisting of mean, 24 hour, and 12 hour components. In this particular case, the diurnal component somewhat overshadows the

Table 6.2

Diurnal tide amplitude and phase versus height.

Height (km)	Jan 17-18, 1975		Feb 28--Mar 1, 1975		Mar 7-8, 1975		Apr 4-5, 1975	
	A m s^{-1}	ϕ hr	A m s^{-1}	ϕ hr	A m s^{-1}	ϕ hr	A m s^{-1}	ϕ hr
82.5	29.95(1.24)	-10.33(.12)	2.87(.35)	9.60(.14)	11.72(.07)	7.51(.29)	17.37(.25)	3.81(.05)
83.5	21.52	-10.46	2.35	11.42	10.37	6.02	16.57	4.16
84.5	19.76	-10.20	2.88	10.05	10.03	5.42	17.48	5.06
85.5	19.38	- 9.79	2.72	10.40	8.97	4.74	18.95	5.43
86.5	16.63	- 8.44	3.35	-11.44	11.48	6.48	18.60	5.44
87.5	16.50	- 8.29	5.11	-10.11	10.21	7.13	20.93	6.59
88.5	17.06(.29)	- 8.54(.07)	6.89(.21)	- 9.83(.12)	11.80(.12)	7.51(.03)	19.40(.04)	6.94(.02)
89.5	16.57	- 8.70	8.90	- 8.95	10.07	7.95	17.60	7.54
90.5	14.98	- 9.17	10.56	- 9.08	9.28	9.16	15.86	8.18
91.5	14.55	- 9.39	10.12	- 8.65	5.89	11.02	14.91	8.75
92.5	13.98	- 9.73	9.69	- 7.94	5.40	-10.91	13.71	9.64
93.5	13.43	- 9.63	9.63	- 7.13	7.90	- 8.54	12.41	10.37
94.5	20.09(1.78)	- 9.68(.31)	8.59(.08)	- 4.69(.17)	8.78(.50)	- 8.04(.22)	7.84(.35)	11.20(.04)

Height (km)	May 27-28, 1975		July 14-15, 1975		July 30-31, 1975		Aug 21-22, 1975	
	A m s^{-1}	ϕ hr	A m s^{-1}	ϕ hr	A m s^{-1}	ϕ hr	A m s^{-1}	ϕ hr
82.5	7.66(.07)	-3.91(.13)	1.51(.18)	- 1.11(.38)	18.96(1.41)	-11.16(.15)	28.12(1.86)	2.60(.25)
83.5	7.31	-3.68	2.99	- 1.38	17.50	-10.79	26.84	2.53
84.5	7.16	-2.86	4.04	0.25	18.21	-10.96	26.67	2.56
85.5	7.76	-2.44	2.79	- 1.01	18.43	-10.94	26.29	2.52
86.5	9.51	-1.92	2.40	- .95	19.01	-10.49	26.96	2.57
87.5	9.72	-1.35	1.83	- 2.86	18.32	-10.33	26.90	2.62
88.5	10.58(.06)	-1.39(.02)	1.77(.08)	- 5.93(.27)	18.51(.30)	- 9.86(.06)	25.69(.39)	2.54(.06)
89.5	10.36	-1.37	3.85	- 7.20	18.85	- 9.41	24.23	2.36
90.5	9.68	-1.02	4.57	- 7.66	19.80	- 9.30	22.15	2.03
91.5	7.68	- .84	6.11	- 8.38	20.59	- 8.89	20.71	1.43
92.5	6.98	- .99	6.80	- 9.08	21.13	- 8.52	17.17	.57
93.5	6.27	- .68	6.11	- 9.55	24.19	- 8.62	12.16	- .47
94.5	3.26(.64)	0.39(.48)	6.59(.34)	-10.98(.17)	18.14(.79)	- 7.57(.21)	8.23(1.78)	-1.71(.13)

Table 6.2 (Continued)

Height (km)	Sept 13-14, 1975 A m s^{-1}	Sept 13-14, 1975 ϕ hr	Oct 13-14, 1975 A m s^{-1}	Oct 13-14, 1975 ϕ hr	Oct 14-15, 1975 A m s^{-1}	Oct 14-15, 1975 ϕ hr	Oct 16-17, 1975 A m s^{-1}	Oct 16-17, 1975 ϕ hr
82	14.28(2.49)	3.35(.69)	14.27	8.07	12.16	7.87	16.81	8.06
83	18.99	3.51	19.27	8.54	11.65	7.27	17.46	8.26
84	24.99	3.88	19.07	8.47	9.53	6.83	17.38	8.90
85	26.66	4.54	17.12	8.38	7.43	5.70	16.13	9.39
86	30.29	5.58	15.57	8.52	7.77	5.22	15.66	9.97
87	29.84	6.25	12.29	8.79	6.54	5.21	15.96	10.25
88	30.12	6.80	9.88	9.29	6.24	6.41	15.41	10.33
89	30.15	7.72	8.50	10.03	6.97	7.71	15.54	10.34
90	27.14	8.43	8.99	10.96	7.20	8.57	16.14	10.46
91	24.15	9.59	8.64	11.38	7.93	9.36	14.85	10.69
92	21.21(.40)	10.67(.03)	11.44	11.47	7.64	9.37	13.69	11.00
93	16.72	-11.72	16.26	11.53	5.04	8.86	11.72	11.32
94	13.74	- 9.31	13.15	11.60	5.58	9.08	9.35	11.39
95	15.07	- 8.02	12.59	11.83	5.19	9.43	6.42	-11.36
96	17.70	- 6.81	6.97	12.13	5.51	9.99	5.47	-11.40
97	20.01	- 6.92	4.97	12.87	1.99	7.48	4.62	-11.44
98	20.75	- 6.00	5.42	14.36	2.99	3.11	2.67	-11.14
99	19.41	- 5.46	4.78	17.11	5.66	1.89	2.50	- 8.87
100	16.26	- 7.20	6.07	17.32	7.95	2.50	2.67	-10.32
101	17.78	- 5.09	4.72	19.06	7.73	3.68	2.65	10.12
102	11.80(3.38)	- 7.74(1.58)			8.50	5.34	2.93	11.43

Height (km)	Dec 4-6, 1975 A m s^{-1}	Dec 4-6, 1975 ϕ hr	Dec 12-13, 1975 A m s^{-1}	Dec 12-13, 1975 ϕ hr	Jan 14-16, 1976 A m s^{-1}	Jan 14-16, 1976 ϕ hr	Jan 21-23, 1976 A m s^{-1}	Jan 21-23, 1976 ϕ hr
80	7.98(.82)	9.00(.39)	15.33(1.10)	10.45(0.18)	5.37(.76)	10.40(.02)		
82	6.85	9.76	18.70	10.11	3.65	-11.89	10.00(.55)	5.49(.19)
83							11.43	5.64
84	7.66	10.75	21.33	10.50	2.70	-11.64	10.97	5.95
85							10.16	5.49
86	8.51	11.89	22.65	11.42	3.80	-11.10	9.47	5.62
87							8.57	6.72
88	9.27	-11.69	23.74	11.82	5.24	-11.53	7.46	8.01
89							6.48	7.87
90	10.30	-11.14	23.95	-11.65	5.57	11.56	4.51	8.96
91							2.79	8.51
92	12.41(.37)	-10.58(.09)	22.69(0.46)	-10.96(0.06)	7.77(.42)	11.86(.14)	0.83(.12)	10.38(1.04)
93							0.44	10.02
94	11.45	- 9.86	18.72	-10.07	7.28	-11.34	1.01	2.43
95							3.34	4.22
96	13.27	- 9.52	17.02	- 9.03	6.74	-10.42	3.91	3.93
97							5.70	4.21
98	13.97	- 9.53	14.74	- 8.99	6.02	- 8.75	5.50	4.27
99							5.16(2.14)	4.16(1.52)
100	14.06	- 9.78	15.81(1.59)	- 9.40(0.35)	7.12	- 7.65	4.77(3.09)	3.91(2.74)
101							2.27(7.65)	2.14(10.25)
102	14.14(.77)	- 9.42(.22)	12.33(8.02)	- 8.83(2.67)	8.27(.63)	- 7.76(.33)	1.70(3.97)	8.32(16.01)

Table 6.3

Semidiurnal tide amplitude and phase versus height.

Height (km)	Jan 17-18, 1975 A m s^{-1}	ϕ hr	Feb 28--Mar 1, 1975 A m s^{-1}	ϕ hr	Mar 7-8, 1975 A m s^{-1}	ϕ hr	Apr 4-5, 1975 A m s^{-1}	ϕ hr
82.5	6.25(.78)	-2.85(.17)	7.48(.83)	1.66(.20)	7.39(.76)	4.01(.06)	7.97(.11)	5.60(.04)
83.5	2.77	-3.40	6.39	1.05	8.74	3.62	7.06	5.83
84.5	2.06	-3.43	8.14	0.50	7.08	3.66	8.49	5.87
85.5	0.54	-2.67	10.79	0.42	6.95	3.43	8.07	-5.91
86.5	7.35	2.99	12.31	0.39	7.12	4.22	7.63	5.79
87.5	8.47	2.74	13.90	0.34	5.15	3.74	10.83	5.35
88.5	9.66(.24)	2.61(.04)	16.89(.19)	0.77(.02)	4.09(.16)	3.06(.08)	8.46(.10)	-5.28(.02)
89.5	12.75	2.56	19.95	1.17	4.46	1.79	4.95	-5.05
90.5	15.24	2.46	20.10	1.60	6.74	1.35	2.34	-5.32
91.5	17.45	2.45	22.08	2.10	8.78	1.38	0.77	1.79
92.5	18.06	2.43	22.53	2.49	10.55	1.56	4.16	1.24
93.5	19.53	2.37	23.29	2.95	11.87	1.88	7.07	1.23
94.5	18.05(1.59)	1.29(.16)	25.89(.33)	3.54(.01)	14.02(.44)	2.53(.06)	11.37(.40)	1.90(.06)

Height (km)	May 27-28, 1975 A m s^{-1}	ϕ hr	July 14-15, 1975 A m s^{-1}	ϕ hr	July 30-31, 1975 A m s^{-1}	ϕ hr	Aug 21-22, 1975 A m s^{-1}	ϕ hr
82.5	5.97(.28)	3.59(.03)	12.40(.14)	3.68(.03)	21.52(.37)	4.34(.02)	17.29(1.04)	5.63(.12)
83.5	5.11	3.98	12.61	3.42	22.70	4.28	16.21	5.69
84.5	7.02	4.02	12.54	3.45	23.67	4.23	15.05	5.72
85.5	6.83	4.14	12.69	3.48	23.83	4.21	16.05	5.98
86.5	6.71	3.99	13.85	3.36	22.47	4.22	16.50	-5.75
87.5	9.22	4.02	14.40	3.54	22.95	4.35	16.91	-5.72
88.5	10.55(.04)	3.73(.01)	16.76(.07)	3.83(.0)	22.47(.07)	4.09(.0)	14.51(.29)	-5.64(.05)
89.5	10.96	3.56	18.57	3.82	22.41	3.95	12.25	-5.84
90.5	10.74	3.76	21.17	3.86	22.52	3.83	11.22	5.97
91.5	10.83	3.97	22.49	4.01	22.15	3.67	8.96	5.50
92.5	10.01	4.08	24.30	4.04	23.18	3.53	6.74	5.69
93.5	9.44	4.14	26.81	4.10	21.82	3.30	6.29	-5.39
94.5	9.70(.05)	4.62(.0)	28.47(.04)	4.26(.0)	29.09(.69)	3.25(.03)	8.84(1.81)	-4.97(.46)

Table 6.3 (Continued)

Height (km)	Sept 13-14, 1975 A m s^{-1}	Sept 13-14, 1975 φ hr	Oct 13-14, 1975 A m s^{-1}	Oct 13-14, 1975 φ hr	Oct 14-15, 1975 A m s^{-1}	Oct 14-15, 1975 φ hr	Oct 16-17, 1975 A m s^{-1}	Oct 16-17, 1975 φ hr
82	8.17(.96)	4.86(.03)	10.88	4.44	5.64	-1.26	8.20	2.19
83	10.20	5.72	12.56	4.46	7.10	- .65	8.52	2.52
84	10.23	5.46	12.98	4.35	9.94	- .03	9.18	3.11
85	9.88	5.94	13.42	4.32	11.67	.35	9.39	3.50
86	9.25	-5.78	13.30	4.55	14.52	.93	8.72	3.92
87	10.32	-4.92	12.58	4.57	16.06	1.18	6.59	4.36
88	12.24	-4.72	11.0	4.52	16.38	1.47	5.41	4.74
89	13.07	-4.55	8.78	4.65	15.04	1.99	5.37	5.52
90	14.61	-4.53	6.82	5.05	14.28	2.31	5.54	-5.80
91	14.61	-4.36	5.32	5.06	12.14	2.75	4.31	-5.09
92	16.05(.64)	-4.25(.07)	6.21	6.20	11.41	3.01	4.12	-4.52
93	19.14	-4.22	10.26	7.23	11.32	3.28	3.42	-4.13
94	19.79	-4.26	10.20	7.31	9.81	3.72	1.89	-4.67
95	16.95	-4.15	12.67	7.96	9.19	4.20	1.81	-2.25
96	14.79	-4.12	10.80	8.44	7.81	4.88	2.49	-2.38
97	16.16	-4.11	13.24	8.83	7.39	4.69	3.16	-2.44
98	12.17	-4.21	17.66	9.03	6.87	4.48	3.01	-1.43
99	12.53	-4.36	17.59	9.34	6.19	4.18	6.00	-1.07
100	23.55(1.24)	-3.67	17.71	9.40	6.56	3.80	4.42	- .83
101	16.57(2.95)	-3.33	12.31	9.66	6.32	4.26	4.55	- .94
102	25.17(3.75)	-3.18(.16)			7.43	4.76	5.13	- .53

Height (km)	Dec 4-6, 1975 A m s^{-1}	Dec 4-6, 1975 φ hr	Dec 12-13, 1975 A m s^{-1}	Dec 12-13, 1975 φ hr	Jan 14-16, 1976 A m s^{-1}	Jan 14-16, 1976 φ hr	Jan 21-23, 1976 A m s^{-1}	Jan 21-23, 1976 φ hr
80	9.00(1.52)	1.18(.35)	6.80(1.96)	2.64(.61)	17.20(1.01)	2.52(.10)		
82	10.76	1.45	8.73	1.71	20.70	2.66	5.50(.31)	-2.14(.05)
83							4.85	-2.06
84	11.57	1.64	11.50	1.20	23.41	2.88	5.21	-1.18
85							3.61	- .18
86	14.00	2.12	15.49	1.23	23.10	3.07	4.31	1.29
87							5.34	2.09
88	15.89	2.44	13.71	1.38	20.33	3.38	7.55	2.55
89							9.48	2.93
90	17.23	2.66	12.10	1.79	16.55	3.95	11.62	3.05
91							13.23	3.22
92	17.35(.31)	2.79(.03)	9.50(0.41)	2.26(0.08)	13.06(.07)	4.59(.02)	14.11(.34)	3.24(.03)
93							12.78	3.48
94	19.01	2.84	11.56	3.40	11.15	5.04	12.12	3.54
95							10.37	3.83
96	16.83	2.91	13.25	3.59	8.95	5.32	9.28	4.48
97							10.10	5.05
98	15.38	2.93	13.07	3.49	7.24	5.37	9.21	5.34
99							8.99	5.18
100	15.66	3.17	8.91(1.30)	3.12(0.14)	5.62	5.19	6.82(1.13)	4.76(.54)
101							6.27(4.17)	4.24(.86)
102	15.58(.62)	2.93(.05)	12.49(7.25)	3.15(0.19)	5.39(.22)	5.36(.14)	5.10(2.37)	4.71(1.39)

Table 6.4

Amplitude shear and vertical wavelength for $S_1(v)$ and $S_2(v)$.

Date	(a) Diurnal Tide		(b) Semidiurnal Tide	
	dA/dz horizontal $ms^{-1}km$	λ km	dA/dz horizontal $ms^{-1}km$	λ km
January 17, 18, 1975	-1.09	470, evanescent		standing wave
February 28, March 1	1.08	34	2.39	59
March 7, 8	-0.48	28	0.57	55*
April 4, 5	-0.89	40		standing wave
May 27, 28	-0.25	80	0.60	377
July 14,15	0.57	25*	2.04	180
July 30, 31	0.38	85	0.26	128*
August 21, 22	-2.02	82*	-1.32	203
September 13, 14	-0.72	27	0.85	78
October 13, 14	-0.92	48	0.27	36
October 14, 15	-0.38	184*	-0.38	41
October 16, 17	-1.29	105	-0.38	24
December 4-6	0.52	94	0.41	140
December 12, 13	-0.37	92	0.14	130
January 14-16, 1976	0.27	108, evanescent 82-94 km	-1.19	78
January 21-23, 1976	-0.69	58 (π shift at 92 km)	0.42	31

*apparent downward propagation

Table 6.5

Mean tidal parameters versus height based on 16 collection periods, January 1975-January 1976.

Height km	a_1 m s^{-1}	b_1 m s^{-1}	a_2 m s^{-1}	b_2 m s^{-1}	$\|S_1\|$ m s^{-1}	$\angle S_1$ hr	$\|S_2\|$ m s^{-1}	$\angle S_2$ hr	$\|S_2\|$ horizontal m s^{-1}	$\angle S_2^*$ hr	r_{p1}	r_{p2}
82	5.7	-3.3	5.7	-1.9	6.6	8.0	6.0	3.6	8.5	8.4	2.9	2.0
84	6.6	-2.7	6.5	-1.6	7.2	7.5	6.7	3.5	9.5	8.5	2.9	2.2
86	5.6	-3.1	7.6	-1.5	6.4	7.9	7.7	3.4	10.9	8.6	3.0	2.3
88	4.2	-5.1	7.8	-1.6	6.6	9.4	8.0	3.4	11.3	8.6	3.0	2.4
90	1.8	-6.8	8.8	-1.8	7.1	11.0	9.0	3.4	12.7	8.6	2.7	2.3
92	-1.4	-7.4	9.1	-2.1	7.6	12.7	9.4	3.4	13.3	8.6	2.3	2.3
94	-4.1	-6.1	9.1	-3.6	7.3	14.2	9.8	3.7	13.9	8.3	1.8	2.8

a_1, a_2 = radial southward cosine component of diurnal, semidiurnal tide, respectively

b_1, b_2 = radial southward sine component of diurnal, semidiurnal tide, respectively

$r_{p1,\ 2}$ = probable error radius of S_1, S_2 mean values

Fit form for $S_i = A_i \sin(\omega_i[t+\phi_i])$, $i = 1, 2$, local time used. Multiply amplitudes by $\sqrt{2}$ to obtain horizontal equivalent

$\angle S_2^* = 12 - \angle S_2$, apparent time of eastward maximum

Table 6.6

90 km seasonal tidal statistics for January 1975 - January 1976 data.

Season	Nr of runs	A ms^{-1}	dA/dz $ms^{-1}km^{-1}$	ϕ hr	$\lvert d\phi/dz \rvert^{-1}$ deg km^{-1}	λ_v km
(a) Diurnal Tide						
W[DJF]	5	16.9	-.5	12.1(11.9)	4.2	86
Sp[MAM]	4	16.0	-1.5	13.8(10.2)	9.6	38
S[JJA]	3	21.9	+0.1	11.0(13.0)	6.6	55
A[SON]	4	21.0	-1.0	9.6(14.4)	9.8	37
YEAR	16	19.0	-.7	11.6(12.4)	7.6	54
(b) Semidiurnal Tide						
W	5	20.6	.5	2.8(9.2)	4.9	74
Sp	4	14.1	.4	0.4(11.6)	6.7	54
S	3	25.9	.1	4.6(7.4)	2.8	127
A	4	14.6	-1.0	5.3(6.7)	8.6	42
YEAR	16	18.8	0.0	3.2(8.8)	5.8	74

Fit Form = $A\sin(\omega[t+\phi])$, where A is horizontal southward and ϕ is in hours local time. (Parentheses give apparent time of eastward maximum wind).

Table 6.7

All height seasonal tidal gradient statistics for January 1975 - January 1976 data.

Season	Nr of runs	dA/dz $ms^{-1}km^{-1}$	$\lvert d\phi/dz \rvert$ deg km^{-1}	λ_v
(a) Diurnal Tide				
W[DJF]	5	-0.3	3.6	164
Sp[MAM]	4	-0.2	7.9	46
S[JJA]	3	-0.5	5.6	64
A[SON]	4	-1.2	4.0	91
YEAR	16	-0.5	5.3 (λ_v=68 km)	91 (median = 81 km)
(b) Semidiurnal Tide				
W	4	0.0	5.4	95
Sp	3	1.7	2.2	164
S	3	0.5	2.1	170
A	4	0.1	8.0	45
YEAR	14	0.6	4.4 (λ_v=82 km)	119

Fit Form = $A\sin(\omega[t+\phi])$, where A is horizontal southward and ϕ is in hours local time

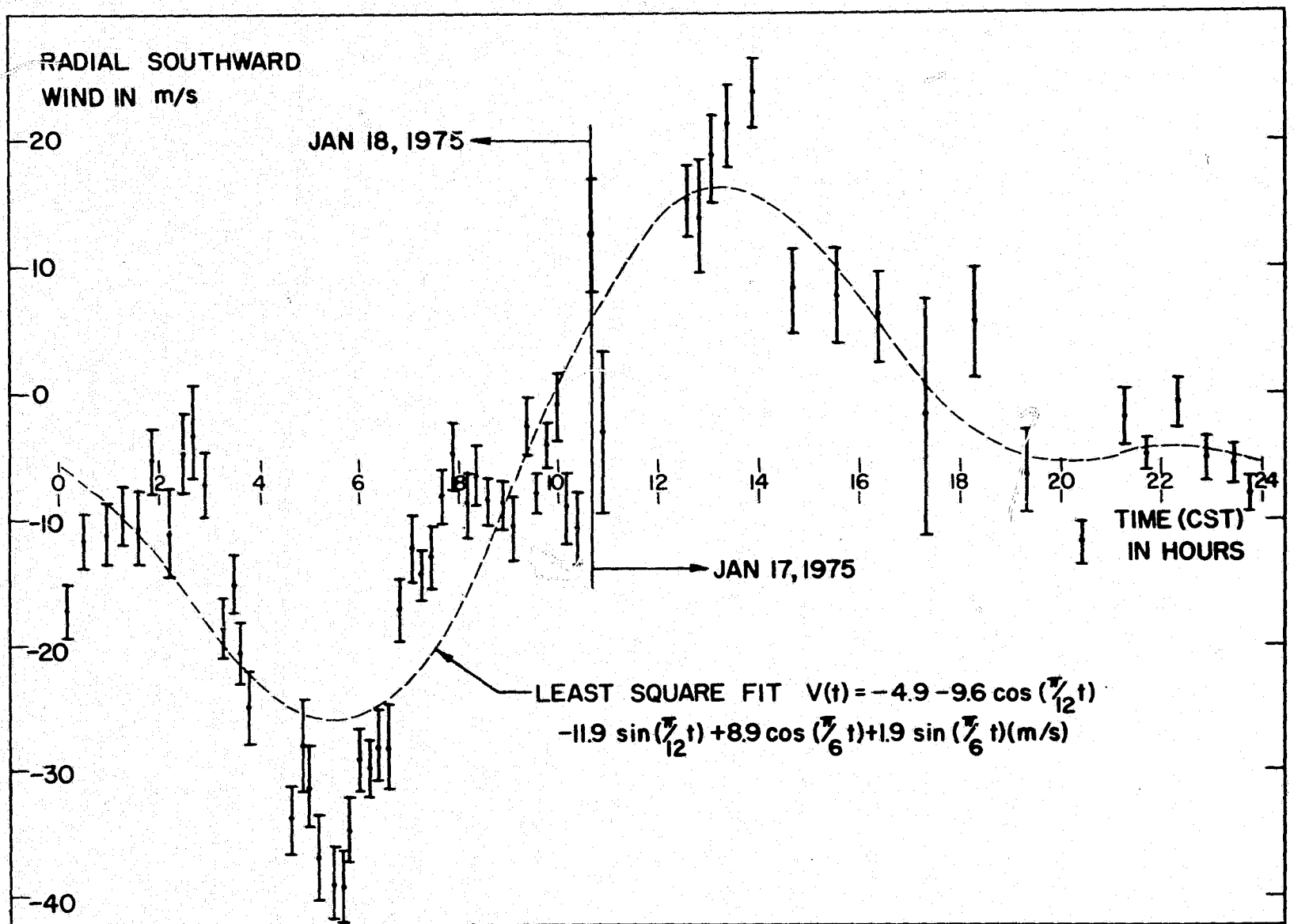

Figure 6.2 24-hour observation of radial southward winds at Urbana on January 17-18, 1975.

semidiurnal component. When winds from many radar runs are averaged, however, we find the semidiurnal component dominant (Tables 5.3 and 5.7). This is in agreement with the Jodrell Bank findings and Lindzen's classical explanation of the latitudinal structure of tides. Also when data from all heights are treated together, the semidiurnal component receives additional enhancement because of its generally longer vertical wavelength than the diurnal component.

The general character of the tidal winds we observe is most succinctly presented in Table 6.5. The semidiurnal parameters $|S_2|$ horizontal and $\angle S_2^*$ can be compared directly with the Garchy values plotted in Figure 6.1(a). Although our vertical span is quite limited because the earliest radar runs used decay height only, the mean structure we observe is quite consistent with the hypothesis of $\Theta_2^{2\Omega,2}$ mode dominance. The predicted wavelength of this mode is quite long, 212 km for an isothermal atmsophere of 300 K, and the mode actually becomes evanescent at temperatures below about 235 K. Our amplitudes are only slightly less than those predicted by *Lindzen* [1968] via classical tidal theory and they exhibit approximately the same growth rate with altitude. It is interesting to note that below 86 km we see a small decrease in apparent time of eastward maximum. This effect shows up at Garchy below about 83 km and is much more pronounced. This phase reversal is an indication of destructive interference and may account for the depressed amplitude of $S_2(v)$ at the lower altitudes at Garchy, as well as the apparent rapid vertical growth rate in $S_2(v)$ amplitude. Since Garchy observes zonal winds, where the prevailing component is normally a dominant factor, it is possible that the peculiar $S_2(v)$ behavior they observe is a result of background wind effects. *Clark* [1975] has cited the importance of such effects and as already noted *Lindzen and Hong* [1974]

have theoretically addressed the problem. They found no unusual behavior at 44.4° N but at 53.2° N the substantial seasonal phase variation causes apparent standing wave behavior at 92 km. Garchy is located at 47° N so an intermediate behavior would be predicted, i.e., the amplitude null would weaken and rather than show a step of π in phase, the vertical phase slope would reverse direction. Such behavior does occur in the Garchy structure of Figure 6.1(a) but there it is much broader in height and present at lower altitudes. Possibly more accurate knowledge of solar tide excitation and background winds would imporve the match.

The mean annual diurnal tidal structure observed at Urbana shows approximately constant amplitude over 82-94 km and a vertical wavelength of 41 km. These findings are in reasonable agreement with the latest Garchy results in *Fellous et al.* [1975]. The phase gradient is too small to support the hypothesis of $\Theta_1^{\Omega,1}$ mode dominance over the entire region. However, we note that a phase gradient opposite that expected for upward propagating waves is shown at the bottom of our observed height span. From 86 to 94 km the phase gradient is 12 deg-km^{-1}, in good agreement with that predicted for the $\Theta_1^{\Omega,1}$ mode. Rather than explain the lack of tidal amplitude growth in height by non-linear loss mechanisms [*Spizzichino*, 1969, 1970a], it might simply be the result of two tidal modes, one propagating, one evanescent, of nearly equal strength at 86 km. If such was the case, the diurnal oscillation could be expressed as

$$V(t,z) = a_1 \exp(z/2H) \cos(\omega t + k_1 z + \phi) + a_2 \exp(z/2H - k_2 z) \cos\omega t \qquad (6.25)$$

where

a_1, a_2 = amplitude of mode component 1,2

H = atmospheric scale height

$\omega = \pi/12$ rad-hr^{-1}

k_1 = wavenumber of mode 1 (propagating)

k_2 = wavenumber of mode 2 (evanescent)

ϕ = phase of mode 1 relative to mode 2 at $z = 0$ (reference altitude).

For minimum amplitude sensitivity with respect to altitude we solve

$$\frac{\partial |V(t,z)|^2}{\partial z} = 0 = \frac{a_1^2}{H} e^{z/H} + a_2^2 \left(\frac{1}{H} - 2k_2\right) e^{z\left(\frac{1}{H} - 2k_2\right)} \tag{6.26}$$

$$+ 2a_1 a_2 \left[\left(\frac{1}{H} - k_2\right) e^{z\left(\frac{1}{H} - k_2\right)} \cos(k_1 z + \phi) - e^{z\left(\frac{1}{H} - k_2\right)} k_1 \sin(k_1 z + \phi)\right]$$

In (6.26) a_1, a_2, and ϕ are free variables but independent of z. Thus (6.26) can be satisfied at only a single altitude. The logical choice is the breakpoint height where both modes are of equal strength, i.e., $a_1 = a_2$ and $z = 0$. Substitution into (6.26) gives

$$(1 - k_2 H)(1 + \cos\phi) - (k_1 H)\sin\phi = 0 \tag{6.27}$$

If $\Theta_1^{\Omega,-4}$ and $\Theta_1^{\Omega,1}$ are the two modes present, $k_1 = (2\pi/27)$ km^{-1}, $k_2 \cong \frac{1}{H}$ (e-folding height), and $\phi \cong 0°$. If $\Theta_1^{\Omega,-2}$ and $\Theta_1^{\Omega,1}$ are the two modes present $k_2 \cong 1/2H$ and $\phi \cong 39°$. In the former situation a change of just 7.5% in $|V(t,z)|$ will occur as z is varied $\pm H$ about $z = 0$. In the latter situation the change is about 10%. Since the scale height will be on the order of 6 km, either evanescent mode along with $\Theta_1^{\Omega,1}$ could produce observations as in Table 6.5 and thus our hypothesis is shown to be a potential explanation for the lack of amplitude growth in height.

Although we have far too few data runs to definitively characterize seasonal tidal behavior, it is nonetheless informative to segment our data into seasons for comparison with the Garchy findings of Table 6.1. Our

Table 6.6 has five columns which can be compared directly. Probably the most satisfying agreement is between the phase at maximum columns. The yearly means for both $S_1(v)$ and $S_2(v)$ are quite close and although seasonal trends appear somewhat displaced this is hardly surprising with so few runs on our part. 90 km Urbana $S_1(v)$ amplitudes are in all cases appreciably larger, but would be depressed if more data was available due to the short-term phase variability of $S_1(v)$. No dramatic seasonal changes in $S_1(v)$ amplitudes are found at either Urbana or Garchy. When $S_2(v)$ is considered, however, both sites show much larger amplitudes in summer and winter. The phase variability of $S_2(v)$ during equinox is responsible for this. Amplitude gradients indicate diurnal tide weakening at both sites. The negative autumn gradient for $S_2(v)$ is probably misleading, and rather than a reflection of the true state of affairs it was probably caused by three of the four runs occurring over Oct. 13-17, 1975. That period was one of pronounced tidal variability. The long vertical wavelength we see for winter $S_1(v)$ is also suspect since it is influenced by two anomalous days of evanescent behavior.

Table 6.7 shows the seasonal behavior of gradient related parameters based on data over the entire resolved height range. Such gradients are probably more indicative of true behavior and extreme extrapolations are avoided in finding vertical wavelength. The growth of $S_2(v)$ and decay of $S_1(v)$ at all times of the year are now apparent as is the longer wavelength of the former.

When our tidal observations are considered on an individual basis, we find numerous examples that support the key findings of *Fellous et al.* [1974]; namely, the existence of anomalous tidal waves and superposed waves. Jan. 17-18, 1975 and a large portion of the Jan. 14-16, 1976 data exhibit

evanescent diurnal tidal structure (Table 6.2). October 1975 and Jan. 21-23, 1976 semidiurnal wavelengths are quite short and indicative of $\Theta_2^{2\Omega,6}$ dominance (Table 6.3). Standing wave patterns in $S_2(v)$ were evident Jan. 17-18 and April 4-5, 1975 and in $S_1(v)$ were evident Jan. 21-23, 1976. Aug. 21-22, 1975 exhibited periodicity in $S_2(v)$ amplitude and phase indicative of a weak standing wave system. $S_1(v)$ on Oct. 13-14, 1975 showed similar variation. We do not necessarily find diurnal and semidiurnal anomalies simultaneously present, nor do we find the occurrence of the anomalies restricted to periods of stratospheric warming.

The potentially sizeable day-to-day variation of tidal structure is best illustrated by the amplitude and phase plots for the five day October run, Figures 6.3 through 6.7. In a period of just 24 hours, $S_1(v)$ appears to develop a backward shift in phase of 180° near 99 km. This is indicative of a downward propagating component interacting with the normal upward component. And indeed after 62.5 hours a backward shift still is visible, though at much reduced magnitude and now near 101 km. The onset and height of the phase shift appear related to a gradient reversal in the prevailing wind. During the same time span $S_2(v)$ appears to be slipping phase over the lower altitudes but leading at higher altitudes. Again phase structure appears related to prevailing winds.

The extent of the October wind variability can be judged by Table 6.8. Here the mean tidal parameters for our entire 96 hr data record are assumed "correct" and the amplitude and phase standard deviations for two 48 hr data records are computed. $S_1(v)$ and $S_2(v)$ amplitude standard deviations found in this manner are of about equal size, but since $|S_2(v)|$ was in general less than $|S_1(v)|$, this means $S_2(v)$ exhibited more amplitude variability. Similarly, in terms of phase degrees $S_2(v)$ was again more variable. This,

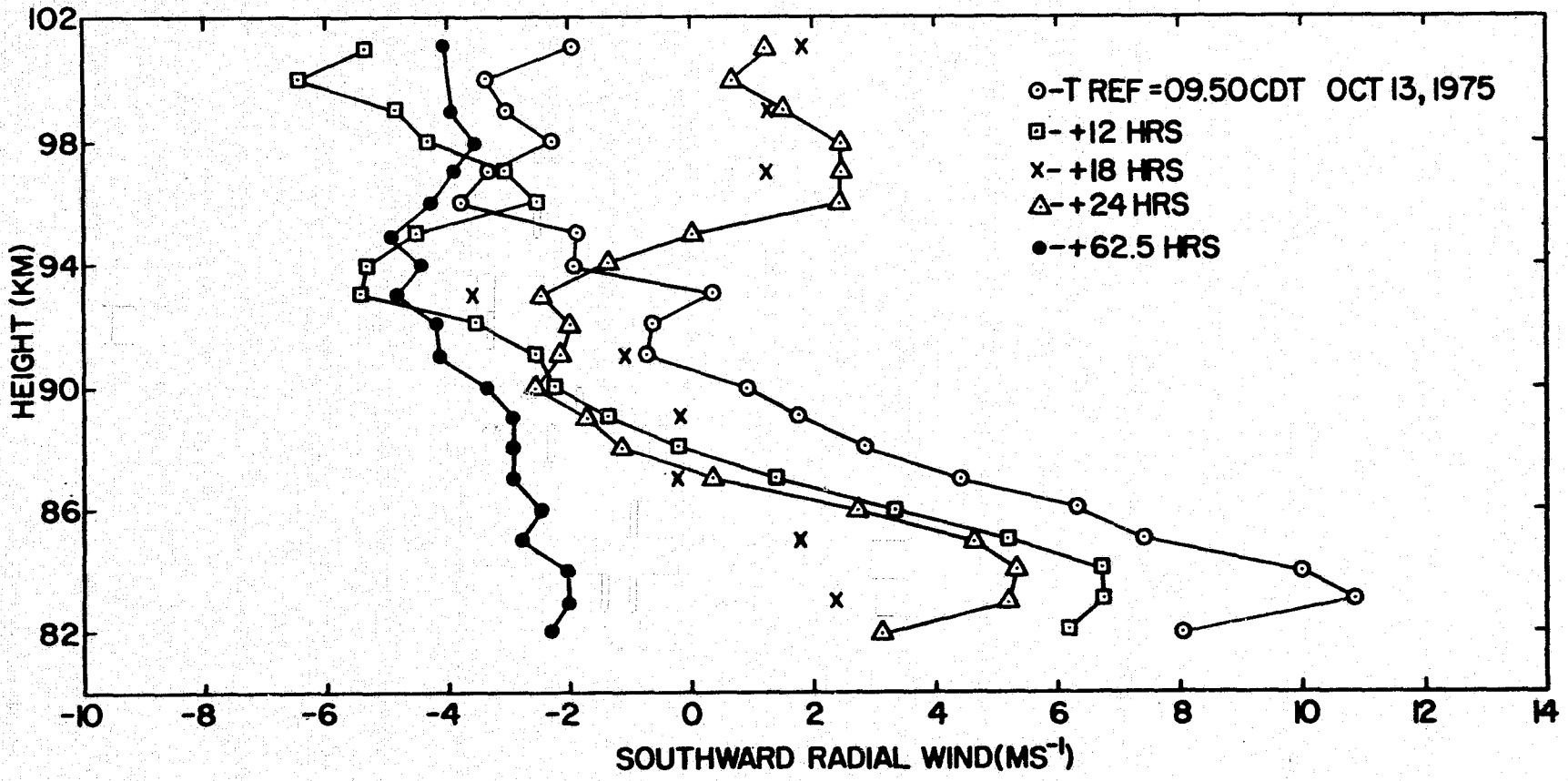

Figure 6.3 Prevailing wind at Urbana, October 13-18, 1975.

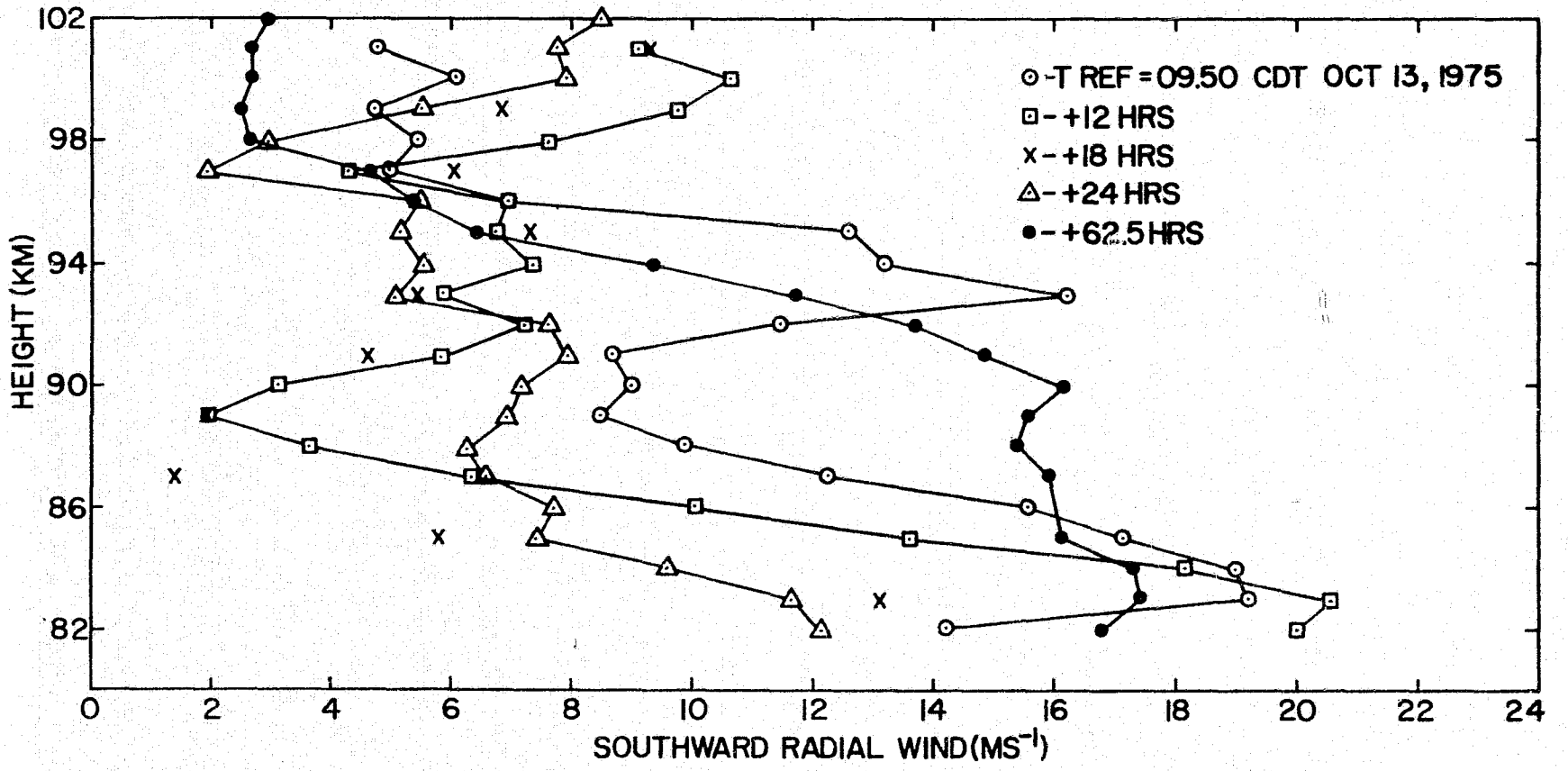

Figure 6.4 Diurnal tide at Urbana, October 13-18, 1975.

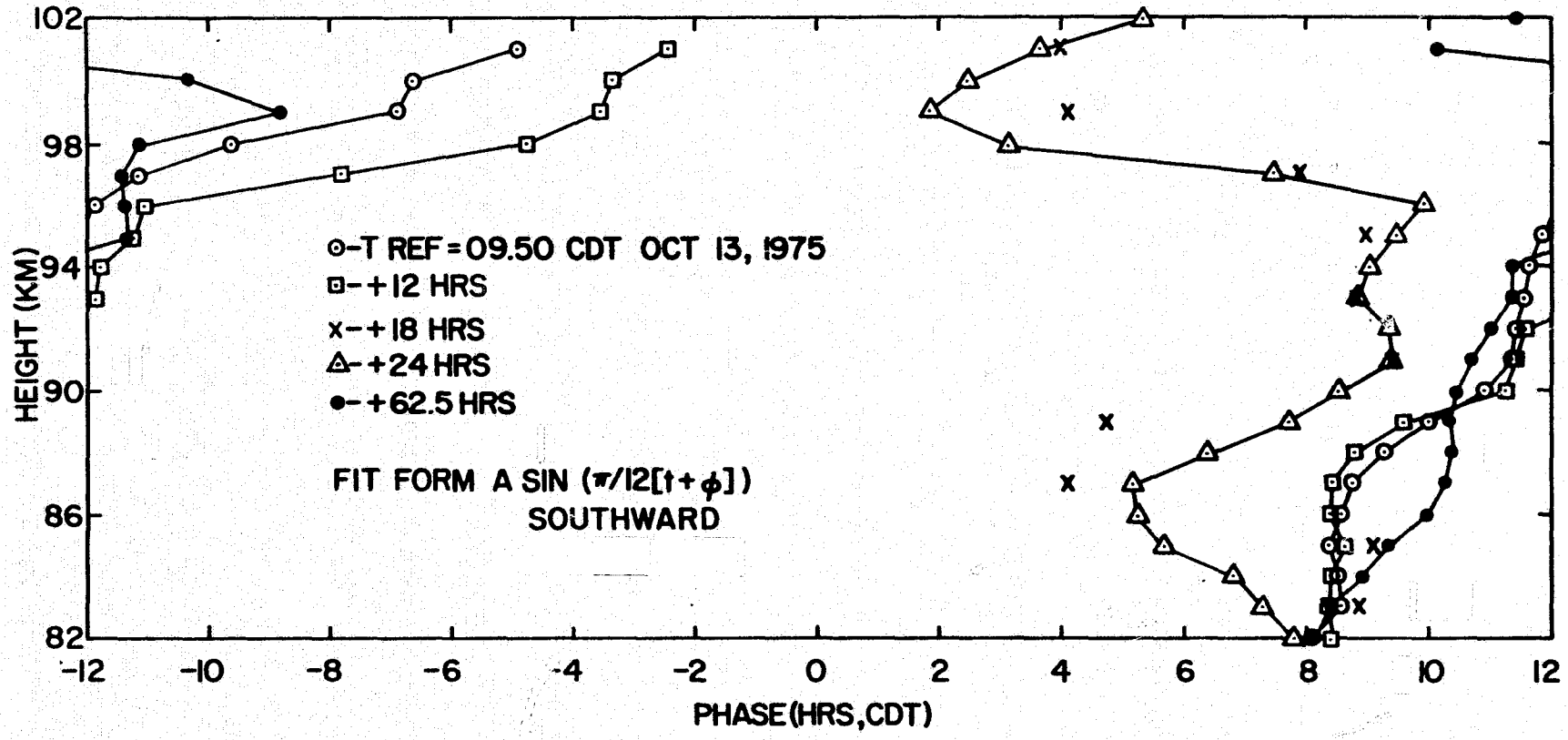

Figure 6.5 Diurnal tide phase at Urbana, October 13-18, 1975.

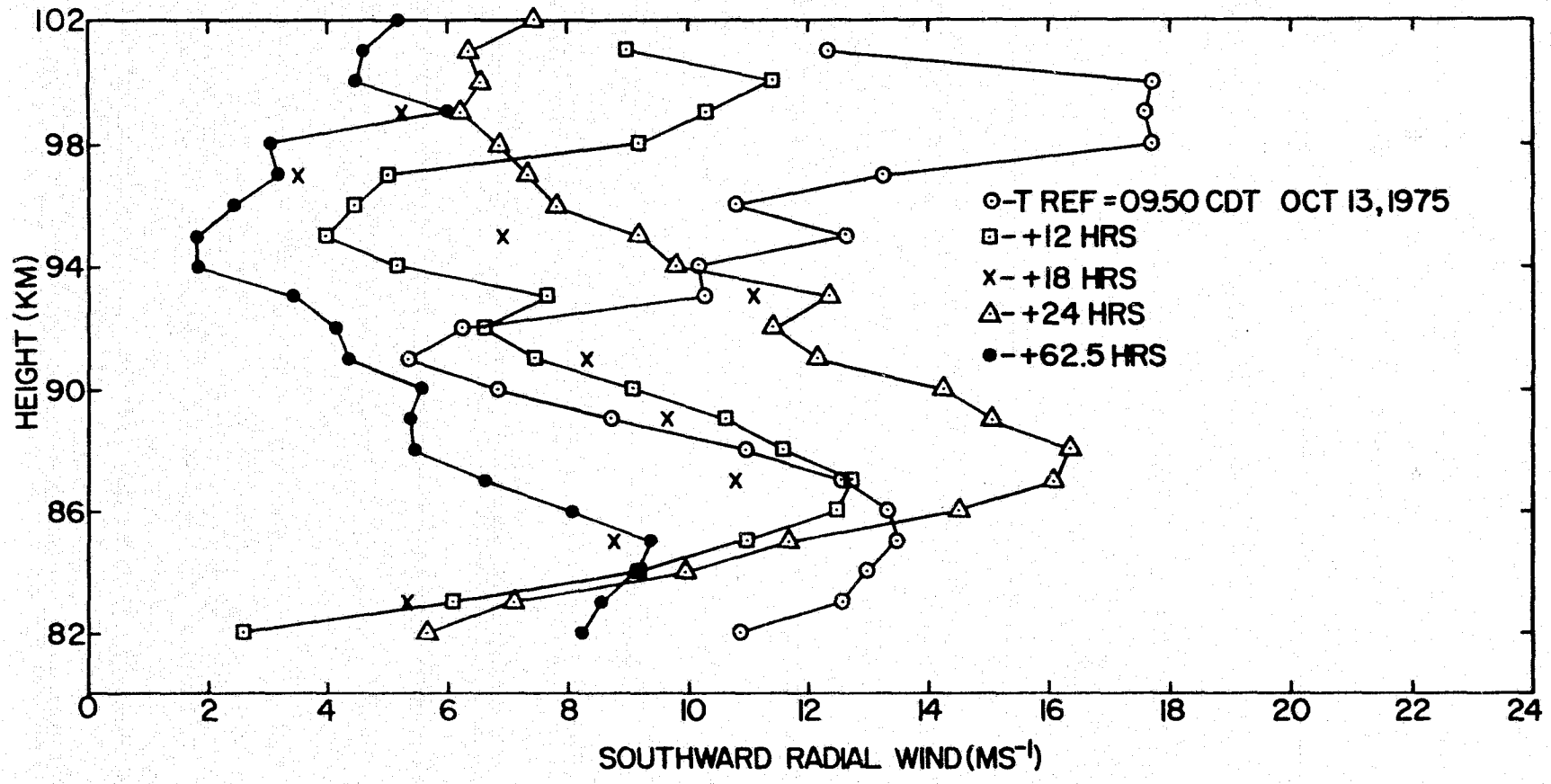

Figure 6.6 Semidiurnal tide at Urbana, October 13-18, 1975.

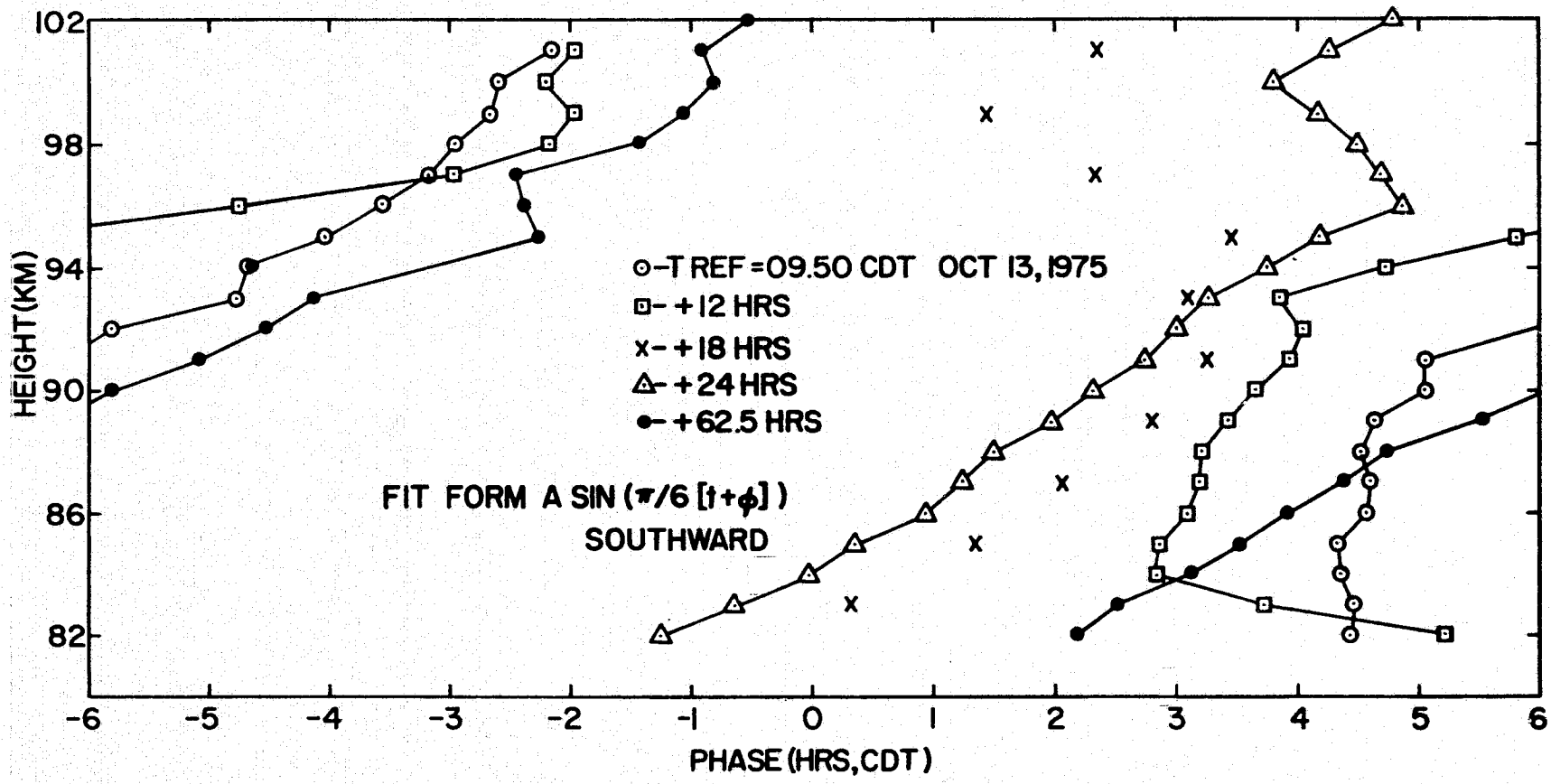

Figure 6.7 Semidiurnal tide phase at Urbana, October 13-18, 1975.

Table 6.8

Prevailing and tidal winds at Urbana, October 13-17, 1975.

Radial southward values, tidal form: $A\sin(\omega[t+\phi])$ -- local time: CDT

Height	Prevailing	$S_1(v)$		$S_2(v)$		$S_1(v)$		$S_2(v)$			
		A	ϕ	A	ϕ	A	ϕ	A	ϕ	A	ϕ
	Date--	13-17		13-17		13-15		16-17		13-15		16-17	
82	1.6	15.0	8.0	4.9	2.6	13.2	8.0	16.8	8.1	2.7	4.1	8.2	2.2
83	3.0	16.3	8.2	5.8	2.8	15.3	8.1	17.5	8.3	3.5	3.6	8.5	2.5
84	2.8	15.6	8.5	7.0	3.0	14.0	7.9	17.4	8.9	4.9	2.7	9.2	3.1
85	1.6	13.5	8.6	7.7	3.1	11.6	7.6	16.1	9.4	6.4	2.6	9.4	3.5
86	1.0	12.5	9.0	7.6	3.3	10.7	7.4	15.7	10.0	8.1	2.6	8.0	3.9
87	-0.3	11.6	9.3	7.1	3.3	8.5	7.6	16.0	10.2	9.1	2.6	6.6	4.4
88	-1.0	11.1	9.6	6.5	3.3	7.5	8.2	15.4	10.3	9.8	2.6	5.4	4.7
89	-1.5	11.3	9.9	5.8	3.8	7.4	9.0	15.5	10.3	9.4	2.9	5.4	5.5
90	-2.1	11.9	10.3	4.9	4.3	7.7	9.9	16.1	10.5	8.3	3.1	5.5	-5.8
91	-2.8	11.4	10.6	3.8	4.5	8.0	10.4	14.8	10.7	7.4	3.4	4.3	-5.1
92	-2.8	11.4	10.9	3.3	5.3	9.2	10.6	13.7	11.0	6.2	4.0	4.1	-4.5
93	-2.9	10.9	11.1	3.5	6.0	10.2	10.9	11.7	11.3	5.9	5.0	3.4	-4.1
94	-3.0	9.1	11.1	3.6	6.0	8.9	10.9	9.4	11.4	5.9	5.6	1.9	-4.7
95	-2.9	7.3	11.8	3.2	-4.9	8.5	11.1	6.4	-11.4	6.2	-5.5	1.8	-2.2
96	-2.4	5.6	11.9	3.4	-4.2	6.0	11.2	5.5	-11.4	5.7	-4.9	2.5	-2.4
97	-2.1	3.7	-11.8	3.9	-3.6	2.8	11.5	4.6	-11.4	5.5	-4.3	3.2	-2.4
98	-1.7	2.0	-10.9	4.2	-3.0	1.3	-10.5	2.7	-11.1	6.8	-3.6	3.0	-1.4
99	-2.3	1.4	-5.7	5.2	-2.1	2.2	-1.8	2.5	-8.9	6.1	-3.1	6.0	-1.1
100	-2.3	0.9	-5.5	4.4	-2.0	2.7	-0.8	2.7	-10.3	5.7	-2.8	4.4	-0.8
101	-2.2	1.1	5.1	3.4	-1.7	3.0	1.2	2.7	10.1	3.3	-2.9	4.6	-0.9

$\sigma|S_1(v)| = 2.8$ ms^{-1} $\quad \sigma\angle S_1(v) = 1.6$ hrs (24°)

% Var = 30.5

$\sigma|S_2(v)| = 2.6$ ms^{-1} $\quad \sigma\angle S_2(v) = 1.6$ hrs (47°)

% Var = 52.2

despite the fact that in winter and summer $S_2(v)$ is generally more stable than $S_1(v)$.

6.3 *The Terdiurnal Tide*

Amplitude and phase parameters for an eight hour tide are often simply the result of the assumed wind form used in least squares fitting to raw meteor wind data for extraction of the prevailing, diurnal, and semidiurnal wind components [*Müller*, 1968b; *Scholefield and Alleyne*, 1975]. While the presence of these latter three wind components is well known, we have no reason *a priori* to assume an eight hour tide is detectable, even if present. Including higher harmonics in our wind model does help us to more accurately resolve the prevailing, diurnal, and semidiurnal wind components (Section 3.1), but the significance of the higher harmonic parameters is questionable. Periodogram analyses at Adelaide generally show the eight hour component to be only marginally greater than the rms deviation. However, when monthly energy spectra for an entire year are averaged a consistent peak at eight hours appears and growth in intensity versus altitude is also evident. Thus it is concluded that the terdiurnal oscillation is a real feature of winds in the meteor region.

The physical nature of such an oscillation is open to question because eight hour waves could be internal gravity waves as well as tides. *Glass* [1973] has shown that the eight hour component is more stable than definite gravity waves and thus a tidal nature seems reasonable. But the vertical wavelength at Garchy is typically only 40 km, whereas a directly excited terdiurnal mode should theoretically have a very large vertical wavelength. Also the theoretical annual variation with phase reversals around the equinoxes is not seen [*Glass and Spizzichino*, 1974]. It is possible that eight hour wind components are the result of nonlinear interaction between

the diurnal and semidiurnal tides [*Spizzichino*, 1969, 1970a].

The University of Illinois results generally show linear phase versus height for the 3 osc-day^{-1} wind component. Furthermore, when the 3 osc-day^{-1} component is not wave-like 4 or 5 osc-day^{-1} wave-like components are present. The sole exception was Dec. 4-6, 1975. Such frequencies could be the result of background wind Doppler shifting of a 3 osc-day^{-1} wave.

Short period spectra illustrate the general dominance of the 3 osc-day^{-1} component and its growth with altitude. The October data confirms the persistence of the eight hour component. The vertical wavelengths given in Table 6.9 are generally short like those observed at Garchy. Table 6.9 also estimates the eight hour wavelength as the result of $S_1(v)$ and $S_2(v)$ nonlinear interaction. Good agreement between observed and predicted wavelength occurs in only three of the ten cases. But since nearly all the wavelength estimates involve substantial extrapolation, five other cases are in potential agreement with the nonlinear interaction hypothesis. The case of Oct. 15-17, 1975 is particularly interesting because here $S_3(v)$ seems to be composed of two superposed waves, one of extremely long wavelength as theoretically we would expect, and one of roughly 16 km wavelength like nonlinear interaction would produce. In two other cases, a standing wave pattern appears in $S_3(v)$ and this may also be the result of the presence of both types of waves just mentioned. It thus seems reasonable to conclude that nonlinear interaction of $S_1(v)$ and $S_2(v)$ is generally an important contributor to $S_3(v)$ behavior.

Solution of the dispersion equation for a frequency of 3 osc-day^{-1} gives a horizontal wavelength on the order of 3000 km for the vertical wavelengths we observe. If $S_3(v)$ is truly tidal in nature, the horizontal wavelength will be about 10,000 km at midlatitudes. We should be able to

Table 6.9

Terdiurnal tide wavelengths, actual, and nonlinear interaction estimate.

Date	λ_1	λ_2	λ_3 Actual	$(k_3^* = k_1 + k_2 \rightarrow \lambda_3^* = \lambda_1\lambda_2/(\lambda_1+\lambda_2)$ Nonlinear interaction estimate	decent agreement with hypothesis $\lambda_3 \simeq \lambda_3^*$
3-7,8-75	28 km	55 km	16.7 km	18.6 km	YES
4-4,5-75	40	88.9*	13.2*	27.6	
5-27,28-75	80	377	44.6	66	YES
7-30,31-75	85	128	36.8**	253 ($k_2=-2\pi/128$)	NO
8-21,22-75	82	203	74.6***	137.6 ($k_1=-2\pi/82$)	NO
9-13,14-75	27	78	36.1	20.0	NO
10-13,14-75	48	36	78.5	20.6	NO
14,15	184	41	31.0***	52.8 ($k_1=-2\pi/184$)	NO
15,17	105	24	$\sim$ evan. but sinusoidal perturb.	19.5	
1-14,16-76	108	78	42.7****	45.3	YES

* π shift in S_2 at 90.5 km
π shift in S_3^2 at 83.5 km

** S_2 downward

*** S_1 downward

**** π shift in ς_3 at 96 km
S_1 $\sim$ evan. 82-94

resolve winds at points in space separated horizontally by 150 km (± 30° azimuth spread, 150 km range). A phase difference of about 18 degrees for $S_3(v)$ implies it is an internal gravity wave. Such a difference might be detectable with our system, whereas the 5 degree difference for a true tide probably could not be discerned. Nevertheless it is apparent that the true nature of the oscillation could be tested.

6.4 *Space-Quadrature Winds*

A three-antenna interferometer configuration became operational in April, 1976. This configuration allowed us to measure both azimuth and elevation angles for each echo collected during the April 18-19, 1976 24-hour meteor-radar run. Consequently, it was possible to estimate both the meridional and zonal components of the prevailing and tidal winds. Figure 6.8 plots the hourly mean southward and westward horizontal winds averaged over all heights. The narrow spread in azimuth (0.39r standard deviation) makes the westward wind estimates typically a factor of 5 less precise than the northward wind estimates. Nevertheless, the substantial semidiurnal tidal component in the meridional wind is also clearly evident in the zonal wind, and it appears delayed by roughly 3 hours as classical tidal theory predicts for the northern hemisphere (clockwise phase rotation when viewed from above).

Table 6.10 summarizes the vertical structure of the prevailing, diurnal, and semidiurnal winds seen April 18-19, 1976 in both N-S and E-W directions. A hodograph of the prevailing component exhibits a clockwise rotation from lowest to highest heights. This is as expected for influence by the Coriolis force.

The 24-hour component was quite weak and, based on N-S results, had a relatively long vertical wavelength. In the E-W direction, an apparent

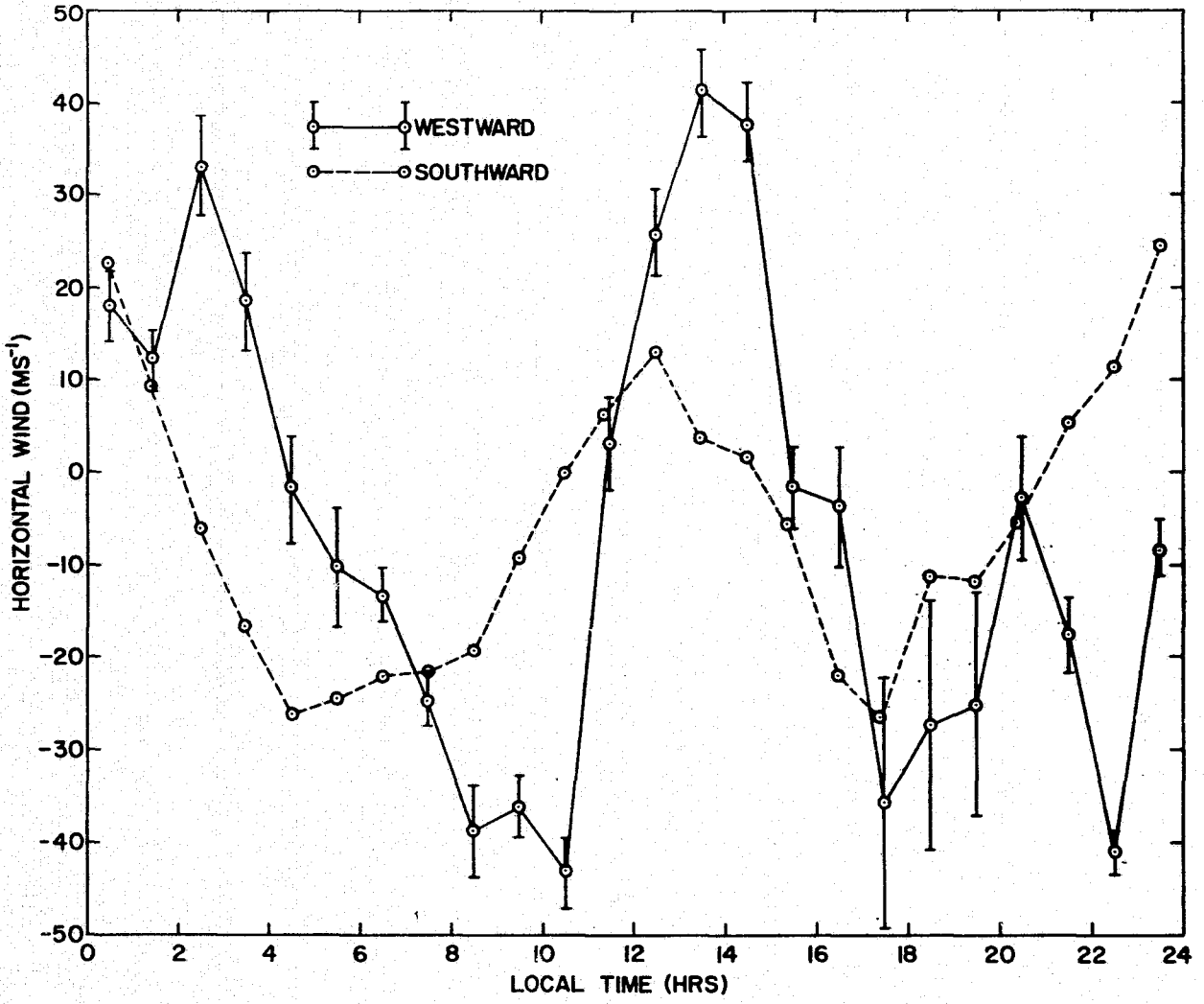

Figure 6.8 Space quadrature meteor winds at Urbana.

Table 6.10
Space quadrature wind components at Urbana.

Prevailing wind versus height

Height	Southward	Westward
82 km	-7.24(1.53)	8.58(5.95)
84	-1.72(1.21)	8.23(4.27)
86	-4.88(0.86)	6.50(2.98)
88	-5.62(0.76)	5.09(2.64)
90	-8.50(0.81)	-12.52(2.80)
92	-7.28(0.79)	-15.29(3.05)
94	-7.46(0.86)	-15.90(3.07)
96	-3.18(0.92)	-16.62(3.34)
98	-3.68(1.04)	- 6.23(4.03)
100	-6.14(1.81)	0.99(9.22)

Diurnal tide amplitude
and phase versus height

	Southward		Westward	
	A	ϕ	A	ϕ
82 km	5.37(1.86)	7.73(3.59)		
84	11.75(2.22)	9.17(0.64)		
86	7.64(0.16)	7.58(0.59)	7.83(4.30)	6.13(8.30)
88	5.22(0.58)	9.13(0.37)	5.56(8.43)	9.73(2.51)
90	3.44(0.50)	9.29(0.37)	5.45(10.84)	-0.93(2.02)
92	6.27(0.50)	9.79(0.07)	12.45(10.68)	-2.00(0.89)
94	5.37(0.44)	8.93(0.34)	10.50(10.09)	-2.51(2.14)
96	10.06(1.07)	10.87(0.07)	16.98(15.67)	-1.04(0.63)
98	11.03(1.27)	10.27(0.04)	8.45(12.31)	-6.18(11.96)
100	4.82(2.66)	9.17(1.82)		

Semidiurnal tide amplitude
and phase versus height

	A	ϕ	A	ϕ
82 km	6.58(2.17)	0.37(1.56)		
84	7.05(1.02)	-1.15(0.52)	39.50(35.96)	-3.52(0.85)
86	8.12(1.01)	0.67(0.32)	35.00(9.09)	-2.03(0.05)
88	13.22(1.10)	1.64(0.15)	42.19(2.10)	-1.26(0.24)
90	24.33(0.98)	2.64(0.06)	36.01(9.41)	0.18(0.58)
92	26.62(0.83)	2.77(0.04)	49.76(10.84)	0.60(0.57)
94	29.59(1.05)	2.87(0.04)	57.09(13.34)	0.94(0.56)
96	24.90(1.10)	3.06(0.05)	63.66(18.63)	1.54(0.55)
98	28.23(1.10)	3.62(0.03)	64.63(26.42)	1.78(0.73)
100	36.66(3.08)	3.77(0.02)		

Horizontal amplitudes in ms^{-1}, phase in hr, April 18-19, 1976 data

standing wave was seen at 90 km. Such diverse behavior is perhaps not real, but rather the result of poor precision in the westward component. Averaging from 86 to 98 km, the southward diurnal phase led the westward phase by 8.9 hours (classical theory predicts a 90° or 6-hour phase advance).

The 12-hour component was of appreciable magnitude and growing with altitude for both N-S and E-W directions. The westward amplitudes seem uniformly high despite the large error bars. This may be indicative of an overestimation bias when we estimate E-W winds from data with only a small azimuth spread about due north. Averaging from 86 to 98 km, the southward semidiurnal phase led the westward phase by 2.22 hours. The N-S estimate for vertical wavelength is about 45 km, the E-W estimate only 32 km. Both estimates suggest a high order mode character to the tide, probably (2,4) or (2,6).

No wave-like behavior at 3 cycles/day was noted in either spatial direction, but 4 cycles/day gave linear phase variation versus height for N-S data (50 km vertical wavelength length) and was quite strong in both southward and westward directions. Power law fits of spectral energy versus frequency give exponents of -1.14 for N-S data and -1.34 for E-W data (see Section 7.3.3). These data from 3 cycles/day to 24 cycles/day have a positive correlation coefficient of 0.35.

7. INTERNAL ACOUSTIC-GRAVITY WAVES IN THE UPPER ATMOSPHERE

7.1 *Review of Internal Acoustic-Gravity Wave Theory*

The purpose of this section is to present a simple mathematical development which leads to the salient features of internal acoustic-gravity waves. In sound waves, a continuous exchange of kinetic energy due to wave motion and potential or stored energy due to compression of the medium occurs. In the presence of a gravitational field, energy can be stored by raising fluid mass. If the medium density varies with height, as in the earth's atmosphere, an exchange of less dense fluid with more dense fluid can result in energy storage. It is this potential energy storage mechanism which is important in considering internal acoustic-gravity waves. Gravity waves can only exist in a medium which is stably stratified, so that a fluid parcel which is displaced vertically from its equilibrium level will experience a net force tending to return the parcel to its equilibrium level.

Rayleigh first discussed gravity waves in incompressible media and Lamb generalized the theory to handle compressible fluids. A classic paper by *Hines* [1960] showed that the irregular winds observed via meteor trail photographs could be explained by gravity wave theory and stimulated substantial theoretical and observational interest in gravity waves. Many of the theoretically predicted features of internal gravity waves have been verified experimentally (see, for example, *Mowbray and Rarity* [1967]).

We begin by noting the three basic equations necessary to describe the dynamics of atmospheric waves; namely, Newton's second law, energy conservation, and mass conservation [*Holton*, 1972]:

$$\rho \frac{d\vec{V}}{dt} = \rho\vec{g} - \vec{\nabla}p - \rho 2\Omega \times \vec{V} + \vec{F} \tag{7.1}$$

$$\frac{dp}{dt} = c^2 \frac{d\rho}{dt} \tag{7.2}$$

$$\frac{d\rho}{dt} + \rho\vec{\nabla}\cdot\vec{V} = 0 \tag{7.3}$$

where

ρ = mass density

$\vec{V}$ = air velocity vector with components u, v, w relative to the earth's rotating reference frame

$\vec{g}$ = vector of acceleration due to gravity

p = pressure

$\vec{\Omega}$ = vector angular velocity of the earth's rotation

$\vec{F}$ = vector of acceleration due to external forces, for example, friction

$\frac{d}{dt}$ = total derivative operator, $\left(\frac{\partial}{\partial t} + \vec{V}\cdot\vec{\nabla}\right)$

c = speed of sound.

Equations (7.1) through (7.3) are based on the "hydrodynamic" approximation, that is we consider only phenomena on a scale much larger than molecular. Equation (7.2) combines the first law of thermodynamics for adiabatic motion with the equation of state for an ideal gas.

To simplify the solution of equations (7.1) through (7.3), we adopt the following six assumptions [*Georges*, 1967]:

1. Time-dependent quantities have magnitudes much smaller than the corresponding basic state parameters; that is, they are of "perturbation magnitude". This assumption allows all dependent variables to be represented by the sum of a basic state and a perturbation,

$$( ) = ( )_o + ( )' \tag{7.4}$$

where

$$\frac{\partial( )}{\partial t} \cong \frac{\partial( )'}{\partial t} \text{ and } ( )' << ( )_o, \text{ except that } v_o = 0.$$

Hence it is possible to linearize equations (7.1) through (7.3) about the basic state.

2. All derivatives with respect to y are zero. This reduces the problem to just two dimensions, x horizontal and z vertical. We then have a wind vector $\vec{V} = u'\hat{i} + w'\hat{k}$.

3. We seek only wavelike solutions, so we assume

$$\frac{p'}{p_o P} = \frac{\rho'}{\rho_o R} = \frac{u'}{U} = \frac{w'}{W} = A \exp[i(\omega t - k_x x - k_z z)] \tag{7.5}$$

where

P, R, U, W are new variables introduced for convenience

k_x, k_z are complex wave numbers

ω = atmospheric wave radian frequency

A = amplitude constant.

Further, we apply the "ray theory" *WKB* approximation by assuming $\vec{k}=k_x\hat{i}+k_z\hat{k}$ is not a strong function of either x or z. That is, the properties of the medium do not change appreciably within a wavelength. Thus we may write perturbation time and space derivatives as

$$\frac{\partial}{\partial t}\,(\;)' = i\omega(\;)' \tag{7.6}$$

$$\vec{\nabla}\cdot\,(\;)' = -i(k_x\hat{i}+k_z\hat{k})(\;)' \tag{7.7}$$

4. We consider only portions of the atmosphere that are isothermal ($\vec{\nabla}T_o=0$) and in hydrostatic equilibrium ($\rho_o\vec{g} = \frac{\partial p_o}{\partial z}\hat{k}$). Furthermore, basic state quantities vary only with height (p_o, $\rho_o \propto \exp[-z/H]$, $H=RT_o/g$),

$$\vec{\nabla}(\;)_o = \frac{\partial(\;)_o}{\partial z} \tag{7.8}$$

5. The earth's rotation has negligible effect ($\vec{\Omega}\cong 0$). This is reasonable for wave periods less than a few hours or horizontal wavelengths under

a few hundred kilometers.

6. There are no damping processes ($\vec{F}$=0) or heat sources (adiabatic motion).

Applying these assumptions results in four equations, which in matrix form are written

$$\begin{bmatrix} \omega & o & -k_x gH & o \\ o & i\omega & -g-ik_z gH & g \\ o & -g+\gamma g & i\omega gH & -i\omega\gamma gH \\ -ik_x & -\frac{1}{H}-ik_z & o & i\omega \end{bmatrix} \begin{bmatrix} U \\ W \\ P \\ R \end{bmatrix} = [0] \qquad (7.9)$$

where

$\gamma = c_p/c_v$, ratio of specific heats

H = atmosphere scale height.

For a nontrivial solution of this system to exist, the determinant of the coefficient matrix must vanish. This condition yields the dispersion relation [*Hines*, 1960]

$$\omega^4 - \omega^2 c^2 (k_x^2 + k_z^2) + (\gamma-1) g^2 k_x^2 + i\gamma g \omega^2 k_z = 0 \qquad (7.10)$$

Since we have already assumed an isothermal basic state and neglected dissipation, it is reasonable to consider k_x entirely real. Two possible solutions to (7.10) then exist:

1. $Re(k_z) = 0$
2. $Im(k_z) = 1/2H$

The former is the Lamb wave solution. The latter holds for a propagating wave and is therefore of the most interest. It illustrates the interesting property of velocity perturbation amplitude growth with height, since $(u,w)' \propto \exp(z/2H)$. This results from the assumptions of no dissipation, because

that implies $\rho|\vec{V}| \equiv \rho|\vec{V}'|^2 = \text{constant}$, and $\rho \propto \exp(-z/H)$. Thus waves unimportant at low heights will tend to dominate in the upper atmosphere until dissipation becomes important.

Noting the following definitions for buoyancy frequency and acoustic frequency,

$$\omega_B^2 \triangleq (\gamma-1)g^2/c^2$$
$$\omega_a^2 \triangleq \gamma g/2c$$

and considering only propagating waves, the dispersion relation can be rewritten as

$$\frac{\omega^2}{c^2} - \omega^2(\tilde{k}_x^2+\tilde{k}_z^2) + \omega_B^2\tilde{k}_x^2 - \omega^2\omega_a^2/c^2 = 0 \qquad (7.11)$$

where

$$\tilde{(\ )} = Re(\ ).$$

For an incompressible medium $c^2 \to \infty$ and (7.11) reduces to

$$\omega^2 = \frac{\omega_B^2\,\tilde{k}_x^2}{\tilde{k}_x^2+\tilde{k}_z^2} \to \omega \lesseqgtr \omega_B \text{ for } \tilde{k}_z \text{ real} \qquad (7.12)$$

the dispersion relation for pure internal gravity waves. For the pure acoustic case let $g \to 0$ but keep $\omega_a \neq 0$ so stratification remains. (7.11) becomes

$$\omega^2 = \omega_a^2 + c^2(\tilde{k}_x^2+\tilde{k}_z^2) \to \omega \gtreqless \omega_a \text{ for } \tilde{k}_z \text{ real} \qquad (7.13)$$

To more clearly see the separation between the acoustic and internal gravity wave regimes we note that (7.11) can be written as

$$\frac{\tilde{k}_x^2}{l^2} + \frac{\tilde{k}_z^2}{m^2} = 1 \qquad (7.14)$$

$$l^2 = \frac{\omega^2 - \omega_a^2}{c^2(1-[\omega_B/\omega]^2)}$$

$$m^2 = (\omega^2 - \omega_a^2)/c^2$$

(7.14) is an equation for a general conic section. The four possible forms are:

1. l^2, $m^2 > 0$ $(\omega > \omega_a > \omega_B)$ → ellipse
2. $l^2 > 0$, $m^2 < 0$ $(\omega < \omega_B < \omega_a)$ → hyperbola
3. $l^2 < 0$, $m^2 > 0$ $(\omega_B > \omega_a)$ → hyperbola
4. l^2, $m^2 < 0$ $(\omega_a > \omega > \omega_B)$ → no real solutions

Furthermore, since $\omega_B > \omega_a \rightarrow \gamma > 2$ and this is not consistent with the value of $\gamma = 7/5$ for a diatomic atmosphere, we discard solution 3. Figure 7.1(a) illustrates the important property of internal gravity waves wherein vertical components of phase velocity and group velocity are oppositely directed. Also note that the asymptotic solution of (7.14) for the internal gravity wave case gives

$$\theta_a' = \tan^{-1} \left([\omega_B/\omega]^2 - 1 \right)^{\frac{1}{2}} \tag{7.15}$$

where

θ_a' is the "launch angle" with respect to ground for the bulk of the energy of nearly pure internal gravity waves.

To find the air motions of acoustic-gravity waves we return to the set of equations in (7.9) and treat W as known. Utilizing the first, third, and fourth rows we obtain the matrix equation

$$\begin{bmatrix} k_x gH & o & -\omega \\ i\omega & -i\omega\gamma & o \\ o & i\omega & -ik_x \end{bmatrix} \begin{bmatrix} P \\ R \\ U \end{bmatrix} = \begin{bmatrix} o \\ (1-\gamma)/H \\ \frac{1}{H} + ik_z \end{bmatrix} W \tag{7.16}$$

Using Cramer's Rule we can solve for the ratios

$$P/W = \frac{\gamma\omega^2 k_z - i\omega^2/H}{\omega^3 - \gamma g H k_x^2 \omega} \tag{7.17}$$

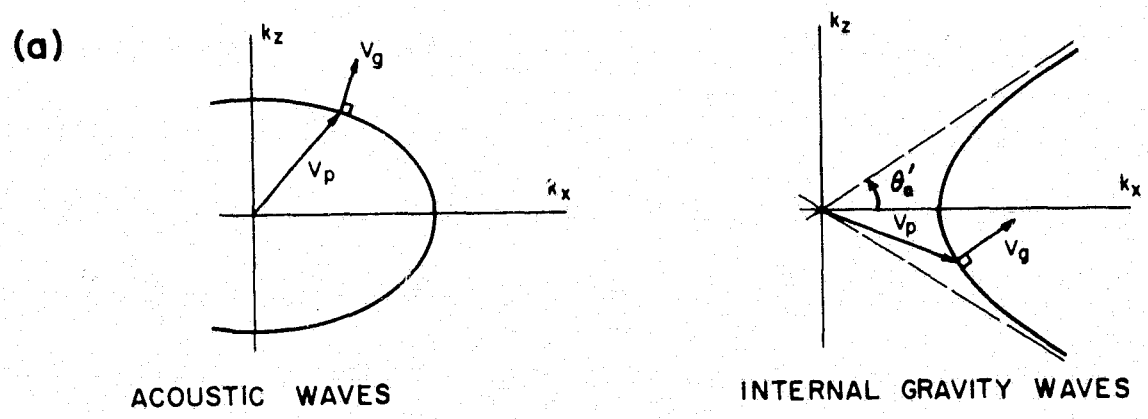

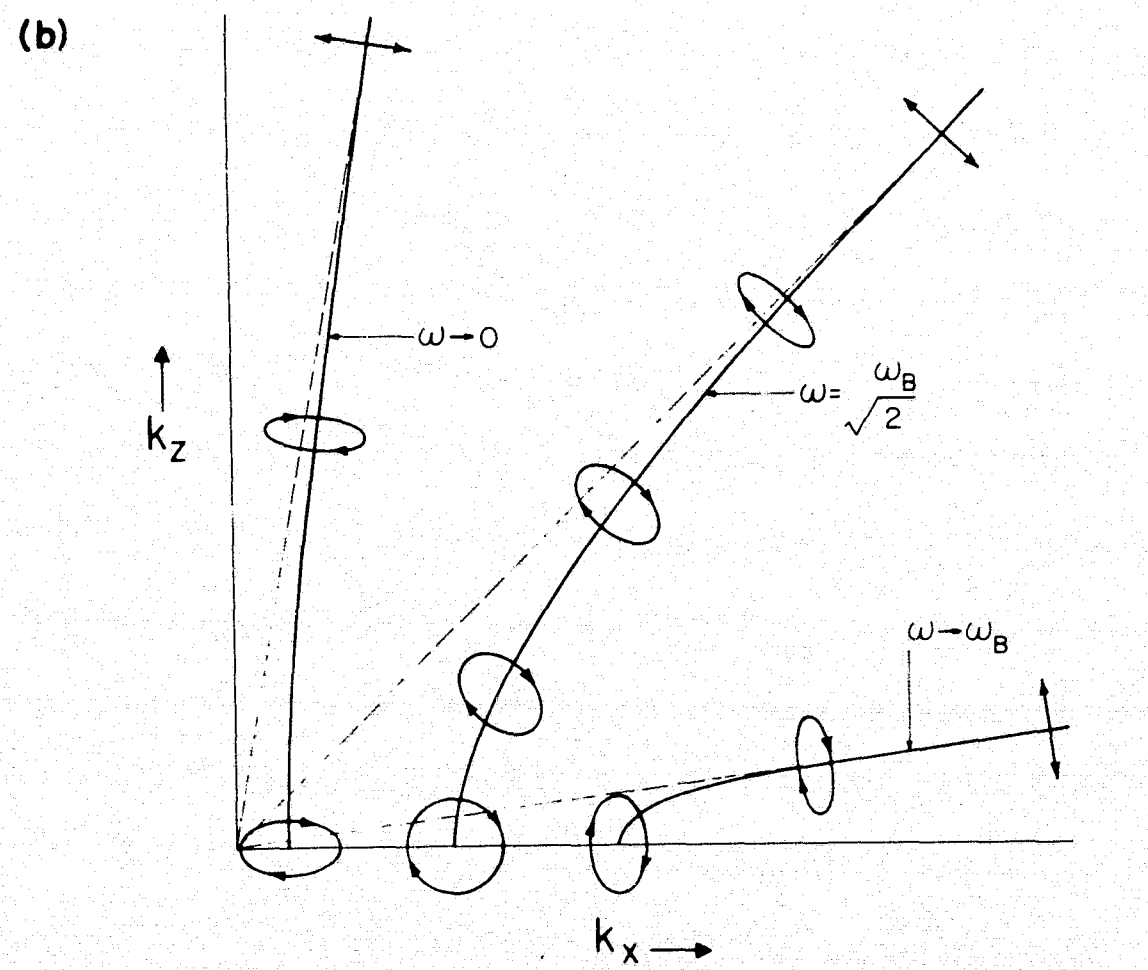

Figure 7.1 (a) The relations between the directions of group and phase propagation for acoustic and internal gravity waves [*Georges*, 1967], (b) Typical air-parcel orbits superimposed on the propagation diagram [*Georges*, 1967].

$$U/W = \frac{\omega\, \gamma g H k_x k_z - i g k_x \omega}{\omega^3 - \gamma g H k_x^2 \omega} \tag{7.18}$$

$$R/W = \frac{\omega^2 k_z - i\omega^2/gH - [(1-\gamma)/\gamma H][i\gamma g H k_x^2 - i\omega^2]}{\omega^3 - \gamma g H k_x^2 \omega} \tag{7.19}$$

These are the "polarization relations" developed by *Hines* [1960]. Since the denominators of (7.17) through (7.19) are identical we can identify them with W. Also note that for $c^2 \to \infty$, as in the case of pure internal gravity waves,

$$\frac{U}{W} \to \frac{-k_z}{k_x} = \frac{-\tilde{k}_z - i/2H}{\tilde{k}_x} \tag{7.20}$$

For simplicity we can let $|W| = 1$, that is, let $w = Re(e^{i\omega t}) = \cos \omega t$, where the small case w refers to the actual physical wind parameter. Thus

$$u = Re \left[\left(\frac{-\tilde{k}_z - i/2H}{\tilde{k}_x} \right) e^{i\omega t} \right] = \frac{-\tilde{k}_z}{\tilde{k}_x} \cos\omega t + \frac{\alpha}{\tilde{k}_x} \sin\omega t \tag{7.21}$$

where

$$\alpha \triangleq 1/2H$$

But since $w = \cos \omega t$

$$u^2 + \frac{2\tilde{k}_z}{\tilde{k}_x} uw + \left(\frac{\tilde{k}_z^2 + \alpha^2}{\tilde{k}_x^2} \right) w^2 = \alpha^2/\tilde{k}_x^2 \tag{7.22}$$

Furthermore, the dispersion relationship for pure internal gravity waves shows

$$\frac{\tilde{k}_z^2 + \alpha^2}{\tilde{k}_x^2} = \frac{\omega_B^2}{\omega^2} - 1 \tag{7.23}$$

Hence the air parcel orbits are described by [*Tolstoy*, 1963]

$$u^2 + w^2 \left(\frac{\omega_B^2}{\omega^2} - 1 \right) + 2 \frac{\tilde{k}_z}{\tilde{k}_x} uw = \frac{\alpha^2}{\tilde{k}_x^2} \tag{7.24}$$

For $w < w_B$ (7.24) is an ellipse. Figure 7.1(c) shows typical air-parcel orbits superimposed on the propagation diagram. We see that internal gravity waves are essentially vertically transverse waves.

A very important result is seen when the effect of mean winds on gravity waves is analyzed. Retaining the *WKB* approximation, if we let

$$\vec{V} = \vec{V}_o(z) + \vec{U}(x,z,t) = V_{ox}\hat{i} + V_{oz}\hat{k} + \vec{U}$$

$$|\vec{U}|/|\vec{V}_o| << 1 \qquad (7.25)$$

and $$\frac{dV_{oz}}{dz} = \dot{V}_{oz} = 0 \quad \text{(zero vertical wind)}$$

Equation (7.9) is modified to

$$\begin{bmatrix} ik_x gH & o & -\dot{V}_{ox} & -i\omega_d \\ ik_x gH + g & -g & -i\omega_d & o \\ i\omega_d & -i\gamma\omega_d & -\frac{1}{H} + \frac{\gamma}{H} & o \\ o & i\omega_d & -\frac{1}{H} - ik_z & -ik_x \end{bmatrix} \begin{bmatrix} p_1 \\ \rho_1 \\ U_z \\ U_x \end{bmatrix} = [0] \qquad (7.26)$$

where

$$p_1 = p'/p_o$$

$$\rho = \rho'/\rho_o$$

$$\omega_d = w - k_x V_{ox} = \text{Doppler shifted wave frequency}$$

The dispersion relation of (7.26) for k_x real requires

$$Im(k_z) = \frac{1}{2H} - \frac{\dot{V}_{ox} k_x}{2\omega_d}$$

for a propagating wave. However, a problem is obvious if $\omega_d \to 0$ and such a phenomena can occur at so-called critical levels. Here the wave orbit would tend to be thin and horizontal and assume the characteristics of the mean

flow. *Booker and Bretherton* [1967] show that propagation through such a level is possible, but only at the expense of a severe attenuation in wave momentum flux. *Grimshaw* [1975] considers the critical layer absorption problem without resorting to linearization techniques. He finds that large-amplitude internal gravity waves can cause changes in the mean flow even in the absence of any initial shear. The changes can introduce shear (and possibly even a critical level) in magnitudes sufficient to cause absorption or "self-destruction" of the wave. Numerical studies of such destruction have also been made by *Jones and Houghton* [1971] and *Breeding* [1972].

A more detailed analysis of the influence of background winds on internal gravity waves is given by *Jones* [1969]. Here the geometric optics and ray tracing approximations are used to describe the behavior of internal gravity waves in fluids with general spatial and temporal variations in mean flow. Jones shows that for internal gravity waves of modest scale (vertical wavelengths $\leq$ 5 km, horizontal wavelengths $\leq$ 50 km), deformational flow in the mean wind will in general stretch the wavenumber, or equivalently shrink the wavelength. A cascade of energy toward higher wave numbers results as in turbulence. Time scales for "wave shrinking" are on the order of hours to days depending on the strength of mean flow deformations. In meridional flow, tides are dominant features in the background wind. However, Jones' analysis indicates that while wave frequency ω will be modulated by the tidal frequencies, the observed or intrinsic wave frequency ω_d will essentially be unchanged.

The response of the upper atmosphere to acoustic-gravity waves excited by various sources is studied by *Liu and Klostermeyer* [1975]. Realistic thermospheric conditions are modeled by allowing for losses due to viscosity, thermal conduction, and ion drag and including the effects of vertical

temperature variations and winds. It is found that the transfer function of the atmosphere is peaked in wave-number space, indicating strong filtering effects, and highly dependent on background wind structure.

7.2 *Partial Reflections of Internal Gravity Waves*

Consider an upward propagating internal gravity wave of the form

$$A \exp(z/2H) \exp[i(\omega t + \tilde{k}_z z + \tilde{k}_x x)] \tag{7.27}$$

with radian frequency ω, vertical wavenumber $\tilde{k}_z$, and horizontal wavenumber $\tilde{k}_x$. Also consider a vertically reflected wave

$$A \exp(z/2H) \exp[i(\omega t - \tilde{k}_z z + \tilde{k}_x x)] \, R_a \exp(-2i\alpha) \tag{7.28}$$

where $R_a \exp(-2i\alpha)$ is the complex reflection coefficient. The observed wave will be the superposition of (7.27) and (7.28):

$$V(z,t)\big|_x = A \exp(z/2H) \exp[i(\omega t + \tilde{k}_x x)] \{\exp(i\tilde{k}_z z) + R_o \exp[-i(\tilde{k}_z z + 2\alpha)]\} \tag{7.29}$$

Without loss of generality we can take x to be zero and remove the time factor by considering the wave envelope versus altitude:

$$V(z) = A \exp(z/2H) \{\exp(i\tilde{k}_z z) + R_a \exp[-i(\tilde{k}_z z + 2\alpha)]\} \tag{7.30}$$

We desire to express (7.30) in the form

$$V(z) = |V(z)| \exp[i(\tilde{k}_z z + \psi)]$$

Factoring (7.30) we obtain

$$|V(z)| = A \exp(z/2H) \left(1 + R_a^2 + 2R_a \cos[2(\tilde{k}_z z + \alpha)]\right)^{1/2} \tag{7.31}$$

and

$$\tan^{-1}\psi = \frac{R_a \sin[2(\tilde{k}_z z + \alpha)]}{1 + R_a \cos[2(\tilde{k}_z z + \alpha)]} \tag{7.32}$$

Nonlinear curve-fitting can be used to evaluate A, H, R_a, $\tilde{k}_z$, and α in (7.31) from meteor radar data [*Revah*, 1970].

7.3 *Discussion of Short Period Observations*

7.3.1 *Garchy studies.* The most informative meteor-radar studies thus far made on internal gravity waves have been those of *Revah* [1969]. He calculated the zonal wind power spectrum for various observational periods and identified spectral peaks as potential propagating waves. The wave form

$$u(t,z) = U(z) \sin (2\pi t/T + \phi(z))$$

was then fitted to the observed winds for each potential oscillation period T. If a pseudo-linear vertical phase variation was found for $\phi(z)$, then one could be confident that indeed a propagating wave was present. Phase slopes indicative of upward energy propagation were found for nearly all waves. The amplitude patterns generally appeared to be the result of weak reflections. On numerous occasions the gravity wave amplitude appeared to grow more rapidly with height than a reasonable scale height could permit. This prompted the interpretation by *Spizzichino* [1969,1970a] that perhaps diurnal tidal energy was being cascaded into the gravity wave regime. If such were the case, the resulting gravity waves might be of vertical wavelengths similar to $S_1(v)$ and in fact that is what Revah observed. This assumes the internal gravity wave vertical wavelengths prior to interaction are large relative to those of the diurnal tide. A second possibility is that the waves are generated *in situ* by non-linear effects in the diurnal tide [*Lindzen*, 1968]. This possibility is enhanced by the fact that all waves had frequencies close to harmonics of the diurnal tide and phase coherency periods on the order of two days.

The hourly rate of only 5-50 usable echoes at Garchy precludes detection of gravity waves with periods under about 2 hours. And in fact, even

for the longest periods of eight hours, the detection and characterization of the waves is highly statistical in nature.

7.3.2 *Jicamarca studies.* *Rastogi and Bowhill* [1976] utilized the incoherent scatter facility at Jicamarca, Peru to probe for gravity waves in the equatorial mesosphere. Much smaller spatial volumes could be probed than with our meteor-radar facility and a time resolution of one minute was attained. For frequencies less than the Brunt-Vaisala frequency f_B, the spectra are comprised of

(1) a secular change with a period $\sim$ 1 hr dominant in some cases, weak in others

(2) a Gaussian peak centered at zero frequency with half power width roughly 7 osc-hr^{-1}

(3) a third component, centered at 5-6 osc-hr^{-1} at 80 km and 3-4 osc-hr^{-1} at 70 km, predominant in the vertical and meridional directions.

On March 25, 1972 a well-defined acoustic-gravity wave packet was observed for one half hour beginning at 1200 hr. This accounts for the distinct spectral peak at frequencies above the acoustic cutoff frequency f_a. The spectral trough between f_a and f_B is as predicted by linear gravity wave theory.

Using the theoretical dispersion and polarization relations for atmospheric gravity waves, it is shown that the waves comprising spectral component (3) are vertically evanescent and have horizontal wavelengths of 200-300 km at periods near 15 minutes. Height variation of the frequency at which the power spectrum peaks is explained in terms of Doppler shifts caused by the background wind vertical shear. Gravity wave propagation opposite to the zonal flow, i.e., from west to east, is necessary to support that explanation.

7.3.3 *Urbana studies.* Table 7.1 tabulates vertical phase and amplitude structure of typical potential gravity waves observed by the University of Illinois meteor-radar system. Even though our echo rate is typically four to five times that of Garchy, we only consider periods down to 1 hour credible in our analysis of 24 hour data records. This is in part due to the appreciable diurnal fluctuation in echo rate we experience and in part due to the large correction factors needed to compensate for the low pass filter action of our two-dimensional wind interpolation (Section 3.1) as the period decreases. Our observations confirm the weak reflection evidence reported by *Revah* [1969]. In fact, on several occasions reflection seems to be strong enough to cause a full 180° phase shift at certain altitudes. Contrary to the French results we do not find evidence of excessive growth of wave amplitude with height. When our amplitude data is fitted to equation (7.31) scale heights too large rather than too small seem to predominate (Table 7.2). Actually a curve fit to the form in equation (1) in *Fellous et al.* [1975] would be more proper, because by ignoring our phase data, misleadingly short vertical wavelengths can result. Compare the estimated vertical wavelengths of Table 7.2, obtained through the use of amplitude data only, with those in Table 7.3, obtained by a straight-line fit to $\phi(z)$. When the waves noted in *Revah* [1969] are classified into the categories of growth, constant, and decay versus altitude, 31 out of 55 are seen to exhibit clear growth. In our case 25 out of 63 exhibit clear growth. However, as Section 6.4 notes, the 8 hour oscillations are probably manifestations of the terdiurnal tide rather than true gravity waves, and thus only about a third of our gravity waves exhibit growth in amplitude through the meteor zone. Such behavior is in line with the theoretical results of *Thomson* [1976], who showed that randomness in the wind leads to a dissipation

Table 7.1

Sample short period wave amplitude and phase height structure.

(a) October 13-14, 1975

Height km	3 c/d A	3 c/d φ	7 c/d A	7 c/d φ	12 c/d A	12 c/d φ	13 c/d A	13 c/d φ	17 c/d A	17 c/d φ
82	5.34	-63.31	2.48	- 36.38						
83	4.39	-48.62	2.97	- 45.30						
84	4.51	-53.53	2.26	- 38.32						
85	5.97	-60.92	1.78	19.27						
86	6.04	-58.02	2.09	25.68	1.18	147.01	1.05	2.52	.62	115.18
87	6.13	-55.11	2.06	30.75	1.50	153.06	1.10	32.16	.85	171.65
88	5.80	-46.96	1.93	53.01	1.94	160.00	1.30	49.61	.80	-145.28
89	5.50	-36.80	2.53	70.81	1.98	-178.22	2.05	71.85	1.08	-123.74
90	5.13	-17.55	3.00	87.40	1.31	-151.28	1.86	92.87	1.00	- 66.66
91	5.02	- 7.44	3.77	90.00	1.01	-155.25	1.78	76.33	1.25	- 26.35
92	6.09	8.11	4.16	100.87	.67	-157.06	1.27	68.61	1.55	- 3.85
93	7.04	20.19	3.52	86.01	.83	- 82.14	1.36	83.37	.78	- 4.91
94	6.72	16.98	3.04	76.92	1.55	- 74.52	2.33	94.52	.96	53.27
95	7.62	13.19	2.79	89.70	1.86	- 20.22	2.81	121.04	1.22	68.04
96	8.68	8.15	2.01	135.16	2.52	3.29	2.78	134.73	1.32	59.39
97	10.43	3.95	2.46	158.50	3.66	19.95	2.56	143.55	1.72	58.36
98	13.78	3.96	1.91	-142.03	2.94	18.54	2.76	125.12	2.68	52.27
99	14.78	4.93	.52	-133.95	1.39	53.78	2.56	93.57	3.28	64.01
100	13.59	3.12	1.27	- 57.54	.41	62.51	2.69	87.56	3.34	67.83
101	10.74	11.93	.88	- 72.42	2.82	164.75			3.27	84.83
102			.94	- 34.66	1.13	-143.01	1.36	95.80	1.82	85.99

(b) January 21-23, 1976 partial listing

Height km	3 c/d A	3 c/d φ	4 c/d A	4 c/d φ	6 c/d A	6 c/d φ	7 c/d A	7 c/d φ
82							3.99	-45.31
83			2.67	-87.43			3.56	-35.42
84			5.43	-72.44			2.76	2.58
85			6.08	-69.45			2.81	24.92
86			6.46	-74.79			2.74	55.54
87			5.62	-75.87			3.04	76.56
88			4.35	-61.54	2.65	-42.41	3.01	78.73
89			4.43	-51.91	2.20	-60.61	3.85	66.34
90			5.02	-21.39	1.63	-32.41	3.17	52.90
91			5.11	0.53	1.01	51.26	3.23	50.86
92			5.15	17.77	3.03	75.11	2.73	49.34
93			4.42	38.89	2.98	105.35	3.40	44.98
94			4.73	46.86	4.44	122.79	3.17	28.07
95	2.72	118.76			3.88	141.68	3.69	42.94
96	3.60	130.76			2.62	131.51	2.84	55.04
97	5.04	136.47					2.84	85.32
98	6.30	133.76					3.98	87.84
99	6.56	139.13					4.84	97.72
100	6.57	143.43					5.73	107.60
101	6.32	167.36					4.78	110.40
102	4.05	176.58					3.71	106.12

Table 7.2

Least square curve fit parameters for partially reflected internal gravity waves.

	A	H	R_a	$\tilde{k}_z$	α	$\lambda_z = 2\pi/\tilde{k}_z$
Jan. 17, 18						
5 c/d	6.72	$\sim \infty$	0.43	0.27	0.97	23.27 km
17 c/d	2.06	$\sim \infty$	0.40	0.21	0.68	29.72
Feb. 28, March 1						
10 c/d	1.76	8.24	0.45	0.28	-0.12	22.44
12 c/d	1.15	17.19	0.66	0.33	0.17	19.04
March 7, 8						
3 c/d	1.44	6.39	0.35	0.34	-0.79	18.48
April 4, 5						
3 c/d	1.91	$\sim \infty$	0.54	0.32	1.05	19.63
7 c/d	1.77	13.28	0.28	0.47	0.37	13.37
May 27, 28						
3 c/d	0.96	4.09	0.24	0.55	1.05	11.42
July 14, 15						
5 c/d	2.07	$\sim \infty$	0.26	0.65	1.66	9.67
7 c/d	1.99	$\sim \infty$	0.69	0.33	3.64	19.04
10 c/d	2.45	$\sim \infty$	0.46	0.61	-0.34	10.30
July 30, 31						
3 c/d	6.86	$\sim \infty$	0.28	0.22	1.87	28.56
5 c/d	4.24	28.88	0.37	0.35	-0.43	17.95
12 c/d	1.86	$\sim \infty$	0.39	0.41	3.89	15.32
18 c/d	0.77	20.46	0.32	0.64	1.98	9.82
Aug. 21, 22						
3 c/d	9.40	$\sim \infty$	0.25	0.49	-1.0	12.82
13 c/d	1.64	$\sim \infty$	0.32	0.44	0.38	14.28

Table 7.3

Wavenumbers and vertical and horizontal wavelengths of short period waves observed at Urbana.

SW → standing wave present

For 3 c/day components, $\lambda_x \approx 10^7$ m if wave is ter-diurnal tide

Date	Freq (c/day)		k_z (km^{-1})	λ_z (km)	λ_x (km)	k_x (km)
1. 1-17,18-75	5		0.124	50.9	2520	.249 E-2
2.	17		0.166	37.9	599	.105 E-1
3. 2-28/3-1	4	SW	0.136	46.3	2956	.213 E-2
4.	7	unseparable superposition				
5.	10		0.256	24.6	707	.889 E-2
6.	12	SW				
7. 3-7,8	3		0.377	16.7	1647	.381 E-2
8.	20		0.243	25.9	370	.17 E-1
9. 4-4,5	3	SW	0.476	13.2	1317	.477 E-2
10.	7		0.432	14.6	620	.101 E-1
11. 5-27,28	3		0.141	44.6	3842	.164 E-2
12.	12	SW				
13. 7-14,15	5		0.386	16.3	966	.65 E-2
14.	7		0.443	14.2	605	.104 E-1
15.	10		0.272	23.1	669	.939 E-2
16. 7-30,31	3		0.171	36.8	3319	.189 E-2
17.	5		0.170	37.0	2000	.314 E-2
18.	7	SW	0.348	18.0	761	.825 E-2
19.	12		0.332	18.9	464	.135 E-1
20.	15	evanescent				
21.	18		0.181	34.7	528	.119 E-1
22. 8-21,22	3		0.084	74.6	5256	.12 E-2
23.	13		0.152	41.4	838	.75 E-2
24.	15	evanescent				
25.	18	SW unseparable superposition				
26.	21	SW				
27. 9-13,14	3		0.174	36.1	3273	.192 E-2
28.	13	evanescent				
29.	14		0.241	26.0	532	.118 E-1
30.	19	SW	0.203	31.0	455	.138 E-1
31. 10-13,14	3		0.080	78.5	5377	.117 E-2
32.	7		0.293	21.4	893	.703 E-2
33.	12		0.414	15.2	376	.167 E-1
34.	13		0.096	65.4	1132	.555 E-2
35.	17		0.330	19.1	329	.191 E-1
36. 10-14,15	3		0.203	31.0	2883	.218 E-2
37.	6	SW	0.375	16.7	828	.759 E-2
38.	10		0.384	16.3	485	.129 E-1
39. 10-16,17	3	evanescent				
40.	4		0.272	23.1	1673	.376 E-2
41.	5		0.403	15.6	927	.667 E-2
42.	6	evanescent				
43.	9		0.417	15.1	499	.126 E-1
44.	13		0.238	26.4	580	.108 E-1
45.	17		0.249	25.2	426	.148 E-1
46. 12-4,6	16		0.200	31.4	547	.115 E-1
47.	18	evanescent				
48.	19		0.104	60.5	740	.849 E-2
49. 1-14,16-76	3	SW	0.147	42.7	3726	.169 E-2
50.	4	evanescent }				
51.	5	evanescent } interaction				
52.	6	evanescent }				
53.	11	evanescent				
54.	17		0.131	47.9	713	.881 E-2
55.	19		0.235	26.7	401	.157 E-1
56.	20		0.392	16.0	238	.264 E-1
57. 1-21,23	3		0.127	49.3 } interaction	4134	.152 E-2
58.	4		0.222	28.3 }	2004	.314 E-2
59.	5		0.086	72.9	3118	.202 E-2
60.	6		0.485	13.0 } interaction	647	.972 E-2
61.	7		0.095	66.1 }	2115	.297 E-2
62.	8		0.192	32.7	1133	.555 E-2
63.	13		0.201	31.3	670	.937 E-2

of wave energy such that the normal upward amplification of waves can be significantly reduced. Table 7.4 tabulates histograms for the vertical wavelengths and frequencies of the short period waves seen at Urbana and Garchy. At Urbana, we find relatively more long wavelengths and fewer short 10-20 km wavelengths. The drop in number of higher frequency waves at Garchy probably stems from inability to resolve them with their lower echo rates.

The gravity wave vertical wavelengths we observe do not necessarily approximate the vertical wavelength of $S_1(\nu)$. For example, $S_1(\nu)$ was evanescent on Jan. 17, 18 1975 yet the very pronounced 5 osc-day^{-1} oscillation had only about a 25 km wavelength. Conversely, on July 30, 31 1975 $S_1(\nu)$ had about an 80 km wavelength and the 15 osc-day^{-1} oscillation appeared evanescent. Also the waves can disappear in less than twelve hours. Figure 7.2 shows that an oscillation of extreme amplitude was present beginning at 9 AM on Jan. 21, 1976. The low data rate obscures the wave during the afternoon and early evening, but throughout the early morning of Jan. 22 it is the largest feature seen. Yet twelve hours later there is scarcely a hint of such a wave; instead, the normal $S_2(\nu)$ variation is seen. We seem to have observed then, on a much larger time scale, a wave packet like that mentioned in Section 7.3.2. It is interesting to note that the temporal behavior of the wave in Figure 7.2 seems to indicate a Doppler shifting toward zero frequency (the initial period of about 3 hrs has increased to almost 5 hrs for the last visible cycle). Table 7.1, which avoids the potentially misleading procedure of averaging winds at all heights, also shows an apparent Doppler shifting between energy at 3 and 4 osc-day^{-1} and 6 and 7 osc-day^{-1}.

Figure 7.3 shows average meridional wind spectra for frequencies of 3

Table 7.4

Histograms of short period vertical wavelengths and frequencies.

Group	Urbana		Garchy	
0-10 km	0	0%	1	1.4%
10-20	15	25.9	29	40.8
20-30	10	17.2	19	26.8
30-40	10	17.2	7	9.9
40-50	6	10.3	2	2.8
50-60	1	1.7	4	5.6
60-70	3	5.2	3	4.2
70-80	3	5.2	1	1.4
>80, evan.	10	17.2	5	7.0
indeterminate	(5)			
	(63)		71	
	58			

Group		Urbana		Garchy	
3-6 c/day	(8-4 hr)	24	49.0%	45	48.9%
6-9	(4-2,40)	9	18.4	24	26.1
9-12	(2,40-2)	7	14.3	13	14.1
12-15	(2-1,36)	9	18.4	10	10.9
15-18	(1,36-1,20)	7		2	
18-21	(1,20-1,09)	7			
21-24	(1,09-1,30)				
		63		94	

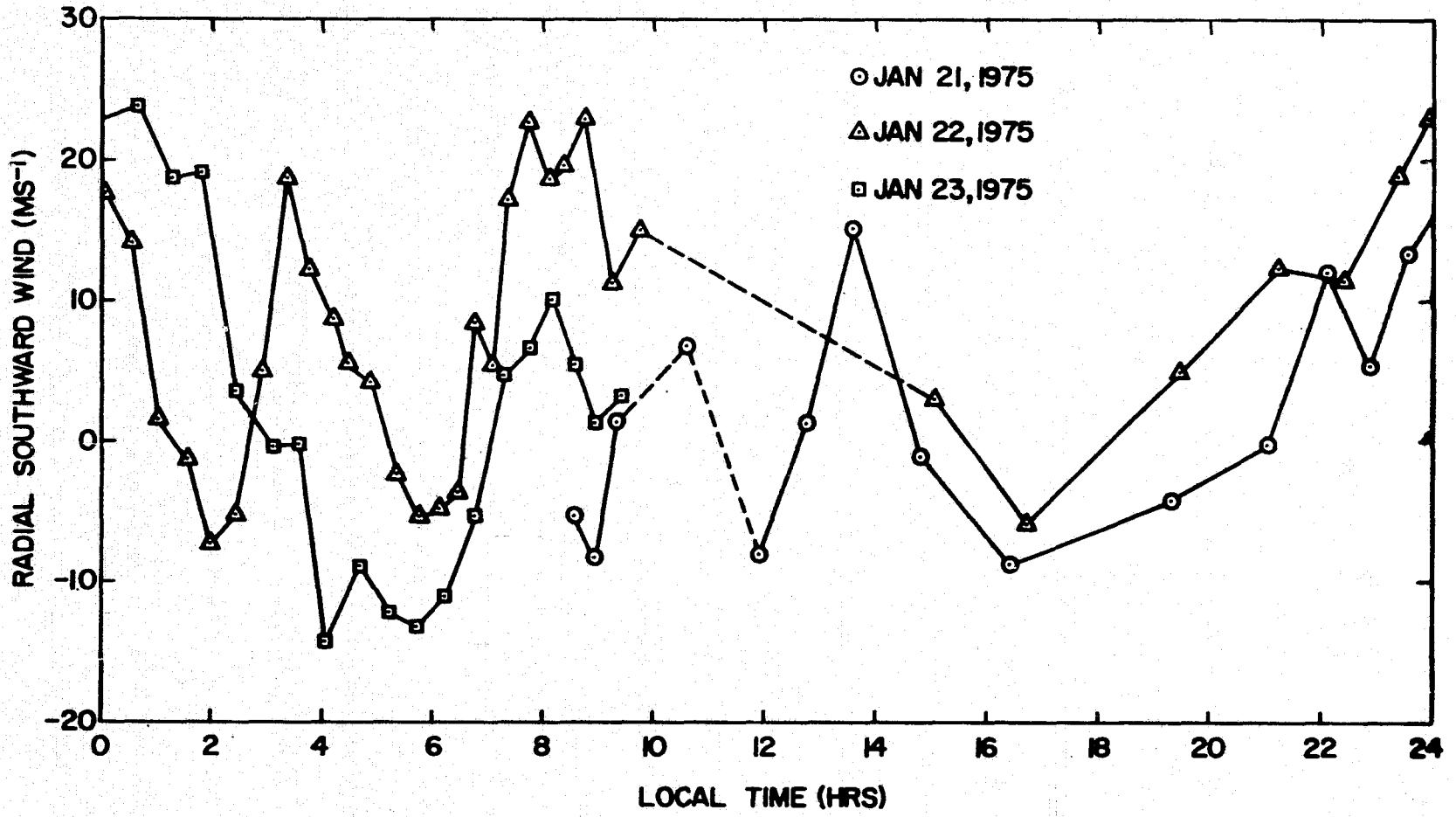

Figure 7.2 Meteor winds at Urbana, January 21-23, 1976.

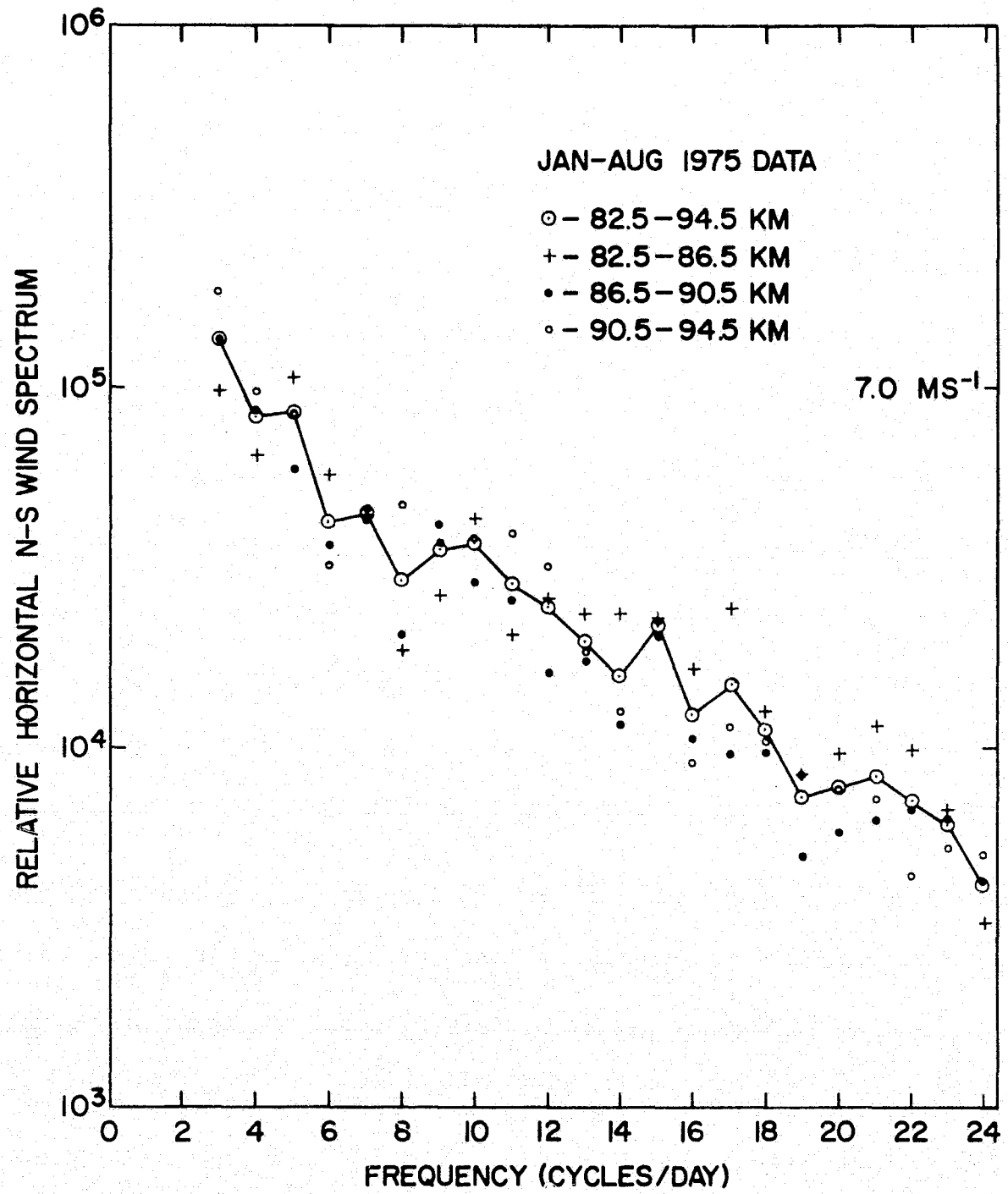

Figure 7.3 Average wind spectra at Urbana using decay height data, 3-24 cycles/day.

to 24 osc-day^{-1} based on all our decay height runs. Fitting these data to a power law results in an exponent of about -1.5 when all heights are considered (Table 7.5). If instead 4-km height segments are considered, the exponent increases from about -1.3 at the bottom of the meteor zone to about -1.7 at the top. Such variation is not necessarily real, despite the small error bars in exponent precision, because the 8 hour component has been included. It is present in nearly all runs with amplitudes growing with height and thus is not averaged downward like the other spectral lines. Also the interpolated winds are least accurate at lower altitudes, and this lack of accuracy makes itself apparent as spurious high frequency energy content in low altitude spectra. Table 7.5 also shows that the power law behavior remains the same whether decay height or interferometer height spectra are treated.

Spizzichino [1970b] has carried out similar power law fits for spectra from 3 to 12 osc-day^{-1}. Using all 1965-1966 data he obtained exponents of just -0.82 at 90 km, decreasing to -0.47 at 100 km. *Revah* [1969], however, reports an exponent of about -4/3 for 90 to 100 km with November 1965 to September 1966 data. *Vinnichenko and Dutton* [1969] have presented average spectra for altitude ranges of 1 to 25 km covering periods from five years to less than a second. The spectrum in the mesoscale region spanning periods from one day to about 10 minutes follows a -5/3 slope fairly well.

On a few occasions our data rate was sufficiently high that spectra over the frequency range 24-96 osc-day^{-1} could be evaluated from 6 hour records. Figure 7.4 shows average spectra for decay height runs in April and July 1975. Each spectral point represents the mean value for spectra at heights from 85.5 km to 93.5 km in 2.5 km steps. Both dates exhibit spectral peaks for periods near 20 and 30 minutes. The average spectra for the

Table 7.5

Summary of power law fits to averaged wind spectra over 3-24 cycle/day.

Fit Form: $S(f) = S_o f^{-k}$

I. Eight 24-hr periods using decay heights only (Jan.-Aug. 1975)

1. 82.5 - 86.5 km, k = -1.33 ± .06
2. 86.5 - 90.5 km, k = -1.56 ± .06
3. 90.5 - 94.5 km, k = -1.67 ± .06
4. 82.5 - 94.5 km, k = -1.52 ± .06

II. Four 24-hr periods using stacked Yagi interferometer heights (Sept.-Oct. 1975)

1. 82 - 86 km, k = -1.12 ± .08
2. 87 - 91 km, k = -1.43 ± .08
3. 92 - 96 km, k = -1.73 ± .08
4. 97 -101 km, k = -1.52 ± .08
5. 82 -101 km, k = -1.47 ± .04

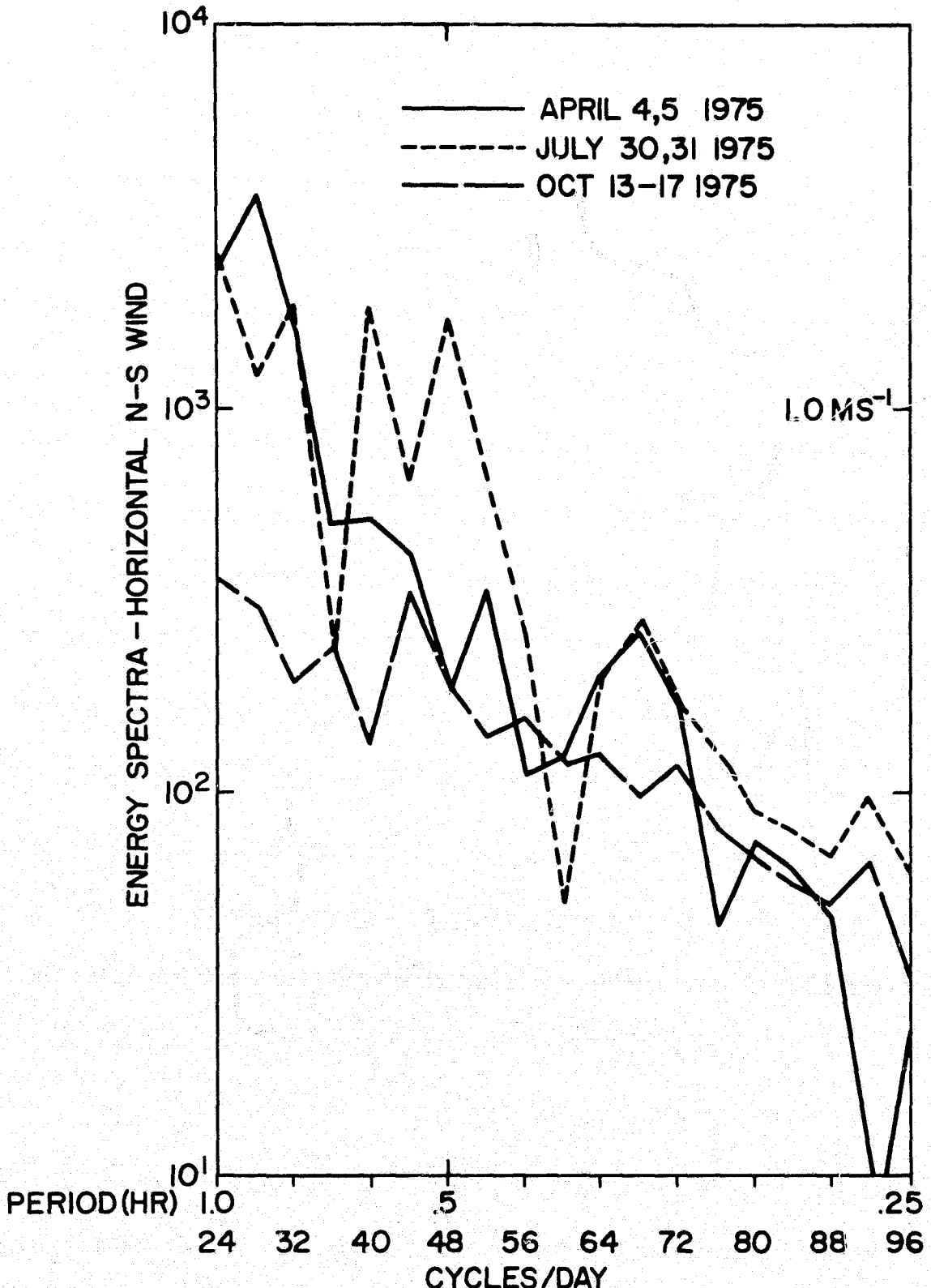

Figure 7.4 Six-hour record wind spectra for three periods at Urbana.

October 1975 data are based on individual spectra for 82 km to 102 km in 1 km steps and three separate 6 hr records: 0-6 AM, 3-9 AM, and 6AM - 12 PM. Here only a peak near 30 minutes is evident. These components are perhaps similar to type (3) observed by *Rastogi and Bowhill* [1976] (Section 7.3.2).

In all our runs the data rate was sufficiently high in the early morning hours and around 92 km height to evaluate a spectrum for 24-96 osc-day^{-1}. Figure 7.5 plots the mean spectral values we obtain from interferometer height runs with 6 hour records centered at 92.5 km and 94.5 km. Also plotted are the mean spectral values obtained from decay height data at 90,5 km and 92.5 km. No differentiation is apparent. The power law spectral fit now requires an exponent of about -3. The 3-24 osc-day^{-1} results of Figure 7.3 have been plotted on Figure 7.5 also to exhibit the apparent break-point behavior of the wind spectrum near 1 hour periods. Such behavior is not present in Vinnechenko's lower altitude spectrum. Neither is it apparent from the Jicamarca spectra, where 24 and 96 osc-day^{-1} spectral intensities differ by roughly a factor of five. In our results they differ by nearly a hundred. Of course only a few Jicamarca spectra are yet available and all are based on quite short record lengths. Still, the absence of appreciable tidal energy in them is puzzling. Application of the dispersion equation shows that as wave frequency increases the horizontal wavelength generally decreases (Table 7.3). This is important in the meteor-radar case, because without azimuthal rejection criteria we will respond to echoes covering about 150 km horizontal extent. Thus it is possible that the break-point behavior is the result of horizontal averaging of wind components with periods 1 hour and less.

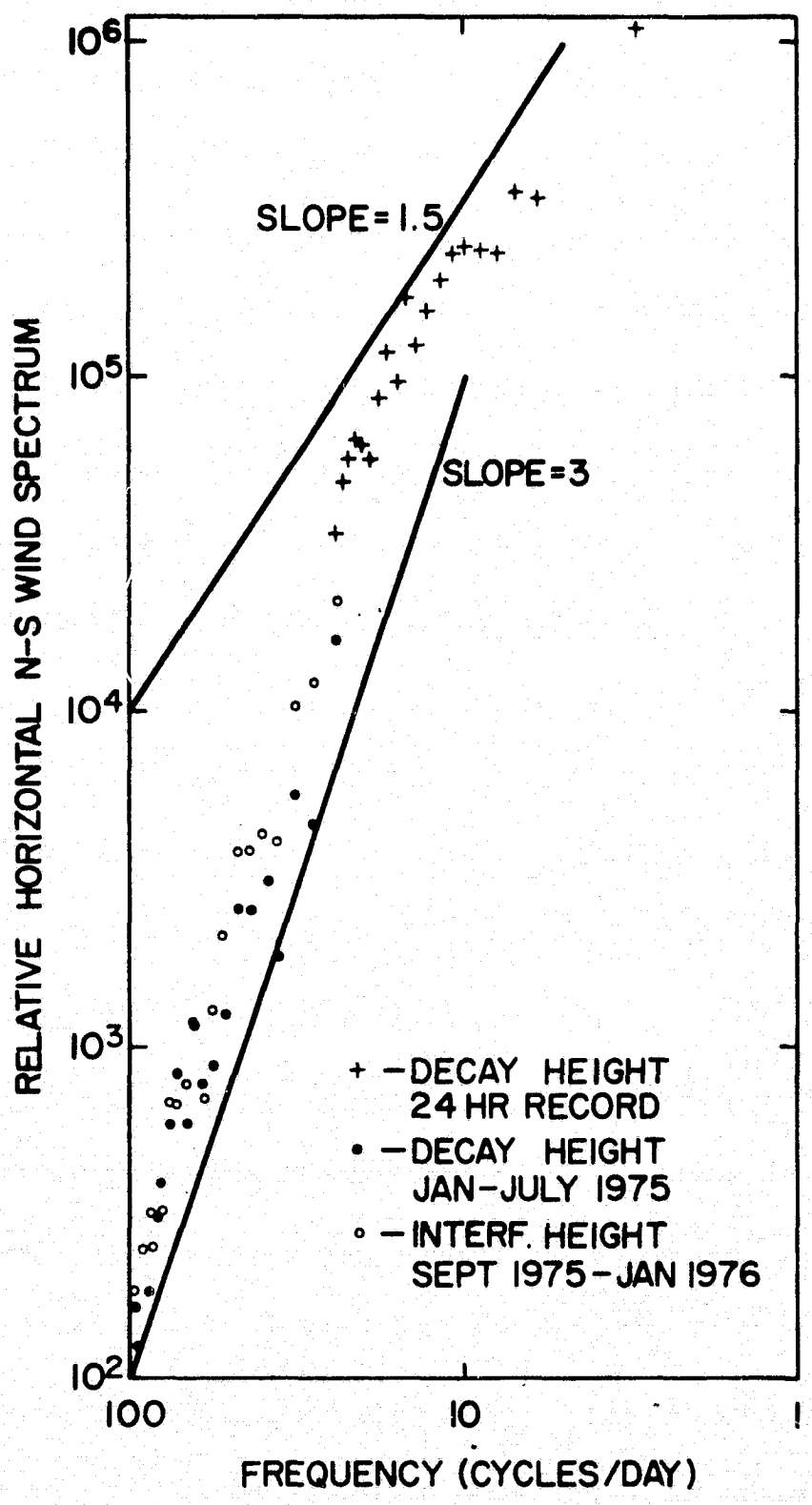

Figure 7.5 Average wind spectra at Urbana, 3-96 cycles/day.

8. SIMULTANEOUS PARTIAL-REFLECTION AND METEOR-RADAR WIND OBSERVATIONS AT URBANA, ILLINOIS

8.1 *Introduction*

This chapter is based on a short paper by *Geller et al.* [1976], but utilizes data collected at Urbana during two winter campaigns, 1974-1975 and 1975-1976.

Many suggestions have been made to explain the observed high levels and variability of radio-wave absorption in the winter *D* region at middle latitudes. These explanations generally fall into three classes: (1) theories suggesting an enhancement in nitric oxide concentration; (2) theories suggesting a decrease in the efficiency of electron loss processes; and (3) theories suggesting that precipitating energetic electrons are an appreciable source of ionization in winter. The first two classes require accompanying changes in the neutral atmospheric dynamics. For instance, *Sechrist* [1967] theorized that temperature increases in the *D* region might lead to the necessary higher nitric oxide concentrations. *Geisler and Dickinson* [1968] theorized that downward vertical velocities accompanying planetary-scale waves would lead to the required greater concentration of nitric oxide. Many of these theories were reviewed by *Geller and Sechrist* [1971].

A theory of the winter anomaly which we can test with our meteor-radar observations was introduced by *Manson* [1971]. Noting that very high concentrations of nitric oxide had been observed in the auroral zone *E* region [*Zipf et al.*, 1970], Manson suggested that during winter periods of enhanced equatorward flow the increased transport of nitric oxide from the auroral zone would give rise to higher *D*-region electron densities at midlatitudes. This type of mechanism was proposed earlier by *Belrose* [1963] to explain

magnetic storm after effects. *Schoeberl and Geller* [1976] have shown that both the Geisler-Dickinson and Manson theories of nitric oxide enhancement of the *D* region by planetary wave transport are consistent with winter anomaly spatial and frequency distributions. Thus both downward and equatorward transport mechanisms might be significant factors in producing the winter anomaly. The purpose of this chapter is to describe a preliminary observational effort using a meteor radar to detect neutral air motions in the 80-100 km altitude region along with simultaneous differential absorption measurements at a single location which supports Manson's hypothesis.

8.2 *Differential absorption technique*

The differential absorption technique is a ground-based method for determining the electron density in the *D* region using medium frequency radio waves [*Gardner and Pawsey*, 1953]. Extraordinary and ordinary mode pulses are alternately transmitted vertically into the atmosphere. The signal that is partially reflected from irregularities in the *D* region for each mode is measured and the A_x/A_o ratio of the r.m.s. values of the extraordinary to ordinary reflected signals is calculated as a function of height. This ratio depends on the collision frequency of electrons with neutral molecules, and the electron density up to the reflection height [*Belrose and Burke*, 1964]. Since the collision frequency is a function only of the atmospheric pressure, changes in electron density are reflected by changes in the A_x/A_o ratio. If certain simplifying assumptions are made [*Belrose and Burke*, 1964], the mean electron density between two heights can be calculated from the difference in the A_x/A_o ratios for the two heights.

The data used in this study were obtained using a frequency of 2.66 MHz and a transmitter pulsewidth of 24 μs. Ordinary and extraordinary mode amplitudes were measured twice per second as a function of height. The

medium values of A_x/A_o and electron density from five 3-min observations spaced over 1 hr were taken with the hour centered at local noon [*Henry*, 1966; *Denny and Bowhill*, 1973].

The electron density accuracy depends on the signal-to-noise ratio of the extraordinary and ordinary mode reflections. Calculations can only be made at heights where the real parts of the extraordinary and ordinary mode refractive indices are sufficiently similar that reflections for either mode received at a given time delay come from the same height. They are also affected by steep height gradients in electron density. For these reasons, the experiment is at its best between about 72 and 82 km.

Figure 8.1 shows a summary of the 1974-1975 winter partial-reflection measurements. The A_x/A_o ratio shown is the mean value for two heights separated by 1.5 km, the central height being 80 km. The electron densities are the means of determinations at three heights, thus depending on four A_x/A_o ratios over a total height range of 4.5 km. The representative height is taken to be 76 km in this case. A low value of A_x/A_o at a given height and vice versa. This is seen in Figure 8.1 where dips in A_x/A_o at 80 km are associated with peaks in the 76 km electron density. These particular heights are graphed because the A_x/A_o ratio is most accurate near 80 km while the electron density accuracy peaks near 76 km. The variation in A_p, the planetary magnetic index, is also shown during this period. The figures by the upper arrows are the meridional wind determinations and will be discussed in the next section.

8.3 *Results*

Table 8.1 summarizes the data obtained on the 1975-1975 winter days when there were simultaneous differential-absorption and meteor-radar measurements made at Urbana. A_x/A_o values are shown at altitudes of

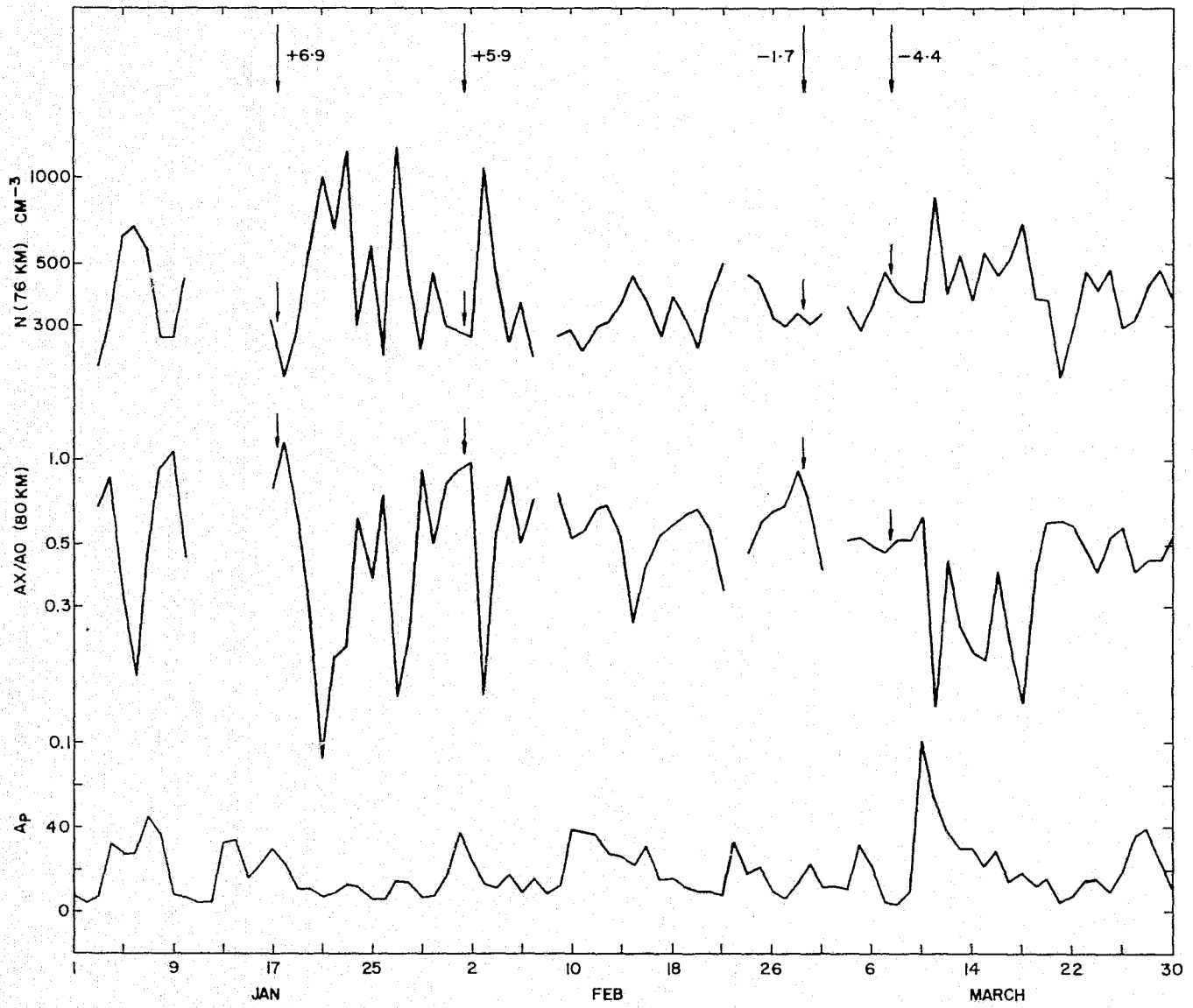

Figure 8.1 Daily values of N, electron density at 76 km altitude, and A_x/A_o at 80 km altitude obtained by the partial-reflection technique at Urbana, January - March 1975. Also pictured are daily values of A_p during the same period [*Geller et al.*, 1976].

Table 8.1

Summary of meteor-radar and partial-reflection observations early in 1975.

	A_x/A_o								Meridional Wind (ms^{-1})
	71 km		76 km		80 km		86 km		
Jan. 17	1.75		1.44		0.78		0.47		
Jan. 18	1.83	(1.79)	1.44	(1.44)	1.14	(0.96)	0.69	(0.58)	+6.9
Jan. 31	1.73		1.31		0.82		0.24		
Feb. 1	1.64	(1.69)	1.51	(1.41)	0.91	(0.87)	0.58	(0.41)	+5.9
Feb. 28	1.82		1.39		0.92		0.30		
Mar. 1	1.75	(1.79)	1.24	(1.32)	0.70	(0.81)	0.27	(0.29)	-1.7
Mar. 7	1.59		0.90		0.47		0.29		
Mar. 8	1.39	(1.49)	0.87	(0.89)	0.52	(0.50)	0.24	(0.27)	-4.4

Values in parentheses are arithmetic averages of figures to the left [*Geller et al.*, 1976].

71 km, 76 km, 80 km and 86 km. Values of A_x/A_o are shown for the local noon at the beginning of the 24-hr meteor-radar run and also at the end. Values in parentheses are arithmetic averages of these beginning and ending values. The right-hand column gives the prevailing meridional velocities that were measured during the 24-hr period. Positive velocities indicate northward flow and negative velocities indicate southward flow. Table 8.2 gives an expanded summary for all simultaneous meteor-radar and partial-reflection observations.

Table 8.3 presents the correlation coefficient for the parameters tabulated in Table 8.2. In general only data from the winter anomaly runs are considered, but in two cases non-winter data are also used so possible differentiation is highlighted, and in one case all data are used.

8.4 *Discussion*

Table 8.3 shows a significant correlation between the winter meridional winds at all three heights and the electron density at 76.5 km. Furthermore, the correlation coefficient becomes near zero for non-winter data. Winter correlations between the A_x/A_o ratio and meridional wind are not quite up to the significance level but again are appreciably larger than non-winter values. There appears to be a decrease in winter correlations as meteor wind height drops. But, since the decrease is small and our wind accuracy also drops with height, this behavior may be instrumental in nature. The winter wind correlations with electron density at 81 km seem negligible. We note, however, that electron density at 81 km and 76.5 km are also indicated as only very weakly correlated. This is almost certainly the result of unreliable data at 81 km.

Since this was a preliminary investigation of the relationship of the sense of the prevailing meridional wind with the level of *D*-region ionization,

Table 8.2

Summary of all simultaneous meteor-radar and partial-reflection observations at Urbana.

Nr	Date	[N] 76.5 km mean	[N] 76.5 km time gradient	A_x/A_o 81 km mean	A_x/A_o 81 km time gradient	V_{s-n} at 92.5 km	horizontal shear	V_{s-n} at 88.5 km	V_{s-n} at 84.5 km	[N] 81 km	A_x/A_o 76.5 km
1	*1/17-18/75	262 cm^{-3}	-205 cm^{-3} day^{-1}	0.89	0.34 day^{-1}	11.72 ms^{-1}	0.29 ms^{-1} km^{-1}	8.99 ms^{-1}	7.54 ms^{-1}	472 cm^{-3}	1.32
2	*2/28, 3/1	370	- 97	0.75	-0.28	- 1.95	-0.95	3.92	8.26	386	1.20
3	*3/7,8	428	- 81	0.44	0.0	- 1.47	0.38	-5.77	-4.09	436	0.82
4	4/4,5	272	-177	0.45	-0.02	- 7.83	-1.29				
5	5/27,28	506	10	0.36	0.02	3.17	1.36				
6	7/14,15	609	- 4	0.22	0.01	- 4.96	1.20				
7	7/30,31	568	- 4	0.26	-0.02	-11.57	1.55				
8	8/21,22	392	166	0.47	-0.18	-10.00	-3.40				
9	9/13,14	260	- 17	0.44	0.0	- 8.85	0.16				
10	10/13,14	368	- 31	0.30	0.07	- .51	1.05				
11	10/14,15	368	- 31	0.30	0.07	3.46	0.18				
12	10/16,17	359	-118	0.34	-0.01	6.82	0.15				
13	*12/4-6	267	- 48	0.74	0.20	14.15	-0.04	15.02	14.55	551	1.09
14	*12/12,13	320	163	0.60	-0.28	12.70	-0.36	15.29	15.45	486	1.08
15	*1/14-16/76	386	6	0.36	0.03	9.17	-0.44	10.87	10.34	871	0.78
16	*1/21-23	410	- 21	0.34	0.13	-12.47	-1.09	-3.90	3.95	796	0.53
17	*1/31, 2/1/75	295	- 10	0.82	0.16	5.90				662	1.39

* winter anomaly run

Table 8.3

Correlation coefficient matrix - winter anomaly runs.

x/y	$[N]$ 76.5 km	$[N]$ 81	A_x/A_o 76.5	A_x/A_o 81	V_{n-s} 92.5	V_{n-s} 88.5	V_{n-s} 84.5
$[N]$ 76.5 km		.23	-.78	[-.67] -.84	(.05) .76	.77	.68
$[N]$ 81			-.53	-.56	.18	.01	-.09
A_x/A_o 76.5				.95	-.64 (.27)	-.56	-.42
A_x/A_o 81					-.50	-.47	-.38
V_{n-s} 92.5						.89	.68
V_{n-s} 88.5							.93
V_{n-s} 84.5							

[ ] all runs

( ) all runs <u>but</u> the winter anomaly runs

require correlation coefficient magnitude $\geq$ 0.62 for significance at 10% level

our conclusions must be tentative. In the future, simultaneous observations of north-south prevailing winds in the 80-100 km altitude range and *D*-region electron densities for an entire winter should be carried out so that statistical inferences between the north-south wind and the level of *D*-region ionization can be put on firmer ground. There is a clear indication, nonetheless, that during winter periods of mean southward *D*-region motions the level of ionization is higher than during periods of northward flow. This is consistent with some results that were reported by *Rose et al.* [1972], and consistent with Manson's hypothesis of increased *D*-region ionization. The region of peak auroral activity is about 2000 km north of Urbana. Thus, a characteristic time scale for the transport of nitric oxide from the region of peak auroral activity by winds of the order 10 ms^{-1} would be about 2-5 days. This is of the right order for winter anomaly type changes in absorption. Also, 10 ms^{-1} is the proper order of magnitude to be expected from planetary-wave activity during the winter at *D*-region altitudes.

9. INFERENCES ABOUT DENSITY AND SCALE HEIGHT VARIATIONS IN THE UPPER ATMOSPHERE

Equation (4.4) in Section 4.3 indicates an inverse relationship between atmospheric density ρ and ambipolar diffusion coefficient D. This latter quantity was also shown to be related to signal decay rate for underdense echoes and thus it is possible to infer density variation from meteor radar data. Furthermore, local scale height can be inferred from the slope of a log D versus true height (h) plot. Nonisothermal temperature structures would cause such a plot to be somewhat curved, but over small height intervals the isothermal assumption seems reasonable. However, three problems must be born in mind when analyzing meteor decay rates.

First, the decay rates exhibit considerable scatter. In fact even simultaneous echoes observed from the same trails using different carrier frequencies give widely different values for D [*Rice and Forsyth*, 1963]. Nevertheless statistical validity for the frequency dependence of decay rate can be demonstrated by averaging results from many echoes. The reason for the large scatter in decay rate, even among echoes collected at similar heights and times, is apparently related to the irregular ionization patterns of meteor trails, including those which exhibit the "ideal" underdense signal characteristics of Fresnel modulation and logarithmic decay of video amplitude in time [*Rice and Forsyth*, 1964].

A second problem is related to the decrease of density with altitude. This implies an increase in ambipolar diffusion coefficient with altitude and thus higher rates of signal decay. The result is a collection bias against higher altitude echoes. Table 9.1 shows the ceiling decay heights imposed by METP5 and METP6 acceptance criteria, namely, the video return must be below saturation and above the detection threshold for a certain

Table 9.1

Decay height ceilings imposed by software acceptance criteria.

	METP5 $\Delta t \geq 42$ms			METP6 $\Delta t \geq 57.5$ms		
Video Amplitude (A/D units)	$10^{-5} D_{max}$ $cm^2 s^{-1}$	$\log D_{max}$	h_{max} km	$10^{-5} D_{max}$ $cm^2 s^{-1}$	$\log D_{max}$	h_{max} km
511,SAT	4.99	5.70	104.1	3.64	5.56	102.3
400	4.77	5.68	103.9	3.48	5.54	102.1
300	4.51	5.65	103.6	3.29	5.52	101.8
200	4.11	5.61	103.1	3.00	5.48	101.5
100	3.32	5.52	102.0	2.42	5.38	100.3

Threshold = 40 A/D units

Heights taken from *Barnes* [1962] based on equation (4.6) and *U.S. Standard Atmosphere* [1962]

minimum time following peaking of the video signal. Based on the cumulative Yagi video strength distribution correction factors can be developed for the true likelihood of various log D values. But we note, for example, that of 11,050 October 1975 echoes, none had a log D value exceeding 5.25 though values up to 5.56 should have been possible. This raises the probability that software velocity and angle acceptance criteria further depress the decay height ceiling and for these criteria we have no ready way of specifying correction factors. Below 95 km we need not worry about the ceiling collection bias but a floor bias exists as well. This bias is not the result of difficulties in acquiring slowly decaying echoes, but rather is the result of contamination by nonspecular or wind influenced echoes which appear to have slow decay rates but are not necessarily at low altitudes.

A third potential problem in the use of meteor echo decay rates involves the influence of magnetic fields on diffusion. The influence of such fields is only appreciable at heights above roughly 100 km and for meteor trails closely aligned with field lines [*Kaiser et al.*, 1969]. The effect of the magnetic field will depend upon the observers orientation.

Since our radar returns are generally far out of line with magnetic field lines and since ceiling biases limit the number of high altitude returns we see anyway, this third problem is not as important as the first two. Furthermore, our radar is ideal for overcoming the difficulties of large scatter due to its high data rate. Lastly, we can limit errors caused by ceiling (and floor) biases by concentrating on the 85-95 km height region.

An early application of echo decay rates involved their use to statistically infer true echo heights. This was done by *Greenhow and Neufeld* [1955], who fitted a regression line to log D and true height data and obtained the equation plotted in Figure 4.5:

$$\log D \ (\mathrm{cm}^2\mathrm{s}^{-1}) = 0.067 \ H(\mathrm{km}) - 1.6 \qquad (9.1)$$

Figure 9.1(a) shows a typical comparison between heights inferred via (9.1) and heights measured by interferometry. On the average, agreement is reasonable with a standard deviation on the order of 2.5 km. Since seasonal density variations would normally only shift heights on the order of 1 km, they are generally ignored. Figure 9.1(b) shows representative seasonal density profiles. Note that near the most probable echo heights the seasonal variation is minimal. As demonstrated in Section 3.2, it is quite feasible to resolve tidal structure with inferred heights using our radar because of the high data rate. The scale height inferred from (9.1) is 6.48 km which seems reasonable at meteor heights.

To find out how well our data conforms to (9.1) and to investigate potential variability in the relation, we performed regression analyses with log D and true height data. Table 9.2 summarizes the results for September 13-14 and October 13-18, 1975 radar runs. It is clear that when all echoes are treated individually, a rather weak correlation between h and log D can occur and the resulting scale heights may be unreasonable. We point out that the September 13-14 data represent a worse case in the correlation sense, since all other interferometer runs gave appreciably better correlations on an hourly means basis. We must be sure to choose the correct dependent y and independent x variables, and the extreme variation in scale height depending on how we assign x and y brings this point home. Because of the large scatter in D and the relatively precise measurement of h, the proper way to assign the variables is log D as y and h as x, although in fact equation (9.1) was obtained with the opposite assignment. The reason we can obtain an unreasonably high scale height when all echoes are considered individually is related to the combination of ceiling and floor

(a)

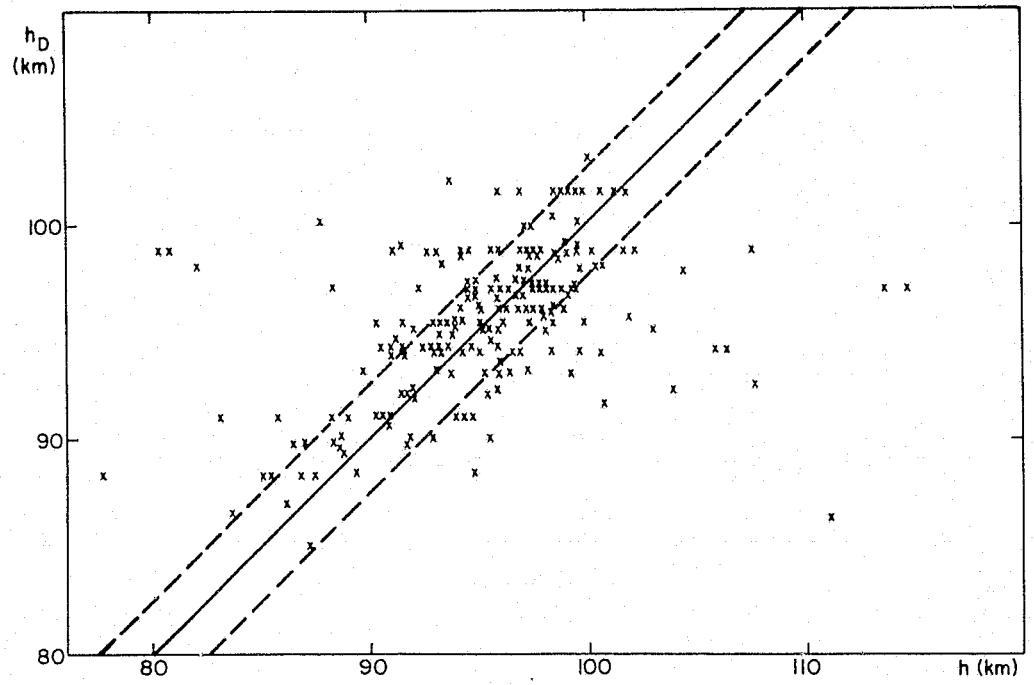

(b)

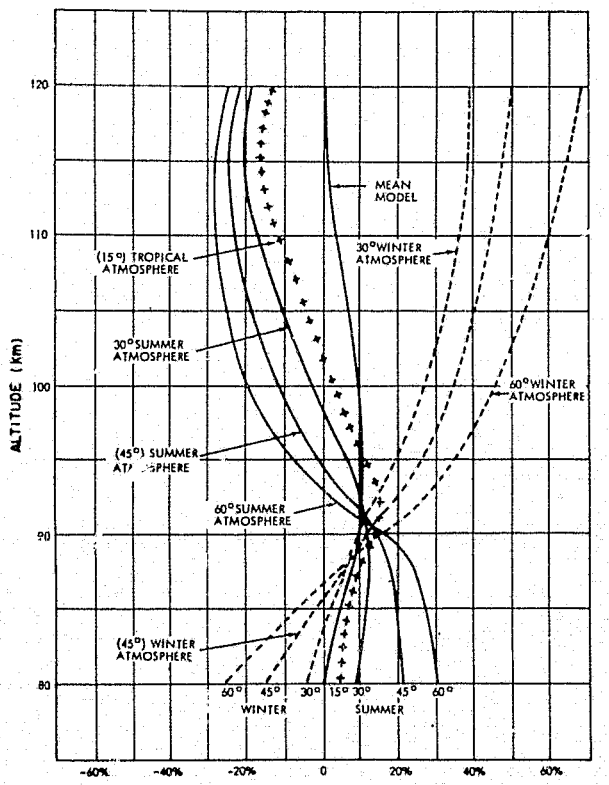

Figure 9.1 (a) Comparison between the height, h_D, deduced from the exponential decay of underdense echoes, and the height, h, measured by the Garchy radar interferometer on December 12-13, 1965 [*Barnes and Pazniokas*, 1968], (b) Mean seasonal density profiles plotted as percent departure from standard [*Barnes and Pazniokas*, 1968].

Table 9.2

Linear regression analysis of log D and true height h data.

	x	y	a	σ_a	b	σ_b	r	H
I. Sept. 13, 14, 1975*	h	Log(D)	2.56	.09	0.025	0.	0.40	17.37**
	Log(D)		57.71	1.60	7.79	.36	0.40	3.40
II. Sept. 13, 14, 1975***	h	Log(D)	0.836	0.542	0.039	0.006	0.52	11.14**
	Log(D)		54.160	6.476	8.592	1.448	0.65	3.73
III. Oct. 13-18, 1975****	h	Log (D)	0.240	0.208	0.044	0.002	0.88	9.87**
	Log(D)		20.185	4.046	16.651	0.930	0.90	7.24

D = ambipolar diffusion coefficient in $cm^2 s^{-1}$
h = true height in km
r_{xy} = correlation coefficient
H = scale height in km
Fit Form: $y = a + bx$

*2482 echoes
**preferable assignment of dependent and independent variables
***hourly means
****hourly means for 11,050 superimposed echoes

biases which decreases the height sensitivity of log D and thus indicates an apparently higher scale height. The effect of such biases can be decreased if instead of considering all echoes individually we perform our linear regression analysis on the hourly mean values of log D and h. For September 13-14 data this decreases the scale height somewhat, though it remains suspiciously high. For October 13-18 data the scale height of 9.87 km ± 0.1 km is more reasonable. Furthermore, the large amount of data for this period brings scale heights deduced from both variable assignments into reasonable agreement. From this we conclude that either (1) 2500 echoes are not sufficient to guarantee an accurate statistical relation between true height and decay rate or (2) day-to-day variability in density and temperature can be large enough to necessitate data smoothing over several days to deduce a representative statistical relation between true height and decay rate.

By investigating the temporal behavior of mean echo decay rate for various height intervals, it is possible to make inferences about the temporal behavior of density and scale height. Such an investigation was first carried out by *Greenhow and Hall* [1960]. Figure 9.2(a) shows the hourly behavior of mean log D for the selected 5 km height intervals using October 13-18, 1975 data. Figure 9.2(b) is similar but plots the ratio of hourly mean D to the daily mean for 85-95 km. Figure 9.3(a) graphs the density-mean density ratio for three observing periods. The structure of the Figure 9.3(a) graphs is interestingly somewhat similar to that found at Jodrell Bank and Palo Alto in the spring, Figure 9.3(b). The data used in Figure 9.3(a) have been least square fitted to identify harmonic content. As Table 9.3 shows we find the diurnal harmonic dominant in all cases. The second strongest harmonic is semidiurnal for 85-90 km but terdiurnal at 90-95 km for September and October. Thus unlike Greenhow and Hall, we do

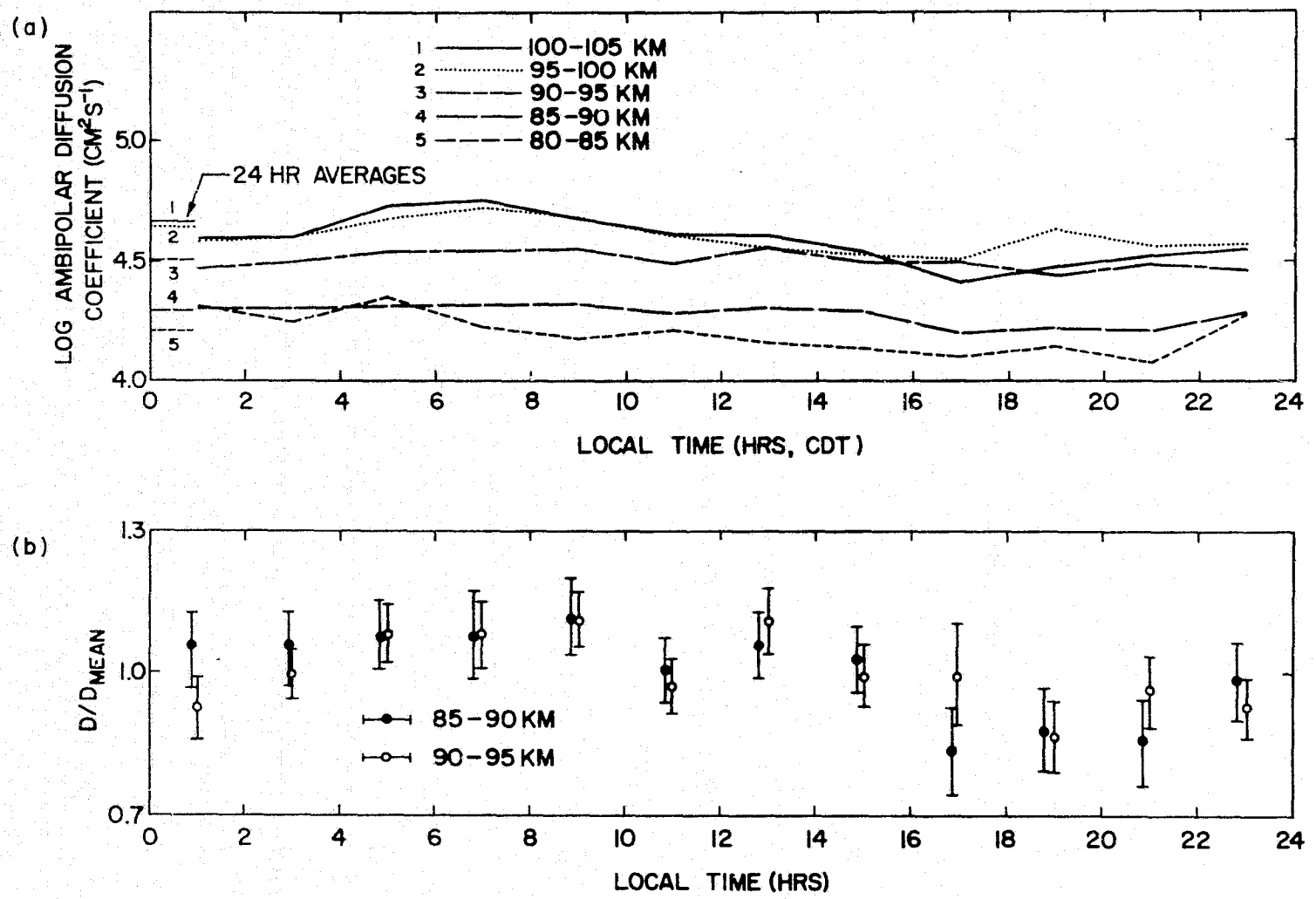

Figure 9.2 (a) Ambipolar diffusion coefficient logarithm versus height and time of day at Urbana.
(b) Variations in normalized ambipolar diffusion coefficient versus height and time of day at Urbana.

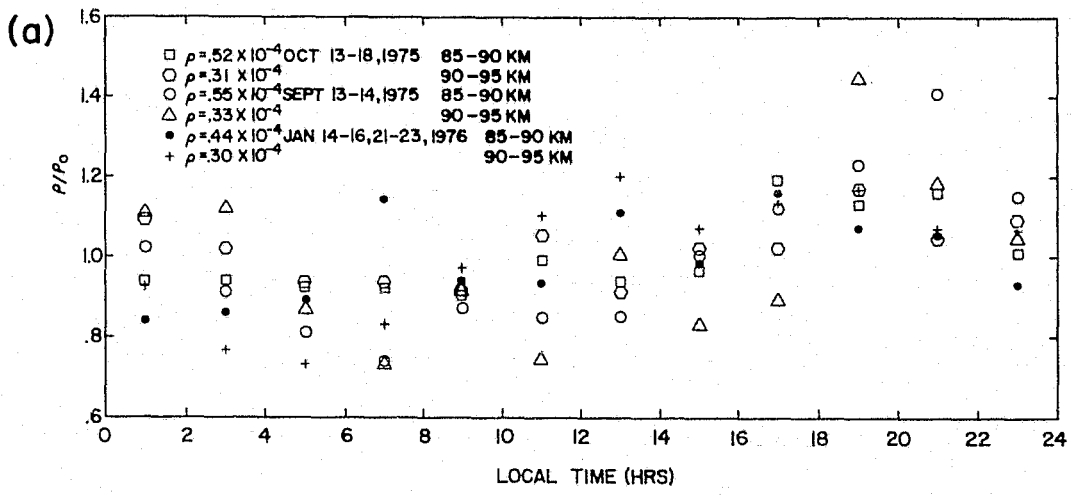

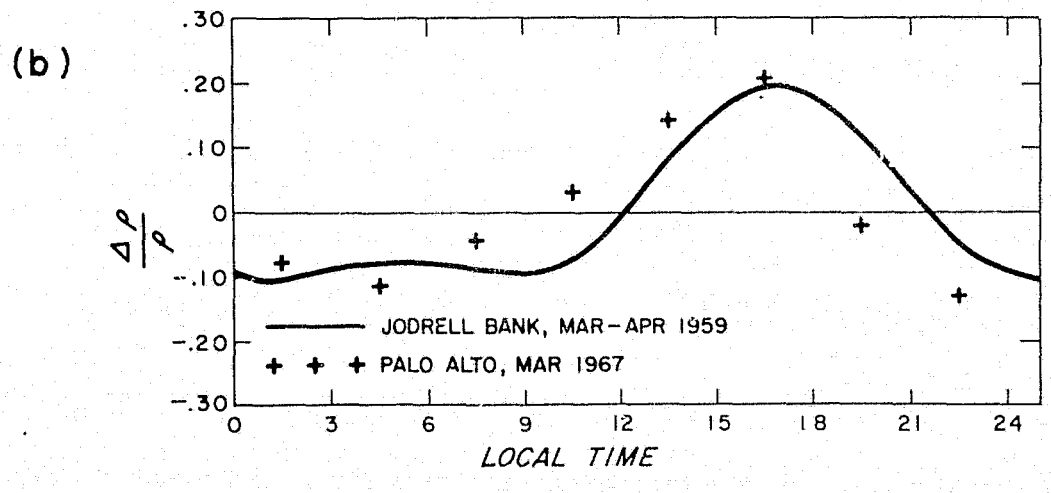

Figure 9.3 (a) Density variations inferred from meteor echo decay rates at Urbana, (b) Diurnal variation of atmospheric density at 97 km deduced from the decay rate of underdense meteor trails at Jodrell Bank, England and Palo Alto, California [*Barnes and Paznickas*, 1972].

Table 9.3

Harmonic fits to inferred density.

(1) Mean +5 harmonics

	ρ_0*	$\lvert\rho_1\rvert/\rho_0$**	ρ_1**	$\lvert\rho_2\rvert/\rho_0$***	ρ_2***
True Height = 85-90km					
Run 1	0.55×10^{-4}	0.25	9.8 hrs.	0.78	6.3 hrs.
2	0.52×10^{-4}	0.11	11.0	0.054	7.9
3	0.44×10^{-4}	0.091	14.7	0.068	8.1
True Height = 90-95km					
Run 1	0.33×10^{-4}	0.21	8.4	0.036	6.5
2	0.31×10^{-4}	0.09	9.0	0.02	1.9
3	0.30×10^{-4}	0.19	14.0	0.08	4.3

(2) Mean +3 harmonics

True Height = 85-90km					
Run 1	0.55×10^{-4}	0.25	9.9	0.076	6.7
2	0.52×10^{-4}	0.11	11.0	0.052	7.6
3	0.43×10^{-4}	0.091	14.1	0.042	7.6
True Height = 90-95km					
Run 1	0.32×10^{-4}	0.21	8.2	0.08	5.7
2	0.31×10^{-4}	0.09	9.3	0.02	2.9
3	0.30×10^{-4}	0.18	14.0	0.083	3.8

(3) Mean +2 harmonics

True Height = 85-90km					
Run 1	0.55×10^{-4}	0.24	9.8	0.065	6.4
2	0.51×10^{-4}	0.094	11.0	0.041	7.4
3	0.43×10^{-4}	0.10	14.0	0.051	8.2
True Height = 90-95km					
Run 1	0.31×10^{-4}	0.18	7.8	0.036	2.9
2	0.31×10^{-4}	0.075	8.6	0.048	2.7
3	0.30×10^{-4}	0.18	14.0	0.087	4.1

(4) Mean +5 harmonics

Order of harmonic dominance--largest first

True Height = 85-90km	
Run 1	ρ_1, ρ_2, ρ_4, ρ_3, ρ_5
2	ρ_1, ρ_2, ρ_3, ρ_5, ρ_4
3	ρ_1, ρ_2, ρ_5, ρ_4, ρ_3
True Height = 90-95km	
Run 1	ρ_1, ρ_3, ρ_4, ρ_5, ρ_2
2	ρ_1, ρ_3, ρ_5, ρ_4, ρ_2
3	ρ_1, ρ_2, ρ_4, ρ_5, ρ_3

*mean
**24 hour component
***12 hour component

Run 1 = Sept. 13-14, 1975	2,837 echoes
Run 2 = Oct. 13-18, 1975	11,050 echoes
Run 3 = Jan. 14-16, 21-23, 1976	6,595 echoes

not find the semidiurnal density oscillation credible, particularly since the semidiurnal wind over 90-95 km was appreciable on September 13-14 and growing with altitude and in January $S_2(v)$ dominated $S_1(v)$ at both 85-90 km and 90-95 km. Our diurnal density component does not grow in amplitude with height as reported by Greenhow and Hall but the diurnal tide amplitude was decreasing in height for both run periods so perhaps this difference is to be expected. Phases appear reasonably stable but lag with height for both the diurnal and semidiurnal harmonics. A leading phase would be expected if tidal perturbations are indeed the cause of our observed density variation. Note from Figure 9.3(a) that the variations for a single day are much larger than those where data from several days has been superimposed. This leads us to the same two possibilities mentioned with respect to the true height-echo decay relation, i.e., 2500 echoes/day being insufficient for resolution of true behavior or significant day-to-day variability.

When straight lines are fitted to the mean log D values for 85-90 km and 90-95 km at 2 hour intervals, the time variation of scale height can be inferred. Table 9.4 shows results of harmonic analysis for the October 13-18 data. A mean value of 8.4 km ± 0.64 km is found with the most statistically significant harmonic being of 12 hour period and 0.77 hour phase. This is in opposition to Greenhow and Hall's finding of a strong diurnal component of 11.6 hour phase, though their mean value of 9.0 km agrees well with ours.

It is important to comment on the measurement errors which Greenhow and Hall quote compared to ours. They use a system PRF of 600 Hz compared to our 400 Hz and this suppresses the height ceiling bias somewhat for them. They quote ± 4 km accuracy in true height and resolution of mean D at a specified mean true height to within ± 5 percent. Gradients of true height - ln D are to be determinable to an accuracy of ± 10 percent. Yet they claim,

Table 9.4

Scale height harmonic analysis.

		Input Data	
Nr	Time	Scale Height km	Std Dev km
1	1.00	0.96E+01	0.19E+01
2	3.00	0.89E+01	0.12E+01
3	5.00	0.87E+01	0.12E+01
4	7.00	0.90E+01	0.20E+01
5	9.00	0.70E+01	0.73E+00
6	11.00	0.86E+01	0.11E+01
7	13.00	0.90E+01	0.16E+01
8	15.00	0.96E+01	0.19E+01
9	17.00	0.87E+01	0.30E+01
10	19.00	0.65E+01	0.17E+01
11	21.00	0.62E+01	0.13E+01
12	23.00	0.95E+01	0.23E+01

fit to mean+24+12+8 hr comp

Tide per	Amp	Amp err	Phase	Phase err
0.24E+02 hr.	0.32E+00km	0.42E+00km	-0.87E+00 hr.	0.38E+01 hr.
0.12E+02	0.13E+01	0.58E+00	0.77E+00	0.10E+01
0.80E+01	0.68E+00	0.38E+00	0.23E+01	0.52E+00
0.60E+01	0.63E+00	0.12E+00	0.19E+01	0.61E+00
0.48E+01	0.30E+00	0.37E+00	-0.10E+01	0.83E+00
mean	0.84E+01	0.64E+00		

October 13-18, 1975 data at 85-90, 90-95 km

for example, that the scale height determined for January-February 1959 is 9.2 ± 0.3 km. From Figure 5 of Greenhow and Hall, the accuracy of ln D in two hour time steps appears to typically be 0.025 (.011 for log D) or just 0.2 percent relative to the mean. We find a typical spread in log D for individual echoes near 96 km of 0.3 (0.69 in ln D). This means we would have to average nearly 800 echoes to obtain their Figure 5 accuracy in ln D. Since that figure is based on only about 3000 echoes spread throughout a typical "day" such accuracy does not seem reasonable. Even with 11,050 echoes throughout a superimposed day we generally only resolve log D to ± 0.02 (ln D to ± 0.046). This means errors of roughly 5 percent in D, the accuracy claimed by Greenhow and Hall with less than one-third the echo total. When we compare the average accuracy of D for our September and October runs against the difference in echo total, we find no indication of excess improvement in resolution for the superimposed data. Such an improvement could perhaps result with smoothed data, and because Greenhow and Hall used data taken over ten days it would then be a possible explanation for their seemingly superior data precision. We also should note the possible non-stationarity of D statistics over time periods of many years (see for example Elford's comments on pp. 273-274 of *Barnes and Pazniokas*, [1968]).

Given our relatively poor accuracy in D we are prevented from resolving density very well. These errors are not sufficiently large to discredit the harmonic analyses in Table 9.3, however, the amplitudes of the various harmonics probably are overestimated, especially in September. *Barnes* [1969] notes that tidal density perturbations should only be on the order of 2 percent of the mean density at meteor heights. Since even our October ρ_1 and ρ_2 magnitudes are substantially in excess of 2 percent, the possibility of a breakdown in the relationship between signal decay rate, ambipolar

diffusion, and atmospheric density must be raised. More likely, contamination by the 24 hour mean height variation resulting from the earth's rotation is overshadowing the true tidal perturbations. The similarity between our density variations and those of Jodrell Bank and Palo Alto (Figure 9.3), despite precautions by all to use fixed height echoes, supports the latter explanation. On the positive side, we observe that ρ_0 decreases substantially between September and January for 85-90 km but is nearly constant for 90-95 km. This is precisely the seasonal behavior we would expect based on Figure 9.1(b).

The scale heights of Table 9.4, which depend on accurate densities at two heights, are even less credible. Until more runs have been analyzed it seems fairest to state that at Urbana no credible harmonic has yet been detected for scale height variation.

Even a cursory reading of Session 3 in *Barnes and Pazniokas* [1968] will point out the numerous difficulties in utilizing echo decay rates to infer density and the substantial distrust of any such inferences. The statistical reproducibility of results such as true height-decay height relations and the repetative behavior of, for example, the temporal log D variation at fixed height, however, lead one to believe that as Dr. Peterson remarks in Session 3 "It is an indication of something." In the January 1976 rocket program at Wallops Island numerous techniques will allow neutral density computations. These computations are not yet available, but when they are, comparisons with densities inferred from our meteor radar may allow us to determine the true usefulness of such inferences.

10. SINGLE STATION MEASUREMENTS OF WIND SHEARS IN THE METEOR REGION

10.1 *Radial Acceleration Technique*

Numerous studies of atmospheric turbulence in the meteor region have been conducted at Adelaide using remote receiving sites [*Roper*, 1966; *McAvaney*, 1970]. A multistation radar configuration is not, however, essential. A theoretical study by *Kaiser* [1955] indicates that magnitudes of wind gradients might be resolved with monostatic radars if the differential Doppler shift due to specular reflection point movement along the meteor trail can be measured. The apparent Doppler velocity seen by the observer will be

$$u_a \cong u_o + u'^2 R_o t \tag{10.1}$$

where time t is taken as zero at the specular reflection point (subscript o), u' is the wind gradient along the meteor trajectory (assumed linear), and positive velocities are toward the observer. If we measure the apparent velocities at two different times, we can solve for the magnitude of the wind gradient and the displacement of the specular reflection point:

$$|u'| = \left[\frac{(u_2-u_1)}{R_o(t_2-t_1)}\right]^{\frac{1}{2}} \tag{10.2}$$

$$|x_2-x_1| = \left[(u_2-u_1)R_o(t_2-t_1)\right]^{\frac{1}{2}} \tag{10.3}$$

To deduce the vertical wind shear one must know the echo elevation and zenith angles, α and Z_R:

$$\left|\frac{\Delta u}{\Delta z}\right| = u'(\cos\alpha\cos Z_R)^{-1} \tag{10.4}$$

Unfortunately, while α can be determined for each echo via interferometry at a single site, Z_R cannot, though $\pi/4$ is an approximate mean value for our facility.

Müller [1968a] apparently was first to utilize this technique to study wind shears at meteor heights. But he was hampered by the need for manual processing of echo data, which consisted of filmed analog records of the returns. This aggravated the inherently difficult task of resolving not just the Doppler frequency returned by each echo, but the time rate of change of that frequency as well. Further problems accrued from the low data rate and lack of an interferometric determination of echo height. In all three of these regards the University of Illinois meteor radar system has distinct advantages. We utilize fully automated digital processing of the echoes with a special Doppler algorithm which can update the echo velocity every few ms. Our high peak power allows the collection of thousands of echoes per day so we can avoid the potential pitfalls of superimposed epoch analysis.

To incorporate the radial acceleration technique at Urbana, the subroutine SLOPE was added to the main collection software program METP6. This subroutine determines the best linear fit in the least squares sense between all acceptable velocity determinations and their time of occurrence. The slope of this line, BCOEFF, multiplied by the useful echo lifetime, t_2-t_1, gives u_2-u_1. These two quantities along with echo range allow us to solve equations (10.2) and (10.3).

Table 10.1 presents histograms and statistics of key parameters for two radar runs made one week apart in January 1976. Note that while the linear wind gradient model predicts only positive Doppler accelerations, we observe only a slight tendency toward positive u_2-u_1 values. This is in opposition to Figure 9 in *Müller* [1968a], where positive accelerations outnumbering negative accelerations by 4 to 1 are typical. However, Table 10.1 also shows that there are no significant differences in any parameters whether or not echoes with apparent negative accelerations are utilized. Table 10.2 tabulates

Table 10.1

Behavior of key parameters in the radial acceleration technique.

Parameter		|BCOEFF|		BCOEFF		DELT (t_1-t_2)				DELV (U_2-U_1)	
Run		1	2	1	2		1	2			1	2
Parameter Bin		% echoes/bin										
0	$10ms^{-2}$	12.79	12.51	12.71	11.86	0.00	.05s 8.00	8.57	-100	$-90ms^{-1}$	.09	.06
10		11.98	11.23	10.56	11.26	.05	24.57	26.06	- 90		0.00	.03
20		9.76	10.61	9.15	10.44	.10	29.60	29.60	- 80		.05	.03
30		9.17	9.44	10.02	8.78	.15	16.86	15.02	- 70		.24	.31
40		7.58	6.80	8.47	7.13	.20	8.12	7.57	- 60		.47	.63
50		6.43	6.95	6.79	7.43	.25	10.47	10.70	- 50		1.03	1.16
60		5.25	5.75	4.91	5.48	.30	2.35	2.47	- 40		2.38	2.00
70		5.14	4.62	4.71	5.18				- 30		4.50	5.26
80		5.03	4.43	5.25	4.50				- 20		11.74	11.92
90		3.81	4.08	4.03	4.20				- 10		24.30	26.60
100		3.20	3.65	3.16	3.53				0		28.07	27.75
110		3.81	3.15	3.77	3.38				10		14.95	14.11
120		2.33	2.53	2.15	2.93				20		6.74	6.04
130		2.81	3.22	3.16	3.45				30		2.97	2.35
140		2.26	1.90	2.49	1.80				40		1.32	1.28
150		1.89	2.21	2.08	2.10				50		.74	.31
160		1.55	1.67	1.68	1.05				60		.38	.09
170		1.85	1.83	1.75	1.80				70		.03	.03
180		2.03	1.71	2.02	1.95				80		0.00	.03
190	$200ms^{-2}$	1.22	1 71	1.08	1.73				90	$100ms^{-1}$	0.00	0.00
										% pos =	55.19	52.00

column 1 uses January 14-16, 1976 data
column 2 uses January 21-23, 1976 data

Table 10.1 (continued)

	|DELV|				DELX (x_2-x_1)				DELVX (u')*		DELVX**	
		1	2			1	2			1	2	1	2
0	$5ms^{-1}$	28.83	30.44	0	50m	1.00	.72	0	$5ms^{-1}km^{-1}$	3.04	2.65	3.18	2.91
5		23.51	23.34	50		2.47	2.75	5		10.23	10.68	10.68	10.48
10		16.27	15.08	100		4.71	4.88	10		14.01	15.16	14.50	15.14
15		10.41	10.95	150		6.15	7.04	15		15.93	14.32	15.03	14.74
20		6.85	6.35	200		7.41	7.85	20		13.64	15.64	14.00	14.39
25		4.38	4.94	250		8.33	8.67	25		10.76	11.55	10.68	11.26
30		3.50	2.32	300		9.62	9.01	30		8.42	7.40	7.91	7.98
35		1.85	2.03	350		9.56	9.17	35		6.29	6.32	6.71	6.23
40		1.59	1.53	400		8.53	9.32	40		5.59	4.69	4.94	4.72
45		.76	.91	450		8.15	8.92	45		3.73	3.61	3.59	3.35
50		.71	.50	500		7.24	6.41	50		1.92	2.95	2.18	2.91
55		.50	.44	550		5.85	6.04	55		1.97	1.68	1.82	1.66
60		.47	.22	600		4.97	4.69	60		1.39	1.26	1.44	1.31
65		.15	.19	650		4.21	3.82	65		.80	.66	1.03	.84
70		.06	.06	700		3.09	2.78	70		.75	.54	.79	.53
75		.03	0.00	750		2.38	2.41	75		.48	.60	.41	.47
80		0.00	0.00	800		1.38	1.47	80		.11	.54	.24	.47
85		0.00	.06	850		1.03	1.13	85		.21	.12	.24	.25
90		.09	.06	900		1.15	.66	90		.32	.12	.24	.06
95	$100ms^{-1}$	0.00	0.00	950	1000m	.82	.88	95	$100ms^{-1}km^{-1}$	.16	.06	.18	.09

*pos DELV only
**all DELV

Table 10.1 (continued)

	Nr	mean	σ	σ mean
$\|BCOEFF\| ms^{-2}$				
1	2705	62.76	51.33	.99
2	2574	63.55	51.97	1.02
$BCOEFF ms^{-2}$				
1	1487	63.60	51.16	1.33
2	1332	64.07	51.64	1.41
DELT s				
1	3399	.15	.07	.00
2	3196	.14	.08	.00
$\|DELV\| ms^{-1}$				
1	3399	13.00	12.29	.21
2	3196	12.58	11.95	.21
$DELV ms^{-1}$				
1	3399	1.67	17.81	.31
2	3196	.43	17.35	.31
DELX m				
1	3399	432.94	225.15	3.86
2	3196	422.76	217.94	3.86

	Nr	mean	σ	σ mean
$DELVX ms^{-1} km^{-1}$*				
1	1877	26.09	16.54	.38
2	1662	25.73	16.01	.39
$DELVX ms^{-1} km^{-1}$**				
1	3399	26.00	16.71	.29
2	3196	25.74	16.38	.29

*pos DELV only
**all DELV

Table 10.2

Mean differential velocity squared versus displacement.

(x_2-x_1)		Jan. 14-16, 1976 $(u_2-u_1)^2$			Jan. 21-23, 1976			
DELX	Nr	$DELV^2$	σ	σ Mean	N	$DELV^2$	σ	σ Mean
25 m	35	.01 $(m\ s^{-1})^2$	.02	0.	23	.03	.04	.01
75	84	.29	.39	.04	88	.41	.61	.06
125	160	2.62	3.33	.26	156	1.97	2.33	.19
175	209	6.89	8.20	.57	225	9.21	10.73	.72
225	252	22.31	29.86	1.88	251	21.02	24.39	1.54
275	283	45.19	53.34	3.17	277	39.26	44.43	2.67
325	327	73.38	84.33	4.66	288	89.50	105.72	6.23
375	325	122.92	144.25	8.00	293	116.50	137.89	8.06
425	290	192.21	231.49	13.59	298	178.13	202.93	11.76
475	277	255.34	333.95	20.06	285	278.17	315.92	18.71
525	246	409.97	523.69	33.39	205	361.40	486.69	33.99
575	199	483.95	592.10	41.97	193	494.45	566.15	40.75
625	169	519.06	671.48	51.65	150	600.46	655.83	53.55
675	143	790.45	796.83	66.63	122	808.49	952.86	86.27
725	105	1071.73	1029.12	100.43	89	739.17	719.59	76.28
775	81	901.72	907.17	100.80	77	842.43	894.73	101.96
825	47	1165.90	1010.93	147.46	47	1029.64	945.18	137.87
875	35	842.09	617.04	104.30	36	1196.13	1059.83	176.64
925	39	1113.51	877.49	140.51	21	1334.40	980.78	214.02
975	28	1156.27	559.84	105.80	28	1891.62	1906.09	360.22

mean velocity difference squared versus specular reflection displacement for both January runs. Although both runs exhibit quite similar performance, the slope between $DELV^2$ and DELX is far steeper than that predicted by turbulence theory assuming an isotropic and inertial region. The latter predicts a slope of only 0.67, while we apparently observe a slope in excess of 3. Figure 15 in *Müller* [1968a] gives a slope near 1.57 for vertical separations, but this must be viewed with caution because an assumed zenith angle of $\pi/4$ is used for all echoes. Slopes near 1.4 for vertical separations have been reported by *Roper* [1966] using spaced receiving stations, but later work by *McAvaney* [1970] failed to show a differentiation between vertical and horizontal shears, both yielding slopes near 0.67. And even if real, such an increase in slope is still not nearly large enough to explain our observations.

To investigate the cause of our failure in applying the radial acceleration technique, a zero-Doppler simulated target from the radar director was applied to all receivers. Table 10.3 lists the standard deviations in apparent Doppler acceleration versus usable echo duration for signal-to-noise levels of 20dB and 30dB. Since typical wind shears are only on the order of 15 m s^{-1} km^{-1}, and a typical range is 140 km, a representative Doppler acceleration is about 30 m s^{-2}. Yet Table 10.3 shows that with our weakest signals, even if the echo lasts 0.2 seconds, our measurement error is likely to be as large as this true value. We can improve our accuracy by measuring over longer time periods or rejecting the weakest echoes. A combination of these two would seem our safest course. Collection software limits our measuring period to under 0.35 s, but this is actually beneficial because longer enduring echoes are often of questionable use due to the occurrence of multiple reflection centers or the nonspecular nature of such echoes.

When the January 1976 echoes were reexamined, accepting only those with

Table 10.3

Standard deviation of Doppler acceleration magnitude versus echo duration and signal-to-noise ratio using zero-Doppler simulated targets.

Echo Duration	$\sigma_{\lvert BCOEFF \rvert}$ ms^{-2}	
	20dB S/N	30dB S/N
.05 - .10 s	96	46
.10 - .15	57	23
.15 - .20	43	12
.20 - .25	28	8
.25 - .30	20	6
.30 - .35	16	5

useful lifetimes in excess of 0.2 s, the wind gradient histogram of Table 10.4 resulted. The mean shear of 14.35 m s^{-1} km^{-1} is now in good agreement with shears observed via sodium clouds [*Kochanski*, 1964]. Nevertheless, the slope of $DELV^2$ versus DELX remains in excess of 3. This lack of improvement prompted a reexamination of equation (10.3). Note that we resolve u_2-u_1 best when t_2-t_1 is longest. Since our software and acceptance criteria limit us to the small span of 0.2 s $\leq t_2-t_1 \leq$ 0.35 s, we force it to be relatively constant. Furthermore, mean range is also relatively constant thus solving (10.3) for $(u_2-u_1)^2$ gives

$$(u_2-u_1)^2 \propto (x_2-x_1)^4 \tag{10.5}$$

i.e., a slope of 4 is predicted, despite the fact the correct slope is probably about 0.67. Actually an inverse dependence of u_2-u_1 on t_2-t_1 causes our slopes to be somewhat less than 4. It seems we can only surmount our difficulty by making independent measurements of u_2-u_1 and x_2-x_1, precisely what multiple site meteor radars do but single site radars utilizing the radial acceleration technique cannot do.

10.2 *Interpolated Winds Technique*

Independent single station measurements of wind velocity differences and height differences are the natural result of our interpolation method for uniform winds in time and height described in Section 3.1. The interpolation method involves smoothing individual meteor winds typically over time spans of ± 15 minutes standard deviation and height spans of ± 1 km standard deviation. Only the large echo rate of our system lets wind shear determinations with such small scales be statistically significant. Table 10.5 shows the mean vertical wind shear magnitude as a function of time of day. Dividing this data into six groups of four hours each, and applying a one criteria of

Table 10.4

Wind gradient histogram
for
specially selected echoes.

DELVX($ms^{-1}km^{-1}$)		Nr
0.0	5.0	94
5.0	10.0	298
10.0	15.0	392
15.0	20.0	320
20.0	25.0	151
25.0	30.0	72
30.0	35.0	23
25.0	40.0	8
40.0	45.0	3
45.0	50.0	0
50.0	55.0	0
55.0	60.0	0
60.0	65.0	0
65.0	70.0	0
70.0	75.0	0
75.0	80.0	0
80.0	85.0	0
85.0	90.0	0
90.0	95.0	0
95.0	100.0	0

Nr	mean	σ	σ mean
1361	14.35	6.99	0.19

January 1976 echoes
DELT > 0.25 s

Table 10.5

Vertical wind shear magnitude
versus time of day.

Time (hrs)	Mean ($m\ s^{-1}\ km^{-1}$)	
0-1	4.47	
1	4.11	
2	4.15	
3	4.50	
4	4.36	
5	4.66	
6	5.14	
7	4.34	
8	4.09	
9	3.78	min
10	4.73	
11	5.46	
12	5.66	
13	5.96	
14	5.13	
15	5.05	
16	5.37	
17	5.20	
18	5.32	
19	6.35	max
20	5.71	
21	4.73	
22	5.30	
23-24	4.89	
mean	4.94	

Results based on 11 radar runs, Jan. 1975 to Jan. 1976.

classification test for significant temporal variation [*Alder and Roessler*, 1960], we fail to find credible variation at the 5% level. When the data are segmented by height as in Table 10.6, a marginally significant increase in shear strength with altitude is found. This is in agreement with Kochanski's average sodium cloud results over 85-95 km [*Kochanski*, 1964]. Also, because the relation is weak it is not particularly incompatible with McAvaney's lack of significant turbulent energy variation with height based on multi-site meteor radar data [*McAvaney*, 1970]. Table 10.7 presents temporal wind shear behavior on a run-by-run basis so a two criteria of classification procedure can be applied [*Alder and Roessler*, 1960]. As previously noted, no significant shear variation with time of day can be found, but significant inter-run variations are found. The latter can be grouped roughly into (1) those with means from 3.92 to 4.99, (2) those with means in excess of 5.0, and (3) one with a mean under 3.9. Interestingly the largest shears occurred in the equinoctial periods of March, late August, and September, in line with the seasonal variation of the rate of dissipation of turbulent energy averaged over 80 to 100 km reported by *Roper* [1966]. However, the two smallest shears were in April and October, also equinoctial periods. This suggests considerable variability in shear character over just one month and places our observations more in line with those of *McAvaney* [1970], who in refining Roper's work failed to find significant seasonal variation of turbulent energy dissipation rate. Until we have more 24 hour runs we will not be in a position to reliably group our data to characterize shear versus season.

Table 10.6

Vertical wind shear
magnitude versus height.

Run	85-90 km	90-95 km
1	4.41	4.27
2	4.86	8.14
3	4.22	5.99
4	4.70	5.09
5	3.47	4.62
6	5.51	5.80
7	7.24	7.62
8	3.81	4.36
9	5.03	4.43
10	3.59	3.10
11	4.13	4.60

units are in m s^{-1} km^{-1}

Table 10.7

Vertical wind shear magnitude grouped by run and time of day.

Run	Local Time (hr) 0-4	4-8	8-12	12-16	16-20	20-24	Mean
1	3.95	4.43	4.32	4.79	5.80	3.63	4.49
2	6.77	5.30	6.51	6.83	5.77	6.27	6.24
3	3.12	3.85	4.20	6.84	6.93	5.01	4.99
4	5.16	4.73	3.99	5.49	5.03	3.69	4.68
5	3.50	2.11	3.15	3.88	5.69	5.20	3.92
6	3.24	4.81	7.72	8.87	5.12	4.28	5.67
7	7.31	7.21	6.15	7.50	8.16	7.34	7.28
8	4.27	3.72	2.96	2.81	5.63	8.15	4.59
9	4.45	6.49	4.06	3.61	5.12	5.01	4.79
10	3.71	3.34	3.00	3.21	4.02	3.76	3.51
11	3.34	4.24	4.70	5.98	4.62	3.85	4.46
mean	4.44	4.57	4.61	5.44	5.63	5.11	

units are in ms^{-1} km^{-1}

11. SUMMARY AND SUGGESTIONS FOR FUTURE RESEARCH

11.1 *Summary*

The principal observations and conclusions of this study are as follows.

(A) Tidal observations

(i) The annual mean semidiurnal tidal structure seen at Urbana is consistent with $\Theta_2^{2\Omega,2}$ mode dominance.

(ii) At Urbana, we observe an annual mean diurnal tidal structure of short vertical wave length like the $\Theta_1^{\Omega,1}$ mode above 86 km, but $S_1(v)$ does not exhibit growth with altitude. An explanation proposed for such behavior is that the mean $S_1(v)$ is a superposition of two tidal modes, one propagating, one evanescent, of nearly equal strength at 86 km.

(iii) We confirm the tidal anomalies reported by *Fellous et al.* [1974]; namely, short wavelength semidiurnal tidal modes ($\Theta_2^{2\Omega,n}, n \geq 4$), evanescent dirunal tidal modes ($\Theta_1^{\Omega,-n}$), and superimposed waves.

(iv) We observe wave-like behavior regularly in the terdiurnal oscillation at meteor heights. The persistence of this oscillation inclines one to identify it as tidal in nature. We have evidence indicating the oscillation is a combination of a directly excited terdiurnal mode and a nonlinear interaction product of $S_1(v)$ and $S_2(v)$.

(v) We have successfully interpolated space-quadrature winds with our narrow beamwidth system directed only toward the north. Clockwise wind rotation (viewed from above) with increasing height was seen as was the quadrature time relation for E-W and N-S tides.

(B) Internal gravity-wave observations

(i) We confirm the presence of wave-like oscillations in the meteor

region with periods of 1-8 hour and evidence of reflections. Such behavior was first reported by *Revah* [1969].

(ii) Contrary to Revah's results, we do not find excessive growth of wave amplitude with height. Instead, 2/3 of our waves exhibit no clear growth with altitude, a behavior predicted by the theoretical work of *Thomson* [1976].

(iii) The vertical wavelengths of our gravity waves are not in general related to the diurnal tide vertical wavelength. This, along with (ii), indicates that *Spizzichino's* [1969-1970] concept of diurnal tide energy being cascaded into the gravity-wave spectrum by nonlinear interaction is not a dominant factor at Urbana, Illinois.

(iv) We have observed a large gravity-wave oscillation undergoing Doppler shifting toward zero frequency and disappearing in a time span of less than 12 hours.

(v) Our average wind spectra over 3-24 osc-day^{-1} exhibit a power law exponent of -1.5. This is similar to the behavior predicted for isotropic turbulence in an inertial regime and observed at lower altitudes [*Vinnichenko and Dutton*, 1969]. An apparent breakpoint in spectral behavior occurs at periods of 1 hour because the average wind spectra over 24-96 osc-day^{-1} are best fit with an exponent near -3. This is more in line with behavior predicted for a bouyancy subrange [*McAvaney*, 1970].

(C) Miscellaneous experiments

(i) Joint meteor-radar and partial-reflection data collected at Urbana support *Manson's* [1971] hypothesis that increased nitric oxide transport from the auroral zone can result in an increase of winter *D*-region ionization at midlatitudes.

(ii) The technique of using echo decay rates to infer density and scale height at meteor altitudes has been shown to be basically unsuccessful. Harmonic variations in density did not behave as predicted by tidal theory, even though the wind harmonics in most cases did. The difficulty in extracting small tidal variations in density is probably related to contamination by the 24-hr mean height variation due to the earth's rotation. The seasonal behavior of inferred mean density was as expected.

(iii) The radial acceleration technique for inferring wind shears via individual echoes and single-site radars has been shown to be unsuccessful. Use of interpolated winds has, however, allowed us to study smoothed shear estimates at Urbana. Our findings are compatible with *McAvaney's* [1970] multi-site results in Adelaide.

11.2 *Suggestions for Future Research*

Three equipment-related suggestions can offer substantial improvement in our system echo rate and height accuracy. The easiest of the three to implement is the inclusion of narrowband active low pass filters at the output of each phase detector. A preliminary unit with 20 kHz bandwidth has already been constructed and tested. This narrower bandwidth improves our S/N ratio by roughly 6 dB and potentially offers a doubling in echo rate.

At present we must discard substantial amounts of echo information because our A/D converter samples so slowly that only a single detector can be sampled per transmit pulse. Furthermore, we sample this detector at 100 range locations even though the target is only in one of them, and thus our data collection is inefficient as well as wasteful. If instead, once we had identified the target location, we simultaneously stored each detector value in a sample-and-hold bank, we could prevent both information loss and inefficiency. With ten

detectors we could read out the sample-and-hold bank in just 100 μs, compared to our present 1 ms for 100 range locations. Thus we could also pick up an additional 900 μs per interpulse period for real-time processing. Such a scheme would allow us to catch faster decaying echoes and improve the accuracy of our parameter estimates because more independent calculations per echo would be available for averaging.

The third equipment improvement for our system should be the calibration of the long arm vernier Yagi in our interferometer. This calibration must be quite precise or the potential improvement in height accuracy will not be realized. Calibration by illuminating satellites of known orbits seems best, both from the point of view of accuracy and cost. Our radar has ample sensitivity for tracking passive satellites and, by using the frequency synthesizer voltage controlled oscillator to set the transmitter frequency, we can establish low Doppler frequency conditions.

In terms of analysis, it is suggested that the spectral estimation procedures of *Gaster and Roberts* [1975] be investigated. They have developed techniques specifically for randomly sampled signals, as are our randomly occurring meteor-wind values. Their techniques should decrease our minimum resolvable gravity-wave period since the low pass filtering and aliasing effects of our present analysis method are eliminated.

As mentioned in Chapter 8, it would be most helpful to have meteor-wind data for an entire winter period to correlate with partial-reflection results, which are collected regularly. It is feasible to operate our radar continuously in the low power mode, but a dedicated controller will be needed since the PDP 15/40 computer is required by other experimenters. The controller can simply be a data storage device if the PDP 15/40 is used to process the echoes collected every few days.

REFERENCES

Abramowitz, M. and I. A. Stegun (1964), *Handbook of Mathematical Functions with Formulas, Graphs, and Mathematical Tables*, Nat. Bur. of Standards.

Alder, H. L. and E. B. Roessler (1960), *Introduction to Probability and Statistics*, W. H. Freeman and Company, San Francisco.

Anderson, T. C. and F. G. Merrill (1960), Crystal controlled primary frequency standards: latest advances for long term stability, *IRE Trans. on Instru., 9/60*, 136-140.

Armstrong, E. B. and A. Dalgarno (1955)(Eds.), *The Airglow and the Aurora*, Pergamon Press, London, 1-420.

Backof, C. A., Jr. and S. A. Bowhill (1974), Collection and processing of data from a phase-coherent meteor radar, *Aeron. Rep. No. 59*, Aeron. Lab., Dep. Elec. Eng., Univ. Ill., Urbana-Champaign.

Baggaley, W. J. and P. J. Wilkinson (1974), The treatment of observational radio-meteor wind data, *Planet. Space Sci. 22*, 777-787.

Barnes, A. A., Jr. and J. J. Pazniokas (1968)(Eds.), Proceedings of the workshop on methods of obtaining winds and densities from radar meteor trail returns, *AFCRL, Special Report 75, AFCRL-68-0228.*

Barnes, A. A., Jr. (1969), Meteor trail radars, *Stratospheric Circulation, AIAA Progress Series, Vol. 22*, Academic Press, New York, 575-598.

Barnes, A. A., Jr. (1972), Using VHF radars to probe the atmosphere, *15th Radar Meteorology Conf.*, 341-352.

Barnes, A. A., Jr. and J. J. Pazniokas (1972), Results from the AFCRL radar meteor trail set, *AFCRL, Environmental Research Papers No. 392, AFCRL-72-0185.*

Bartman, F. J., L. W. Chaney, L. M. Jones, and V. C. Liu (1956), Upper-air

density and temperature by the falling-sphere method, *J. Applied Phys. 27*, 706-712.

Bedinger, J. F. (1973), Photography of a lithium vapor trail during the daytime, *J. Atmos. Terr. Phys. 35*, 377-381.

Beer, T. (1972), Atmospheric waves and the ionosphere, *Contemp. Phys. 13*, 247-271.

Belrose, J. S. (1963), AGARDograph 74: *Propagation of Radio Waves at Frequencies below 300 Kc/s*, Pergamon Press, Oxford.

Belrose, J. S. and M. J. Burke (1964), Study of the lower ionosphere using partial reflection 1. Experimental technique and method of analysis, *J. Geophys. Res. 69*, 2799-2818.

Bernard, R. (1974), Tides in the *E*-region observed by incoherent scatter over Saint Sautin, *J. Atmos. Terr. Phys. 36*, 1105-1120.

Booker, J. R. and F. P. Bretherton (1967), The critical layer for internal gravity waves in a shear flow, *J. Fluid Mech. 27*, 513-539.

Breeding, R. J. (1972), A nonlinear model of the break-up of internal gravity waves due to their exponential growth with height, *J. Geophys. Res. 77*, 2681-2692.

Brown, G. H., W. C. Morrison, W. L. Behrend, and J. G. Reddeck (1949), Method of multiple operation of transmitter tubes particularly adapted for television transmission in the ultra-high-frequency band, *RCA Review X*, 161-172.

Chapman, S. A. and R. S. Lindzen (1970), *Atmospheric Tides, Thermal and Gravitational*, D. Reidel, Dordrecht-Holland.

Charney, J. G. and P. G. Drazin (1961), Propagation of planetary-scale disturbances from the lower into the upper atmosphere, *J. Geophys. Res. 66*, 83-109.

Clark, R. R. (1975), Meteor wind measurements at Durham, New Hampshire (43°N, 71°W), *J. Atmos. Sci. 32*, 1689-1693.

David, H. A. (1970), *Order Statistics*, Wiley, New York.

Denny, B. W. and S. A. Bowhill (1973), Partial-reflection studies of *D*-region winter variability, *Aeron. Rep. No. 56*, Aeron. Lab., Dep. Elec. Eng., Univ. Ill., Urbana-Champaign.

Dickinson, R. E. and M. A. Geller (1968), A generalization of "Tidal theory with Newtonian cooling", *J. Atmos. Sci. 25*, 932-933.

Edwards, B. (1973a)(Ed.), Research in Aeronomy, October 1, 1972 - March 31, 1973, *Prog. Rep. 73-1*, Aeron. Lab., Dep. Elec. Eng., Univ. Ill., Urbana-Champaign.

Edwards, B. (1973b)(Ed.), Research in Aeronomy, April 1 - September 30, 1973, *Prog. Rep. 73-2*, Aeron. Lab., Dep. Elec. Eng., Univ. Ill., Urbana-Champaign.

Edwards, B. (1974)(Ed.), Research in Aeronomy, April 1 - September 30, 1974, *Prog. Rep. 74-2*, Aeron. Lab., Dep. Elec. Eng., Univ. Ill., Urbana-Champaign.

Elford, W. G. (1959), Winds in the upper atmosphere, *J. Atmos. Terr. Phys. 15*, 132-136.

Elford, W. G. (1974), A 6-year synoptic study of winds between 80 and 100 km, from meteor trail drifts, *IAMAP/IAPSO combined 1st special assembly*, Melbourne, 624-641.

Eshelman, V. R. (1955), Theory of radio reflections from electron-ion clouds, *IRE Trans. Ant. Prop. AP-3*, 32-39.

Eshelman, V. R. (1957), The theoretical length distribution of ionized meteor trails, *J. Atmos. Terr. Phys. 10*, 57-72.

Evans, J. V. (1969), Theory and practice of ionosphere study by Thomson

scatter radar, *Proc. IEEE 57*, (4), 496-530.

Fedele, D. (1968), in *Winds and Turbulence in Stratosphere, Mesosphere, and Ionosphere*, (Ed.) K. Rawer, North Holland, Amsterdam.

Fellous, J. L., A. Spizzichino, M. Glass, and M. Massebeuf (1974), Vertical propagation of tides at meteor heights, *J. Atmos. Terr. Phys. 36*, 385-396.

Fellous, J. L., R. Bernard, M. Glass, M. Massebeuf, and A. Spizzichino (1975), A study of the variations of atmospheric tides in the meteor zone, *J. Atmos. Terr. Phys. 37*, 1511-1524.

Flattery, T. W. (1967), Hough functions, *Tech. Rep. No. 21*, Dep. Geophys. Sci., Univ. Chicago.

Gardner, F. F. and J. L. Pawsey (1953), Study of the ionospheric *D* region using partial reflections, *J. Atmos. Terr. Phys. 3*, 321-344.

Gaster, M. and J. B. Roberts (1975), Spectral analysis of randomly sampled signals, *J. Inst. Maths. Applics 15*, 195-216.

Geisler, J. E. and R. E. Dickinson (1968), Vertical motions and nitric oxide in the upper mesosphere, *J. Atmos. Terr. Phys. 30*, 1505-1521.

Geller, M. A. and C. F. Sechrist, Jr. (1971), Coordinated rocket measurements on the *D*-region winter anomaly - II. Some implications, *J. Atmos. Terr. Phys. 33*, 1027-1040.

Geller, M. A., G. C. Hess, and D. Wratt (1976), Simultaneous partial reflection and meteor radar wind observations at Urbana, Illinois, during the winter of 1974-1975, *J. Atmos. Terr. Phys. 38*, 287-290.

Georges, T. M. (1967), Ionospheric effects of atmospheric waves, *ESSA Tech. Rep. IER 57 - ITSA 54*.

Glass, M., A. Spizzichino, and I. Revah (1972), *AGARD Conf. Proc. 115*.

Glass, M. (1973), Thése d'Etat, Paris.

Glass, M. and A. Spizzichino (1974), Waves in the lower thermosphere: Recent experimental investigations, *J. Atmos. Terr. Phys. 36*, 1825-1839.

Glass, M., J. L. Fellous, M. Massebeuf, A. Spizzichino, I. A. Lysenko, and Y. I. Portniaghin (1975), Comparison and interpretation of the results of simultaneous wind measurements in the lower thermosphere at Garchy (France) and Obninsk (U.S.S.R.) by meteor radar technique, *J. Atmos. Terr. Phys. 37*, 1077-1087.

Grebene, A. B. (1972), *Analog Integrated Circuit Design*, Van Nostrand Reinhold Co., New York, 230-238.

Green, J. L., H. G. Selberg, and E. E. Ferguson (1960), Longbranch radio propagation transmitting station WWI at Havana, Illinois, *NBS Rep. 6096*, U. S. Dep. Commer., Washington, D. C.

Greenhow, J. S. (1952), A radio echo method for the investigation of atmospheric winds at altitudes of 80 to 100 km, *J. Atmos. Terr. Phys. 2*, 282-291.

Greenhow, J. S. and E. L. Neufeld (1955), The diffusion of ionized meteor trails in the upper atmosphere, *J. Atmos. Terr. Phys. 6*, 133-140.

Greenhow, J. S. and E. L. Neufeld (1959), Measurements of turbulence in the upper atmosphere, *Proc. Phys. Soc. 74*, (*1*), 1-10.

Greenhow, J. S. and J. E. Hall (1960a), Diurnal variations of density and scale height in the upper atmosphere, *J. Atmos. Terr. Phys. 18*, 203-214.

Greenhow, J. S. and J. E. Hall (1960b), The importance of initial trail radius on the apparent height and number distributions of meteor echoes, *Mon. Not. Roy. Astron. Soc. 121*, 183-196.

Greenhow, J. S. and E. L. Neufeld (1961), Winds in the upper atmosphere, *Quart. J. Roy. Meteorol. Soc. 87*, 472-489.

Grimshaw, R. (1975), Nonlinear internal gravity waves and their interaction with the mean wind, *J. Atmos. Sci. 32*, 1779-1793.

Groves, G. V. (1959), A theory for determining upper-atmosphere winds from radio observations on meteor trails, *J. Atmos. Terr. Phys. 16*, 344-356.

Groves, G. V. (1960), Wind and temperature results obtained in Skylark experiments, *Space Res. I*, 144-153.

Guha, D. (1968), Studies of lower ionosphere drifts by the three-receiver technique, *Aeron. Rep. No. 27*, Aeron. Lab., Dep. Elec. Eng., Univ. Ill., Urbana-Champaign.

Guha, D. and M. A. Geller (1972), Computer simulation of the three-receiver drift experiment, *Aeron. Rep. No. 50*, Aeron. Lab., Dep. Elec. Eng., Univ. Ill., Urbana-Champaign.

Harrington, T. A. and M. A. Geller (1975), Performance of the University of Illinois meteor-radar system - A preliminary report, *Aeron. Rep. No. 65*, Aeron. Lab., Dep. Elec. Eng., Univ. Ill., Urbana-Champaign.

Hawkins, B. S. (1956), A radio survey of sporadic meteor radiants, *Mon. Not. Roy. Astron. Soc. 116*, 92-104.

Hawkins, G. S. and F. L. Whipple (1958), The width of meteor trails, *Astron. J. 63*, 283-291.

Hawkins, G. S. and E. K. L. Upton (1958), The influx rate of meteors in the earth's atmosphere, *Astrophys. J. 128*, 727-735.

Healy, D. J., III (1966), Measurement of electrical parameters of VHF quartz crystal units, Radar and Microwave Development, *Engineering Tech. Memo. No. 121*, Westinghouse Aerospace Division, Baltimore, Md., 1-5.

Healy, D. J., III and M. M. Driscoll (1967), Design manual for voltage-

controlled crystal oscillators (VCXO), Westinghouse Defense and Space Center, Baltimore, Md.

Henry, G. W., Jr. (1966), Instrumentation and preliminary results from shipboard measurements of vertical incidence ionospheric absorption, *Aeron. Rep. No. 13*, Aeron. Lab., Dep. Elec. Eng., Univ. Ill., Urbana-Champaign.

Herlofson, N. (1951), Plasma resonance in Ionospheric Irregularities, *Ark. Fys. 3*, 247-297.

Hernandez, G. and R. G. Roble (1976), Direct measurements of nighttime thermospheric winds and temperatures 1. Seasonal variations during geomagnetic quiet periods, *J. Geophys. Res. 81*, 2065-2074.

Hines, C. O. (1960), Internal gravity waves at ionospheric heights, *Can. J. Phys. 38*, 1441-1481.

Hogg, D. C. and W. W. Mumford (1960), The effective noise temperature of the sky, *Microwave J. 3*, (3), 80-84.

Holton, J. R. (1972), An *Introduction to Dynamic Meteorology*, Academic Press, New York, 1-319.

Hook, J. L. (1970), Winds at the 75-110 km level at College, Alaska, *Planet. Space Sci. 18*, 1623-1638.

Hough, S. S. (1898), The application of harmonic analysis to the dynamical theory of the tides, Part II. On the general integration of Laplace's dynamical equations, *Phil. Trans. Roy. Soc. London A191*, 139-185.

Huxley, L. G. H. (1952), The persistence of meteor trails, *Aust. J. Sci. Res. A5*, 10-16.

Jones, W. L. (1969), Ray tracing for internal gravity waves, *J. Geophys. Res. 74*, 2028-2033.

Jones, W. L. and D. D. Houghton (1971), The coupling of momentum between

internal gravity waves and mean flow: A numerical study, *J. Atmos. Sci. 28*, 604-608.

Kaiser, T. R. (1953), Radio echo studies of meteor ionization, *Phil. Mag. 2, Suppl.*, 495-544.

Kaiser, T. R. (1955), *Meteors*, Pergamon Press, London, 1-55.

Kaiser, T. R. (1961), The determination of the incident flux of radio-meteors, II. Sporadic meteors, *Mon. Not. Roy. Astron. Soc. 123*, 265.

Kaiser, T. R., W. M. Pickering, and C. D. Watkins (1969), Ambipolar diffusion and motion of ion clouds in the earth's magnetic field, *Planet. Space Sci. 17*, 519-552.

Karimov, K. A., V. Ya. Ogurtsov, and V. V. Sidorov (1971), Mean monthly characteristics of the wind regime, in *Investigation of the Ionosphere and Meteors*, (Ed.) I. B. Bujbosunov, NASA TT F-744, 50-56.

Kent, G. S. and R. W. H. Wright (1968), Movements of ionospheric irregularities and atmospheric winds, *J. Atmos. Terr. Phys. 30*, 657-691.

Kochanski, A. (1964), Atmospheric motions from sodium cloud drifts, *J. Geophys. Res. 69*, 3651-3662.

Kohavi, Z. (1970), *Switching and Finite Automata Theory*, McGraw-Hill, New York.

Kraus, J. D. (1950), *Antennas*, McGraw-Hill, New York.

Lee, W. and M. A. Geller (1973), Preliminary design study of a high-resolution meteor radar, *Aeron. Rep. No. 70*, Aeron. Lab., Dep. Elec. Eng., Univ. Ill., Urbana-Champaign.

Lindzen, R. S. (1968), The application of classical atmospheric tidal theory, *Proc. Roy. Soc. A303*, 299-316.

Lindzen, R. S. (1969), Data necessary for the detection and description of

tides and gravity waves in the upper atmosphere, *J. Atmos. Terr. Phys. 31*, 449-456.

Lindzen, R. S. and S. Hong (1974), Effects of mean winds and horizontal temperature gradients on solar and lunar semidiurnal tides in the atmosphere, *J. Atmos. Sci. 31*, 1421-1446.

Liu, C. H. and J. Klostermeyer (1975), Excitation of acoustic-gravity waves in a realistic thermosphere, *J. Atmos. Terr. Phys. 37*, 1099-1108.

Lysenko, I. A., Yu. I. Portnyagin, K. Sprenga, K. M. Greisiger, and R. Schminder (1972), Results of a comparison between radar meteor wind measurements and simultaneous lower ionosphere drift measurements in the same area, *J. Atmos. Terr. Phys. 34*, 1435-1444.

Manning, L. A., O. G. Villard, and V. M. Peterson (1950), Meteoric echo study of upper atmospheric winds, *Proc. I.R.E. 38*, 877-883.

Manning, L. A. (1958), The initial radius of meteoric ionization trails, *J. Geophys. Res. 63*, 181-196.

Manson, A. H. (1971), The concentration and transport of minor constituents in the mesosphere and lower thermosphere (70-110 km) during periods of anomalous absorption, *J. Atmos. Terr. Phys. 33*, 715-722.

Manson, A. H., J. B. Gregory, and D. G. Stephenson (1974), Winds and wave motions to 110 km at mid-latitudes - I. Partial reflection radiowave soundings, 1972-73, *J. Atmos. Sci. 31*, 2207-2215.

Martin-Vegue, C. A. (1961), A 16 megawatt, 100 microsecond pulse modulator, Cathode Press *18*, 16-19.

McAvaney, B. J. (1970), Small scale wind structure in the upper atmosphere, *Ph.D. Thesis*, Univ. of Adelaide, Physics Dep., 1-181.

McKinley, D. W. R. (1961), *Meteor Science and Engineering*, McGraw-Hill, 1-309.

Meyer, C. S., D. K. Lynn, and D. J. Hamilton (1968)(Eds.), *Analysis and Design of Integrated Circuits*, McGraw-Hill, New York, 416-459.

Mowbray, D. E. and B. S. H. Rarity (1967), A theoretical and experimental investigation of the phase configuration of internal waves of small amplitude in a density stratified liquid, *J. Fluid Mech. 28*, 1-16.

Müller, H. G. (1968a) Wind shears in the meteor zone, *Planet. Space Sci. 16*, 61-90.

Müller, H. G. (1968b), Atmospheric tides in the meteor zone, in Proceedings of the Workshop on Methods of Obtaining Winds and Densities from Radar Meteor Trail Returns, (Eds.) A. A. Barnes, Jr. and J. J. Pazniokas, *AFCRL-68-0228, Special Rep. No. 75*, 319-337.

Murphy, C. H., G. V. Bull, and H. D. Edwards (1966), Ionospheric winds measured by gun-launched projectiles, *J. Geophys. Res. 71*, 4535-4544.

Nunn, D. (1967), Thesis, McGill Univ., Montreal.

Pokrovskiy, G. B., V. M. Starostin, and G. M. Teptin (1969), *Izvestia. Atmos. Oceanic Phys. 5*, 631.

Rastogi, P. K. and S. A. Bowhill (1976), Gravity waves in the equatorial mesosphere, *J. Atmos. Terr. Phys. 38*, 51-60.

Revah, I. (1969), Etude des vents de petite echelle observes au moyen des trainees meteoriques, *Ann. Geophys. 25*, 1-45.

Revah, I. (1970), Partial reflections of gravity waves observed by means of a meteoric radar, *J. Atmos. Terr. Phys. 32*, 1313-1318.

Rice, D. W. and P. A. Forsyth (1963), Variations in meteoric radio signal decay rates, *Can. J. Phys. 41*, 679-690.

Rice, D. W. and P. A. Forsyth (1964), The distribution of ionization along underdense meteor trails, *Can. J. Phys. 42*, 2035-2047.

Vinnichenko, N. K. and J. A. Dutton (1969), Empirical studies of atmospheric structure and spectra in the free atmosphere, *Radio Sci. 4*, 1115-1126.

Webb, W. L., W. E. Hubert, R. L. Miller, and J. F. Spurling (1961), *Bull. Am. Met. Soc. 42*, 482.

Weeks, W. L. (1968), *Antenna Engineering*, McGraw-Hill, New York, 72-78.

Weiss, A. A. (1959), The temporal variation of the heights of reflection points of meteor trails, *Aust. J. Phys. 12*, 116-126.

Weiss, A. A. (1961), The distribution of meteor masses for sporadic meteors and three showers, *Aust. J. Phys. 14*, 102.

Whipple, F. L. and G. S. Hawkins (1956), The Harvard radio meteor project, a revised edition of the Final Summary Report of August 16, 1955, *AFCRL (122)*, 458.

Witt, G. (1969), The nature of noctilucent clouds, *Space Res. IX*, 157-169.

Woodman, R. F. and A. Guillen (1974), Radar observations of winds and turbulence in the stratosphere and mesosphere, *J. Atmos. Sci. 31*, 493-503.

Zipf, E. C., W. L. Borst, and T. M. Donahue (1970), A mass spectrometer observation of NO in an auroral arc, *J. Geophys. Res. 75*, 6371-6376.

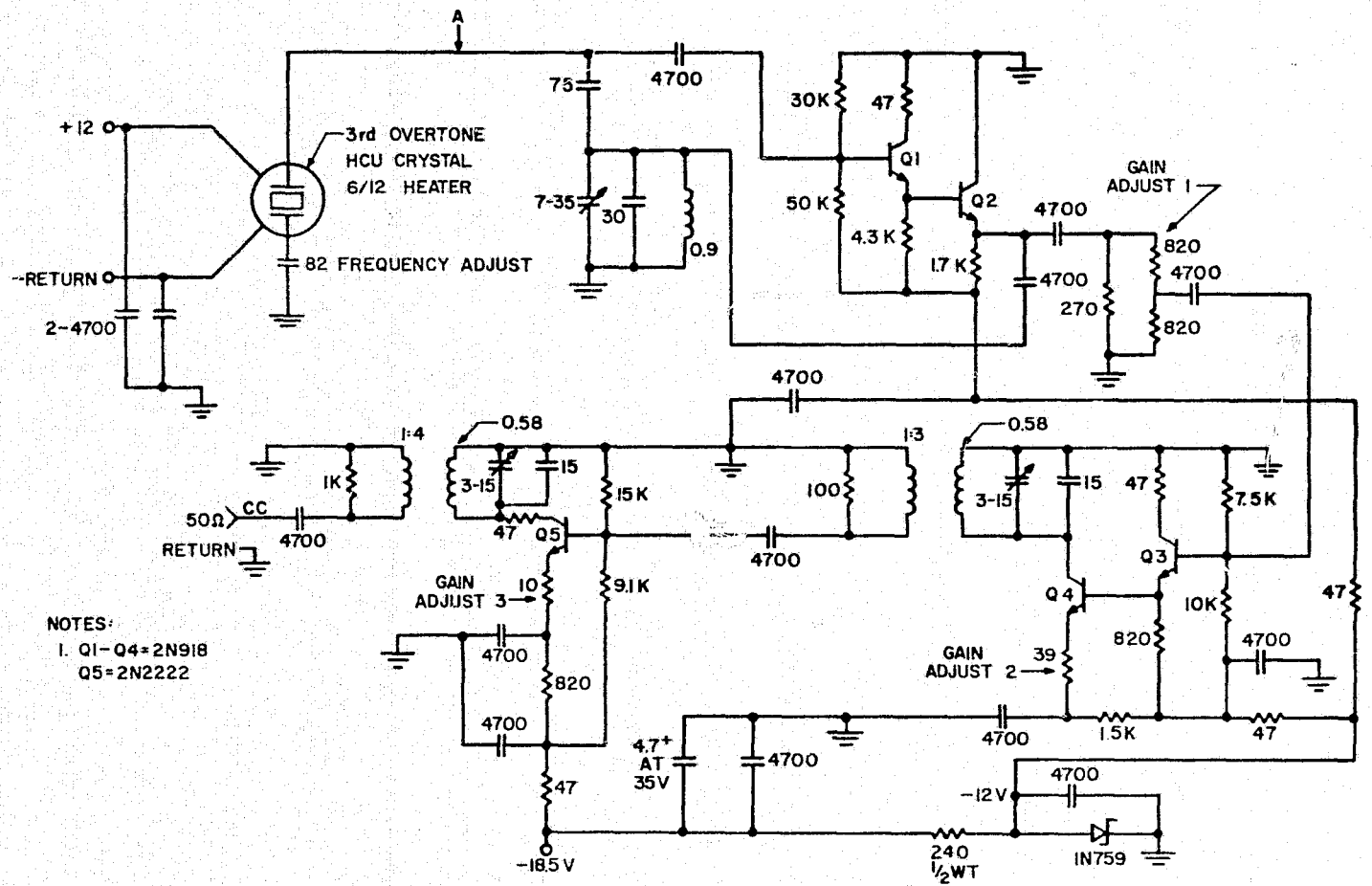

Figure I.1 FS-FS1 Carrier oscillator, 40.92 MHz TCXO.

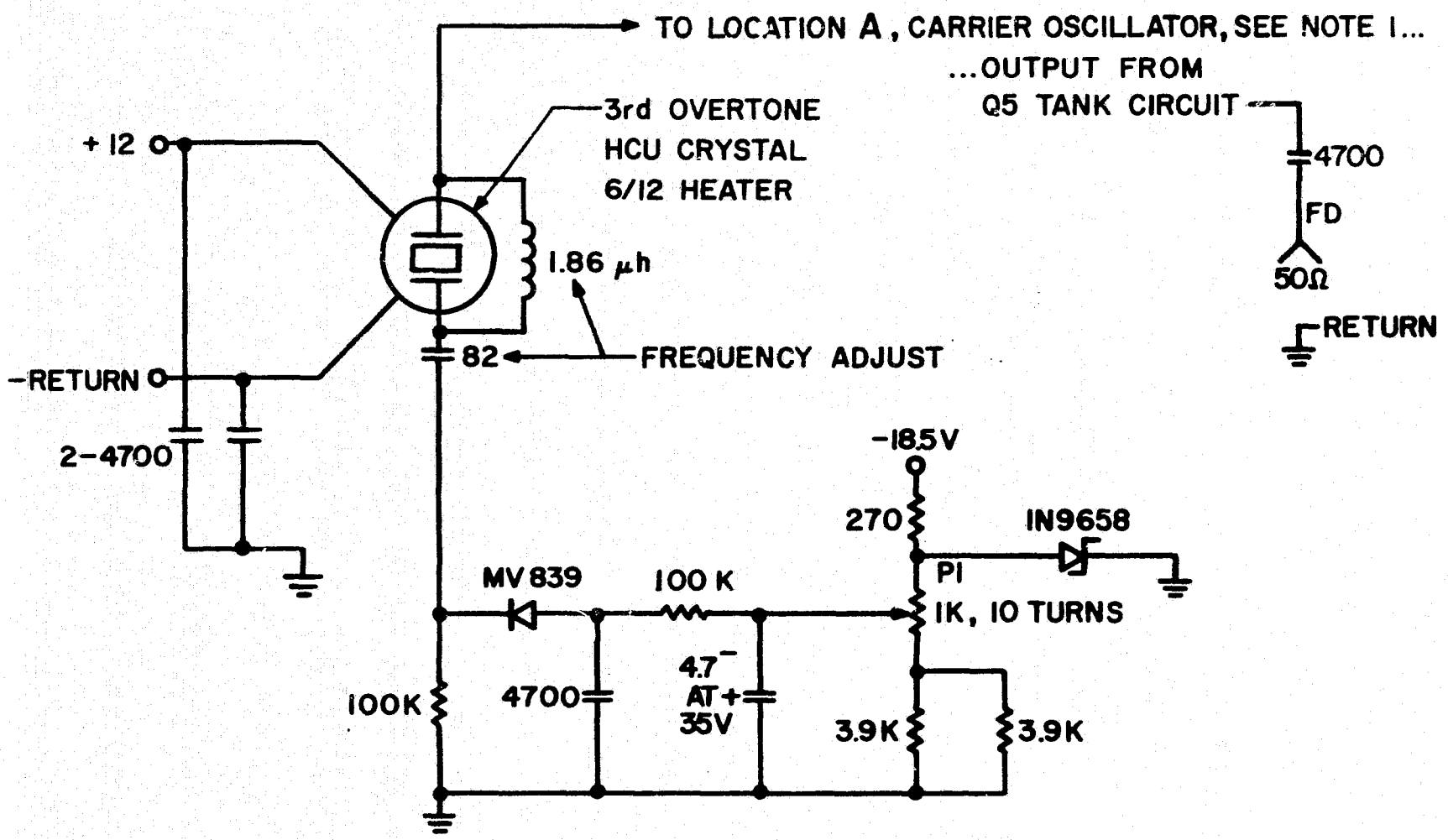

NOTES:

1. REST OF SCHEMATIC IDENTICAL TO THAT OF CARRIER OSCILLATOR FS1.

Figure I.2 FS-FS2 Doppler oscillator, 40.92 MHz TCVCXO.

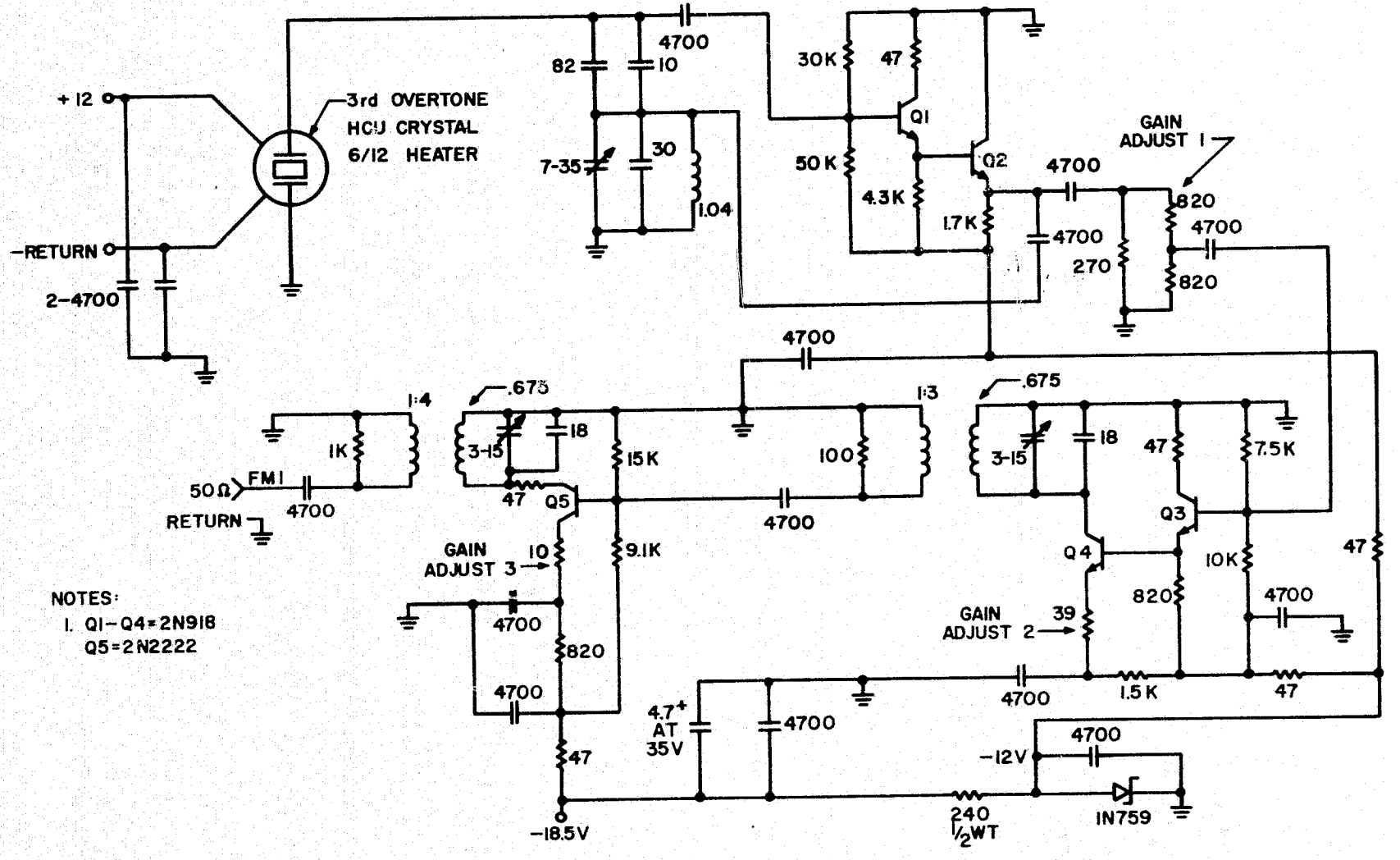

Figure I.3 FS-FS3 First mixer oscillator, 35.42 MHz TCXO.

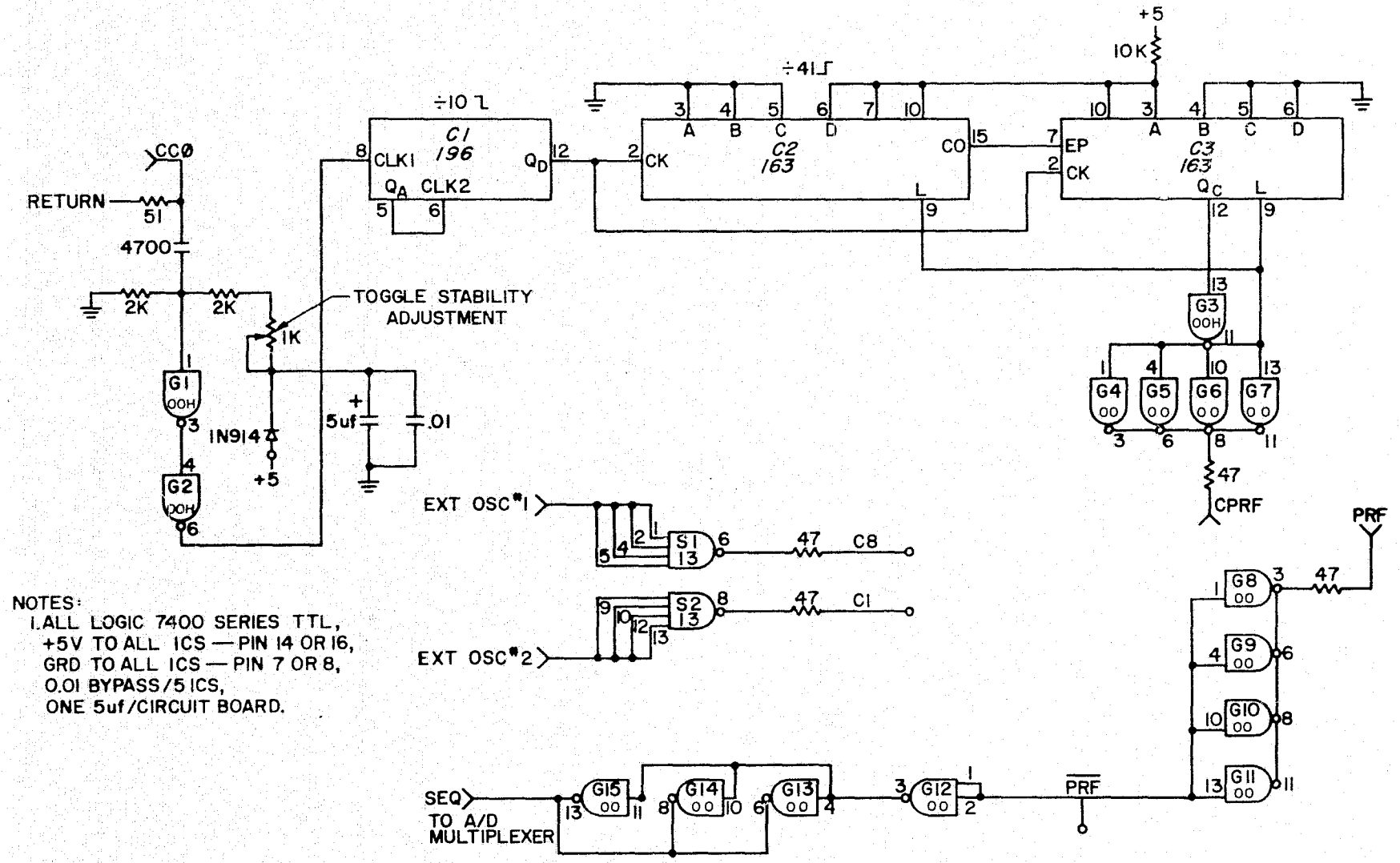

Figure I.4 FS-FS4 PRF Clock formation.

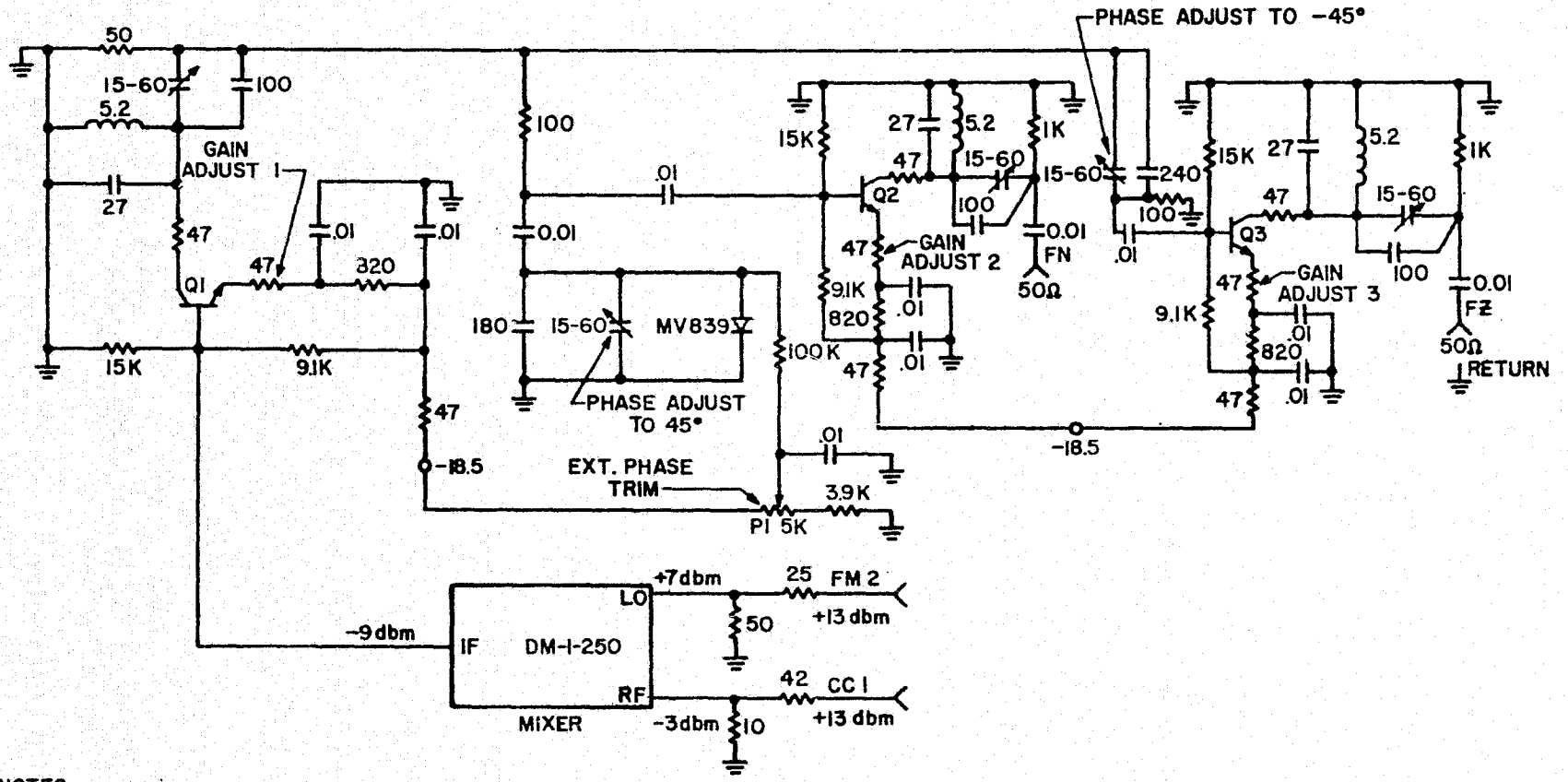

NOTES:
1. NOMINAL POWER LEVELS FOR MIXER SHOWN
2. Q1,2,3 = 2N2222

Figure I.5 FS-FS5 Quadrature phase generation.

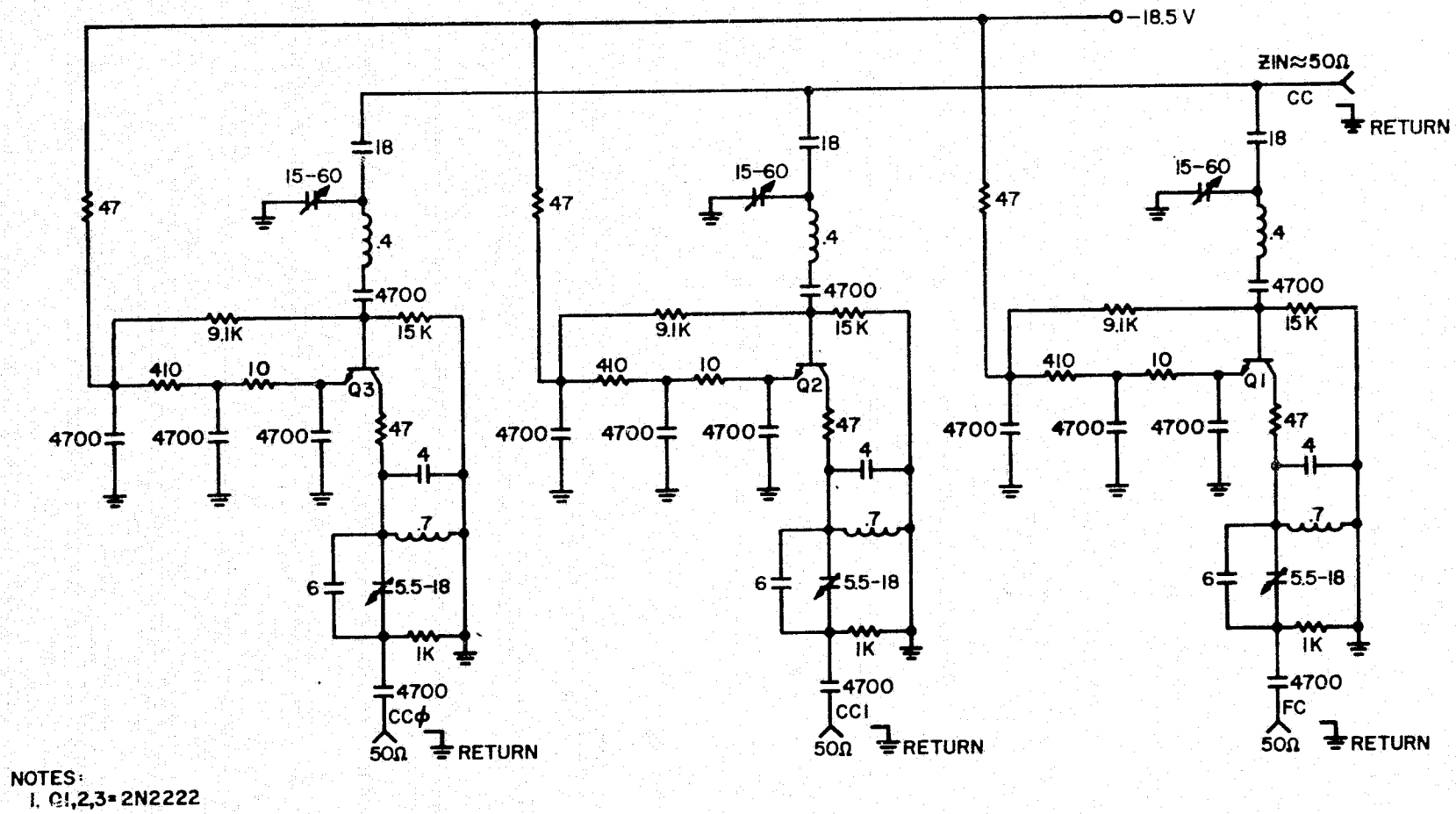

Figure I.6 FS-FS6 40.92 MHz Buffer amplifiers, three-way split.

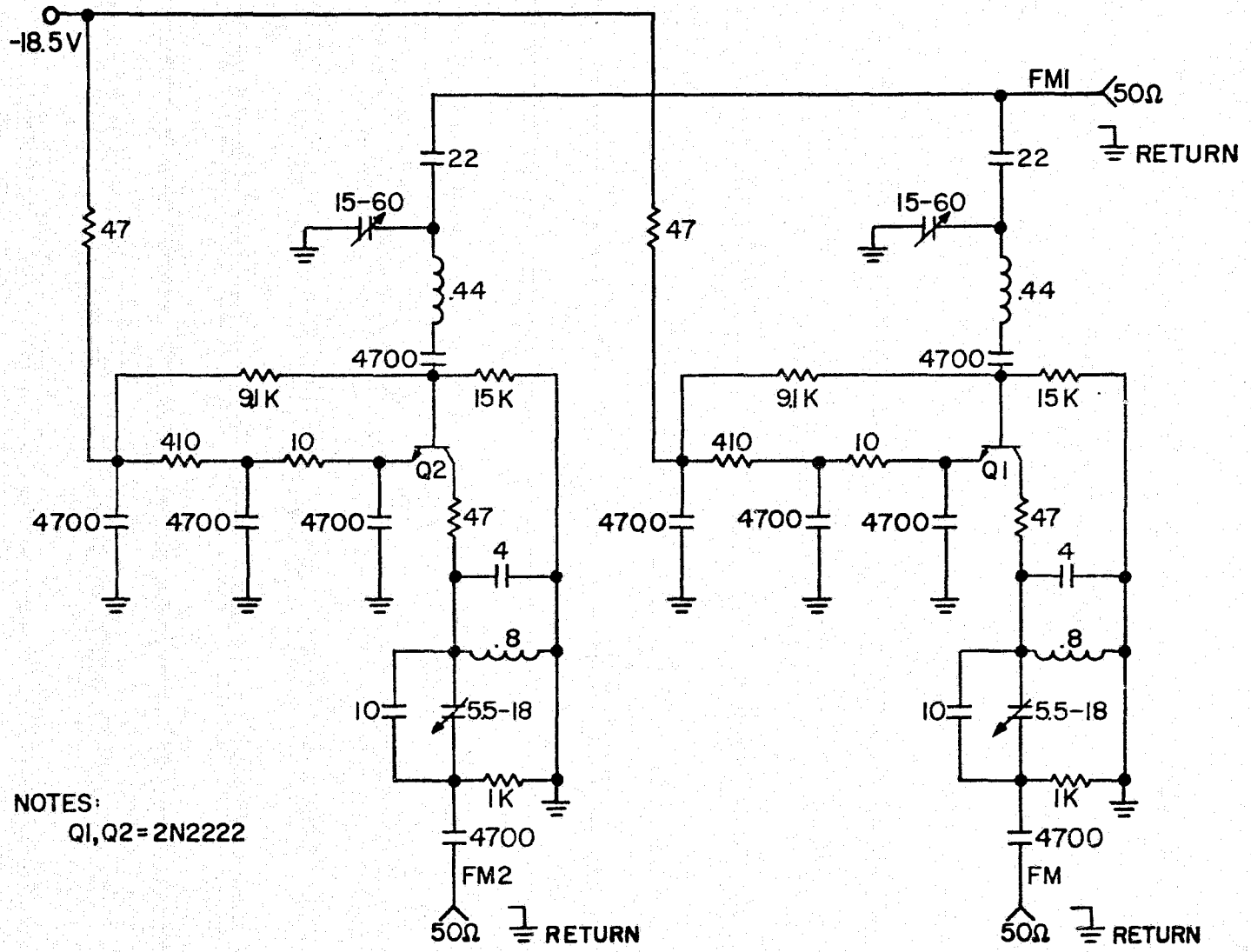

Figure I.7 FS-FS7 35.42 MHz buffer amplifiers, two-way split.

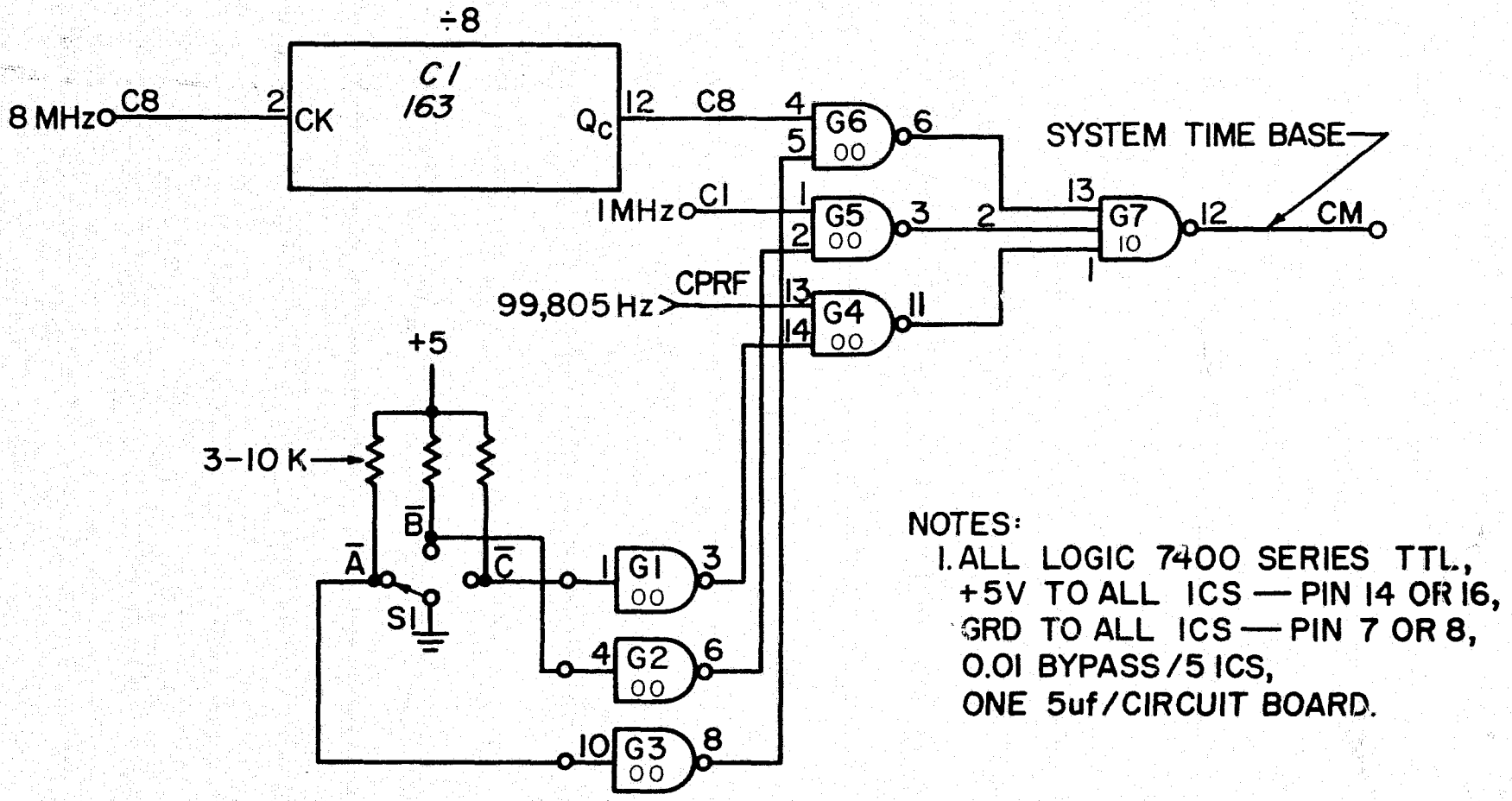

Figure I.8 TG-FS1 Main clock selector.

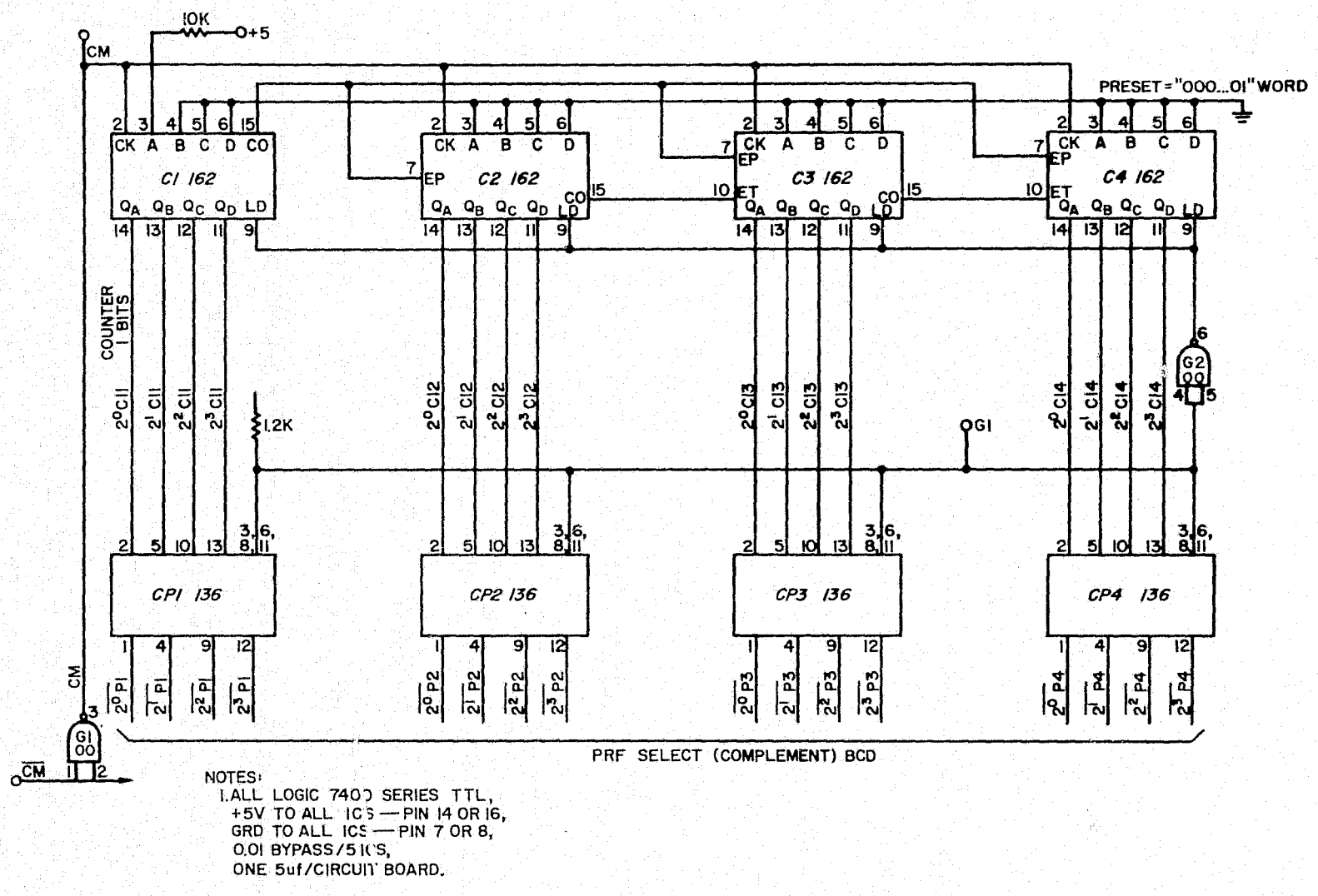

Figure I.9 TG-FS2 Master counter.

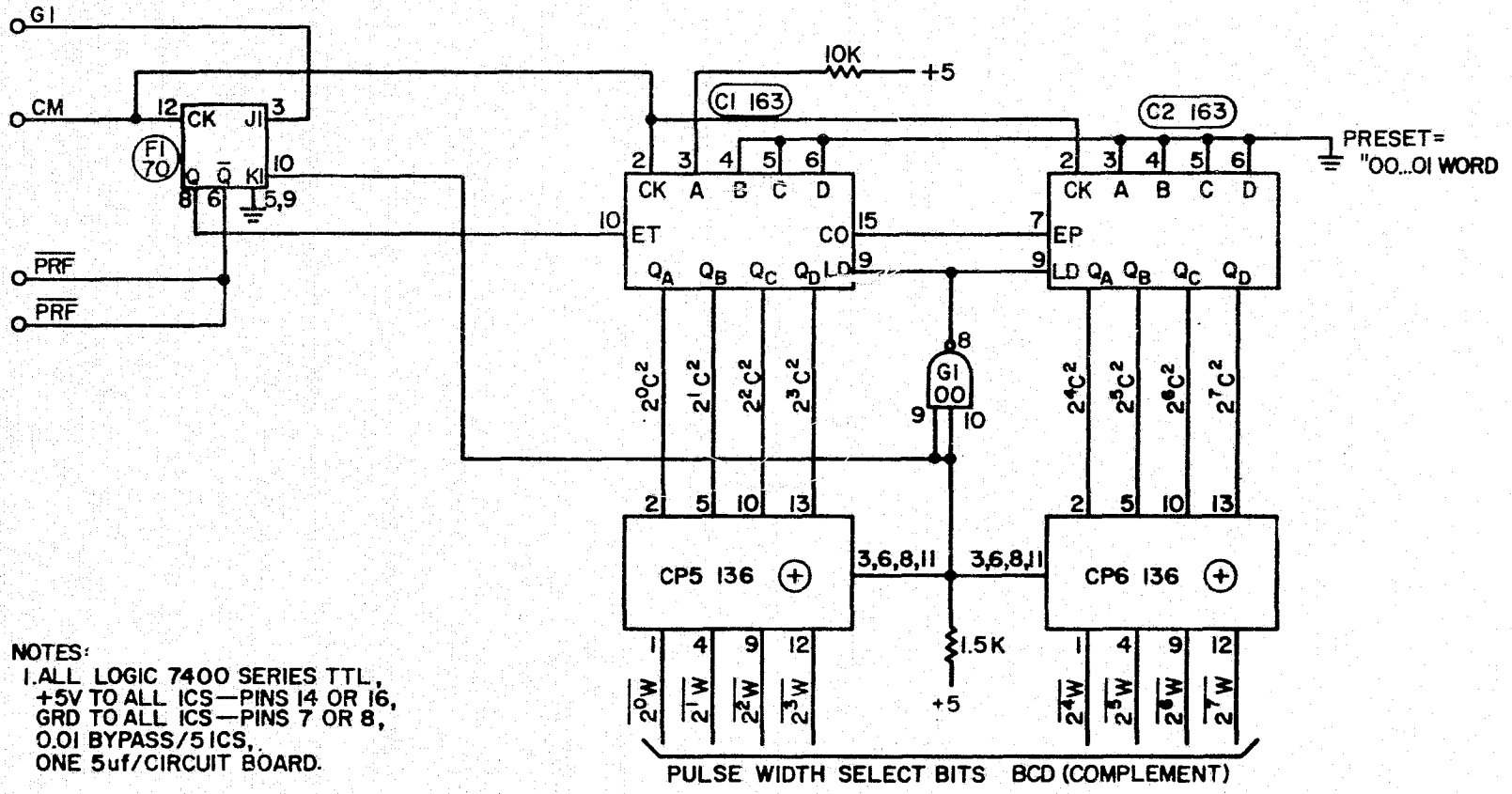

Figure I.10 TG-FS3 PRF pulse width control.

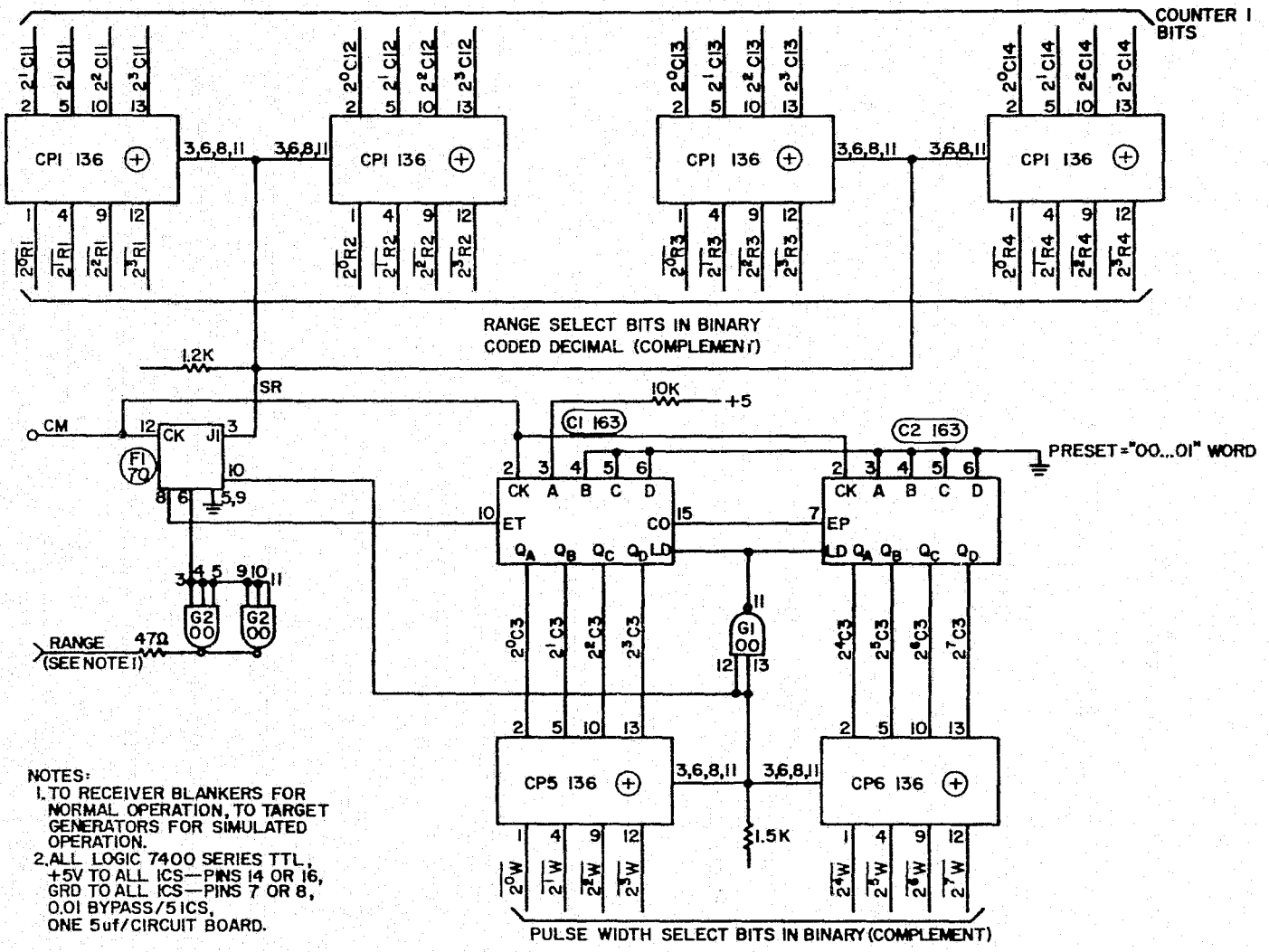

Figure I.11 TG-FS4 Range pulse generation.

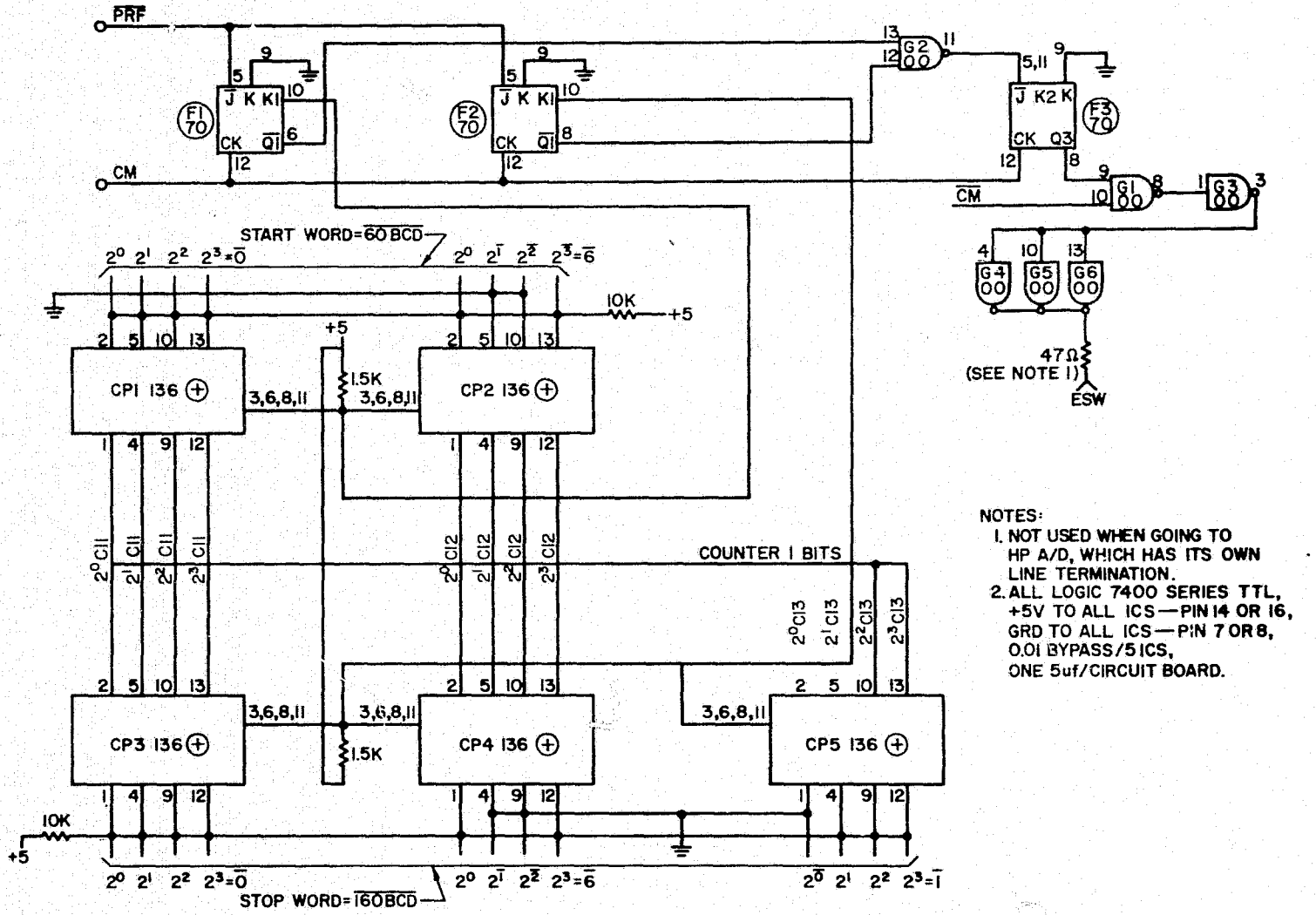

Figure I.12 TG-FS5 Echo sample window.

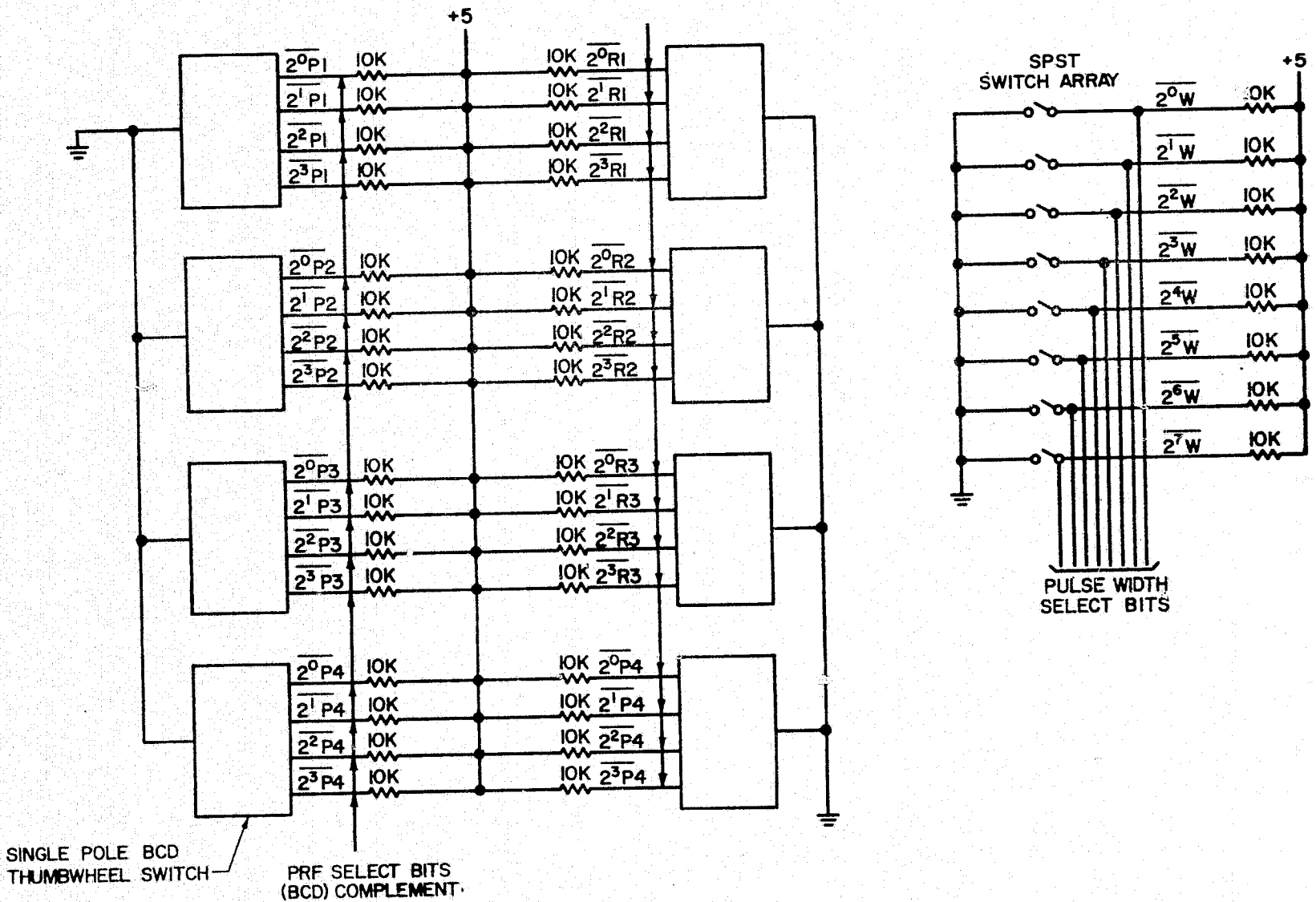

Figure I.13 TG-FS6 35.42 MHz buffer amplifiers, two-way split.

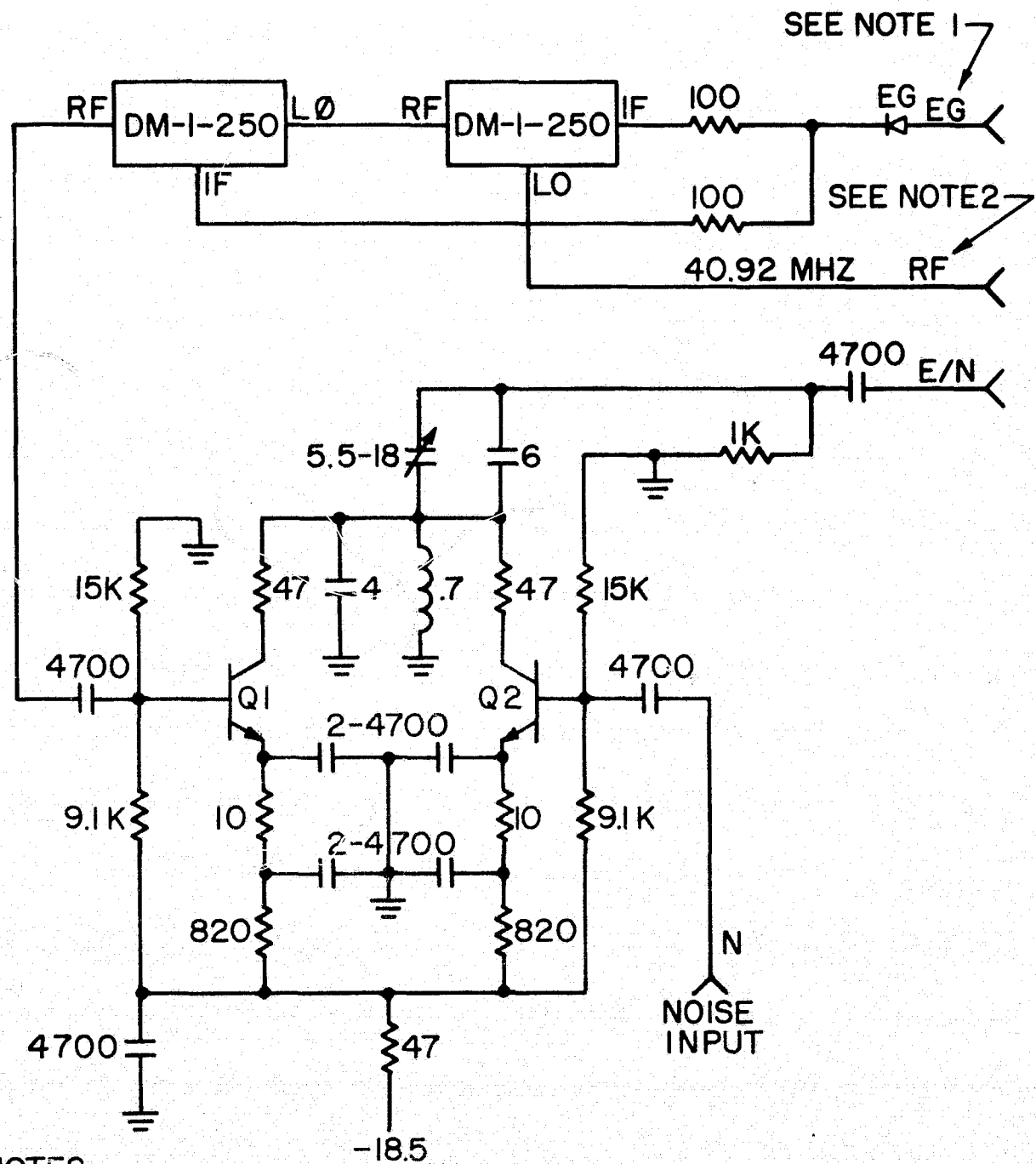

NOTES:

1. ENABLE RF ON LOGIC ONE
2. FC FOR ZERO DOPPLER TARGET, FD FOR DOPPLER TARGET; NORMALLY 20db PAD IS USED IN EITHER CASE (LOCATED ON RADAR DIRECTOR RACK) AND POWER SPLITTER FOR DOUBLE TARGET.
3. Q1-Q2=2N2219

Figure I.14 TG-FS7 Echo gater.

APPENDIX II

COMPUTER PROGRAMS

```
C METP6 IS THE DRIVER FOR THE METEOR RADAR SUBROUTINES AND OUTPUTS
C PROCESSED ECHO DATA TO DATA SLOT 2 (DATA SLOT 1 IS USED FOR TEMP-
C ORARY STORAGE)
C G C HESS
C 4-24-75
C EDIT #1
C
      DIMENSION FNR1(2)
      DIMENSION DATE(2),FNAM(2),FOUT(2)
      COMMON/A/ITIM(4),ISEC
      COMMON/B/IFR(135,3),KM(100),LM(1400),IF1(1500),IF2(1500),
     1ARNG(18),AVEL(27),AVSD(27),ACEL(9),AFEL(9),AAZ(9)
      COMMON/C/HIT(81),DC(81)
      COMMON/D/EL92(13),ELC(13)
      DATA FNR1(1),FNR1(2)/5HTESTA,4H00DA/
C USER SPECIFIED VALUES
      NSAMP=100
      NCPF=15
      NCH2=NCPF-1
      NSAMP1=NCH2*NSAMP
      NSAMP2=NCPF*NSAMP
      NSAMP3=NSAMP-1
C LOAD DECAY HEIGHT ARRAYS
      CALL TABLE
      WRITE(6,5)
5     FORMAT(55H REM SWITCH0 MUST BE IN 1 POSITION FOR NORMAL OPERATION)
      WRITE(6,6)
6     FORMAT(43H     SWITCH0 IN 0 POSITION HALTS PROCESSING)
C GET DATE, TIME, AND THRESHOLD
      WRITE(6,10)
10    FORMAT(5H DATE)
      READ(4,15)DATE
15    FORMAT(2A5)
      WRITE(6,20)
20    FORMAT(5H TIME)
      READ(4,25)ITIM
25    FORMAT(4I1)
      CALL TICK(ISEC)
      WRITE(6,23)
23    FORMAT(18H TIME BASE (FLOAT))
      READ(4,24)TB
24    FORMAT(F8.4)
      WRITE(6,16)
16    FORMAT(4H PRF)
      READ(4,17)KPRF
17    FORMAT(I4)
      PRF=FLOAT(KPRF)*0.583413
      WRITE(6,26)
26    FORMAT(10H THRESHOLD)
      READ(4,17)ITHR
      WRITE(6,28)
28    FORMAT(7H OFFSET)
      READ(4,17)LI
      WRITE(6,31)
31    FORMAT(39H RAW DATA FILENAME-1,FORM IS TESTA00DAT)
      READ(4,15)FNAM
      WRITE(6,330)
330   FORMAT(26H PROCESSED DATA FILENAME-1)
      READ(4,15)FOUT
      WRITE(6,33)
33    FORMAT(36H NUMBER OF METEORS PER RAW DATA FILE)
      READ(4,17)KK
      WRITE(6,340)
340   FORMAT(45H NR OF ECHOES WITH RAW DATA PRESENTLY ON DISK)
      READ(4,17)LMN
C CHST CHECKS FOR COLLECTION MALFUNCTION AND RESTARTS COLLECTION
C IF NECESSARY
      CALL CHST(JK,IST,MA)
30    CONTINUE
      MA=1
      KL=0
      CALL AFILE(FNAM)
      WRITE(6,320)FNAM,ITIM
320   FORMAT(5X,2A5,5X,4I1)
      CALL ENTER(1,FNAM)
      WRITE(1,37)
37    FORMAT(//)
35    CONTINUE
C SWITCH0 NORMALLY 1, SETTING IT TO 0 HALTS ECHO COLLECTION
```

```
        CALL PPO
C SET CHST FLAGS TO ZERO
        MA=0
        IST=0
C SYNCHRONIZE THE COMPUTER TO THE A/D
        CALL INPAD(KM,NSAMP,IC)
        CALL ID2(KM,NSAMP,IER)
40      CONTINUE
        IF(IC.EQ.-513.OR.IST.EQ.1)GO TO 35
        IF(IC.NE.1)GO TO 40
        JK=1
        IF(IER.EQ.1)GO TO 35
42      CONTINUE
C GET CHANNEL 1, THE FIRST METEOR RADAR VIDEO CHANNEL
C REMEMBER THAT A/D CHANNEL ID'S ARE ALWAYS ONE LESS THAN CHANNEL NUMBER
        CALL INPAD(KM,NSAMP,IC)
45      CONTINUE
        IF(IC.EQ.-513.OR.IST.EQ.1)GO TO 35
        IF(IC.NE.1)GO TO 45
        JK=1
        JBK=0
        CALL CHAN(KM,0,JBK)
        IF(JBK.EQ.1)GO TO 42
        NK=0
C COLLECT REST OF FRAME 1 WHILE EXAMINING VIDEO FOR TARGET PRESENCE
        CALL INPAD(LM,NSAMP1,IC)
        CALL LOOK(KM,ITHR,MRNG,NK)
        IF(NK.EQ.0)GO TO 35
C METEOR PRESENT, CALCULATE STARTING ADDRESS OF DATA
        IF(MRNG.LT.2.OR.MRNG.GT.NSAMP3)GO TO 42
        JST=MRNG-1
50      CONTINUE
        IF(IC.EQ.-513.OR.IST.EQ.1)GO TO 35
        IF(IC.NE.1)GO TO 50
        JK=1
C RECORD SIGNAL VALUES FOR FIRST FRAME WHILE COLLECTING SECOND FRAME
        CALL INPAD(IF1,NSAMP2,IC)
        CALL REC1(JST,1)
        MM=JST
        DO 55 I=2,NCPF
        CALL REC2(MM,I)
        MM=MM+NSAMP
55      CONTINUE
C MASK CHANNEL ID AND CONVERT TO PDP NEGATIVE NR FORMAT
        CALL MSN(1,NCPF)
C CHECK FOR SPURIOUS RETURN
        IF(IFR(NCH2,2).LT.ITHR)GO TO 35
70      CONTINUE
        IF(IC.EQ.-513.OR.IST.EQ.1)GO TO 35
        IF(IC.NE.1)GO TO 70
        JK=1
C GET THIRD FRAME WHILE RECORDING SIGNAL VALUES OF THE SECOND
        CALL INPAD(IF2,NSAMP2,IC)
        CALL RECF(JST,2,NCPF,NSAMP)
        CALL MSN(2,NCPF)
71      CONTINUE
        IF(IC.EQ.-513.OR.IST.EQ.1)GO TO 35
        IF(IC.NE.1)GO TO 71
        JK=1
C GET FOURTH FRAME WHILE RECORDING SIGNAL VALUES FOR THIRD
        CALL INPAD(IF1,NSAMP2,IC)
        CALL RECF(JST,3,NCPF,NSAMP)
        CALL MSN(3,NCPF)
72      CONTINUE
        IF(IC.EQ.-513.OR.IST.EQ.1)GO TO 35
        IF(IC.NE.1)GO TO 72
        JK=1
C GET FIFTH FRAME WHILE RECORDING SIGNAL VALUES FOR FOURTH
        CALL INPAD(IF2,NSAMP2,IC)
        CALL RECF(JST,4,NCPF,NSAMP)
        CALL MSN(4,NCPF)
73      CONTINUE
        IF(IC.EQ.-513.OR.IST.EQ.1)GO TO 35
        IF(IC.NE.1)GO TO 73
        JK=1
C GET SIXTH FRAME WHILE RECORDING SIGNAL VALUES FOR FIFTH
        CALL INPAD(IF1,NSAMP2,IC)
        CALL RECF(JST,5,NCPF,NSAMP)
        CALL MSN(5,NCPF)
74      CONTINUE
        IF(IC.EQ.-513.OR.IST.EQ.1)GO TO 35
        IF(IC.NE.1)GO TO 74
        JK=1
```

```
C GET SEVENTH FRAME WHILE RECORDING SIGNAL VALUES FOR SIXTH
      CALL INPAD(IF2,NSAMP2,IC)
      CALL RECF(JST,6,NCPF,NSAMP)
      CALL MSN(6,NCPF)
75    CONTINUE
      IF(IC.EQ.-513.OR.IST.EQ.1)GO TO 35
      IF(IC.NE.1)GO TO 75
      JK=1
C GET EIGHTH FRAME WHILE RECORDING SIGNAL VALUES FOR SEVENTH
      CALL INPAD(IF1,NSAMP2,IC)
      CALL RECF(JST,7,NCPF,NSAMP)
      CALL MSN(7,NCPF)
76    CONTINUE
      IF(IC.EQ.-513.OR.IST.EQ.1)GO TO 35
      IF(IC.NE.1)GO TO 76
      JK=1
C GET NINTH FRAME WHILE RECORDING SIGNAL VALUES FOR EIGHTH
      CALL INPAD(IF2,NSAMP2,IC)
      CALL RECF(JST,8,NCPF,NSAMP)
      CALL MSN(8,NCPF)
77    CONTINUE
      IF(IC.EQ.-513.OR.IST.EQ.1)GO TO 35
      IF(IC.NE.1)GO TO 77
      MA=1
C RECORD SIGNAL VALUES FOR NINTH FRAME
      CALL RECF(JST,9,NCPF,NSAMP)
      CALL MSN(9,NCPF)
C ALL DATA INPUTTED,BEGIN PROCESSING
C
C GET TIME
      CALL CTIME2
C APPLY RANGE ALGORITHM
      CALL RANGE(NCPF,TB,MRNG,LI,IPKC,IPKF,IPKYV)
      IF(IPKYV.LE.ITHR)GO TO 35
      DMAXY=20.*ALOG10(FLOAT(IPKYV))
      KLOC=(IPKF-1)*NCPF+15
      IF(IPKC.EQ.1.AND.IPKF.GT.1)KLOC=KLOC-NCPF
      IDV=IFR(KLOC,2)
      IF(IDV.LE.0)IDV=1
      DYD=FLOAT(IPKYV)/FLOAT(IDV)
      IF(DYD.LE.0.)DYD=999.
      IF(DYD.GT.0.)DYD=20.*ALOG10(DYD)
C ACCEPTANCE CRITERIA #1
      CALL ACC1(NCPF,ITHR,RNG,RNGSD,IGO)
C APPLY BOWHILL VELOCITY ALGORITHM
      CALL VEL(PRF,NCPF,ICOL,IPKF)
      CALL ACC2(IPKC,IPKF,ICOL,NCPF,VM,VSD,VM1,VSD1,IGO)
      IF(IGO.EQ.0)GO TO 35
C DETERMINE ECHO DECAY HEIGHT
      CALL DECAYH(IPKC,IPKF,NCPF,PRF,DHT,DECAY)
C APPLY ANGLE OF ARRIVAL ALGORITHM
      CALL ANGLE(NCPF,ICOL,KPRF)
      CALL ACC3S(AZ,AZSD,EL,ELSD,IGO)
      IF(IGO.EQ.0)GO TO 510
      CALL HEIGHT(RNG,RNGSD,EL,ELSD,HT,HTSD)
      GO TO 520
510   AZ=999.
      AZSD=999.
      EL=999.
      ELSD=999.
      HT=999.
      HTSD=999.
C STORE PROCESSED DATA TEMPORARILY ON DATA SLOT 1
520   CONTINUE
      WRITE(1)(ITIM(I),I=1,4),DMAXY,DYD,RNG,RNGSD,VM,VSD,VM1,VSD1,
     1AZ,AZSD,EL,ELSD,HT,HTSD,DHT,DECAY
C AC SW 01 MUST BE IN POSITION 1 FOR HARD COPY PRINTOUT OF ECHO RESULTS
      CALL INTER(MO1)
      IF(MO1.NE.-65536)GO TO 661
      WRITE(6,640)DMAXY,DYD,RNG,RNGSD,VM,VSD,VM1,VSD1
640   FORMAT(//8(1X,F7.2))
      WRITE(6,650)AZ,AZSD,EL,ELSD,HT,HTSD,DHT,DECAY
650   FORMAT(/7(1X,F7.2),1X,G10.3)
      DO 660 I=1,9
      WRITE(6,670)I,ACEL(I),AFEL(I),AAZ(I)
670   FORMAT(1X,I4,3(1X,F7.2))
660   CONTINUE
661   CONTINUE
      LMN=LMN+1
C EVERY 50 ECHOES STORE DATA ON DATA SLOT 2
      IF(LMN.GE.50)GO TO 500
      KL=KL+1
      IF(KL.GE.KK)GO TO 110
      GO TO 35
```

```
110     CALL CLOSE(1)
        GO TO 30
500     CONTINUE
        CALL CLOSE(1)
        CALL STORE(KK,FNR1,FOUT)
        FNAM(1)=FNR1(1)
        FNAM(2)=FNR1(2)
        LMN=0
        GO TO 30
        END


        SUBROUTINE TABLE
C FILLS UP HEIGHT AND DIFFUSION VECTORS BASED ON 1962 STANDARD
C ATMOSPHERE DATA (BARNES)
C G C HESS, EDIT #1, 8/15/75
        DIMENSION DECF(2),ACF(2)
        COMMON/C/HHT(81),DC(81)
        COMMON/D/EL92(13),ELC(13)
        DATA DECF(1),DECF(2)/5HDECAY,4HOODA/
        DATA ACF(1),ACF(2)/5HANGLE,4HCORR/
        GO TO 10
20      WRITE(6,30)
30      FORMAT(16H TYPE DECAYOODAT)
        READ(4,40)DECF
40      FORMAT(2A5)
10      CONTINUE
        CALL FSTAT(3,DECF,IF)
        IF(IF.EQ.0)GO TO 20
        CALL SEEK(3,DECF)
        READ(3,50)
50      FORMAT(//)
        DO 60 I=1,81
        READ(3,70)IC,HHT(I),DC(I)
70      FORMAT(5X,I2,5X,F7.2,5X,1PE10.3)
60      CONTINUE
C ALSO FILL ELEVATION AND ELEVATION CORRECTION VECTORS USED TO
C LINEARIZE THE STACKED YAGI PHASE RESPONSE
        GO TO 400
410     WRITE(6,420)
420     FORMAT(16H TYPE ANGLECORRF)
        READ(4,430)ACF
430     FORMAT(2A5)
400     CONTINUE
        CALL FSTAT(3,ACF,IF)
        IF(IF.EQ.0)GO TO 410
        CALL SEEK(3,ACF)
        READ(3,440)
440     FORMAT(//)
        DO 450 I=1,13
        READ(3,460)IC,EL92(I),ELC(I)
460     FORMAT(5X,I2,5X,F7.2,5X,F7.2)
450     CONTINUE
        RETURN
        END


        .GLOBL TICK,.DA
/ TICK COUNTS SECONDS
/ FORTRAN IV CALL: CALL TICK(ISEC)
TICK    0
        JMS*    .DA
        JMP     .+2
ISEC    0
        DZM*    ISEC            /ZERO SECONDS
        .TIMER  60,S1,5         /START CLOCK
        JMP*    TICK            /RETURN
S1      0                       /SERVICE ROUTINE FOR INTERRUPT
        DAC     TEMP            /STORE ACCUMULATOR
        ISZ*    ISEC            /INCREMENT BY ONE SECOND
        .TIMER  60,S1,5         /DO AGAIN
        LAC     TEMP            /RESTORE ACCUMULATOR
        .RLXIT  S1              /RETURN
TEMP    0
        .END


        .GLOBL CHST,.DA
        .IUDEV 6
/ CHECKS FOR A/D INTERFACE FAILURE AND RESTARTS COLLECTION IF
/ NECESSARY.  FORTRAN IV CALL: CALL CHST(IGO1,IST,LA)
/
CHST    0
```

```
        JMS*    .DA             /GET ARGUMENTS
        JMP     .+4             /JUMP AROUND ARGUMENTS
IGO1    0                       /CONTINUE FLAG
IST     0                       /STOP FLAG
LA      0                       /PRINTING FLAG
        DZM*    IGO1            /ZERO FLAG
        .INIT   6,1,CHST
        .TIMER  120,SERV,7      /START CLOCK FOR 1.5 SECONDS
        JMP*    CHST            /RETURN
SERV    0                       /SERVICE ROUTINE
        DAC     HOME            /SAVE ACCUMULATOR
        LAC*    LA              /GET PRINTER FLAG
        SZA                     /IF ZERO, CONTINUE
        JMP     HP              /PRINTING OUTPUT, RESET
        LAC*    IGO1            /GET CONTINUE FLAG
        SNA                     /IS IT GREATER THAN ZERO?
        JMP     BAD             /NO, ERROR
HP      DZM*    IGO1            /RESET COUNTER TO ZERO
        .TIMER  120,SERV,7      /DO AGAIN
        LAC     HOME            /RESTORE ACCUMULATOR
        .RLXIT  SERV            /RETURN
BAD     ISZ*    IST             /SET STOP FLAG
        DZM*    IGO1            /INSURE IGO1 IS ZERO
        .WRITE  6,2,MSG2,0      /RING BELL SEVERAL TIMES
        .WAIT   6
        .TIMER  120,SERV,7      /START CLOCK
        LAC     HOME            /RESTORE ACCUMULATOR
        .RLXIT  SERV            /RETURN
MSG2    2000
        0
        .ASCII  <7><7><7><7><7><7><7><7><7><15>
HOME    0                       /ACCUMULATOR SAVE LOCATION
        .END


        .GLOBL AFILE,.DA
/ AUTOMATIC FILE NAMING SUBROUTINE
/ FORTRAN IV CALL: CALL AFILE(REM)
/
AFILE   0
        JMS*    .DA
        JMP     .+2
REM     0                       /ADDRESS OF ADDRESS OF ARRAY
        LAC*    REM             /GET ARRAY ADDRESS
        TAD     FR              /ADD 4 TO ADDRESS
        DAC     REM             /STORE ADDRESS OF 2ND WORD
        LAC*    REM             /GET 2ND WORD
        DAC     TE              /STORE WORD TEMPORARILY
        AND     B2              /MASK ALL BUT 2ND ALPHANUMERIC
        SAD     S1              /CHECK FOR 9 PRESENT
        JMP     INK             /YES
        LAC     TE              /NO, CONTINUE
        TAD     S2              /INCREMENT BY ONE
        DAC*    REM             /DEPOSIT NEW NAME
        JMP*    AFILE           /RETURN
INK     LAC     TE              /GET WORD
        AND     (774000         /MASK ALL BUT 1ST ALPHANUMERIC
        SAD     S3              /CHECK FOR 9 PRESENT
        JMP     NINE            /YES
        LAC     TE              /NO, CONTINUE
        AND     (774017         /MASK OUT 2ND ALPHANUMERIC
        TAD     (5400           /INCREMENT 1ST AND SET 2ND ALPHA TO ZERO
        DAC*    REM             /NEW FILE NAME
        JMP*    AFILE           /RETURN
NINE    LAC     TE              /BOTH ALPHANUMERICS ARE 9
        AND     (17             /MASK BOTH ALPHANUMERICS
        TAD     (301400         /SET ALPHANUMERICS TO ZERO
        DAC     REM             /STORE NEW FILE NAME
        JMP*    AFILE           /RETURN
FR      2                       /TWO
TE      0                       /TEMPORARY STORAGE
S1      1620                    /9 IN 2ND ALPHANUMERIC
S2      20                      /INCREMENT 2ND ALPHANUMERIC
S3      344000                  /9 IN 1ST ALPHANUMERIC
B2      003760                  /MASK FOR 2ND ALPHANUMERIC
        .END


/ROUTINE PPO CHECKS DATA SWITCH 00 FOR A 1 OR 0
/
        .GLOBL PPO
PPO     0
PR      LAS                     /GET THE CONSOLE DATA SWITCH
        AND     (400000         /NUMBER 00
        SNA                     /IS IT A 1 ?
        JMP     PR              /NO, CHECK AGAIN
        JMP*    PPO             /RETURN TO SIMTST
        .END
```

```
        .TITLE  A/D CONVERTER SERVICE ROUTINES FOR BG.-FG.
/       BFKM15 V3A SERVICE ROUTINES FOR THE HP 5610A A TO D
/  CONVERTER.  THESE ROUTINES PERMIT INPUT OF ANY SPECIFIED
/  NUMBER OF SAMPLES INTO A CORE BUFFER.  INPUT MAY BE OVER-

/  LAPPED WITH PROGRAM EXCUTION, AND CONTROL MAY BE RELINQUISHED
/  TO LOWER PRIORITY PROGRAMS WHILE DATA TRANSFER TAKES PLACE.
/    MACRO-15 CALLING SEQUENCE:
/       JMS     INPAD
/       NUMBER OF SAMPLES REQUIRED
/       BUFFER ADDRESS
/       COMPLETION FLAG ADDRESS
/       REAL-TIME SUBROUTINE ADDRESS, PRIORITY LEVEL IN BITS 0-2
/  (EXAMPLE: 500000+RTSUBA)
/  (RETURNS HERE IMMEDIATELY)
/       IF THE 4TH WORD AFTER THE JMS IS 0, NO REAL-TIME SUBROUTINE
/  WILL BE ACTIVATED.  NOTE:  THE PRIORITY CODE FOR MAINSTREAM IS 1
/       THE COMPLETION FLAG IS CLEARED BY THE CALL TO INPAD,
/  AND SET TO +1 FOR NORMAL COMPLETION OR -1001 IF A DATA
/  TIMING ERROR OCCURS.
/
/
ADWCR=26                        /A-D WORD COUNT
ADCAR=ADWCR+1                   /AND CURRENT ADDRESS REGISTERS
.SCOM=100                       /MONITOR'S COMMUNICATION AREA
ADWI=703724                     /A-D CONVERTER WRITE INITIALIZE
ADSO=703701                     /SKIP ON WORD COUNT OVERFLOW
ADST=703721                     /SKIP ON DATA TIMING ERROR
ADCO=703704                     /CLEAR OVERFLOW FLAG
ADCT=703744                     /CLEAR TIMING FLAG
/
/  ENTRY POINT FOR A-D INTERFACE INITIALIZATION
/
        .GLOBL  INPAD,.DA
INPAD   0
        JMS*    .DA
        JMP     .+4
INAR    0
INWC    0
INFLAG  0
INR     JMP     INSET           /REPLACED BY "LAC*      INWC"
        TCA
        DAC*    (ADWCR)         /SET WORD COUNT
        LAW     -1
        TAD*    INAR            /BUFFER ADDRESS -1
        DAC*    (ADCAR)         /   TO CURRENT ADDRESS REG.
        DZM*    INFLAG          /CLEAR FLAG
        DZM     INSUB#          /CLEAR REAL-TIME SUBROUTINE
        ADWI                    /INITIALIZE INTERFACE
        JMP*    INPAD           /RETURN
/
/   THE FOLLOWING CODE IS EXECUTED ONLY ONCE
INSET   LAC*    (.SCOM+55)      /GET ENTRY POINT ADDERSS OF .SETUP
ADSVA   DAC     .
        JMS*    .-1             /CALL .SETUP TO CONNECT ADINT TO API
        ADSO
        ADINT
        DZM*    (204
        LAC     (LAC*   INWC
        DAC     INR             /MODIFY INSTRUCTION
        JMP     INR             / AND JUMP TO IT
/
/
/INTERRUPT SERVICE ROUTINE.  EXECUTED IMMEDIATELY AFTER COMPLETION
/  OF DATA TRANSFER.  DETERMINES STATUS OF A-D INTERFACE, SETS
/  COMPLETION FLAG AND ACTIVATES REAL-TIME SUBROUTINE.
/  RUNS AT API LEVEL 0.
/
/
ADINT   0
        DBA                     /PAGE ADDRESSING MODE
        DAC     ADSVA           /SAVE AC
        ADST                    /TIMING ERROR?
        SKP!CLA!IAC             /NO,+1 TO AC
        LAW     -1001           /YES, ERROR CODE
        DAC*    INFLAG          /SET FLAG
        ADCO                    /CLEAR
        ADCT                    /   INTERFACE FLAGS
ADXIT   LAC     ADSVA           /RESTORE AC
        DBR                     /SET TO LEAVE HARDWARE API LEVEL
        JMP*    ADINT           / ETURN TO INTERRUPTED PROGRAM
        .END
```

```
        .GLOBL ID2,.DA
/ CHECK FOR SYNCHRONIZATION WITH A/D
/ FORTRAN IV CALL: CALL ID2(STOR,IMP,IFLAG)
/ W. OWENS
/ 8-6-74
/ EDIT #1
ADW=26
ID2     0
        JMS*    .DA
        JMP     .+4             /JUMP AROUND BUFFER AND IFLAG
STOR    0                       /A/D SAMPLE BUFFER ADDRESS
IMP     0                       /NUMBER OF SAMPLES
IFLAG   0                       /ERROR FLAG ADDRESS
        LAC*    IMP             /GET WORD COUNT
        TCA                     /NEGATE
        DAC     IMP             /AND STORE
        DAC     COUNT   /SET COUNTER TO NUMBER OF SAMPLES
IFF     LAC     ADW             /GET INPAD CURRENT WORD COUNT
        SAD     IMP             /HAS INPAD STARTED YET
        JMP     IFF             /NO, TRY AGAIN
        DZM*    IFLAG           /SET FLAG TO ZERO
        LAC*    STOR            /GET ADDRESS OF ARRAY
        DAC     STOR            /AND STORE
        LAC*    STOR            /GET FIRST SAMPLE
        AND     (740000         /MASK OUT A/D WORD
        DAC     CHI             /STORE CHANNEL ID
CIR     ISZ     COUNT           /DONE?
        JMP     FI              /CONTINUE
        JMP*    ID2             /YES, RETURN WITH NO ERROR
FI      ISZ     STOR            /INCREMENT ARRAY ADDRESS
        LAC*    STOR            /GET NEXT A/D SAMPLE
        AND     (740000         /MASK OUT A/D WORD
        SAD     CHI             /CHECK FOR CHANNEL CHANGE
        JMP     CIR             /NO, SAME CHANNEL
        ISZ*    IFLAG           /TO ONE
        JMP*    ID2             /RETURN
CHI     0
COUNT   0
        .END


        .GLOBL CHAN,.DA
/ CHECK FOR RIGHT CHANNEL
/ FORTRAN IV CALL: CALL CHAN(IJ,IDC,JER)
/ W. OWENS
/ 6-28-74
/EDIT #3
/
CHAN    0
        JMS*    .DA             /GET ARGUMENTS
        JMP     .+4             /JUMP AROUND ARGUMENTS
IJ      0                       /FIRST A/D SAMPLE ADDRESS
IDC     0                       /DESIRED CHANNEL ADDRESS
JER     0                       /WRONG CHANNEL FLAG ADDRESS
        LAC*    IDC             /GET DESIRED CHANNEL NUMBER
        DAC     WCH             /AND STORE
        LAC*    IJ              /GET ADDRESS OF ARRAY
        DAC     IJ              /AND STORE
        LAC*    IJ              /GET FIRST SAMPLE
        RCR                     /ZERO LINK AND MOVE AC ONE RIGHT
        LRS     15              /SHIFT 13 (DEC) RIGHT
        SAD     WCH             /IS THIS THE RIGHT DATA CHANNEL?
        JMP*    CHAN            /YES, RETURN
        ISZ*    JER             /SET ERROR FLAG TO ONE
        JMP*    CHAN            /RETURN WITH ERROR
WCH     0                       /CHANNEL NUMBER
        .END


        .GLOBL LOOK,.DA
/ LOOK FINDS THE LARGEST SAMPLE FROM THE VIDEO CHANNEL NOT A
/ NEGATIVE NUMBER AND SETS FLAG IF IT IS LARGER THAN A GIVEN
/ THRESHOLD.  ALSO RETURNS THE LARGEST SAMPLE POSITION.
/ FORTRAN IV CALL: CALL LOOK(IP,ITH,LRG,ISW)
LOOK    0
        JMS*    .DA
        JMP     .+5             /JUMP AROUND ARGUMENTS
IP      0                       /ADDRESS OF SAMPLE ARRAY ADDRESS
ITH     0                       /THRESHOLD
LRG     0                       /POINTER TO METEOR POSITION
ISW     0                       /METEOR PRESENT FLAG
        LAC*    ITH             /GET THRESHOLD LEVEL
        DAC     ITH             /AND STORE
        LAC*    IP              /GET ARRAY ADDRESS
```

```
        TAD     (-1             /MINUS ONE
        DAC     IP              /AND STORE
        DZM*    ISW             /SET METEOR PRESENT FLAG TO ZERO
        DZM     IMAX            /SET MAXIMUM AMPLITUDE TO ZERO
        LAW     -145            /SET COUNTER
        DAC     NN              /TO -101 (DEC)
AG      ISZ     NN              /DONE PROCESSING?
        JMP     FI              /NO, CONTINUE
        LAC     ITH             /YES, GET THRESHOLD
        TCA                     /NEGATE THRESHOLD
        TAD     IMAX            /ADD TO MAXIMUM LEVEL
        SPA                     /IS IMAX >= THRESHOLD
        JMP*    LOOK            /NO, RETURN WITH NO METEOR
        ISZ*    ISW             /YES, SET METEOR PRESENT FLAG TO ONE
        JMP*    LOOK            /RETURN
FI      ISZ     IP              /BUMP ARRAY POINTER
        LAC*    IP              /LOAD SAMPLE
        DAC     XX              /STORE TEMPORARILY
        AND     (001000         /MASK ALL BUT HP SIGN BIT
        CLL                     /CLEAR LINK
        SZA                     /NEGATIVE NUMBER?
        JMP     AG              /YES, DO NEXT SAMPLE
        LAC     XX              /NO, GET SAMPLE
        TCA                     /NEGATE CURRENT SAMPLE
        TAD     IMAX            /ADD TO CURRENT MAXIMUM
        SMA                     /IS XX > IMAX
        JMP     AG              /NO, DO NEXT SAMPLE
        LAC     XX              /GET CURRENT SAMPLE
        DAC     IMAX            /AND STORE AS NEW MAXIMUM
        LAC     NN              /GET COUNT
        TAD     (145            /AND ADD 101 (DEC)
        DAC*    LRG             /AND STORE IN METEOR POINTER
        JMP     AG              /DO NEXT SAMPLE
IMAX    0                       /CURRENT MAXIMUM AMPLITUDE
NN      0                       /COUNTER
XX      0                       /TEMPORARY STORAGE
        .END
```

```
      SUBROUTINE REC1(JST,JCH)
C RECORDS METEOR ECHO DATA FOR A SINGLE CHANNEL (FIRST FRAME)
C DATA CONSISTS OF THE THREE SAMPLES CENTERED ABOUT THE INITIAL
C TARGET DETECTION LOCATION
C G C HESS
C 4-24-75
C EDIT #1
C
      COMMON/B/IFR(135,3),KM(100),LM(1400),IF1(1500),IF2(1500),
     1ARNG(18),AVEL(27),AVSD(27),ACEL(9),AFEL(9),AAZ(9)
      J=JST
      DO 10 I=1,3
      IFR(JCH,I)=KM(J)
      J=J+1
10    CONTINUE
      RETURN
      END


      SUBROUTINE REC2(MM,I)
C RECORDS METEOR ECHO DATA FOR ALL CHANNELS EXCEPT THE FIRST
C (COMPLETION OF THE FIRST FRAME)
C DATA CONSISTS OF THE SAMPLES CENTERED ABOUT THE INTIAL TARGET DETECTION
C LOCATION
C G C HESS
C 4-24-75
C EDIT #1
C
      COMMON/B/IFR(135,3),KM(100),LM(1400),IF1(1500),IF2(1500),
     1ARNG(18),AVEL(27),AVSD(27),ACEL(9),AFEL(9),AAZ(9)
      J=MM
      DO 10 K=1,3
      IFR(I,K)=LM(J)
      J=J+1
10    CONTINUE
      RETURN
      END


      SUBROUTINE MSN(JFR,NCPF)
C REMOVES CHANNEL ID'S AND CHANGES A/D NEGATIVE NUMBERS TO PDP15
C NUMBER FORMAT
C HANDLES ONE FRAME AT A TIME
C G C HESS
C 4-24-75
C EDIT #1
```

```
C
      DIMENSION IFS(7)
      COMMON/B/IFR(135,3),KM(100),LM(1400),IF1(1500),IF2(1500),
     1ARNG(18),AVEL(27),AVSD(27),ACEL(9),AFEL(9),AAZ(9)
      DO 10 I=1,NCPF
      JL=(JFR-1)*NCPF+I
      DO 20 J=1,3
      IFS(J)=IFR(JL,J)
20    CONTINUE
      CALL MSK(IFS)
      DO 30 K=1,3
      IFR(JL,K)=IFS(K)
30    CONTINUE
10    CONTINUE
      RETURN
      END


      .GLOBL MSK,.DA
/ MASKS CHANNEL ID AND CONVERTS FROM HP NDGATIVE NUMBER TO PDP
/ NEGATIVE NUMBER.
/ W. OWENS
/ 7-16-74
/ EDIT #2
/
MSK   0
      JMS*   .DA
      JMP    .+2
RD    0
      LAC*   RD            /GET ADDRESS OF ARRAY
      DAC    RD            /AND STORE
      LAW    -7            /SET COUNTER
      DAC    REP
ML    LAC*   RD            /GET SAMPLE
      AND    (001777       /REMOVE CHANNEL ID
      DAC*   RD            /AND STORE
      AND    (001000       /MASK ALL BUT HP SIGN BIT
      CLL                  /CLEAR THE LINK
      SNA                  /NEGATIVE NUMBER?
      JMP    TN            /NO, GET NEXT SAMPLE
      LAC*   RD            /RELOAD FULL SAMPLE
      .DEC                 /YES, CHANGE TO
      TAD    (261120       /PDP NEGATIVE NUMBER
      .OCT
      DAC*   RD            /AND STORE
TN    ISZ    REP           /DONE?
      JMP    .+2           /NO, CONTINUE
      JMP*   MSK           /YES, RETURN
      ISZ    RD            /BUMP ARRAY POINTER
      JMP    ML            /DO AGAIN
REP   0
      .END


      SUBROUTINE RECF(JST,JFR,NCPF,NSAMP)
C RECORDS METEOR ECHO DATA FOR ONE COMPLETE FRAME
C DATA CONSISTS OF THE THREE SAMPLES CENTERED ABOUT THE INITIAL TARGET
C DETECTION LOCATION
C G C HESS
C 4-24-75
C EDIT #1
C
      COMMON/B/IFR(135,3),KM(100),LM(1400),IF1(1500),IF2(1500),
     1ARNG(18),AVEL(27),AVSD(27),ACEL(9),AFEL(9),AAZ(9)
C ODD FRAME SAMPLES STORED IN ARRAY IF2
C EVEN FRAME SAMPLES STORED IN ARRAY IF1
      K=0
      JK=JST
      IF(JFR.EQ.2.OR.JFR.EQ.4.OR.JFR.EQ.6.OR.JFR.EQ.8)K=1
      DO 10 I=1,NCPF
      JL=(JFR-1)*NCPF+I
      DO 20 J=1,3
      IF(K.EQ.0)IFR(JL,J)=IF2(JK)
      IF(K.EQ.1)IFR(JL,J)=IF1(JK)
      JK=JK+1
20    CONTINUE
      JK=JK+NSAMP-3
10    CONTINUE
      RETURN
      END
```

```
C
C
C  W. OWENS
C  7-26-74
C  EDIT #2
C  CALCULATES THE TIME OF DAY
C
      SUBROUTINE CTIME2
      COMMON /A/ITIM(4),ISEC
C
C  LOAD CURRENT ELAPSED TIME SINCE LAST CALL TO CTIME2
C
      ITSEC=ITSEC+ISEC
      ISEC=0
C
C  KEEPS TRACE OF SECONDS AND INCREMENTS MINUTES
C
5     CONTINUE
      IF(ITSEC.GE.60) ITIM(4)=ITIM(4)+1
      IF(ITSEC.GE.60) ITSEC=ITSEC-60
      IF(ITSEC.GE.60) GO TO 5
C
C  INCREMENT TENS OF MINUTES
C
10    IF(ITIM(4).GT.9) ITIM(3)=ITIM(3)+1
      IF(ITIM(4).GT.9) ITIM(4)=ITIM(4)-10
      IF(ITIM(4).GT.9) GO TO 10
C
C  INCREMENT HOURS
C
20    IF(ITIM(3).GT.5) ITIM(2)=ITIM(2)+1
      IF(ITIM(3).GT.5) ITIM(3)=ITIM(3)-6
      IF(ITIM(3).GT.5) GO TO 20
C
C  INCREMENT TENS OF HOURS
C
      IF(ITIM(2).GT.9) ITIM(1)=ITIM(1)+1
      IF(ITIM(2).GT.9) ITIM(2)=ITIM(2)-10
      IF(ITIM(1).GT.2) ITIM(1)=0
      RETURN
      END


      SUBROUTINE RANGE(NCPF,TB,MRNG,LI,IPKC,IPKF,IPKYV)
C APPLIES RANGE ALGORITHM TO YAGI VIDEO CHANNELS
C (ASSUMED TO BE CHANNELS 1 AND 14)
C G C HESS
C 4-24-75
C EDIT #1
C
C CALCULATE THE RANGE IN KM BY FITTING A PARABOLA TO THE PEAK YAGI VIDEO
C A/D SAMPLE AND THE TWO ADJACENT SAMPLES IN TIME
C BASE THE RANGE ON T=TB US INTERSAMPLE PERIOD, WITH THE FIRST SAMPLE
C OCCURING AT 620T FOLLOWING TRANSMISSION AND ALLOW FOR A 2 US A/D SAMPLING
C DELAY
C ALSO PROVIDE FOR A TRANSMITTER TURNON DELAY OF LI US
C
      COMMON/B/IFR(135,3),KM(100),LM(1400),IF1(1500),IF2(1500),
     1ARNG(18),AVEL(27),AVSD(27),ACEL(9),AFEL(9),AAZ(9)
      IPKC=1
      IPKF=1
      IPKYV=0
      DO 10 I=1,9
      JT=(I-1)*NCPF
      JC=0
      DO 20 J=1,14,13
      JS=JT+J
      TAU=(TB/2.)*FLOAT(IFR(JS,1)-IFR(JS,3))/(FLOAT(IFR(JS,1)+IFR(JS,3)
     1-IFR(JS,2)-IFR(JS,2)))
      JC=JC+1
      JR=(I-1)*2+JC
      ARNG(JR)=(FLOAT(10*MRNG)+TAU-FLOAT(LI))*0.015*TB+9.15*TB+.3
C FIND FRAME WITH PEAK YAGI VIDEO SIGNAL
      IF(IFR(JS,2).GE.IPKYV)GO TO 30
      GO TO 20
30    IPKYV=IFR(JS,2)
      IPKF=I
      IPKC=J
20    CONTINUE
10    CONTINUE
      RETURN
      END
```

```
      SUBROUTINE ACC1(NCPF,ITHR,RNG,RNGSD,IGO)
C DETERMINES WHETHER METEOR ECHO IS ACCEPTABLE BASED ON RANGE RESULTS
C G C HESS
C 4-42-75
C EDIT #1
C
      COMMON/B/IFR(135,3),KM(100),LM(1400),IF1(1500),IF2(1500),
      1ARNG(18),AVEL(27),AVSD(27),ACEL(9),AFEL(9),AAZ(9)
      IUSE=0
      DO 10 I=1,9
      J1=0
      DO 20 J=1,14,13
      J1=J1+1
      K=(I-1)*NCPF+J
      IF(IFR(K,2).LT.ITHR)GO TO 20
      IUSE=IUSE+1
      K1=(I-1)*2+J1
      ARNG(IUSE)=ARNG(K1)
20    CONTINUE
10    CONTINUE
      IF(IUSE.LE.2)GO TO 60
      RH=ARNG(1)
      RL=ARNG(1)
      DO 30 I=2,IUSE
      IF(ARNG(I).GT.RH)RH=ARNG(I)
      IF(ARNG(I).LT.RL)RL=ARNG(I)
30    CONTINUE
C REQUIRE THE DIFFERENCE BETWEEN MAX AND MIN RANGE TO BE UNDER 3 KM
      IF(ABS(RH-RL).GE.3.)GO TO 60
C CALCULATE THE MEAN RANGE AND SAMPLE STD DEV (UNWEIGHTED)
      RNG=0.
      DO 40 I=1,IUSE
      RNG=RNG+ARNG(I)
40    CONTINUE
      RNG=RNG/FLOAT(IUSE)
      RNGSD=0.
      DO 50 I=1,IUSE
      RNGSD=RNGSD+(ARNG(I)-RNG)**2
50    CONTINUE
      RNGSD=SQRT(RNGSD/FLOAT(IUSE-1))
      IF(RNGSD.GT.1.)GO TO 60
      IGO=1
      RETURN
C DEFAULT CASE
60    IGO=0
      RETURN
      END


      SUBROUTINE VEL(PRF,NCPF,ICOL,IPKF)
C APPLIES DOWNHILL VELOCITY ALGORITHM THREE TIMES PER FRAME
C FIRST TO CH 3,5,7,9, SECOND TO CH 5,7,9,11, THIRD TO CH 7,9,11,13
C G C HESS
C 4-24-75
C EDIT #1
C
      DIMENSION M(4)
      COMMON/B/IFR(135,3),KM(100),LM(1400),IF1(1500),IF2(1500),
      1ARNG(18),AVEL(27),AVSD(27),ACEL(9),AFEL(9),AAZ(9)
C DETERMINE SAMPLE COLUMN WITH MAXIMUM SIGNAL STRENGTH
      JS=(IPKF-1)*NCPF
      M(1)=IABS(IFR(JS+2,2))
      M(2)=IABS(IFR(JS+4,2))
      M(3)=IABS(IFR(JS+2,3))
      M(4)=IABS(IFR(JS+4,3))
      IF(M(1)+M(2)+M(3)+M(4).LE.0)GO TO 60
      IPK=1
      IPKM=M(1)
      DO 30 K=2,4
      IF(M(K).LE.IPKM)GO TO 40
      IPKM=M(K)
      IPK=K
40    CONTINUE
30    CONTINUE
      ICOL=2
      IF(IPK.GE.3)ICOL=3
      DO 10 I=1,9
      JT=(I-1)*NCPF
      JC=0
      DO 20 J=3,7,2
      JS=JT+J
      JC=JC+1
      JR=(I-1)*3+JC
```

```
C REJECT FRAMES WITH PHASE MAGNITUDE UNDER 40 AS TOO WEAK
C REJECT FRAMES WITH PHASE MAGNITUDE OF 511 DUE TO A/D SATURATION
      NPK=MAXO(IABS(IFR(JS,ICOL)),IABS(IFR(JS+2,ICOL)),IABS(IFR
     1(JS+4,ICOL)),IABS(IFR(JS+6,ICOL)))
      IF(NPK.GE.511.OR.NPK.LT.40)GO TO 60
C CALCULATE DOPPLER BASED ON SINE,COS,SINE,COS SEQUENCE
      B1=FLOAT(IFR(JS,ICOL))
      B2=FLOAT(IFR(JS+2,ICOL))
      B3=FLOAT(IFR(JS+4,ICOL))
      B4=FLOAT(IFR(JS+6,ICOL))
      B5=B2*B3-B1*B4
      B6=B2*B2+B1*B3
      B7=B3*B3+B2*B4
      B8=B6*B7
      IF(B8.LE.0.)GO TO 60
      B9=2.*SQRT(B8)
      DOPL1=B5/B9
      SSQ1=DOPL1*DOPL1
      CSQ1=1.-SSQ1
      IF(CSQ1.LT.0.)GO TO 60
      COS1=SQRT(CSQ1)
      IF(COS1.LE.0.)GO TO 60
      ALPHA1=ATAN2(DOPL1,COS1)
C ADJUSTMENT REQUIRED IF SEQUENCE WAS REALLY COS,SINE,COS,SINE
      IF(J.EQ.5)ALPHA1=-ALPHA1
      AVEL(JR)=PRF*ALPHA1*0.5
      GO TO 50
C DEFAULT CASE
60    AVEL(JR)=999.
50    CONTINUE
20    CONTINUE
10    CONTINUE
      RETURN
      END


      SUBROUTINE ACC2(IPKC,IPKF,ICOL,NCPF,VM,VSD,VM1,VSD1,IGO)
C DETERMINES WHETHER METEOR ECHO IS ACCEPTABLE ON THE BASIS OF
C WIND VELOCITY RESULTS
C G C HESS
C 4-24-75
C EDIT #1
C
      COMMON/B/IFR(135,3),KM(100),LM(1400),IF1(1500),IF2(1500),
     1ARNG(18),AVEL(27),AVSD(27),ACEL(9),AFEL(9),AAZ(9)
C REQUIRE AT LEAST 2 FULL FRAMES (6 VELOCITY CALCULATIONS) OF USEFUL
C VELOCITY RESULTS TO ACCEPT AN ECHO
C ONLY FRAMES FOLLOWING THE YAGI VIDEO PEAK ARE CONSIDERED SO FRESNEL
C OSCILLATION EFFECTS ARE MINIMIZED
      IUSE=0
      IF(IPKC.EQ.14)IPKF=IPKF+1
      IF(IPKF.GE.9)GO TO 60
      DO 10 I=1,9
      DO 20 J=1,3
      ILOC=(I-1)*3+J
      IF(I.LT.IPKF)AVEL(ILOC)=999.
      IF(AVEL(ILOC).GT.200.)GO TO 15
      IUSE=IUSE+1
      K=(IPKF-1)*NCPF+1+2*J
      NPK=MAXO(IABS(IFR(K,ICOL)),IABS(IFR(K+2,ICOL)),IABS(IFR(K+4,
     1ICOL)),IABS(IFR(K+6,ICOL)))
C CALCULATE INSTRUMENTAL ACCURACY BASED ON PEAK SIGNAL STRENGTH
      AVSD(ILOC)=720./FLOAT(NPK)
      GO TO 20
C IN UNUSEABLE CASES VEL AND STD DEV ARE SET TO 999.
15    AVSD(ILOC)=999.
20    CONTINUE
10    CONTINUE
      IF(IUSE.LT.4)GO TO 60
C CALCULATE THE MEAN VELOCITY AND INSTRUMENTAL STD DEV (WEIGHTED)
      VM=0.
      VSD=0.
      DO 30 I=1,27
      IF(AVEL(I).GT.200.)GO TO 30
      VM=VM+(AVEL(I)/(AVSD(I)*AVSD(I)))
      VSD=VSD+(1./(AVSD(I)*AVSD(I)))
30    CONTINUE
      VSD=1./SQRT(VSD)
      VM=VM*VSD*VSD
C CALCULATE THE MEAN VELOCITY AND SAMPLE STD DEV (UNWEIGHTED)
      VM1=0.
      VSD1=0.
      DO 40 I=1,27
```

```
      IF(AVEL(I).GT.200.)GO TO 40
      VMI=VMI+AVEL(I)
40    CONTINUE
      VMI=VMI/FLOAT(IUSE)
      DO 50 I=1,27
      IF(AVEL(I).GT.200.)GO TO 50
      VSDI=VSDI+(AVEL(I)-VMI)**2
50    CONTINUE
      VSDI=SQRT(VSDI/FLOAT(IUSE-1))
C REQUIRE WEIGHTED AND UNWEIGHTED WINDS TO AGREE WITHIN 15 M/S
      IF(ABS(VM-VMI).GE.15.)GO TO 60
C REQUIRE SAMPLE DEVIATION TO BE UNDER 30 M/S
      IF(VSDI.GE.30.)GO TO 60
      IGO=1
      RETURN
C DEFAULT CASE
60    IGO=0
      RETURN
      END


      SUBROUTINE DECAYH(IPKC,IPKF,NCPF,PRF,DHT,DECAY)
C CALCULATES ECHO HEIGHT BASED ON RATE OF YAGI VIDEO DECAY
C G C HESS, EDIT#1,8/15/75
      COMMON/C/HHT(81),DC(81)
      COMMON/B/IFR(135,3),KM(100),LM(1400),IF1(1500),IF2(1500),
      1ARNG(18),AVEL(27),AVSD(27),ACEL(9),AFEL(9),AAZ(9)
      SUMYV=0.
      SUMTI=0.
      SUMVT=0.
      SUMT2=0.
      ICT=0
      IF(IPKF.GT.8)GO TO 30
      DO 10 I=IPKF,9
      JT=(I-1)*NCPF
      DO 20 J=1,14,13
      IF(I.EQ.IPKF.AND.J.EQ.1.AND.IPKF.EQ.14)GO TO 20
      JS=JT+J
C STOP WHEN YAGI VIDEO FALLS BELOW 40
      IF(IFR(JS,2).LT.40)GO TO 40
      ICT=ICT+1
      S1=ALOG(FLOAT(IFR(JS,2)))
C CONSIDER TIME OF FIRST ACCEPTED YAGI SAMPLE AS ZERO
      IF(ICT.EQ.1)JS1=JS
      S2=FLOAT(JS-JS1)*0.583413/PRF
      SUMYV=SUMYV+S1
      SUMTI=SUMTI+S2
      SUMVT=SUMVT+S1*S2
      SUMT2=SUMT2+S2*S2
20    CONTINUE
10    CONTINUE
30    CONTINUE
C REQUIRE AT LEAST 3 POINTS FOR DECAY CURVE FIT
C USE 999KM AS THE DEFAULT VALUE
40    IF(ICT.LT.3)GO TO 70
C DECAY RATE LEAST SQUARE FIT SOLUTION
      SLOPEN=FLOAT(ICT)*SUMVT-SUMYV*SUMTI
      SLOPED=FLOAT(ICT)*SUMT2-SUMTI*SUMTI
      IF(SLOPED.EQ.0.)GO TO 70
      SLOPE=SLOPEN/SLOPED
      DECAY=-3404.*SLOPE
C LINEARLY INTERPOLATE ECHO HEIGHT FROM THE HHT AND DC ARRAYS
      DO 50 I=1,80
      IF(DC(I).LE.DECAY.AND.DC(I+1).GE.DECAY)GO TO 60
      IF(I.EQ.80)GO TO 70
50    CONTINUE
60    DHT=HHT(I)+(HHT(I+1)-HHT(I))*(DECAY-DC(I))/(DC(I+1)-DC(I))
      RETURN
70    DHT=999.
      RETURN
      END


      SUBROUTINE ANGLE(NCPF,ICOL,KPRF)
C DETERMINES ANTENNA ANGLE DIFFERENCES FOR USE IN CALCULATING METEOR
C ECHO ELEVATION AND AZIMUTH ANGLES
C COARSE ELEV FROM CH 2,3,4,5
C FINE ELEV FROM CH 6,7,8,9
C AZIMUTH FROM CH 10,11,12,13
C G C HESS
C 4-24-75
C EDIT #1
C
```

```
      COMMON/B/IFR(135,3),KM(100),LM(1400),IF1(1500),IF2(1500),
      1ARNG(18),AVEL(27),AVSD(27),ACEL(9),AFEL(9),AAZ(9)
      T=(1./FLOAT(KPRF))*1.714048
C PHASE CALIBRATION VALUES (USER INSERTED)
      CEADJ=-3.83
      FEADJ=-3.83
      AZADJ=-3.83
      DO 10 I=1,9
      II=(I-1)*3
      JS=(I-1)*NCPF
C COARSE ELEVATION
      M1=FLOAT(IFR(JS+2,ICOL))
      M3=FLOAT(IFR(JS+3,ICOL))
      M2=FLOAT(IFR(JS+4,ICOL))
      M4=FLOAT(IFR(JS+5,ICOL))
      IF(AVEL(II+1).GT.200.)GO TO 20
      D1=AVEL(II+1)
      D1=D1*T
      D2=-3.*D1
      D3=-D1
      D4=-D1
      Y=YTERM(M1,M2,M3,M4,D1,D2,D3,D4)
      X=XTERM(M1,M2,M3,M4,D1,D2,D3,D4)
      Z=X*X+Y*Y
      IF(Z.LE.0.)GO TO 20
      SCE=Y
      CCE=X
      IF(CCE.EQ.0.)GO TO 20
      CEANG=-ATAN2(SCE,CCE)
      CEANG=CEANG-CEADJ
      ACEL(I)=CEANG
C PUT ALL ANGLES IN UNIPOLAR FORMAT
      IF(ACEL(I).LT.0.)ACEL(I)=ACEL(I)+6.28319
      GO TO 30
C DEFAULT CASE
20    ACEL(I)=999.
C FINE ELEVATION
30    M1=FLOAT(IFR(JS+6,ICOL))
      M3=FLOAT(IFR(JS+7,ICOL))
      M2=FLOAT(IFR(JS+8,ICOL))
      M4=FLOAT(IFR(JS+9,ICOL))
      D1=(AVEL(II+1)+AVEL(II+2))/2.
      IF(AVEL(II+1).GT.200.)D1=AVEL(II+2)
      IF(AVEL(II+2).GT.200.)D1=AVEL(II+1)
      IF(D1.GT.200.)GO TO 40
      D1=D1*T
      D2=-3.*D1
      D3=-D1
      D4=-D1
      Y=YTERM(M1,M2,M3,M4,D1,D2,D3,D4)
      X=XTERM(M1,M2,M3,M4,D1,D2,D3,D4)
      Z=X*X+Y*Y
      IF(Z.LE.0.)GO TO 40
      SFE=Y
      CFE=X
      IF(CFE.EQ.0.)GO TO 40
      FEANG=-ATAN2(SFE,CFE)
      FEANG=FEANG-FEADJ
      AFEL(I)=FEANG
      IF(AFEL(I).LT.0.)AFEL(I)=AFEL(I)+6.28319
      GO TO 50
40    AFEL(I)=999.
C AZIMUTH
50    M1=FLOAT(IFR(JS+10,ICOL))
      M3=FLOAT(IFR(JS+11,ICOL))
      M2=FLOAT(IFR(JS+12,ICOL))
      M4=FLOAT(IFR(JS+13,ICOL))
      D1=(AVEL(II+2)+AVEL(II+3))/2.
      IF(AVEL(II+2).GT.200.)D1=AVEL(II+3)
      IF(AVEL(II+3).GT.200.)D1=AVEL(II+2)
      IF(D1.GT.200.)GO TO 60
      D1=D1*T
      D2=-3.*D1
      D3=-D1
      D4=-D1
      Y=YTERM(M1,M2,M3,M4,D1,D2,D3,D4)
      X=XTERM(M1,M2,M3,M4,D1,D2,D3,D4)
      Z=X*X+Y*Y
      IF(Z.LE.0.)GO TO 60
      SAZ=Y
      CAZ=X
      IF(CAZ.EQ.0.)GO TO 60
      AZANG=-ATAN2(SAZ,CAZ)
      AZANG=AZANG-AZADJ
```

```
      AAZ(I)=AZANG
      IF(AAZ(I).LT.0.)AAZ(I)=AAZ(I)+6.28319
      GO TO 70
60    AAZ(I)=999.
70    CONTINUE
10    CONTINUE
      RETURN
      END


      FUNCTION XTERM(M1,M2,M3,M4,O1,O2,O3,O4)
      XTERM=FLOAT(M1*M3)*COS(O3)+FLOAT(M1*M4)*SIN(O1)-
     1FLOAT(M2*M3)*SIN(O2)+FLOAT(M2*M4)*COS(O4)
      RETURN
      END


      FUNCTION YTERM(M1,M2,M3,M4,O1,O2,O3,O4)
      YTERM=FLOAT(M1*M4)*COS(O1)-FLOAT(M2*M3)*COS(O2)-
     1FLOAT(M1*M3)*SIN(O3)-FLOAT(M2*M4)*SIN(O4)
      RETURN
      END


      SUBROUTINE ACC3S(AZ,AZSD,EL,ELSD,IGO)
C EXTRACTS ELEVATION ANGLE FROM STACKED YAGI RECEIVE ANTENNA CONFIGURATION
C G C HESS
C 6-4-75
C EDIT#1
C
      COMMON/B/IFR(135,3),KM(100),LM(1400),IF1(1500),IF2(1500),
     1ARNG(18),AVEL(27),AVSD(27),ACEL(9),AFEL(9),AAZ(9)
      COMMON/D/EL92(13),ELC(13)
C ANTENNA SPACING PARAMETER (USER INPUT)
      DCEL=.2114
C CALIBRATION VALUE
      IUSE=0
      PI=3.141593
      PI1=2.*PI
      REF=4.73
      DO 10 I=1,9
      IF(ACEL(I).GT.200.)GO TO 20
      IF(ACEL(I).GT.PI1)ACEL(I)=ACEL(I)-PI1
      IF(ACEL(I).GT.REF)ACEL(I)=REF
      SEL=ACEL(I)*DCEL
      IF(SEL.GE.1.)GO TO 20
      CEL=SQRT(1.-SEL*SEL)
      ACEL(I)=ATAN2(SEL,CEL)
      IUSE=IUSE+1
20    CONTINUE
      IF(AFEL(I).GT.200.)GO TO 30
      IF(AFEL(I).GT.PI1)AFEL(I)=AFEL(I)-PI1
      IF(AFEL(I).GT.REF)AFEL(I)=REF
      SFEL=AFEL(I)*DCEL
      IF(SFEL.GE.1.)GO TO 30
      CFEL=SQRT(1.-SFEL*SFEL)
      AFEL(I)=ATAN2(SFEL,CFEL)
      IUSE=IUSE+1
30    CONTINUE
      IF(AAZ(I).GT.200.)GO TO 40
      IF(AAZ(I).GT.PI1)AAZ(I)=AAZ(I)-PI1
      IF(AAZ(I).GT.REF)AAZ(I)=REF
      SAZ=AAZ(I)*DCEL
      IF(SAZ.GE.1.)GO TO 40
      CAZ=SQRT(1.-SAZ*SAZ)
      AAZ(I)=ATAN2(SAZ,CAZ)
      IUSE=IUSE+1
40    CONTINUE
10    CONTINUE
      IF(IUSE.LT.4)GO TO 50
C CALCULATE MEAN AND STD DEV FOR ELEVATION ANGLE
      I2ND=0
90    CONTINUE
      EL=0.
      IUSE=0
      DO 60 I=1,9
      IF(AAZ(I).GT.200.)GO TO 61
      EL=EL+AAZ(I)
      IUSE=IUSE+1
61    IF(ACEL(I).GT.200.)GO TO 62
      EL=EL+ACEL(I)
      IUSE=IUSE+1
62    IF(AFEL(I).GT.200.)GO TO 60
```

```
        EL=EL+AFEL(I)
        IUSE=IUSE+1
60      CONTINUE
        EL=EL/FLOAT(IUSE)
        ELSD=0.
        DO 70 I=1,9
        IF(AAZ(I).LT.200.)ELSD=ELSD+(AAZ(I)-EL)**2
        IF(ACEL(I).LT.200.)ELSD=ELSD+(ACEL(I)-EL)**2
        IF(AFEL(I).LT.200.)ELSD=ELSD+(AFEL(I)-EL)**2
70      CONTINUE
        ELSD=SQRT(ELSD/FLOAT(IUSE-1))
        IF(I2ND.EQ.1)GO TO 100
C REJECT VALUES NOT WITHIN 2 SIGMA OF MEAN
        EUP=EL+ELSD
        ELW=EL-ELSD
        DO 80 I=1,9
        IF(AAZ(I).LT.ELW.OR.AAZ(I).GT.EUP)AAZ(I)=999.
        IF(ACEL(I).LT.ELW.OR.ACEL(I).GT.EUP)ACEL(I)=999.
        IF(AFEL(I).LT.ELW.OR.AFEL(I).GT.EUP)AFEL(I)=999.
80      CONTINUE
        I2ND=1
        GO TO 90
100     IGO=1
        AZ=0.
        AZSD=0.
        IF(EL.GT.EL92(1))GO TO 120
        DO 140 I=1,12
        IF(EL.LE.EL92(I).AND.EL.GE.EL92(I+1))GO TO 110
140     CONTINUE
C EL.LT.EL92(13)
110     J=I+1
        ADJ=ELC(I)+(ELC(J)-ELC(I))*(EL-EL92(I))/(EL92(J)-EL92(I))
        GO TO 130
120     ADJ=0.
130     EL=EL+ADJ
        RETURN
90      IGO=0
        RETURN
        END


        SUBROUTINE HEIGHT(RNG,RNGSD,EL,ELSD,HT,HTSD)
C CALCULATES HEIGHT FROM RANGE AND ELEVATION DATA
C ALLOWS FOR CURVATURE OF THE EARTH
C G C HESS
C 4-24-75
C EDIT #1
C
C SPECIFY EARTH'S RADIUS IN KM
        A=6371.
        X=RNG/A
C EVALUATE MEAN HEIGHT
        HT=(SIN(EL)+.5*X-.5*X*SIN(EL)*SIN(EL))*RNG
C EVALUATE ACCURACY
        IF(ELSD.GT.200.)GO TO 10
        HTSD=SQRT((SIN(EL)*RNGSD)**2+(RNG*COS(EL)*ELSD)**2)
        RETURN
10      HTSD=999.
        RETURN
        END


/###############   INTER SUBROUTINE TO RETURN DATA SWITCH VALUE   ##########
/                                 USED WITH PULCHK
/
/
        .TITLE  INTER
        .GLOBL  INTER,.DA
INTER   0
        JMS*    .DA
        JMP     .+2
A       0
        LAS
        DAC*    A
        JMP*    INTER
        .END


        SUBROUTINE STORE(KK,FNR1,FOUT)
C STORES ECHO DATA PERMANENTLY ON DATA SLOT 2
C HANDLES 50 ECHOES AT A TIME
C G C HESS
C 4-25-75
C EDIT #1
```

```
C
      DIMENSION FSRT(2),ITIM(4),FOUT(2),RG(50),V(50),A(50)
      DIMENSION E(50),H(50),T(50),FREF(2)
      DATA FREF(1),FREF(2)/5HTESTA,4H00DA/
      FSRT(1)=FREF(1)
      FSRT(2)=FREF(2)
5     CONTINUE
      CALL AFILE(FOUT)
      WRITE(6,120)FOUT
120   FORMAT(//5X,21H PROCESSED DATA FILE=,2A5/)
      CALL ENTER(2,FOUT)
      WRITE(2,18)
18    FORMAT(//)
      IFN=50/KK
      LMN=0
      DO 15 I=1,IFN
      CALL AFILE(FSRT)
      CALL FSTAT(1,FSRT,IF)
      IF(IF.EQ.0)GO TO 5
      CALL SEEK(1,FSRT)
      READ(1,18)
      DO 10 J=1,KK
      LMN=LMN+1
      READ(1)(ITIM(II),II=1,4),DMAXY,DYD,RG(LMN),RNGSD,V(LMN),VSD,
     1VM1,VSD1,A(LMN),AZSD,E(LMN),ELSD,H(LMN),HTSD,DHT,DECAY
      T(LMN)=FLOAT((ITIM(1)*10+ITIM(2))*60+(ITIM(3)*10+ITIM(4)))/60.
      WRITE(2)T(LMN),DMAXY,DYD,RG(LMN),RNGSD,V(LMN),VSD,VM1,VSD1,
     1A(LMN),AZSD,E(LMN),ELSD,H(LMN),HTSD,DHT,DECAY
10    CONTINUE
15    CONTINUE
90    CALL CLOSE(2)
C CALCULATE MEAN TIME,WIND,RANGE,AZIMUTH,ELEVATION,AND HEIGHT
      TM=0.
      VM=0.
      RGM=0.
      AM=0.
      EM=0.
      HM=0.
      IA=0
      IE=0
      IH=0
      DO 30 I=1,50
      TM=TM+T(I)
      VM=VM+V(I)
      RGM=RGM+RG(I)
      IF(A(I).GT.200.)GO TO 200
      IA=IA+1
      AM=AM+A(I)
200   IF(E(I).GT.200.)GO TO 210
      IE=IE+1
      EM=EM+E(I)
210   IF(H(I).LT.75..OR.H(I).GT.120.)GO TO 220
      IH=IH+1
      HM=HM+H(I)
220   CONTINUE
30    CONTINUE
      TM=TM/50.
      VM=VM/50.
      RGM=RGM/50.
      AM=(AM/FLOAT(IA))*57.29578
      EM=(EM/FLOAT(IE))*57.29578
      HM=HM/FLOAT(IH)
      WRITE(6,520)TM,VM,RGM,AM,EM,HM
520   FORMAT(/4H TM=,F7.2,4H VM=,F7.2,4H RM=,F7.2,4H AM=,F7.2,4H EM=,
     1F7.2,4H HM=,F7.2//)
      WRITE(6,530)IA,IE,IH
530   FORMAT(3(1X,I4)//)
      RETURN
      END
```

APPENDIX III

BIAS OF CLIPPED MEAN ESTIMATOR

$$P(v) = \frac{K}{\sqrt{2\pi\sigma^2}} \exp\left[-\frac{(v-V_o)}{2\sigma 2}\right] \qquad \text{III.1}$$

where K is value required to make

$$\int_{-V_L}^{V_L} p(v)dv = 1$$

i.e.,

$$K = \frac{2}{erf\left(\frac{(V_L-V_o)}{\sqrt{2\sigma}}\right) + erf\left(\frac{(V_L+V_o)}{\sqrt{2\sigma}}\right)} \qquad \text{III.2}$$

with

$$erf(x) \triangleq \frac{2}{\sqrt{\pi}} \int_o^x \exp(-t^2)dt$$

The expected value of our estimator is given by

$$V_E = \frac{K\sigma}{\sqrt{\pi}}\left[\exp(-a^2)-\exp(-b^2)\right] + V_o \qquad \text{III.3}$$

where

$$a \triangleq (V_L+V_o)/\sqrt{2\sigma}$$

$$b \triangleq (V_L-V_o)/\sqrt{2\sigma}$$

Estimator bias is given by

$$V_E - V_o = \sqrt{\frac{2}{\pi}}\,\sigma\left[\frac{\exp(-a^2) - \exp(-b^2)}{erf(a) + erf(b)}\right] \qquad \text{III.4}$$

Case

1. $V_o > o \rightarrow b^2 < a^2 \rightarrow V_E - V_o < o \rightarrow V_E < V_o$

2. $V_o < o \rightarrow b^2 > a^2 \rightarrow V_E\ V_o > o \rightarrow V_E > V_o$

i.e., magnitude is underestimated in both cases.

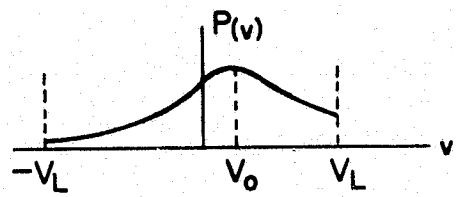

Figure III.1 Probability density model of wind velocities I.

APPENDIX IV

BIAS OF ZERO CROSSING ALGORITHMS WHICH DISCRIMINATE AGAINST LOW VELOCITIES

$$p(v) = \frac{K}{\sqrt{2\pi\sigma^2}} \exp\left[-\frac{(v-V_o)^2}{2\sigma^2}\right] \qquad \begin{matrix} -\infty < v \leq -V_D \\ V_D \leq v < \infty \end{matrix} \qquad \text{IV.1}$$

where

K is the value required to make

$$1 = \int_{-\infty}^{-V_D} p(v)dv + \int_{V_D}^{\infty} p(v)dv$$

i.e., $$K = 2/[2\text{-}erf(a) - erf(b)] \qquad \text{IV.2}$$

where

$$a \triangleq (V_D+V_o)/\sqrt{2}\,\sigma$$

$$b \triangleq (V_D-V_o)/\sqrt{2}\,\sigma$$

The expected value of the mean wind is

$$V_E = \sqrt{\frac{2}{\pi}}\,\sigma\left[\frac{\exp(-b^2) - \exp(-a^2)}{2\text{-}erf(b) - erf(a)}\right] + V_o \qquad \text{IV.3}$$

implying a bias of

$$V_E - V_o = \sqrt{\frac{2}{\pi}}\,\sigma \frac{\left[\exp\left[-\left(\frac{V_o(\alpha-1)}{\sqrt{2}\,\sigma}\right)^2\right] - \exp\left[-\left(\frac{V_o(\alpha+1)}{\sqrt{2}\,\sigma}\right)^2\right]\right]}{\left[2\text{-}erf\left(\frac{V_o(\alpha-1)}{\sqrt{2}\,\sigma}\right) - erf\left(\frac{V_o(\alpha+1)}{\sqrt{2}\,\sigma}\right)\right]}$$

where $\alpha \triangleq V_D/V_o$. Note that for finite V_D, only the cases of true mean wind zero or infinite result in no bias. A typical value of α might be 0.4 (V_D = 10 m s^{-1}, V_o = 25 m s^{-1}) and along with a representative geophysical noise of 25 m s^{-1} this results in a bias of 5.7 m s^{-1}.

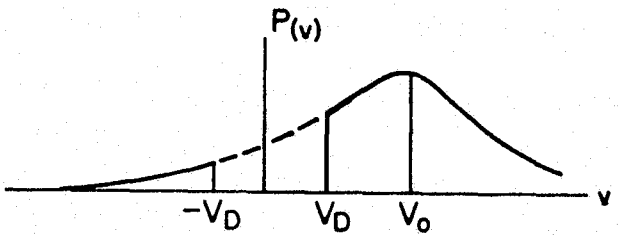

Figure IV.1 Probability density model of wind velocities II.